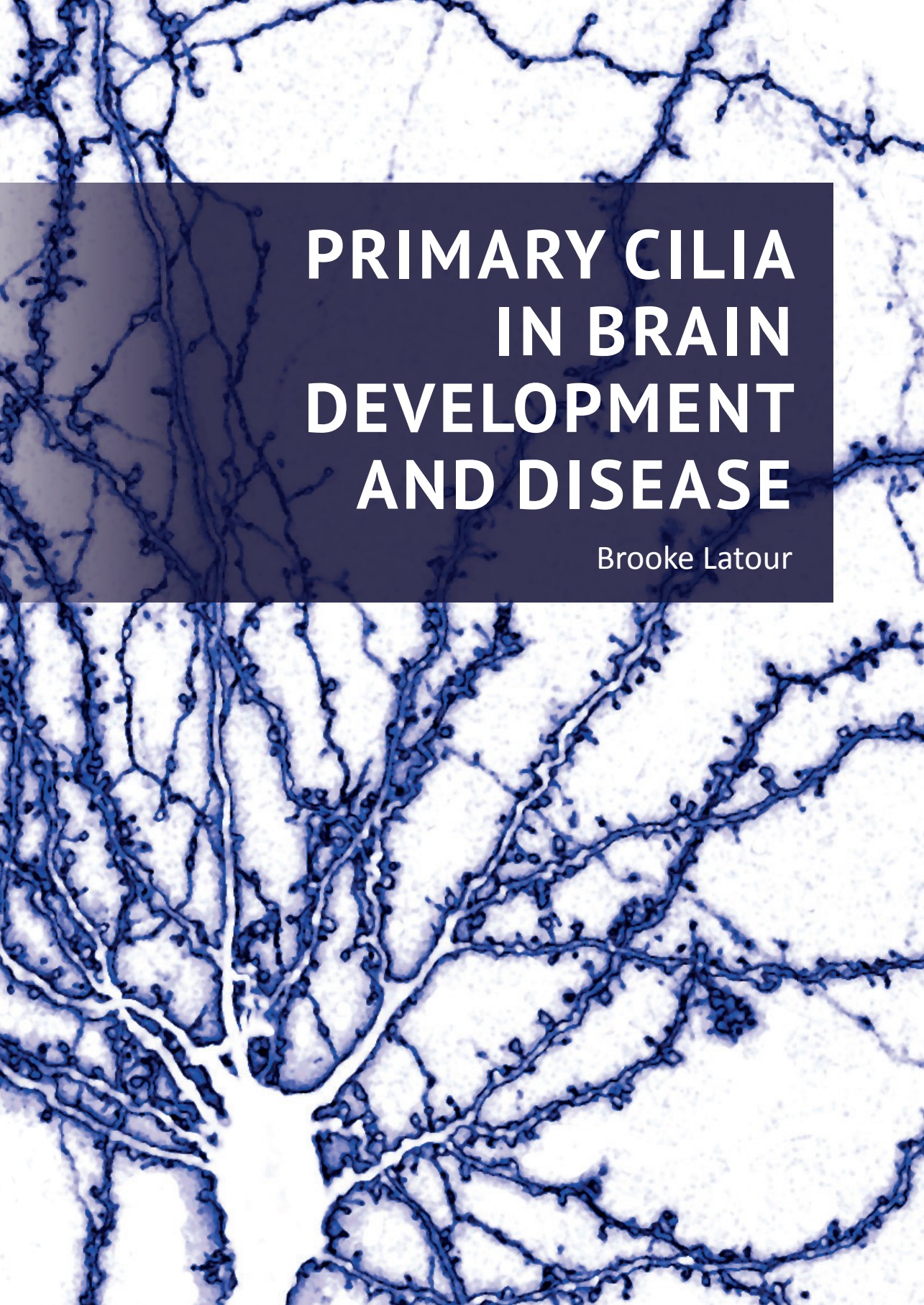

PRIMARY CILIA IN BRAIN DEVELOPMENT AND DISEASE

Brooke Latour

Primary cilia in brain development and disease

Brooke Latour

The work presented in this thesis was carried out within the Radboud Institute for Molecular Life Sciences (RIMLS), at the Department of Human Genetics of the Radboud university medical center (Radboudumc) in Nijmegen, the Netherlands.

The printing of this thesis was generously funded by the Radboudumc.

About the cover: “A Self Portrait” rendered from a collapsed z-stack imaged on the LSM880 confocal microscope equiped with airyscan technology, of a biocytin filled pyramidal neuron in the auditory cortex layer 2/3 (P12-P15 mouse).

ISBN:	978-94-6458-006-8
Cover image & idea:	Brooke Latour
Cover design & lay-out:	Publiss | www.publiss.nl
Print:	Ridderprint | www.ridderprint.nl

Primary cilia in brain development and disease

Proefschrift ter verkrijging van de graad van doctor
aan de Radboud Universiteit Nijmegen
op gezag van de rector magnificus,
volgens besluit van het college voor promoties
in het openbaar te verdedigen op

donderdag 16 juni 2022
om 12.30 uur precies

door

Brooke Latour
geboren op 15 september 1983
te Los Angeles, California, USA

Promotor(en):

Prof. dr. Ronald Roepman

Co-promotor(en):

Prof. dr. Nael Nadif Kasri

Manuscriptcommissie:

Prof. dr. Alessandra Cambi (Radboud University Medical Centre, Netherlands)

Prof. dr. Anna Akhmanova (Utrecht University Medical Centre, Netherlands)

Prof. dr. Colin Johnson (University of Leeds, United Kingdom)

Primary cilia in brain development and disease

Dissertation to obtain the degree of doctor
from Radboud University Nijmegen
on the authority of the Rector Magnificus,
according to the decision of the Doctorate Board
to be defended in public on

Thursday, June 16, 2022
at 12.30 pm

by

Brooke Latour
born on September 15, 1983
in Los Angeles, California, USA

Promotor:

Prof. dr. Ronald Roepman

Co-promotor:

Prof. dr. Nael Nadif Kasri

Manuscript committee:

Prof. dr. Alessandra Cambi (Radboud University Medical Centre, Netherlands)

Prof. dr. Anna Akhmanova (Utrecht University Medical Centre, Netherlands)

Prof. dr. Colin Johnson (University of Leeds, United Kingdom)

Content

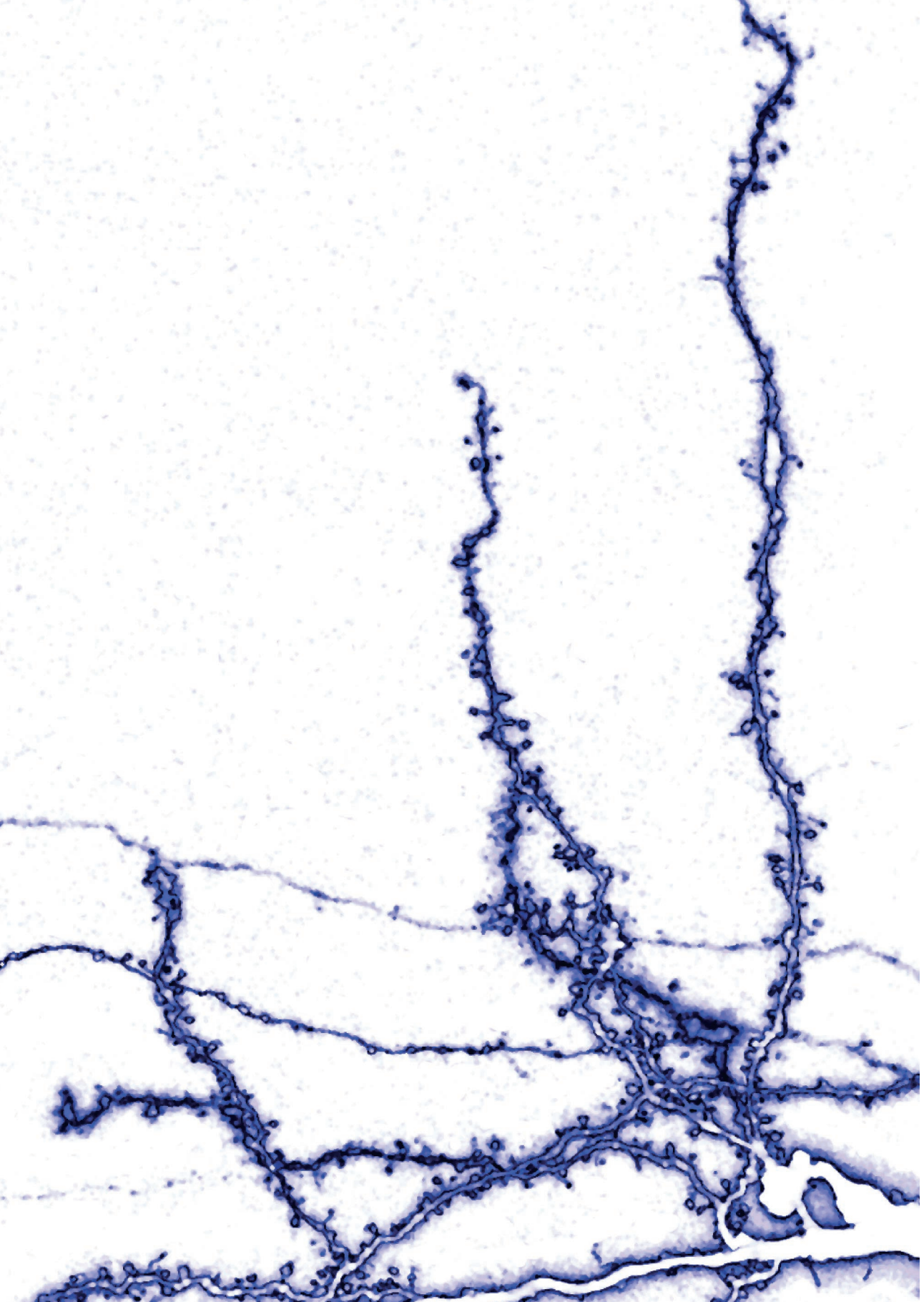

CHAPTER 1

Introduction

CHAPTER 1: GENERAL INTRODUCTION OUTLINE

1. THE PRIMARY CILIUM AND BRAIN DEVELOPMENT

Brain development is a complex and dynamic process that requires fine-tuned regulation of neural progenitor specification, neurogenesis, neuronal migration, and neuronal wiring to form complex neural networks and higher-order cognition. At a volumetric size of about 1350 cubic centimeters, the human brain contains approximately 100 billion neurons, 20% of which lie within the cerebral cortex. Each of these cortical neurons forms an average of 7000 synaptic connections to other neurons, resulting in roughly 150 trillion synapses and more than 150,000 km of myelinated nerve fiber [1]. During the process of corticogenesis, an effective intracellular response to extracellular cues is essential for the proper coordination of temporal and spatial events that underlie the formation of the cerebral cortex.

Named for its eyelash-like appearance, the cilium, or plural cilia, is a microtubule based, mother centriole derived, antenna-like structure that protrudes from the surface of most vertebrate cell types [2]. Primary cilia are cellular signaling hubs, highly enriched with receptors, ion channels, and effector proteins. They effectively decode a variety of extracellular cues including sensory stimuli such as light, sound, odor, chemical and signaling ligands [3–6] (Figure 1) to facilitate appropriate cellular responses. The primary cilium is essential for integration and transmission of signal transduction and due to the complexities in their architecture, multiple independent regulatory mechanisms and signaling cascades are able to effectively coincide. Hedgehog [7], Wnt [8], Notch [9], mTOR [10,11], and TGFβ [12] signaling have all been associated with the primary cilium.

Due to their function as a signaling hub, primary cilia play a unique and essential role in central nervous system patterning via progenitor cell specification [13,14], neuronal migration [15], and neuronal circuitry formation [16]. Neurons, in addition to their complex web of axons and dendrites, rely on primary cilia to sense and respond to their environment [17]. The importance of primary cilia in brain development and neuronal network formation is highlighted by the vast array of neurodevelopmental disorders, including neural tube defects, cortical and cerebellar malformation, and intellectual disabilities, that result from genetic disruption of ciliary architecture and/or function [18–21]. Genetic disorders that result from dysfunction of the cilium are known as ciliopathies. A large subset of ciliopathy-associated genes are linked to neurological defects [22] indicating that impaired ciliary function impacts brain development.

1.1. The cilium: structure and function

There are two types of cilia: motile and immotile (primary) cilia, also known as sensory cilia (Figure 1). The microtubules of the eukaryotic primary ciliary axoneme are typically structured

in a 9+0 fashion (reviewed in [23]) (Figure 1) and motile cilia have a core of 9 + 2 microtubule doublet structure with nine radially arranged microtubule doublets centering around a pair of singlets (Figure 1) known as the central pair. Motile cilia propel fluid, thereby controlling fluid and particle flow over epithelium as seen in airways [24], fallopian tubes [25], and brain ventricles [26]. The ependymal cilia that line the ventricles of the brain possess mechanoreceptive and chemoreceptive properties and are essential for directional cerebrospinal fluid flow (CSF) and proper ventricular development [27]. Primary cilia exist in solitude and were long believed to be vestigial remnants of their motile counterpart. However, research over the past several decades has demonstrated that this highly structured, polarized cellular organelle plays a critical part in neuronal development [28], tumorigenesis [29] and cellular homeostasis [30], as mutations in genes encoding ciliary proteins cause defects in these processes.

The cilium is composed of several subdomains that function together to regulate proper signal integration and transduction from the extracellular to intracellular space. Ciliogenesis is cell cycle dependent and requires cellular quiescence. The centrosome, made up of the mother and daughter barrel shaped centrioles and surrounded by pericentriolar material (PCM), acts as the main microtubule organizer of the cell. As the centrosome does not have a known function during interphase, it can repurpose its microtubule organizing potential at the cell surface to generate a cilium. The cilium is nucleated by microtubules extending from the basal body, a modified mother centriole (Figure 1). The ciliary axoneme is made up of αβ tubulin heterodimers that are post-translationally modified for mechanical stability [31–33] (Figure 1). The mother centriole docks at the plasma membrane via fibrous distal and subdistal appendages and matures into the basal body [34]. The basal body is a g-tubulin based, cartwheel-like structure formed from a core of nine triplets of A-, B-, and C-tubules. At the distal end of the basal body, the region where the centriolar microtubule triplets change to the microtubule doublets of the ciliary axoneme is called the transition zone (TZ). The transition fibers (TFs), also called distal appendages, which serve to mount the basal body to the plasma membrane, are a vesicle docking site where Golgi derived vesicles containing membrane lipids and transmembrane proteins are processed for ciliary entry [35] (Figure 1). Collectively the TFs and the TZ form the ciliary gate, a specialized permeability barrier between the ciliary compartment and the cytosol [36] (Figure 1).

The cilium relies on intraflagellar transport (IFT) for formation, maintenance and function [37–39]. IFT particles A and B are biochemically distinct complexes that participate in retrograde and anterograde transport respectively [40,41] (Figure 1). IFT-B and the molecular motor protein kinesin-II are required for transport from the ciliary base to the tip, mutations in IFT-B complex members, such as IFT88, or kinesin-II components, such as KIF3A, result in absent or acutely stunted cilia and severely attenuated intracellular signaling [42]. IFT-A and the cytoplasmic motor

protein dynein mediate transport from the ciliary tip to the cell. In the absence of proper IFT function, signal transduction pathways essential for tissue development and homeostasis are disrupted [42]. Mutations in components of IFT-A or dynein result in abnormal ciliary morphology due to the accumulation of proteins within the tip of the cilium [43,44]. This accumulation can result in a blockade of signal transduction or cause ectopic activation of signaling pathways.

1.2. Hedgehog signaling and neural specification

During mammalian development cell patterning and neuronal diversity in the ventral neural tube is coordinated in a temporal spatial fashion by ciliary specific signal transduction [19,43,45,46]. One of the principal ways in which the cilium shapes embryonic development is via its role in organizing hedgehog signaling. Hedgehog (Hh) signaling regulates a diverse array of cellular processes from tissue patterning during embryogenesis to adult tissue homeostasis and repair [47]. Erroneous activity associated with aberrant activation or inhibition of Hh signaling results in a variety of congenital malformations [48], defects in neuronal patterning [49,50], as well as tumorigenesis [51]. Specifically, Hh signaling is essential for proper dorsoventral patterning of the central nervous system [52,53]. Hh signaling propagates via the cilium, and all core components of the transduction pathway localize dynamically to the cilium upon pathway activation (Figure 2). In the absence of ligand, the membrane associated Patched (PTCH1) receptor acts as a repressor of Smoothened (SMO) by inhibiting its localization to the cilium. Upon ligand binding, the receptor ligand-complex is removed from the cilium and the co-receptor SMO moves into the cilium, allowing for downstream transcription of GLI dependent target genes via a complex interplay of post-translational modifications and protein translocations [47].

There are three mammalian Hh proteins that act as ligands to PTCH1: Sonic Hedgehog (SHH), Indian Hedgehog (IHH), and Desert Hedgehog (DHH). SHH and IHH have several, sometimes overlapping, functions in multiple tissues. SHH is essential in nervous system development and specification [59]. IHH plays an important role in endochondral ossification and other aspects of skeletal development, and DHH is restricted to the granulose cells of ovaries and Sertoli cells of testis [60].

The primary function of PTCH1 is to inhibit the activity of SMO and maintain pathway inactivation. Without SMO activation, the GLI transcriptional regulators are proteolytically cleaved into their repressive forms preventing transcription of Hh target genes. Proteolytic processing of GLI2 and GLI3 is contingent upon cAMP-dependent PKA activation, which is controlled by the Hh negative regulating GPCR, GPR161. Additionally, in the absence of ligand, GLI2 and GLI3 are sequestered by the Suppressor of Fused (SUFU) within the cilium and in the cytosol.

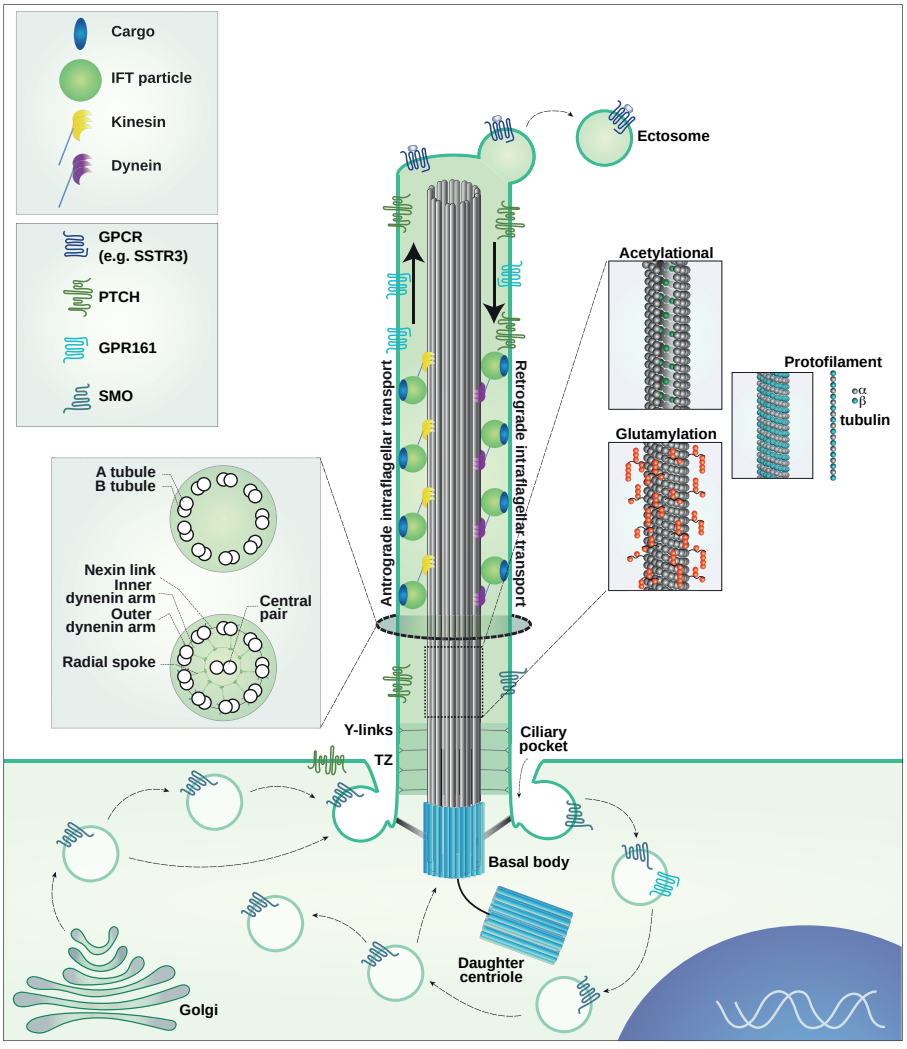

The formation of both activated and repressive forms of the GLI transcription factors requires trafficking into and out of the cilium. Upon induction, KIF7 blocks SUFU resulting in the dissociation of the SUFU/GLI complex and allowing for the induction of GLI2 activation [61]. Via activation, the Hh pathway potentiates transcription of negative regulators such as PTCH1 to maintain activation within an optimal range [47].

Localized at the ciliary tip, the kinesin 4 family motor protein KIF7 acts as both a negative and positive regulator of Hh signaling (Figure 2). KIF7 limits MT growth, increases the frequency of MT catastrophe, and controls ciliary architecture to create a single cilium tip compartment

◀**Figure 1: The cilium.** The cilium is a microtubule (MT) based structure that extends from the basal body, which is docked at the plasma membrane via transition fibers (TFs) [23]. The transition zone (TZ) is the intervening compartment between the basal body and the cilium proper. It is characterized by Y-links which anchor the MT to the ciliary membrane. The TZ acts to regulate the ingress and egress of proteins to the cilium. The ciliary pocket is an endocytic vesicle trafficking membrane domain contiguous with the cell membrane and found at the base of the cilium [54]. The ciliary membrane is enriched with ion channels and receptors concordant with the role of cilia in transducing signaling cascades. Motile and primary cilia differ in their core distribution of axonemal microtubules. The microtubules of the primary ciliary axoneme are typically structured in a 9+0 fashion and motile cilia have a core of 9 + 2 microtubule doublet structure with nine radially arranged microtubule doublets centering around a pair of singlets known as the central pair. Motile cilia utilize ATPase dependent dynein motors to generate sliding motions between the MT in order to beat. MT are tubular, cytoskeletal components consisting of α/β tubulin heterodimers organized in a plus to minus end fashion to form protofilaments. These protofilaments associate laterally to form a hollow tubular structure which have the capacity for dynamic changes in length and architecture. The radial doublets are formed from a complete A tubule, made up of 13 protofilaments, and an incomplete B tubule, made up of 10 protofilaments. The basal body and ciliary microtubules undergo a variety of highly conserved post-translational modifications, including acetylation and glutamylation, that function in a variety of processes including signal transduction [55,56], ciliary stability [32] and length regulation [57] Intraflagellar transport (IFT) involves the bidirectional movement of various proteins along microtubules via protein complexes termed IFT particles or trains. IFT-A mediates retrograde transport via dynein motors and IFT-B mediates anterograde transport via kinesin motor proteins. IFT functions in organizing effector proteins for signal transduction, ciliary assemble, disassembly and maintenance. In instances where activated G-protein coupled receptor (GPCR) cannot exit the cilium via IFT, ectocytosis at the ciliary tip attenuates signaling via the release of activated GCPR in extracellular vesicles called ectosomes [58].

for proper SUFU-GLI regulation [62]. Mutations in KIF7 disrupt Hh signaling via the impaired GLI3 processing and subsequent dysregulation of GLI target genes [63], resulting in fetal hydrolethalus and acrocallosal syndromes in humans [20], and agenesis of the corpus callosum in mice [46], suggesting an important role in neuronal tract formation.

Extensive research over the past decades has shown that Hh signaling is essential for regulating the development, patterning, and positioning of neural cell types in the central nervous system (CNS) during both early and late stages of embryogenesis [52,59,64,65].

1.3. Neurulation

During embryogenesis, following specification of the germ layers, neural fate is induced in the ectoderm by the underlying notochord, giving rise to the neural plate, a uniform sheet of neuroepithelium [45]. Neurulation, the first step in human brain development, subsequently follows and results in the folding of the neural plate into the neural tube (NT). The vertebrate neural tube is formed via the progressive adhesion and tissue fusion of opposing neural folds along the rostral caudal edge of the body axis. The opposing neural folds are comprised of neuroepithelium beneath non-neural, surface ectoderm. Both the neuroepithelium and surface ectoderm play an essential role in NT closure [45,66]. The surface ectoderm, made up of a single cell layer is the source of several signaling molecules such as bone morphogenic proteins (BMPs) [66] that regulate bending of the NT in the lower spinal region and mediate

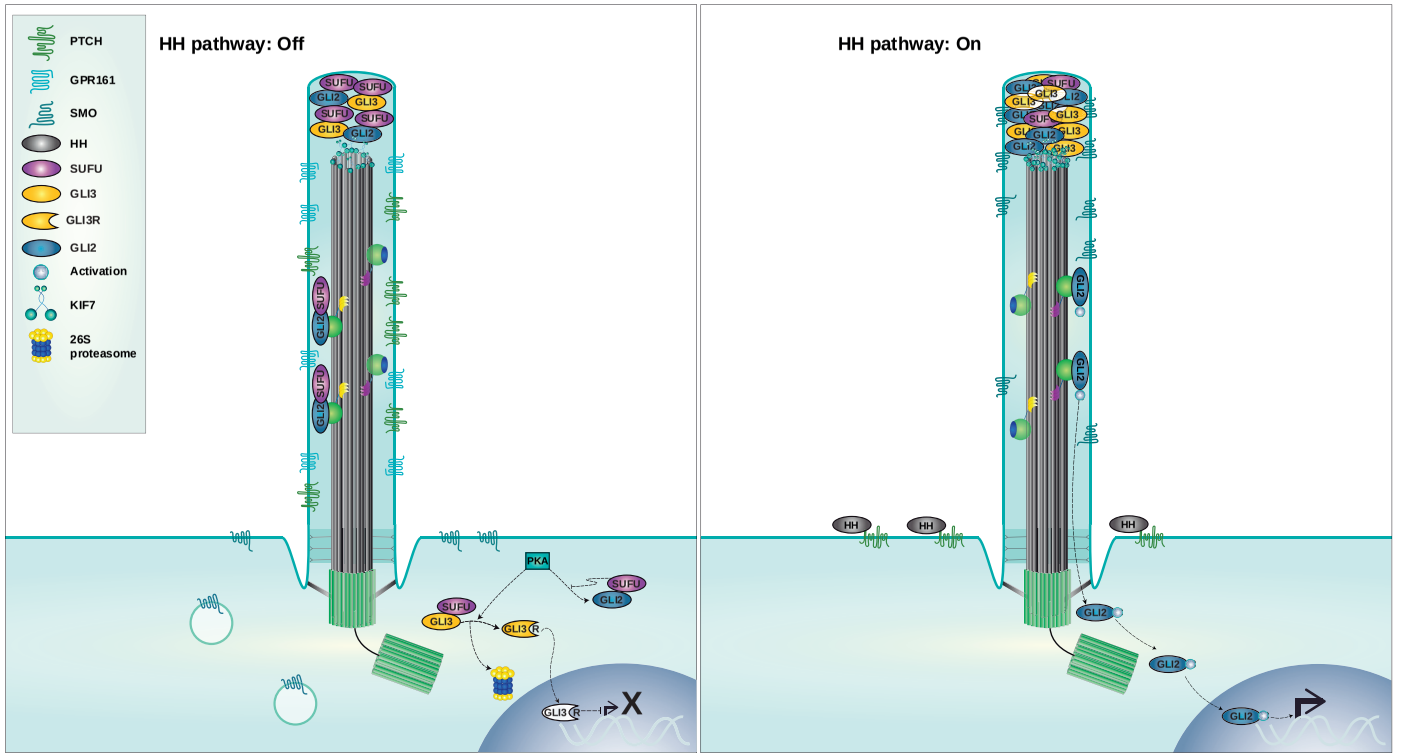

Figure 2: Hedgehog signaling. Hh signaling is transduced via the cilium [47]. The cilium contains several distinct subdomains that organize effective Hh signal transduction. The TZ acts as a critical regulator of ciliary composition and effectors of the Hh signaling pathway localize to the cilium in a dynamic manner. During basal conditions, in the absence of ligand, the 12-pass transmembrane receptor PTCH1 [7] is enriched in the ciliary membrane and inhibits the activity and entry of SMO in the ciliary compartment. In the absence of SMO activation, several negative regulators of Hh signaling, including GPR161 and SUFU, inhibit downstream GLI-mediated transcription of Hh target genes. The GPCR GPR161[69] is targeted to the cilium to activate adenylyl cyclases which in turn leads to increased levels of cAMP-mediated protein kinase A (PKA) activation. Activated PKA phosphorylates full length GLI3 resulting in its proteolytic cleavage into repressor form (GLI3R). GLI3R translocates to the nucleus and blocks transcription of Hh target genes. Both response to Hh ligand and the formation of the repressor form of the GLI transcription factors are dependent upon an intact cilium. SUFU prevents GLI activation in the absence of ligand by sequestering GLI3 and promoting its proteolytic processing. The ciliary tip compartment, defined by the kinesin motor protein KIF7, is enriched with GLI transcription factors that are held in SUFU/GLI complexes which are trafficked into the cilium under basal conditions. Upon pathway activation, Hh ligand binds PTCH1, PTCH1 and GPR161 exit the cilium and SMO [70] becomes enriched in the ciliary membrane. The GLI transcription factors are further enriched and the dissociation of the SUFU/GLI complex allows for the formation of the activated form of GLI2 which is trafficked out of the cilium to the cytosol where it translocates into the nucleus to induce downstream transcription of Hh target genes.

contact between the neural folds at the mid-hindbrain and spinal region [67]. The neural tube is a hollow structure that gives rise to the entirety of the central nervous system, the anterior portion of which expands and gives rise to the telencephalon [68].

NT patterning and specification occurs via progressive subdivisions along the dorsoventral and rostro caudal axes governed by multiple signaling cascades associated with the primary cilium [19]. The apically located, primary cilia of the neuroepithelium extend into the luminal space of the NT and coordinates responses to patterning factors associated with various signaling pathways including Hedgehog (Hh), Wingless-related integration site (Wnt), and mechanistic target of rapamycin (mTOR). The notochord induces the formation of the floor plate and specifies neural subpopulations via secretion of Hh ligand. Specification depends on ligand concentration and the duration of exposure time. Due to their proximity to the notochord, the ventral cells at the midline are exposed to the highest concentration of Hh and specified as the floor plate and p3 domain, which gives rise to V3 interneurons. The floor plate is a key organizing center in the morphogenesis of the neural tube as it provides positional cues that instruct neural fate, axonal guidance and connectivity. Adjacent to the floor plate and p3 domain, the formation of the pMN, p2, p1, and p0 domains which give rise to motor neurons and dorsal V2, V1, and V0 interneurons respectively, are specified by intermediate and lower levels of Hh (Figure 3). Hh also serves to inhibit dorsal cell type specification and identity [19]. The Hh gradient serves to both activate and repress GLI family transcription. In the neural tube, GLI2 acts as the primary activator and GLI3 as the major repressor of transcriptional activity. The ciliary compartment is essential for the formation of the GLI activator and repressor forms and thereby acts to maintain the balance between these two opposing patterning factors. Genetic studies in mice have demonstrated that the knockout of ciliary Ift88 and Kif3a, which results in the absence of cilia, gives rise to patterning defects due to altered Gli3 processing [42,43,71].

The NT is made up of pseudostratified neuroepithelial cells (NECs). NECs display apicobasal polarity and extend bipolar processes to span the epithelium, their apical and basal endfeet attaching to the ventricular surface and pial laminin respectively [72–74]. NECs proliferate at the luminal surface of the neural tube. NECs divide symmetrically, with their cleavage plane perpendicular to the ventricular surface, to form the cortical progenitor pool that gives rise to all subsequent neurons and later glial cells [75]. During proliferation, NECs retract their basal processes and both daughter cells regrow a new process following cytokinesis [76]. The proper establishment of this initial apicobasal polarity in NECs is essential for the development of distinctive stratification and proper organization of the cerebral cortex. Stage specific disruption of Arl13b, encoding a membrane associated ciliary specific GTPase, in the early

neuroepithelium of the developing mouse embryo results in abnormal patterning of the telencephalon due to the inversion of apicobasal polarity of radial progenitors [77].

1.4. Neurogenesis

At the onset of neurogenesis, NECs give rise to radial glial cells (RGCs). Polarized RGCs have a pear-shaped soma that localizes within the ventricular zone, where they are anchored by a short apical process to the ventricular surface and a long basal process that extends to the pial surface transversing the cerebral wall. With the appearance of apical radial glial cells (aRGCs), also called ventricular RGCs (vRGCs), the neural progenitor pool switches from symmetrical autoreplicative division to asymmetrical neurogenic cell division (Figure 4) [75]. RGCs are capable of self-renewal via symmetrical division however they primarily undergo neurogenic cell division giving rise to a neuron (direct neurogenesis) or an intermediate progenitors (IPCs) (indirect neurogenesis) and a RGC to sustain the progenitor pool [75,78,79].

During this time the primary cilium functions to regulate the proliferation and differentiation of RGs [80]. Temporal regulation of symmetrical to asymmetrical cell division is essential for balancing neuron production with progenitor maintenance. The orientation of the mitotic spindle is predictive of whether a cell division will be symmetrical or asymmetrical (reviewed in [81]), this difference as a function of orientation is hypothesized to result from differences in the distribution of cell fate determinants to the resulting daughter cells during cell division. Knockdown of Bubr1, Ift80, Kif7, and Tmem216 in embryonic mice was shown to result in decreased aRGCs and basal IPCs proliferation suggesting that these ciliopathy-associated genes contribute to the modulation of progenitor cell proliferation and thereby affect cortical formation [82]. aRGCs undergo an overall increase in cell cycle length, due to an extended G1 phase, just prior to neuronal differentiation. The length of the G1 phase is a determining factor in proliferative division versus neurogenic differentiation and manipulation of nearly all G1 regulators have been shown to affect neurogenesis in some way [83]. During early corticogenesis a shortened G1 phase results in an increase in autoreplicative self-renewal leading to an expansion of the progenitor population at the expense of differentiation. Ciliary instability or factors that favor ciliary reabsorption can result in a shortened G1 phases. Ablation of ciliary structure via the disruption of IFT88 in neural progenitors, results in the expansion of progenitor cells and a decrease in neuron production [84]. In Kif3a murine mutants, the increased proliferation observed in the RGC population results from defects in GLI3 processing. As an intact cilium is required for the conversion of full length GLI3 into its repressor form, therefore in the absence of the ciliary compartment there is an expansion of neural progenitor cells. Reciprocally, an arrest in G1 induces cell cycle exit and differentiation.

Delayed ciliary disassembly results in a stall in the G1 to S phase transition causing premature differentiation of neural progenitor cells and microcephaly.

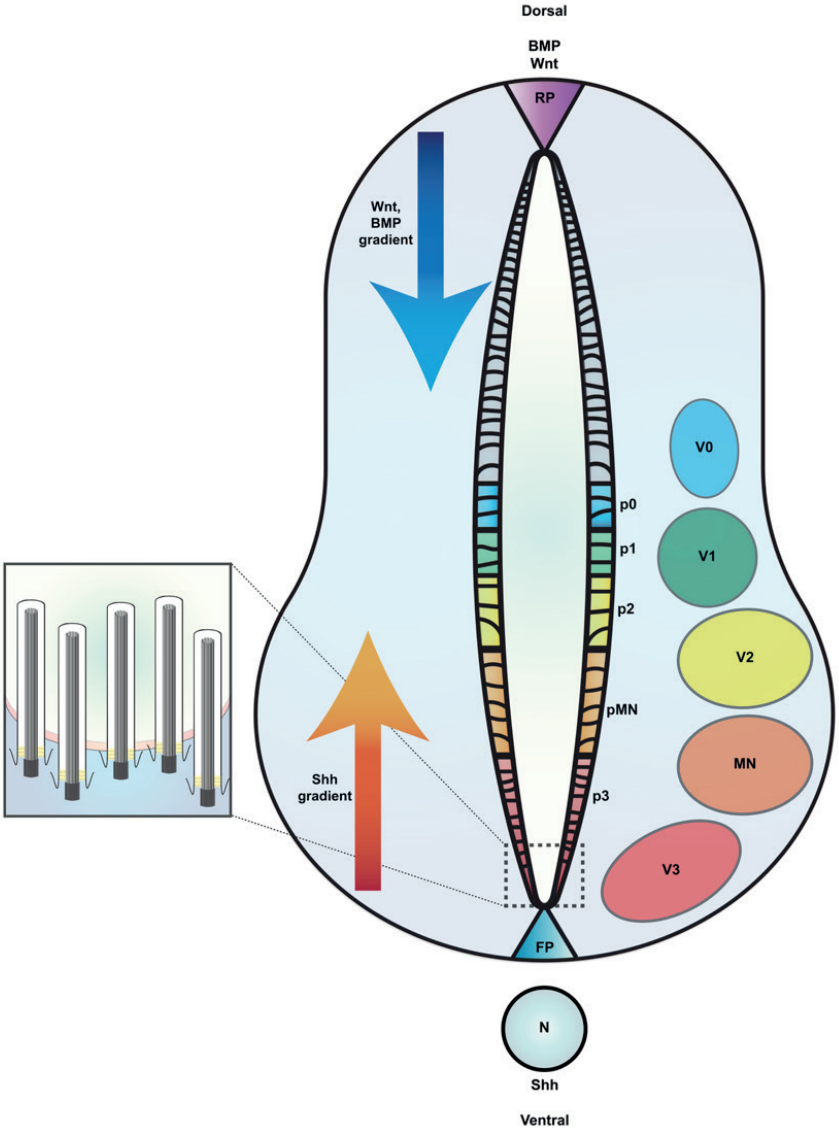

Figure 3: Cilia orchestrate neural tube development. Primary cilia are located at the apical side of the neuroepithelial layer lining the neural tube. They project into the luminal space and coordinates responses to patterning factors such as hedgehog, Wnt, and BMP signaling molecules. The notochord (N) induces the formation of the floor plate (FP) and specifies neural subpopulations via a of Hh gradient. The ectoderm and neural tube roof plate (RP) secrete BMP and Wnt ligands, which directly oppose the ventrally secreted Shh from the notochord and floor plate (FP). The opposing gradient of BMP and Shh establishes the dorsal–ventral axis and specifies neuron populations along the axis of the neural tube.

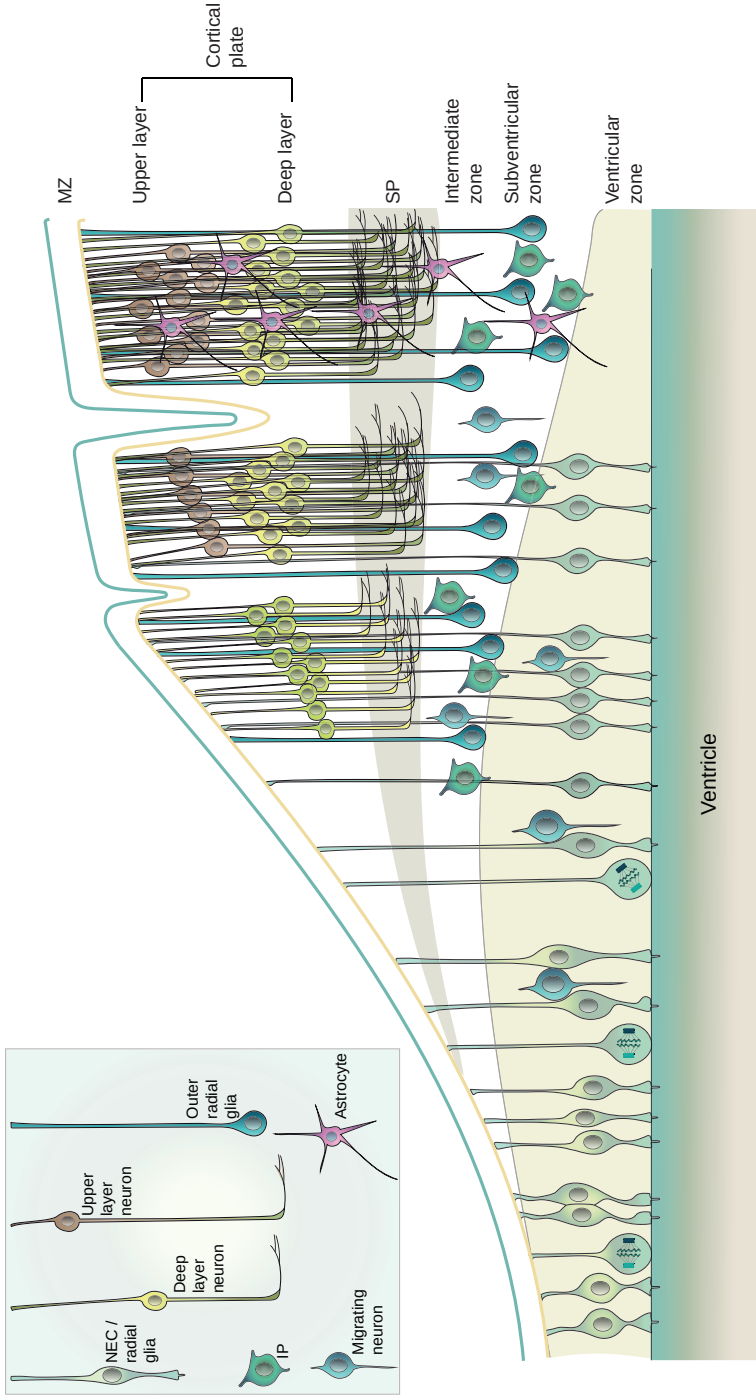
MZ
Upper layer
Cortical plate
Deep layer
SP
Intermediate zone
Subventricular zone
Ventricular zone
Ventricle
NEC / radial glia
Upper layer neuron
Deep layer neuron
Outer radial glia
IP
Migrating neuron
Astrocyte

Figure 4: Brain development. Corticogenesis is a protracted process that occurs via a series of discrete steps that culminate in the fully formed cerebral cortex. The major developmental steps in this process rely on signaling via the primary cilium and due to the length of development and its meticulous regulation, the human brain is particularly vulnerable to minute disruptions that can result in neurological disruptions. Dysfunction in ciliary trafficking (IFT80, KIF7), centrosomal function (TMEM216, BUBR1), BBsome formation (BBS1, BBS4, BBS7, BBS9, BBS10 BBS11, BBS12), and Hh signaling (ARL13B, KIF7) leads to defects in the maintenance of the RG scaffold and neuroprogenitor proliferation. Disruption RG scaffolding maintenance and signal transduction leads to aberrant neuronal migration and lamination defects. Neurite outgrowth occurs in post-mitotic neurons to generate neural circuitry, defects in ciliary signaling rescue in an abrogated response to midline structure guidance cues necessary for guiding axonal tracts and corpus callosum formation. There are two molecularly distinct types of neural progenitor cells that give rise to the entirety of the neurons and glia cells in the brain and these are: the ventricular radial glia and the outer radial glia. The aRG are bipolar cells that formed directed from the stratified NECs in the neural tube, while the oRG are unipolar cells that form early in the second trimester of embryonic development. During early stages of embryogenesis, the neural tube is made up of stratified NEC. NECs proliferate at the luminal surface of the neural tube. Neurogenesis begins when NECs transition to RG, neural progenitor cells. NECs divide symmetrically, with their cleavage plane perpendicular to the ventricular surface, to form the cortical progenitor pool that gives rise to all subsequent neurons and later glial cells. Proper regulation of the switch from symmetrical to asymmetrical cell division is essential for balancing neuron production with progenitor maintenance. During symmetrical division RG cells divide to form identical daughter stem cells, during asymmetrical division RG cells give rise to one daughter stem cell and one cell committed to a more differentiated fate, which can either be an intermediate progenitor or a neuron. Neurogenic progenitors migrate along the RG scaffold to the newly formed SVZ. By the second trimester, the SVZ formed of the intermediate progenitor cells and oRG is the major proliferative zone in the developing brain. Both IP and oRG are capable of self-renewal and generating terminally differentiated neurons. Newly born neurons migrate out of the VZ and SVZ along the RG scaffold to the transient structure known as the PP. The PP is divided into the MZ and the SP and between these two layers the CP forms via the sequential neurogenic waves of migrating neurons that build up the cortex in an inside out fashion, with the neurons that are generated first forming the deepest cortical layers followed by later born neurons forming the more superficial layers. Radial glia (RG), subventricular zone (SVZ), entircular zone (VZ), intermediate progenitor (IP), neuroepithelial cell (NEC), pre-plate (PP) marginal zone (MZ), subplate (SP), cortical plate (CP).

Centrosomal proteins are essential regulators of ciliary length and resorption. Disruption of centrosomal-P4.1-associated protein (CPAP), a negative regulator of ciliary length, leads to delayed cell cycle re-entry and premature differentiation of human iPSC derived NPCs [85]. RGC specific deletion of Cenpj, encoding another centrosomal protein involved in centriolar biogenesis and ciliary disassembly, results in incomplete cell division, attenuated proliferation, apoptosis, and microcephaly [86].

The brain forms around the cerebral spinal fluid filled ventricular cavity. Ventricular morphogenesis is governed in part by mTOR signaling via the cilium. The cilium determines the size of the apical domain of neuroprogenitor cells via mTORC1 signaling. In RGC mutations without a cilium due to conditional ablation of Ift88 or Kif3a in proliferating radial glial cells, the orientation of the mitotic spindle is disrupted and results in an increase in basal progenitor cells, an enlarged apical endfeet of RGCs, and enlarged ventricles (ventriculomegaly) [87]. Hypermorphic somatic mutations in MTOR gene result in focal malformations due to autophagy dysregulation in ciliogenesis and Wnt signaling resulting in migration and cortical lamination defects [10,88].

An analysis of cilia positioning in the embryonic mouse brain illustrated the presence of a basolateral cilium on basal progenitor cells in the telencephalon upon apical detachment and differentiating cells in the hindbrain [89]. During asymmetrical cell division in the ventricular zone, the cilium is not completely disassembled and the cilium remnant is inherited by the neural progenitor cell [90], the differentiating cell retracts its apical process anchoring it to the neuroepithelium and reestablishes a cilium on their basolateral membrane. This relocalization of the cilium likely results in coordinated exposure to differing extrinsic environmental cues then their more primitive sister cell [89]. This change results in cell fate and delamination. Alternatively, delamination can occur via abscission of the apical endfoot. Prior to abscission the centrosome dissociated from the apical primary cilium resulting in the retention of the centrosome and the shedding of the apical / ciliary membrane [91]. This results in the loss of apical polarity, cell cycle exit, and differentiation [91].

Delamination of neural progenitor cells from the apical adherens junction belt of the neuroepithelium is a hallmark of cortical development and is essential for proper tissue architecture. Neuronal delamination is the process by which new born neurons detached from the neuroepithelium and migrate out of the proliferative zone, along the RG scaffold and differentiate. Delamination requires the disassembly of adheren junctions, acto-myosin mediated abscission, and intact centrosomal architecture [92]. The sequential generation of discrete neuronal subtypes and directed migration to specific cortical laminae functions in the assembly of the neocortex. After the formation of the preplate, the cortical plate is formed in a temporal inside out fashion. New born neurons utilize the processes from aRG cells as scaffolding for radial migration and proper neuronal placements within the developing cortex.

1.5. Neuronal migration

Cilia play an indispensable role in neuronal differentiation and migration and thereby guide cortical formation and function. Proper neuronal migration and localization organizes the six layered cortex to ensure the emergence of discrete cellular identities and functional neuronal connectivity [93]. There are two major types of cortical neurons: glutamatergic excitatory projection (pyramidal) neurons and GABAergic inhibitory interneurons, and these arise from distinctive progenitor populations within the telencephalon which migrate to their respective destinations within the developing neocortex [93]. Radial migration is the process by which newly born projection neurons migrate via their apicobasal processes to their target locations. Waves of migrating neurons build up the cortex in an inside out fashion, with the neurons that are generated first forming the deepest cortical layers followed by later born neurons forming the more superficial layers. The earliest arriving neurons generate the transient preplate (PP), followed by emerging neurons that form the cortical plate (CP). The CP divides the PP into the layer 1 marginal zone (MZ) and the subplate (SP), which is located directly below layer 6 (Figure 4).

Inhibitory neurons arise from the medial and caudal ganglionic eminences and the preoptic area within the ventral telencephalon and move in an orthogonal fashion relative to the radial glial scaffold through the cortex [15,94,95]. Cilia play an indispensable role in the migration and localization of post-mitotic interneurons [15]. Similar to projection neurons, interneurons pattern in an inside-out fashion. The origin of interneurons is predictive of their destination, as interneurons are a heterogenous group of cells with differing molecular identities. The guidance cues that dictate interneuronal migration require an intact cilium [15]. Conditional ablation of Arl13b from post-mitotic projection neurons and interneurons during cortical development resulted in the abrogation of interneuron migration, whereas radially migration neurons were unaffected in their terminal localization [15]. Arl13b mutant interneurons are unable to respond appropriately to guidance cues from the dorsal cortex, because in the absence of ARL13B, the localization and enrichment of ciliary signaling receptors is attenuated, resulting in an increased cAMP and Erk signaling [15]. Post-mitotic stage specific Arl13b disruption did not affect post-migratory differentiation in interneurons, however conditional disruption of Arl13b in medial ganglionic eminence (MGE) Parvalbumin and somatostatin positive striatal interneurons resulted in perturbed interneuronal circuit development, altered interneuronal morphology, reduced axonal length, axonal branching, and dendritic complexity as well as a disbalance in inhibitory / excitatory connectivity [94] (Table 2).

1.6. Axonal tract formation and connectivity

Developmental defects associated with axonal tract formation, such as agenesis of the corpus callosum and disrupted decussation of the superior cerebellar peduncle and pyramidal tract, are often associated with ciliopathies. Neuronal architecture is shaped and functionally supported by a highly organized microtubule cytoskeleton that forms the axon and dendrites. During axonogenesis, developing axons navigate guidance cues presented via specialized populations of cells that partition the distance transversed by the growing axon. These intermediate targets coordinate the movement of axons by providing attractive and repulsive guidance molecules. The floor plate of the neural tube is a critical intermediate during development and essential for the extension of the commissural axon across the ventral midline. Appropriate axon growth relies on the axonal growth cone, located at the tip of the axon, which is enriched with signaling receptors, ensuring the developing axon innervates its intended target location. Axonal arborization and presynaptic differentiation occurs once the axon has reached its intended location.

Primary cilia and growth cones are environmental sensing organelles enriched in similar signaling receptors, allowing them to curate responses to extrinsic cues that result in cytoskeletal rearrangement and orientation. Mature CNS neurons have a cilium on their perikaryal surface that are enriched in signal transduction machinery, such as neurotransmitter receptors, that act to modulate neurons non-synaptically [17]. Cilia have been show to regulate the location and length of the axonal initial segment (AIS) [96]. Changes in ciliary morphology result in aberrant localization of ankyrinG and Nav1.2, and subsequently lead to changes in action potential dynamics and spike firing, suggesting that cilia influence neuronal excitability [96]. Cilia regulate axonal tract formation, growth, and connectivity of glutamatergic pyramidal neurons. Conditional disruption of the JBST-associated genes Inpp5e and Arl13b in post-mitotic pyramidal cells and deep cerebellar nuclei within the developing mouse embryo, result in misorientation and defasciculation of axonal tracts due to hyperactivated PI3K/AKT signaling [16]. Similar to the congenital brain malformations observed in JTBS, the cerebrospinal tract was deformed and showed disrupted decussation in both Arl13b and Inpp5e deficient neurons. Corpus callosum defects were apparent including disorganized, less dense, and poorly fasciculated callosal axons which resulted in a wider CC tract due to a downregulation of the adhesion protein PCD17. Decussation defects were also present in the pontine nuclei, transverse pontine tegmental axons were additionally misoriented. Arl13b and Inpp5e deficient deep cerebellar nuclei neurons displayed less axonal branching and reduced dendrite outgrowth. Interestingly recent work has demonstrated that ARL13B function in Hedgehog-mediated axonal guidance is independent of it its ciliary localization. Specifically ciliary-

localization-deficient ARL13B, with a non-JBTS associated point mutation (V358A) that disrupt the ciliary targeting sequence resulting in cytosolic sequestration, is sufficient to rescue Hh signaling defects associated with ARL13B disruptions such as axonal guidance issues [97] and abnormal neural patterning [98].

In the adult hippocampus, hippocampal NPCs give rise to dentate granule cells (DGCs) throughout life. This process is thought to be essential for learning and memory (reviewed in [99]). Newborn DGCs migrate to their final destination and integrate into existing neural circuitry within the within the granule cell layer. Primary cilia are essential in orchestrating the morphological and physiological maturation of DGCs in the dentate gyrus, and are required for proper synaptogenesis. Cilia are absent during initial stages of DGCs migration to the granule cell layer, however upon reaching their destination, synaptic formation and integration co-occurs with ciliary assembly in DGCs. Kumamoto et al. [100] found that expression of a dominant negative form of Kif3a in these cells abolished cilia, resulting in blunted dendritic arborization and drastically attenuated glutamatergic innervation from the entorhinal projections. These results were concordant with shRNA-mediated knockdown of Ift88 [100].

1.7. The cerebellum

Primary cilia are essential for progenitor cell proliferation during cerebellar development [16,101,102] and Purkinje cell (PC) maintenance throughout adulthood [103,104]. Locomotor specialization and sensorimotor control are regulated by the cerebellum, and research over the last decade has also implicated that it plays a role in cognition, emotion, and autonomic function (reviewed in [105]).

During human cerebellar neurogenesis, PCs are born around the 7th gestation week and the cerebellum continues to form until postnatal month 11. This protracted period of development results in an increased vulnerability to cerebellar dysfunction during critical periods of development and circuitry formation. To date, five neuronal subtypes have been described to inhabit the cerebellar cortex, the most abundant among them being granule cell (GCs). In contrast to most other neuronal subtypes that originate along the ventricular surface, GCs are formed in the external germinal layer (EGL), located along the dorsal surface of the cortex during cerebellar formation [106]. GC precursors undergo extensive proliferation in the EGL during the first 2 to 3 weeks after birth. Upon cell cycle exit, they extend axons to the molecular layer where they eventually synapse on the dendrites of PCs, and migrate through the PC layer to the internal granule layer. The mature cerebellar cortex is made up of 3 layers: a ganglion or PC layer (made up of PC bodies) sandwiched between the molecular layer (consisting of inhibitory interneurons including stellate and basket cells) and the internal granular layer (populated by Golgi cells and GCs) [107].

Interestingly, the primary cilium has been shown to play an essential role in medulloblastoma (MB) propagation, a severe pediatric brain tumor characterized by overactivation of the Hh signaling pathway that originates in GC progenitor cells during their proliferative period in the EGL. Previous work suggests that the role of the cilium in tumorigenesis is cell context-specific and depends heavily on the driving transformational event as it pertains to SHH activation [108]. For example, constitutively active SMO (SMOM2), but not constitutively active GLI2, culminates in MB. MB formation requires an intact cilium in this context as genetic ablation of essential ciliary genes in SMOM2 mouse models of MB suppress tumor formation [109]. Ablation of Arl13b leads to decreased levels of the active form of GLI1, without compromising the downstream repressive form, GLI3, resulting in MB tumor suppression [109].

PCs, GC, molecular layer interneurons and Bergmann glia (BG) are ciliated in the developing and mature cerebellum, however the role of cilia in adult cerebellar homeostasis is just beginning to be defined [110]. In the earliest postnatal stages of development, PCs secrete SHH which is essential for GC progenitor pool proliferation [101] and maturation of Bergmann glia [111]. Genetic ablation of the Hh signaling results in decreased GC progenitor proliferation and premature differentiation of Bergmann glia and PCs [112]. GC proliferation is mediated by cilium-transduced SHH signaling, as loss of Ift88 or Kif3a results in cerebellar hypoplasia due to a lack of GC expansion [102]. GC are glutamatergic cells that function to regulate the cerebellar output by controlling the activity of the inhibitory PCs.

Tau Tubulin Kinase 2 (TTBK2) is an essential regulator of ciliogenesis via its role in mediating the removal of CP110 from the mother centriole, thereby allowing axonemal extension and ciliary formation [104]. Mutations in TTBK2are causative of spinocerebellar ataxia 11 (SCA11), a hereditary form of cerebellar ataxia [113] that results from progressive loss of PCs. Ttbk2 null mutations lead to attenuated SHH signaling and a loss of cilia. Ttbk2$^{-/-}$ mouse embryos display holoprosencephaly due to a lack of SHH associated patterning in the neural tube. Rescue experiments in the Ttbk2 null mice performed with SCA11 associated truncating mutants of TTBK2 demonstrate that the mutated protein localizes to the basal body but fails to allow for the initiation of ciliogenesis [104]. Adult-specific Ttbk2 knock out leads degenerative cerebellar phenotypes via the loss of input to PC from climbing fibers and parallel fibers and eventually loss of PC. Specifically, loss of Ttbk2 leads to both an absence of cilia and altered intracellular Ca^{2+} levels in PCs, as well as loss of VGLUT2+ synapses on PC dendrites. The central role of the cilium was further validated as Ift88 knock out mice displayed an almost identical phenotype to the one observed with Ttbk2 knockout in terms of their cerebellar phenotype [103]. These data suggest that both TTBK2 and cilia are essential for PC maintenance and function, and provide a novel ciliary link to neurodegeneration.

2. DEVELOPMENTAL ABNORMALITIES OF THE CENTRAL NERVOUS SYSTEM AS A CORE FEATURE OF CILIOPATHIES

Ciliopathies are a genetically heterogeneous group of disorders that manifest in phenotypically similar diseases. As cilia are found in a wide variety of cell types, ciliopathies affect a variety of tissues and organ systems where ciliary function is critical. Their overlapping set of symptoms include (but is not restricted to) cognitive impairment, renal disease, blindness, deafness, obesity, polydactyly, skeletal abnormalities, Dandy Walker malformation, and hepatic disease [114]. A large subset of ciliopathy-associated genes have been linked to neurological defects such as intellectual disability and anatomical abnormalities [22] suggesting that impaired ciliary function hinders brain development and function. Pathological manifestation of ciliopathies can be attributed to both structural and functional defects in cilia and their associated basal body. Ciliopathies provide an invaluable model to dissect intrinsic mechanisms of ciliary biology. Examination of these mostly monogenic conditions has led to the identification of many of the associated genes, and has produced a wealth of information about the functional role of cilia in neural development.

While CNS associated phenotypes are observed in more than 50% of ciliopathies [21], considerable variation of symptomatic manifestation and severity exists within and among syndromes. The core features associated with neuronal ciliopathies are structural brain abnormalities including cerebellar vermis hypoplasia, Dandy-Walker malformation, hydrocephalus, hypoplasia, and agenesis of the corpus callosum, and posterior encephalocoele formation [115]. Additional CNS functional phenotypes without a clear structural correlation also exist including intellectual disability and behavioral phenotypes for many ciliopathies.

Why specific neurological abnormalities such as agenesis of the corpus callosum or hydrocephalus are associated with some ciliopathies and not others remains to be elucidated. Specifically, why the frequency and severity of these CNS symptoms differs between individuals given the same diagnosis is a question of great interest that can likely be answered with further evaluation.

3. AIM AND OUTLINE OF THIS THESIS

The aim of this thesis was to investigate ciliopathies that arise due to disruptions in ciliary genes and/or their temporal-spatial protein networks with a specific focus on neurodevelopmental abnormalities. In Chapter 1, I provide a general introduction on the role of cilia and ciliary signal transduction during neuro- and cortico- genesis, followed by a brief discourse on neuronal abnormalities and associated mechanisms of disease observed in these so termed ‘neuronal ciliopathies’.

The first part of this thesis describes the use of functional studies to identify disease associated genes. In Chapter 2, variants in armadillo repeat containing 9 (ARMC9) were characterized and found to be causative of JBTS. Zebrafish studies in genetically-edited armc9 mutant zebrafish demonstrated ciliopathy phenotypes including curved body shape, retinal dystrophy, coloboma, and a decrease in ciliary number. On the basis of subcellular localization and interactome studies, many ciliopathy genes can be classified into functional networks. In turn, many disease-causing genes demonstrate genetic and/or direct interactions, suggesting resulting defects arise due to disruptions in a shared cellular mechanism. In Chapter 3, ARMC9 was further characterize in a JBTS associated functional module that was found to include CEP104, CCDC66, CSPP1, and the tubulin binding protein TOGARAM1. As a result of this interactome analysis, variants in TOGARAM1 were identified in patients with JBTS. Additionally, this study demonstrates that both aberrant hedgehog signaling and post-translational modifications of microtubules contribute to the underlying pathology of JBTS.

The second part of this thesis addresses the assessment of a previously undefined ciliopathy-like syndrome presenting with severe neuroanatomical defects and intellectual disability resulting from loss-of-function mutations in USP9X in Chapter 4 and a method to model and functionally assess neuronal abnormalities observed in LOF USP9X iPSC derived neuroepithelium in Chapter 5. In this study, 3D modeling of subcellular structures including mitochondria in Mitochondrial Encephalopathy, Lactic acidosis, and Stroke-like episodes (MELAS) and cilia in USP9X-affected individuals are evaluated in neurons utilizing high resolution microscopy and subsequent segmentation and volumetric reconstruction analysis. I include a general discussion of disease modeling and the research studies performed in this thesis in Chapter 6.

REFERENCES

1. Budday, S., Steinmann, P. & Kuhl, E. Physical biology of human brain development. *Front. Cell. Neurosci.* **9**, 1–17 (2015).
2. Satir, P. & Christensen, S. T. Overview of Structure and Function of Mammalian Cilia. *Annu. Rev. Physiol.* **69**, 377–400 (2007).
3. Tobin, D. M. *et al.* Combinatorial expression of TRPV channel proteins defines their sensory functions and subcellular localization in C. elegans neurons. *Neuron* **35**, 307–318 (2002).
4. Kulaga, H. M. *et al.* Loss of BBS proteins causes anosmia in humans and defects in olfactory cilia structure and function in the mouse. *Nat. Genet.* **36**, 994–998 (2004).
5. Elias, R. V, Sezate, S. S., Cao, W. & McGinnis, J. F. Temporal kinetics of the light/dark translocation and compartmentation of arrestin and alpha-transducin in mouse photoreceptor cells. *Mol. Vis.* **10**, 672–681 (2004).
6. Abou Alaiwi, W. A., Lo, S. T. & Nauli, S. M. Primary cilia: highly sophisticated biological sensors. *Sensors (Basel).* **9**, 7003–7020 (2009).
7. Huangfu, D. *et al.* Hedgehog signalling in the mouse requires intraflagellar transport proteins. *Nature* **426**, 83–87 (2003).
8. Gerdes, J. M. *et al.* Disruption of the basal body compromises proteasomal function and perturbs intracellular Wnt response. *Nat. Genet.* **39**, 1350–1360 (2007).
9. Ezratty, E. J. *et al.* A role for the primary cilium in notch signaling and epidermal differentiation during skin development. *Cell* **145**, 1129–1141 (2011).
10. Park, S. M. *et al.* Brain Somatic Mutations in MTOR Disrupt Neuronal Ciliogenesis, Leading to Focal Cortical Dyslamination. *Neuron* **99**, 83–97.e7 (2018).
11. Wang, S., Livingston, M. J., Su, Y. & Dong, Z. Reciprocal regulation of cilia and autophagy via the MTOR and proteasome pathways. *Autophagy* **11**, 1–30 (2015).
12. Clement, C. A. *et al.* TGF-β signaling is associated with endocytosis at the pocket region of the primary cilium. *Cell Rep.* **3**, 1806–1814 (2013).
13. Nadadhur, A. G. *et al.* Patterning factors during neural progenitor induction determine regional identity and differentiation potential in vitro. *Stem Cell Res.* **32**, 25–34 (2018).
14. Kirkeby, A. *et al.* Generation of regionally specified neural progenitors and functional neurons from human embryonic stem cells under defined conditions. *CellReports* **1**, 703–714 (2012).
15. Higginbotham, H. *et al.* Arl13b in Primary Cilia Regulates the Migration and Placement of Interneurons in the Developing Cerebral Cortex. *Dev. Cell* **23**, 925–938 (2012).
16. Guo, J. *et al.* Primary Cilia Signaling Promotes Axonal Tract Development and Is Disrupted in Joubert Syndrome- Related Disorders Models. *DEVCEL* **51**, 759–774.e5 (2019).
17. Green, J. A. & Mykytyn, K. Neuronal Primary Cilia: An Underappreciated Signaling and Sensory Organelle in the Brain. **39**, 244–245 (2013).
18. Ross, A. J. *et al.* Disruption of Bardet-Biedl syndrome ciliary proteins perturbs planar cell polarity in vertebrates. *Nat. Genet.* **37**, 1135–1140 (2005).
19. Bay, S. N. & Caspary, T. What are those cilia doing in the neural tube? *Cilia* **1**, 1 (2012).
20. Putoux, A. *et al.* KIF7 mutations cause fetal hydrolethalus and acrocallosal syndromes. *Nat. Genet.* **43**, 601–606 (2011).
21. Braun, D. A. & Hildebrandt, F. Ciliopathies. *Cold Spring Harb. Perspect. Biol.* **9**, a028191 (2017).

22. Reiter, J. F. & Leroux, M. R. Genes and molecular pathways underpinning ciliopathies. *Nat. Rev. Mol. Cell Biol.* **18**, 533–547 (2017).

23. Satir, P., Pedersen, L. B. & Christensen, S. T. The primary cilium at a glance. *J. Cell Sci.* **123**, 499–503 (2010).

24. Horvath, J. *et al.* Identification and analysis of axonemal dynein light chain 1 in primary ciliary dyskinesia patients. *Am. J. Respir. Cell Mol. Biol.* **33**, 41–47 (2005).

25. Nayak, R. K. & Wu, A. S. Ultrastructural demonstration of cilia and ciliary rootlets in mammalian uterine tube epithelium in different functional states. *Am. J. Vet. Res.* **36**, 1623–1630 (1975).

26. Ibanez-Tallon, I. *et al.* Dysfunction of axonemal dynein heavy chain Mdnah5 inhibits ependymal flow and reveals a novel mechanism for hydrocephalus formation. *Hum. Mol. Genet.* **13**, 2133–2141 (2004).

27. Olstad, E. W. *et al.* Ciliary Beating Compartmentalizes Cerebrospinal Fluid Flow in the Brain and Regulates Ventricular Development. *Curr. Biol.* **29**, 229–241.e6 (2019).

28. Lepanto, P., Badano, J. L. & Zolessi, F. R. Neuron's little helper: The role of primary cilia in neurogenesis. *Neurogenesis* **3**, 1–9 (2016).

29. Barakat, M. T. & Scott, M. P. Tail Wags Dog: Primary Cilia and Tumorigenesis. *Cancer Cell* **16**, 276–277 (2009).

30. Gerdes, J. M., Davis, E. E. & Katsanis, N. The vertebrate primary cilium in development, homeostasis, and disease. *Cell* **137**, 32–45 (2009).

31. Eshun-Wilson, L. *et al.* Effects of α-tubulin acetylation on microtubule structure and stability. *Proc. Natl. Acad. Sci. U. S. A.* **116**, 10366–10371 (2019).

32. Xu, Z. *et al.* Microtubules acquire resistance from mechanical breakage through intralumenal acetylation. *Science (80-.).* **356**, 328–332 (2017).

33. Dorota Wloga, Ewa Joachimiak & Hanna Fabczak. Tubulin Post-Translational Modifications and Microtubule Dynamics. *Int. J. Mol. Sci.* **18**, 2207–2218 (2017).

34. Kobayashi, T. & Dynlacht, B. D. Regulating the transition from centriole to basal body. *J. Cell Biol.* **193**, 435–444 (2011).

35. Kim, H. *et al.* Ciliary membrane proteins traffic through the Golgi via a Rabep1/GGA1/Arl3-dependent mechanism. *Nat. Commun.* **5**, 5482 (2014).

36. Garcia-Gonzalo, F. R. & Reiter, J. F. Open Sesame: How Transition Fibers and the Transition Zone Control Ciliary Composition. *Cold Spring Harb. Perspect. Biol.* **9**, (2017).

37. Cole, D. G. Kinesin-II, coming and going. *J. Cell Biol.* **147**, 463–466 (1999).

38. Ray, K. *et al.* Kinesin-II is required for axonal transport of choline acetyltransferase in Drosophila. *J. Cell Biol.* **147**, 507–518 (1999).

39. Signor, D. *et al.* Role of a class DHC1b dynein in retrograde transport of IFT motors and IFT raft particles along cilia, but not dendrites, in chemosensory neurons of living Caenorhabditis elegans. *J. Cell Biol.* **147**, 519–530 (1999).

40. Blacque, O. E. *et al.* The WD repeat-containing protein IFTA-1 is required for retrograde intraflagellar transport. *Mol. Biol. Cell* **17**, 5053–5062 (2006).

41. Cole, D. G. *et al.* Chlamydomonas kinesin-II-dependent intraflagellar transport (IFT): IFT particles contain proteins required for ciliary assembly in Caenorhabditis elegans sensory neurons. *J. Cell Biol.* **141**, 993–1008 (1998).

42. Huangfu, D., Liu, A., Rakeman, A. S. & Murcia, N. S. Hedgehog signalling in the mouse requires intraflagellar transport proteins why less severe than Shh mutants but similar to disruption of L / R nodal assymetry ! *Lett. to Nat.* **426**, 83–87 (2003).
43. Huangfu, D. & Anderson, K. V. Cilia and Hedgehog responsiveness in the mouse. *Proc. Natl. Acad. Sci. U. S. A.* **102**, 11325–11330 (2005).
44. May, S. R. *et al.* Loss of the retrograde motor for IFT disrupts localization of Smo to cilia and prevents the expression of both activator and repressor functions of Gli. *Dev. Biol.* **287**, 378–389 (2005).
45. Nikolopoulou, E., Galea, G. L., Rolo, A., Greene, N. D. E. & Copp, A. J. Neural tube closure: cellular, molecular and biomechanical mechanisms. *Development* **144**, 552–566 (2017).
46. Putoux, A. *et al.* Altered GLI3 and FGF8 signaling underlies acrocallosal syndrome phenotypes in Kif7 depleted mice. *Hum. Mol. Genet.* **28**, 877–887 (2019).
47. Bangs, F. & Anderson, K. V. Primary cilia and Mammalian Hedgehog signaling. *Cold Spring Harb. Perspect. Biol.* **9**, (2017).
48. Sasai, N., Toriyama, M. & Kondo, T. Hedgehog Signal and Genetic Disorders. *Front. Genet.* **10**, 1103 (2019).
49. Chiang, C. *et al.* Cyclopia and defective axial patterning in mice lacking Sonic hedgehog gene function. *Nature* **383**, 407–413 (1996).
50. Briscoe, J., Chen, Y., Jessell, T. M. & Struhl, G. A hedgehog-insensitive form of patched provides evidence for direct long-range morphogen activity of sonic hedgehog in the neural tube. *Mol. Cell* **7**, 1279–1291 (2001).
51. Oro, A. E. *et al.* Basal cell carcinomas in mice overexpressing sonic hedgehog. *Science* **276**, 817–821 (1997).
52. Briscoe, J. & Ericson, J. Specification of neuronal fates in the ventral neural tube. *Curr. Opin. Neurobiol.* **11**, 43–49 (2001).
53. Rallu, M. *et al.* Dorsoventral patterning is established in the telencephalon of mutants lacking both Gli3 and Hedgehog signaling. *Development* **129**, 4963 LP – 4974 (2002).
54. Yang, H. & Huang, K. Dissecting the Vesicular Trafficking Function of IFT Subunits. *Front. Cell Dev. Biol.* **7**, 352 (2020).
55. Hong, S.-R. *et al.* Spatiotemporal manipulation of ciliary glutamylation reveals its roles in intraciliary trafficking and Hedgehog signaling. *Nat. Commun.* **9**, 1713–1732 (2018).
56. OHagan, R. *et al.* Glutamylation Regulates Transport, Specializes Function, and Sculpts the Structure of Cilia. *Curr. Biol.* **27**, 3430–3441.e6 (2017).
57. Wloga, D., Joachimiak, E., Louka, P. & Gaertig, J. Posttranslational Modifications of Tubulin and Cilia. *Cold Spring Harb. Perspect. Biol.* **9**, (2017).
58. Nager, A. R. *et al.* An Actin Network Dispatches Ciliary GPCRs into Extracellular Vesicles to Modulate Signaling. *Cell* **168**, 252-263.e14 (2017).
59. Briscoe, J., Pierani, A., Jessell, T. M. & Ericson, J. A homeodomain protein code specifies progenitor cell identity and neuronal fate in the ventral neural tube. *Cell* **101**, 435–445 (2000).
60. Nygaard, M. B., Almstrup, K., Lindbæk, L., Christensen, S. T. & Svingen, T. Cell context-specific expression of primary cilia in the human testis and ciliary coordination of Hedgehog signalling in mouse Leydig cells. *Sci. Rep.* **5**, 10364 (2015).
61. Liem, K. F. J. *et al.* The IFT-A complex regulates Shh signaling through cilia structure and membrane protein trafficking. *J. Cell Biol.* **197**, 789–800 (2012).

62. He, M. *et al.* The kinesin-4 protein Kif7 regulates mammalian Hedgehog signalling by organizing the cilium tip compartment. *Nat. Cell Biol.* **16**, 663–672 (2014).

63. Cheung, H. O. L. *et al.* The kinesin protein Kif7 is a critical regulator of Gli transcription factors in mammalian Hedgehog signaling. *Sci. Signal.* **2**, 1–9 (2009).

64. Briscoe, J. & Thérond, P. P. The mechanisms of Hedgehog signalling and its roles in development and disease. *Nature Reviews Molecular Cell Biology* **14**, 418–431 (2013).

65. Patel, S. S., Tomar, S., Sharma, D., Mahindroo, N. & Udayabanu, M. Targeting sonic hedgehog signaling in neurological disorders. *Neurosci. Biobehav. Rev.* **74**, 76–97 (2017).

66. Nikolopoulou, E. *et al.* Spinal neural tube closure depends on regulation of surface ectoderm identity and biomechanics by Grhl2. *Nat. Commun.* **10**, 2487 (2019).

67. Ray, H. J. & Niswander, L. Mechanisms of tissue fusion during development. *Development* **139**, 1701–1711 (2012).

68. Greene, N. D. E. & Copp, A. J. Development of the vertebrate central nervous system: formation of the neural tube. *Prenat. Diagn.* **29**, 303–311 (2009).

69. Mukhopadhyay, S. *et al.* TULP3 bridges the IFT-A complex and membrane phosphoinositides to promote trafficking of G protein-coupled receptors into primary cilia. *Genes Dev.* **24**, 2180–2193 (2010).

70. Corbit, K. C. *et al.* Vertebrate Smoothened functions at the primary cilium. *Nature* **437**, 1018–1021 (2005).

71. Huangfu, D. & Anderson, K. V. Signaling from Smo to Ci/Gli: conservation and divergence of Hedgehog pathways from Drosophila to vertebrates. *Development* **133**, 3 LP – 14 (2006).

72. Jiang, X. & Nardelli, J. Cellular and molecular introduction to brain development. *Neurobiol. Dis.* **92**, 3–17 (2016).

73. Lui, J. H., Hansen, D. V & Kriegstein, A. R. Development and evolution of the human neocortex. *Cell* **146**, 18–36 (2011).

74. Worzfeld, T. & Schwaninger, M. Apicobasal polarity of brain endothelial cells. *J. Cereb. Blood Flow Metab.* **36**, 340–362 (2016).

75. Anthony, T. E., Klein, C., Fishell, G. & Heintz, N. Radial Glia Serve as Neuronal Progenitors in All Regions of the Central Nervous System. *Neuron* **41**, 881–890 (2004).

76. Bershteyn, M., Paredes, M. F., Subramanian, L. & Kriegstein, A. R. Dynamic behaviour of human neuroepithelial cells in the developing forebrain. *Nat. Commun.* 1–12 (2019).

77. Higginbotham, H. *et al.* Arl13b-regulated cilia activities are essential for polarized radial glial scaffold formation. *Nat. Neurosci.* **16**, 1000–1007 (2013).

78. Hansen, D. V, Lui, J. H., Parker, P. R. L. & Kriegstein, A. R. Neurogenic radial glia in the outer subventricular zone of human neocortex. *Nature* 1–10 (2010).

79. Pollen, A. A. *et al.* Molecular identity of human outer radial glia during cortical development. *Cell* **163**, 55–67 (2015).

80. Wilson, S. L., Wilson, J. P., Wang, C., Wang, B. & McConnell, S. K. Primary cilia and Gli3 activity regulate cerebral cortical size. *Dev. Neurobiol.* **72**, 1196–1212 (2012).

81. Morin, X. & Bellaïche, Y. Mitotic Spindle Orientation in Asymmetric and Symmetric Cell Divisions during Animal Development. *Dev. Cell* **21**, 102–119 (2011).

82. Guo, J. *et al.* Developmental disruptions underlying brain abnormalities in ciliopathies. *Nat. Commun.* **6**, 511–513 (2015).

83. Hardwick, L. J. A., Ali, F. R., Azzarelli, R. & Philpott, A. Cell cycle regulation of proliferation versus differentiation in the central nervous system. *Cell Tissue Res.* **359**, 187–200 (2015).

84. Snedeker, J. *et al.* Unique spatiotemporal requirements for intraflagellar transport genes during forebrain development. *PLoS One* **12**, e0173258–24 (2017).

85. Gabriel, E. *et al.* CPAP promotes timely cilium disassembly to maintain neural progenitor pool. *EMBO J.* **35**, 803–819 (2016).

86. Ding, W., Wu, Q., Sun, L., Pan, N. C. & Wang, X. Cenpj Regulates Cilia Disassembly and Neurogenesis in the Developing Mouse Cortex. *J. Neurosci.* **39**, 1994–2010 (2019).

87. Foerster, P. *et al.* mTORC1 signaling and primary cilia are required for brain ventricle morphogenesis. *Development* **144**, 201–210 (2017).

88. Reijnders, M. R. F. *et al.* Variation in a range of mTOR-related genes associates with intracranial volume and intellectual disability. *Nat. Commun.* **8**, 1052 (2017).

89. Wilsch-Bräuninger, M., Peters, J., Paridaen, J. T. M. L. & Huttner, W. B. Basolateral rather than apical primary cilia on neuroepithelial cells committed to delamination. *Development* **139**, 95–105 (2012).

90. Paridaen, J. T. & Huttner, W. B. Neurogenesis during development of the vertebrate central nervous system. *EMBO Rep.* **15**, 351–364 (2014).

91. Das, R. M. & Storey, K. G. Apical Abscission Alters Cell Polarity and Dismantles the Primary Cilium During Neurogenesis. *Science (80-.).* **343**, 200–204 (2014).

92. Kasioulis, I. & Storey, K. G. Cell biological mechanisms regulating chick neurogenesis. *Int. J. Dev. Biol.* **62**, 167–175 (2018).

93. Evsyukova, I., Plestant, C. & Anton, E. S. Integrative Mechanisms of Oriented Neuronal Migration in the Developing Brain. *Annu. Rev. Cell Dev. Biol.* **29**, 299–353 (2013).

94. Guo, J. *et al.* Primary Cilia Signaling Shapes the Development of Interneuronal Connectivity. *Dev. Cell* **42**, 286–300.e4 (2017).

95. Wonders, C. P. & Anderson, S. A. The origin and specification of cortical interneurons. *Nat. Rev. Neurosci.* **7**, 687–696 (2006).

96. Wang, B. *et al.* Cilia function is associated with axon initial segment morphology. *Elsevier*

97. Ferent, J. *et al.* The Ciliary Protein Arl13b Functions Outside of the Primary Cilium in Shh-Mediated Axon Guidance. *CellReports* **29**, 3356–3366.e3 (2019).

98. Gigante, E. D., Taylor, M. R., Ivanova, A. A., Kahn, R. A. & Caspary, T. ARL13B regulates Sonic Hedgehog signaling from outside primary cilia. **127**, 4252–4293 (2020).

99. Gonçalves, J. T., Schafer, S. T. & Gage, F. H. Adult Neurogenesis in the Hippocampus: From Stem Cells to Behavior. *Cell* **167**, 897–914 (2016).

100. Kumamoto, N. *et al.* A role for primary cilia in glutamatergic synaptic integration of adult-born neurons. *Nat. Neurosci.* **15**, 399–405 (2012).

101. Wechsler-Reya, R. J. & Scott, M. P. Control of neuronal precursor proliferation in the cerebellum by Sonic Hedgehog. *Neuron* **22**, 103–114 (1999).

102. Chizhikov, V. V *et al.* Cilia proteins control cerebellar morphogenesis by promoting expansion of the granule progenitor pool. *J. Neurosci.* **27**, 9780–9789 (2007).

103. Bowie, E. & Goetz, S. C. TTBK2 and primary cilia are essential for the connectivity and survival of cerebellar Purkinje neurons. *Elife* **9**, (2020).

104. Goetz, S. C., Liem, K. F. J. & Anderson, K. V. The Spinocerebellar Ataxia-Associated Gene Tau Tubulin Kinase 2 Controls the Initiation of Ciliogenesis. *Cell* **151**, 847–858 (2012).

105. Schmahmann, J. D. The cerebellum and cognition. *Neurosci. Lett.* **688**, 62–75 (2019).

106. Lackey, E. P., Heck, D. H. & Sillitoe, R. V. Recent advances in understanding the mechanisms of cerebellar granule cell development and function and their contribution to behavior. *F1000Research* **7**, 1112–1142 (2018).

107. Butts, T., Green, M. J. & Wingate, R. J. T. Development of the cerebellum: simple steps to make a 'little brain'. *Development* **141**, 4031–4041 (2014).

108. Han, Y.-G. *et al.* Dual and opposing roles of primary cilia in medulloblastoma development. *Nat. Med.* **15**, 1062–1065 (2009).

109. Bay, S. N., Long, A. B. & Caspary, T. Disruption of the ciliary GTPase Arl13b suppresses Sonic hedgehog overactivation and inhibits medulloblastoma formation. *Proc. Natl. Acad. Sci. U. S. A.* **115**, 1570–1575 (2018).

110. Di Pietro, C. *et al.* Primary Cilia in the Murine Cerebellum and in Mutant Models of Medulloblastoma. *Cell. Mol. Neurobiol.* **37**, 145–154 (2016).

111. Dahmane, N. & i Altaba, A. Sonic hedgehog regulates the growth and patterning of the cerebellum. *Development* **126**, 3089–3100 (1999).

112. Marazziti, D. *et al.* Precocious cerebellum development and improved motor functions in mice lacking the astrocyte cilium-, patched 1-associated Gpr37l1 receptor. in *Proceedings of the National Academy of Sciences* 16486–16491 (National Academy of Sciences, 2013).

113. Vakharia, H., Oh, M.-K. & Pulst, S.-M. Spinocerebellar Ataxia 11 (SCA11). in *Genetics of Movement Disorders* 117–119 (Elsevier, 2003).

114. Sun, S.-C. CYLD: a tumor suppressor deubiquitinase regulating NF-κB activation and diverse biological processes. *Cell Death Differ.* **17**, 25–34 (2009).

115. Baker, K. & Beales, P. L. Making sense of cilia in disease: the human ciliopathies. *Am. J. Med. Genet. C. Semin. Med. Genet.* **151C**, 281–295 (2009).

Table 1: Genes mutated in ciliopathies

Gene	Cytogenetic location	Gene / Locus MIM number	Inheritance	Phenotype(s)	Associated syndrome(s)
AHI1	6q23.3	608894	AR	Neurodevelopmental	JBTS3
ALMS1	2p13.1	606844	AR	Isolated and syndromic obesity	ALMS
ANKS6	9q22.33	615370	AR	Renal	NPHP16
ARL13B	3q11.1-q11.2	608922	AR	Neurodevelopmental	JBTS8
ARL3	10q24.32	604695	AR	Neurodevelopmental	JBTS35
ARL6	3q11.2	608845	AR, AD	Isolated and syndromic obesity	BBS1, BBS3, RP55
ARMC9	2q37.1	617612	AR	Neurodevelopmental	JBTS30
ATXN10	22q13.31	611150	AD	Neurodevelopmental	SCA10
B9D1	17p11.2	614144	AR	Neurodevelopmental	JBTS27
B9D2	19q13.2	611951	AR	Neurodevelopmental	JBTS34, MKS10
BBIP1	10q25.2	613605	AR	Isolated and syndromic obesity	BBS18
BBS1	11q13.2	209901	AR, AD	Isolated and syndromic obesity	BBS1
BBS10	12q21.2	610148	AR	Isolated and syndromic obesity	*BBS10*
BBS12	4q27	610683	AR	Isolated and syndromic obesity	*BBS12*
BBS4	15q24.1	600374	AR	Isolated and syndromic obesity	*BBS4*
BBS5	2q31.1	603650	AR	Isolated and syndromic obesity	*BBS5*
BBS7	4q27	607590	AR	Isolated and syndromic obesity	*BBS7*
BBS9	7p14.3	607968	AR	Isolated and syndromic obesity	*BBS9*
C21ORF2	21q22.3	603191	AR	Skeletal	ATD
C2CD3	11q13.4	615944	AR	Neurodevelopmental / Skeletal	OFD14
C5ORF42 / CPLANE1	5p13.2	614571	AR	Neurodevelopmental	JBTS17, OFD6
CC2D2A	4p15.32	612013	AR	Neurodevelopmental	JBTS9
CCDC28B	1p35.2	610162	AR, AD	Isolated and syndromic obesity	BBS1
CEP104	1p36.32	616690	AR	Neurodevelopmental	JBTS25
CEP120	5q23.2	613446	AR	Neurodevelopmental / Skeletal	JBTS31, SRTD13
CEP164	11q23.3	614848	AR	Renal	NPHP15

Gene	Cytogenetic location	Gene / Locus MIM number	Inheritance	Phenotype(s)	Associated syndrome(s)
CEP19	3q29	615586	AR	Isolated and syndromic obesity	
CEP290	12q21.32	610142	AR	Neurodevelopmental	JBTS5, BBS14
CEP41	11q12.2	610523	AR	Neurodevelopmental	JBTS15
CEP83	12q22	615847	AR	Renal	NPHP18
CSPP1	8q13.1-q13.2	611654	AR	Neurodevelopmental	JBTS21
DCDC2	6p22.3	605755	AR	Renal	NPHP19
DDX59	1q32.1	615464	AR	Skeletal	OFD5
DYNC2H1	11q22.3	603297	AR, DR	Skeletal	SRTD3
DYNC2LI1	2p21	617083	AR	Skeletal	SRTD15
EVC	4p16.2	604831	AR	Skeletal	EVC
EVC2	4p16.2	607261	AR	Skeletal	Ellis-van Creveld syndrome
GLIS2	16p13.3	608539	AR	Renal	NPHP7
HYLS1	11q24.2	610693	AR	Neurodevelopmental	MKS-like, Hydrolethalus syndrome
ICK	6p12.1	612325	AR	Neurodevelopmental	ECO
IFT122	3q21.3-q22.1	606045	AR	Skeletal	CED1
IFT140	16p13.3	614620	AR	Skeletal	SRTD9, MZSDS, RP80
IFT144	4p14	608151	AR	Skeletal	SRTD5, NPHP13, CED4
IFT172	2p23.3	607386	AR	Neurodevelopmental / Skeletal	RP71, SRTD10
IFT27	22q12.3	615870	AR	Isolated and syndromic obesity	BBS19
IFT43	14q24.3	614068	AR	Skeletal	CED3, SRTD18, RP81
IFT52	20q13.12	617094	AR	Skeletal	SRTD16
IFT57	3q13.12-q13.13	606621	AR	Neurodevelopmental	OFD18
IFT80	3q25.33	611177	AR	Skeletal	SRTD2
INPP5E	9q34.3	613037	AR	Neurodevelopmental	JBTS1
INTU	4q28.1	610621	AR	Skeletal	OFD17, SRTD20
INVS	9q31.1	243305	AR	Renal	NPHP2
IQCB1	3q13.33	609237	AR	Renal	SLSN5

Gene	Cytogenetic location	Gene / Locus MIM number	Inheritance	Phenotype(s)	Associated syndrome(s)
KIAA0556 / KATNIP	16p12.1	610178	AR	Neurodevelopmental	JBTS26
KIAA0586 / TAPLID3	14q23.1	616650	AR	Neurodevelopmental	JBTS23
KIAA0753 / OFIP	17p13.1	617112	AR	Neurodevelopmental	OFD15
KIF7	15q26.1	611254	AR	Neurodevelopmental	JBTS12, Acrocallosal syndrome
LZTFL1	3p21.31	606568	AR	Isolated and syndromic obesity	BBS17
MKKS	20p12.2	604896	AR	Isolated and syndromic obesity	BBS6, MKKS
MKS1	17q22	609883	AR	Neurodevelopmental	JBTS28, MKS1, BBS13
NEK1	4q33	604588	AR	Skeletal	SRTD6
NEK8	17q11.2	609799	AR	Renal	NPHP9, RHPD2
NEK9	14q24.3	609798	AR	Skeletal	LCCS10
NPHP1	2q13	607100	AR	Neurodevelopmental	JBTS4
NPHP3	3q22.1	608002	AR	Neurodevelopmental	MKS7, NPHP3, Renal-hepatic-pancreatic dysplasia 1
NPHP4	1p36.31	607215	AR	Neurodevelopmental	SLSN4, NPHP4
OFD1	Xp22.2	300170	XLD	Neurodevelopmental	JBTS10, OFD1, RP23
PDE6D	2q37.1	602676	AR	Neurodevelopmental	JBTS22
PIBF1	13q21.3-q22.1	607532	AR	Neurodevelopmental	JBTS33
PIK3R4	3q22.1	602610	AR	Renal, retinal	?OFD9
PKD1	16p13.3	601313	AD	Renal	*PKD1*
PKD2	4q22.1	173910	AD	Renal	*PKD2*
PKHD1	6p12.3-p12.2	606702	AR	Renal	PKD4
RPGRIP1L	16q12.2	610937	AR	Neurodevelopmental	JBTS7
TTC8	14q31.3	608132	AR	Isolated and syndromic obesity	BBS8, RP51
SCLT1	4q28.2	611399	AR	Skeletal	OFD9
SDCCAG8	11q43-q44	613524	AR	Renal	BBS16, SLSN7
SUFU	10q24.32	617757	AR	Neurodevelopmental	JBTS32

Gene	Cytogenetic location	Gene / Locus MIM number	Inheritance	Phenotype(s)	Associated syndrome(s)
TBC1D32	6q22.31	615867	AR	Skeletal	OFD9
TCTEX1D2	3q29	617353	AR	Skeletal	SRTD17
TCTN1	12q24.11	609863	AR	Neurodevelopmental	JBTS13
TCTN2	12q24.31	613846	AR	Neurodevelopmental	JBTS24
TCTN3	10q24.1	613847	AR	Neurodevelopmental	JBTS18, OFD4
TMEM107	17p13.1	616183	AR	Neurodevelopmental	JBTS29, MKS13
TMEM138	11q12.2	614459	AR	Neurodevelopmental	JBTS16
TMEM216	11q12.2	613277	AR	Neurodevelopmental	JBTS2
TMEM231	16q23.1	614949	AR	Neurodevelopmental	JBTS20
TMEM237	7q32.2	614423	AR	Neurodevelopmental	JBTS14
TMEM67	8q22.1	609884	AR	Neurodevelopmental	JBTS6, BBS14
TOGARAM1	14q21.2	617618	AR	Neurodevelopmental	N/A
TRAF3IP1	2q37.3	607380	AR	Renal	SLSN9
TRIM32	9q33.1	602290	AR	Isolated and syndromic obesity	BBS11
TTBK2	15q15.2	611695	AD	Neurodevelopmental	SCA11
*TTC21B**	2q24.3	612014	AR, AD	Neurodevelopmental	JBTS11, NPHP12
TUB	11p15.4	601197	AR	Isolated and syndromic obesity, ?retinal dystrophy	
VHL	3p25.3	608537	AD	Renal	VHL
WDPCP	2p15	613580	AR	Isolated and syndromic obesity	BBS15
WDR34	9q34.11	613363	AR	Skeletal	SRTD11
WDR35	2p24.1	613602	AR	Skeletal	CED2, SRTD7
WDR60	7q36.3	615462	AR	Skeletal	SRTD8
XPNPEP3	22q13.2	613553	AR	Renal	NPHP-like1
*ZNF423**	16q12.1	604557	AR, AD	Neurodevelopmental	JBTS19, NPHP14

Abbreviation	Syndrome	Abbreviation	Inheritance
ACLS	Acrocallosal syndrome	?AD	?Autosomal dominant
ATD	asphyxiating thoracic dysplasia (Jeune Syndrome)	?XLR	?X-linked recessive
ECO	Endocrine-cerebroosteodysplasia	AD	Autosomal dominant
EvC	Ellis-van Creveld syndrome	AR	Autosomal recessive
JBTS	Joubert syndrome	XL	X-linked
MKKS	McKusick-Kaufman syndrome	XLD	X-linked dominant
MKS	Meckel syndrome	XLR	X-linked recessive
N/A	Not Available		
NPHP	Nephronophthisis		
LCCS	Lethal congenital contracture syndrome		
OFD	Orofaciodigital syndrome		
RDMS	Retinal dystrophy with macular staphyloma		
RHPD	Renal-hepatic-pancreatic dysplasia		
RP	Retinitis pigmentosa		
SCA	spinocerebellar ataxia		
SLSN	Senior-Loken syndrome		
SMD	Spondylometaphyseal dysplasia, axial		
SRTD	Short-rib thoracic dysplasia with or without polydactyly		
VHL	von Hippel-Lindau syndrome		
PKD	Polycystic kidney disease		

*Insufficient evidence that these genes are associated with JBTS due to only one family (*ZNF423*) or lack of biallelic variants (*TTC21B*).

Table 2: Mouse models of brain development and stage specific necessities for specific ciliopathy genes

Driver	Gene disrupted	Stage of ablation	Cell type	Cilia	Effect
Foxg1 Cre	*Arl13b*	E9	Neuroepithelium	intact, impaired signaling	inversion of apicobasal polarity [79]
Nestin Cre	*Arl13b*	E10.5	radial glia (expansion phase)	intact, impaired signaling	no inversion of apicobasal polarity [79]
hGFAP Cre	*Arl13b*	E13.5	radial glia (differentiation phase)	intact, impaired signaling	no inversion of apicobasal polarity [79]
Nex Cre	*Arl13b*	E13.5	Post mitotic pyramidal neurons	intact, impaired signaling	no migration defect [79]
Dlx5/6 Cre	*Arl13b*	E12.5	Post mitotic interneurons	intact, impaired signaling	migration defect, no morphological / differentiation defect [17]
Nkx2.1 Cre	*Arl13b*	E10.5	MGE, POA (interneurons)	intact, impaired signaling	morphological abnormalities, disrupted connectivity, disbalance in I/E network [96]
Nex Cre	*Arl13b*	E13.5	Post mitotic pyramidal neurons	intact, impaired signaling	axonal tract defects [18]
Nex Cre	*Inpp5e*	E13.5	Post mitotic pyramidal neurons	intact, impaired signaling	axonal tract defects [18]
Foxg1 Cre	*Ift88*	E9	Neuroepithelium	ablated	patterning defects, altered Gli3 processing [89]
Foxg1 Cre	*Kif3a*	E9	Neuroepithelium	ablated	patterning defects, altered Gli3 processing [89]
Nestin Cre	*Ift88*	E10.5	radial glia (expansion phase)	ablated	increase in mTORC1 signaling, misorientation of the mitotic spindle, increased BP proliferation, enlarged apical endfeet of RG, enlarged ventricles [89]
Nestin Cre	*Kif3a*	E10.5	radial glia (expansion phase)	ablated	increase in mTORC1 signaling, misorientation of the mitotic spindle, increased BP proliferation, enlarged apical endfeet of RG, enlarged ventricles [89]

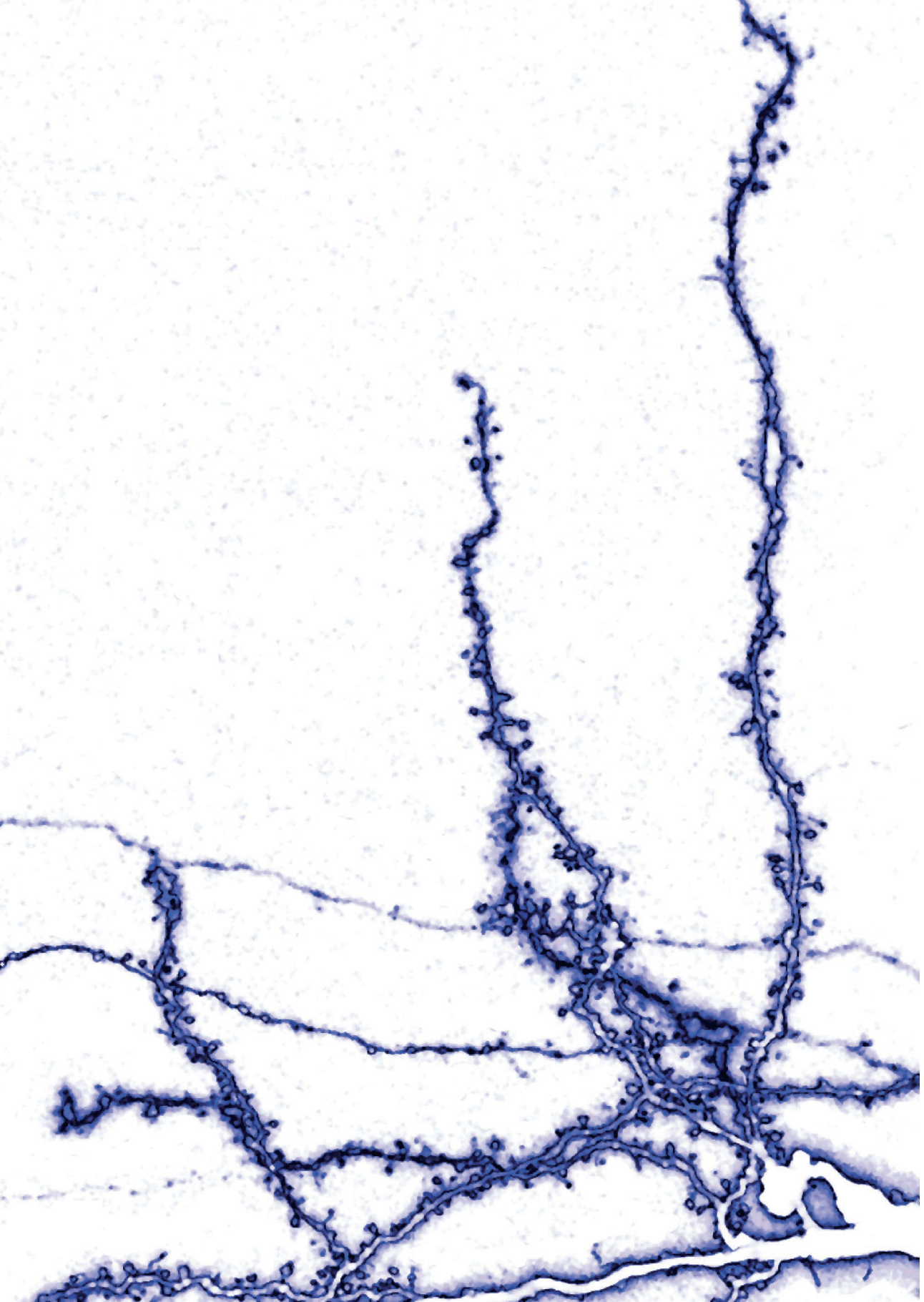

CHAPTER

2

Mutations in *ARMC9*, which encodes a basal body protein, cause Joubert syndrome in humans and ciliopathy phenotypes in zebrafish

Van De Weghe Julie C,[1,2] Rusterholz Tamara DS,[1,3] **Latour Brooke**,[1,4,5] Grout Megan E,[2] Aldinger Kimberly A,[2,6] Shaheen Ranad,[7] Dempsey Jennifer C,[2] Maddirevula Sateesh,[7] Cheng Yong-Han H,[2] Phelps Ian G,[2] Gesemann Matthias,[3] Goel Himanshu,[8,9] Birk Ohad S,[10] Alanzi Talal,[7] Rawashdeh Rifaat,[7] Khan Arif O,[7,11] University of Washington Center for Mendelian Genomics, Bamshad Michael J,[2,12] Nickerson Deborah A,[12] Neuhauss Stephan CF,[3] Dobyns William B,[2,6,13] Alkuraya Fowzan S,[14,15] Roepman Ronald,[1,4,5] Bachmann-Gagescu Ruxandra,[1,3,16] Doherty Dan[1,2,6]

1. Equal authorship
2. Department of Pediatrics, University of Washington, Seattle, WA, 98195 USA
3. Institute of Molecular Life Sciences, University of Zurich, 8057 Zurich, Switzerland
4. Department of Human Genetics, Radboud University Medical Center, 6500 HB Nijmegen, The Netherlands
5. Radboud Institute for Molecular Life Sciences, Radboud University Medical Center, 6525 GA Nijmegen, The Netherlands
6. Center for Integrative Brain Research, Seattle Children's Research Institute, Seattle, WA, 98101 USA
7. Department of Genetics, King Faisal Specialist Hospital and Research Center, Riyadh 12713, Saudi Arabia
8. Hunter Genetics, Waratah, NSW 2298, Australia
9. University of Newcastle, Callaghan, NSW 2308, Australia
10. Genetics Institute, Soroka Medical Center and National Institute for Biotechnology in the Negev (NIBN), Ben Gurion University, Beer Sheva, 8499000 Israel 653
11. Eye Institute, Cleveland Clinic Abu Dhabi, Abu Dhabi, United Arab Emirates
12. Department of Genome Sciences, University of Washington, Seattle, WA, 98195 USA
13. Department of Neurology, University of Washington, Seattle, WA, 98195 USA
14. Department of Anatomy and Cell Biology, College of Medicine, Alfaisal University, Riyadh 11533, Saudi Arabia
15. Saudi Human Genome Program, King Abdulaziz City for Science and Technology, Riyadh 12371, Saudi Arabia
16. Institute of Medical Genetics, University of Zurich, 8952 Schlieren, Switzerland

Published: Am J Hum Genet. 2017 Jul 6;101(1):23-36. doi: 10.1016/j.ajhg.2017.05.010.

ABSTRACT

Joubert syndrome (JS) is a recessive, neurodevelopmental disorder characterized by hypotonia, ataxia, abnormal eye movements and variable cognitive impairment. It is defined by a distinctive brain malformation recognized as the “molar tooth sign” on axial MRI. Subsets of affected individuals have malformations such as coloboma, polydactyly, and encephalocele, as well as progressive retinal dystrophy, fibrocystic kidney disease and liver fibrosis. More than 35 genes have been associated with JS, but the genetic cause remains unknown in a subset of families. All of the gene products localize in and around the primary cilium, making JS a canonical ciliopathy. Ciliopathies are unified by their overlapping clinical features and underlying mechanisms involving ciliary dysfunction. In this work, we identify biallelic rare, predicted-deleterious ARMC9 variants (stop-gain, missense, splice-site, and single exon deletion) in 11 individuals with JS from 8 families, accounting for approximately 1% of the disorder. The associated phenotypes range from isolated neurological involvement, to JS with retinal dystrophy, additional brain abnormalities (e.g. heterotopia, Dandy-Walker malformation), pituitary insufficiency, and/or synpolydactyly. We show that ARMC9 localizes to the basal body of the cilium and is upregulated during ciliogenesis. Typical ciliopathy phenotypes (curved body shape, retinal dystrophy, coloboma, and decreased cilia) in a CRISPR/Cas9-engineered zebrafish mutant model provide additional support for ARMC9 as a ciliopathy associated gene. Identifying ARMC9 mutations as a cause of JS takes us one step closer to a full genetic understanding of this important disorder and enables future functional work to define the central biological mechanisms underlying JS and other ciliopathies.

INTRODUCTION

Joubert syndrome (JS OMIM: P213330) is a recessive neurodevelopmental disorder characterized by motor and cognitive impairments and a distinctive hindbrain malformation giving the appearance of the "molar tooth sign" (MTS) on axial MRI. In addition to the obligate neurological features, subsets of individuals with JS have progressive retinal dystrophy, fibrocystic kidney disease and liver fibrosis, as well as malformations such as chorioretinal coloboma and polydactyly. Despite this distinctive clinical presentation, mutations in more than 35 genes cause JS, highlighting its marked genetic heterogeneity.[1-24] All of the genes to date encode proteins that function in or around the primary cilium, rendering JS a canonical ciliopathy; ciliopathies are disorders grouped by their overlapping clinical features and molecular disease mechanisms involving cilium dysfunction.[24-27] The primary cilium is a nearly ubiquitous microtubule-based organelle sheathed in a specialized membrane that projects from the cellular surface and functions like an antenna, detecting light, mechanical, and chemical cues, as well as regulating key signaling pathways such as Hedgehog [28-34] and PDGF. [35; 36] Significant advances have been made in recent years on the complex genetics underlying JS, and multiple cellular and developmental defects have been associated with loss of function for JS-associated genes in model systems.[11; 22; 31; 37-45] Despite this remarkable progress identifying candidate mechanisms, the common cellular dysfunction across genetic causes of JS is elusive. Therefore it is essential to identify the complete set of genetic defects that underlie JS to pinpoint the unifying molecular mechanism. In this work, we present evidence for mutations in armadillo repeat containing 9 (ARMC9) as a cause of JS, based on human genetic, protein localization, and zebrafish model data.

RESULTS

Exome sequencing reveals ARMC9 mutations as a cause for JS

To identify novel genetic causes of JS, we performed whole exome sequencing on a cohort of 53 individuals (51 families) with a clinical diagnosis of JS enrolled in the University of Washington (UW) Joubert Syndrome Research Program. Inclusion criteria comprised the presence of clinical findings of JS (developmental delays, hypotonia, ataxia, and/or oculomotor apraxia), diagnostic brain imaging findings, and lack of mutations in 28 JS-associated genes (NPHP1, AHI1, CEP290, RPGRIP1L, TMEM67, CC2D2A, ARL13B, INPP5E, OFD1, TMEM216, CEP41, TMEM237, TCTN2, KIF7, TCTN1, TMEM138, MKS1, C5ORF42, TMEM231, TCTN3, CSPP1, PDE6D, IFT172, ZNF423, TTC21B, B9D1, B9D2, and C2CD3) based on targeted sequencing.[46; 47] Variants from the exome sequencing data that were rare (minor allele frequency <1% in the

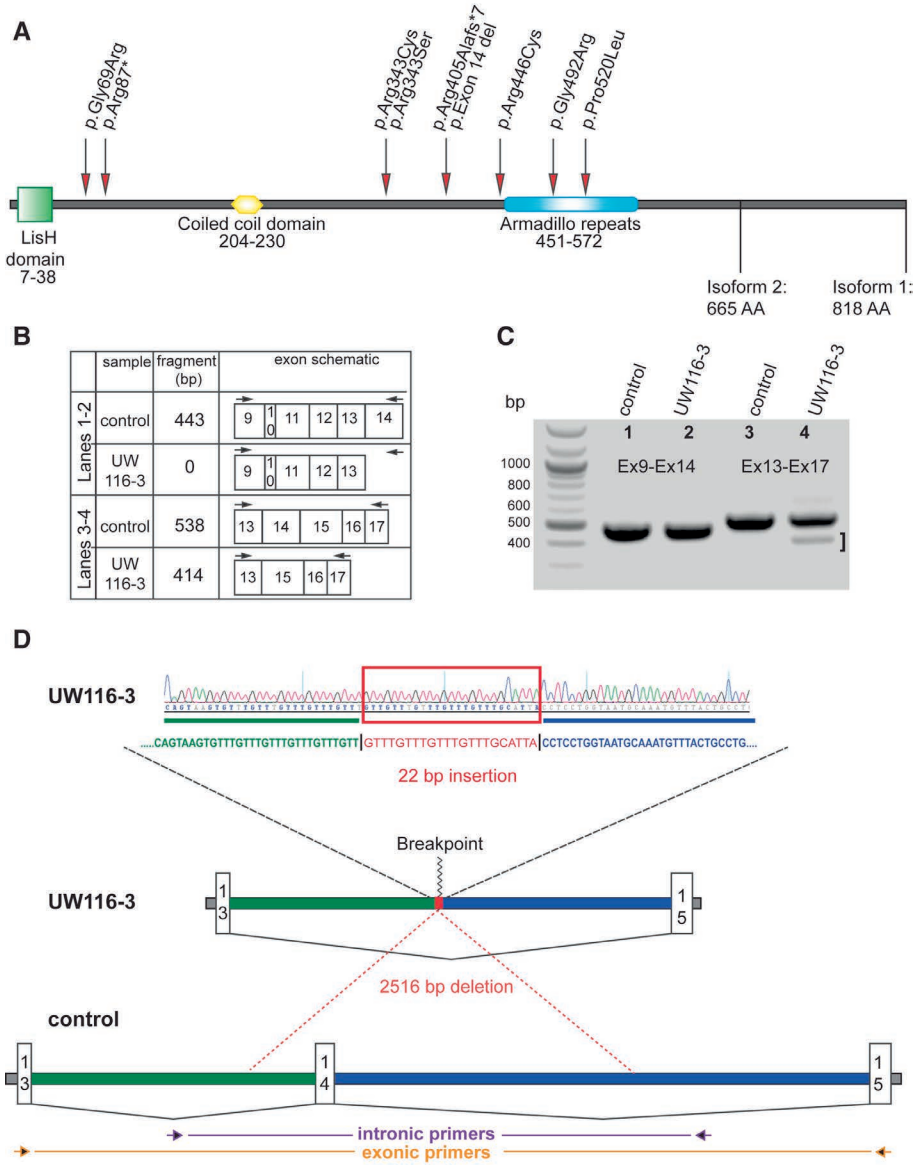

Figure 1. ARMC9 mutations cause JS: (A) The ARMC9 gene encodes a protein with an N-terminal LisH domain (green square), a coiled coil domain (yellow polygon), and a series of armadillo repeats (blue oval). Patient mutations are indicated by red arrows. (B-D) Confirmation of ARMC9 exon 14 deletion in UW116-3. No difference in the size or number of PCR products is observed between cDNA isolated from UW116-3 and two unaffected control cell lines using primers in exons 9 and 14 (C-D). Primers in exons 13 and 17 amplify a full-length product and a shorter product (bracket) in UW116-3, but only the full-length product in the two control lines. Sequencing genomic DNA amplified by primers flanking exon 14 reveals a 2516bp deletion with a 22bp insertion (D).

exome variant server [EVS] database) and predicted to be deleterious (stop-gain, frameshift, canonical splice variants and variants with CADD score >15) were retained for further analysis.

We identified pairs of siblings in two families that shared two rare, predicted-deleterious variants (RDVs) in ARMC9 (NM_025139.4): UW132-3 and -4 carry c.205G>A, p.Gly69Arg and c.1336C>T, Arg446Cys, while UW335-3 and -4 carry c.259C>T, p.Arg87* and c.1027C>A, p.Arg343Ser (Table 1 and Figure 1).

We then performed targeted sequencing of ARMC9 using the Molecular Inversion Probe (MIPs) capture method followed by next generation sequencing on samples from 534 individuals in 456 families with and without known causes. Three additional individuals in three families have ARMC9 RDVs: UW348-3 has a homozygous c.51+5G>T, predicted splice variant, UW349-3 has two RDVs (predicted splice c.1474+1G>C and missense c.1027C>T, p.Arg343Cys), while UW116-3 has a single heterozygous c.1027C>T, p.Arg343Cys. Based on decreased sequence coverage for two consecutive MIPs covering exon 14 in UW116-3, we suspected a deletion in UW116-3. We performed comparative genomic hybridization using a custom array targeting the JS genes,[58; 64; 65] and identified a 2.5kb deletion encompassing exon 14 in UW116-3 (Figure 1B-D). Exon 14 is 124 basepairs long, so its loss is predicted to result in a frameshift and truncation of the protein, or nonsense mediated decay of the transcript.

In parallel, exome sequencing in two other cohorts identified biallelic RDVs in ARMC9: three individuals (SA1-3, SA2-3 and -4) from two families in a cohort of 47 Saudi Arabian families[66] affected by JS had homozygous ARMC9 missense RDVs (c.1027C>T, p.Arg343Cys and c.1559C>T, p.Pro520Leu), and a single individual with JS (LR09-023) from a mixed cohort of 100 individuals with Dandy-Walker malformation and cerebellar hypoplasia had compound heterozygous ARMC9 RDVs (c.1474G>A, p.Gly492Arg and c.1027C>T, p.Arg343Cys). In total, we identified 10 different ARMC9 RDVs (1 stop-gain, 2 splice, 6 missense, and 1 single exon deletion) in 11 individuals from 8 families. All variants were validated by Sanger sequencing, and for seven individuals from five families their segregation with the disease was confirmed in parents and siblings; segregation was not performed in the remaining four families because DNA was not available from parents (Table 1). c.1027C>T, p.Arg343Cys appears to be a recurrent mutation rather than a founder variant, since it is present in families of diverse ethnicities, and a second variant (c.1027C>A, p.Arg343Ser) affects the same position. ARMC9 is predicted to have a Lissencephaly type-1-like homology (LisH) motif, a coiled-coil domain, and armadillo repeats (Figure 1A). Two of the missense RDVs are in the armadillo repeats, while the other four missense RDVs are not located in known domains.

ARMC9-related JS is indistinguishable from JS due to other genetic causes

All of the affected individuals have typical features of JS including hypotonia and developmental disability, most severely affecting motor and speech function (Table 1). Ages range from 2 to 33 years. Most of the individuals have isolated neurodevelopmental issues, including two with seizures (UW132-3 and UW116-3). Two individuals (UW132-4 and SA2-3) have postaxial polydactyly, while SA2-3 also has syndactyly. Two individuals (UW348-3 and SA2-3) also have retinal dystrophy, but none have kidney or liver involvement. UW349-3 has a more complex presentation with hypopituitarism, bilateral optic nerve hypoplasia, bifid uvula, and an abnormal brainstem (see below).

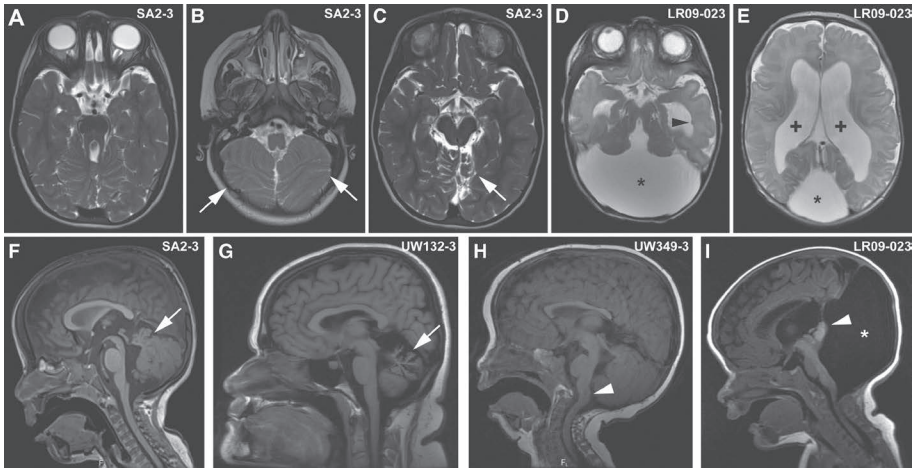

Figure 2. Brain imaging findings in individuals with ARMC9-related Joubert syndrome. (A-C) MTS (A), inferior cerebellar dysplasia (white arrows in B), and superior cerebellar dysplasia (white arrow in C) in SA2-3. (D-E) MTS (D), posterior fossa cyst (asterisks in D-E), and ventriculomegaly (plus signs in E) in LR09-023. Note the single periventricular nodular heterotopia (black arrowhead in D). (F) Vermis hypoplasia and elevated roof of the 4th ventricle in SA2-3 (white arrow). (G) Cerebellar vermis hypoplasia and atrophy in UW132-3 (white arrow). (H) Kinked brainstem and cervicomedullary heterotopia in UW349-3 (white arrowhead). (I) Enlarged posterior fossa fluid collection (white asterisk) and rotated vermis (white arrowhead) in LR09-032. (A-E) are axial T2-weighted images; (F-I) are sagittal T1-weighted images.

Based on direct review of the brain MRIs, all of the affected individuals have the "molar tooth sign," as well as dysplasia of the superior cerebellar folia (Figure 2A-B, F and Table S2). Three individuals (UW335-4, LR09-023, and SA2-3) have cerebellar hemisphere dysplasia, seen in up to 1/3 of individuals with JS (Figure 2C).[67] In addition to the MTS, LR09-023 has a large posterior fossa with a rotated cerebellar vermis consistent with Dandy-Walker malformation, (Figure 2D-E, I). LR09-023 also has a single periventricular heterotopia (Figure 2D), as do

UW116-3 and UW335-4. The two oldest individuals (UW132-3 and -4) have an atrophic appearance to their cerebellum, more severely affecting the vermis than the hemispheres (Figure 2G). UW349-3 has a kinked brainstem and cervicomedullary junction heterotopia (Figure 2H) seen in a small subset of individuals with JS,[67-71] and UW349-3 and SA2-3 have an absent posterior pituitary bright spot, but only UW349-3 has known pituitary insufficiency.

ARMC9 localizes to the basal bodies of primary cilia

JS-associated proteins have been shown to localize in and around primary cilia;[40; 45; 72-74] therefore, we used a commercially available ARMC9 antibody to evaluate endogenous ARMC9 localization in ciliated hTERT-RPE1 cells. ARMC9 localized to the ciliary basal body (Figure 3A, white arrowhead), basal to but not overlapping with the transition zone marker RPGRIP1L, as well as to the daughter centriole (Figure 3A, white arrow) marked by acetylated α-tubulin antibody (Figure 3A). ARMC9 co-localizes with γ-tubulin at the basal body (Figure 3B, white arrow), as marked by RPGRIP1L, and at the daughter centriole (Figure 3B, white arrowhead).

ARMC9 expression is upregulated in ciliated cells

Based on data from model systems and humans, many genes involved in cilium function are upregulated in ciliated cells.[75-79] We evaluated ARMC9 expression by quantitative PCR in control human fibroblasts with and without serum in the medium. In the presence of serum, fibroblasts actively divide and few have cilia, but in response to serum starvation, 80-90% drop out of the cell cycle and make cilia, similar to other published results.[80] ARMC9 expression was 2.0- to 2.7-fold higher in serum-starved cells than cells grown with serum (Figure 3C). For comparison, expression of another JS-associated gene, ARL13B, was 2.4-fold higher in serum-starved cells.

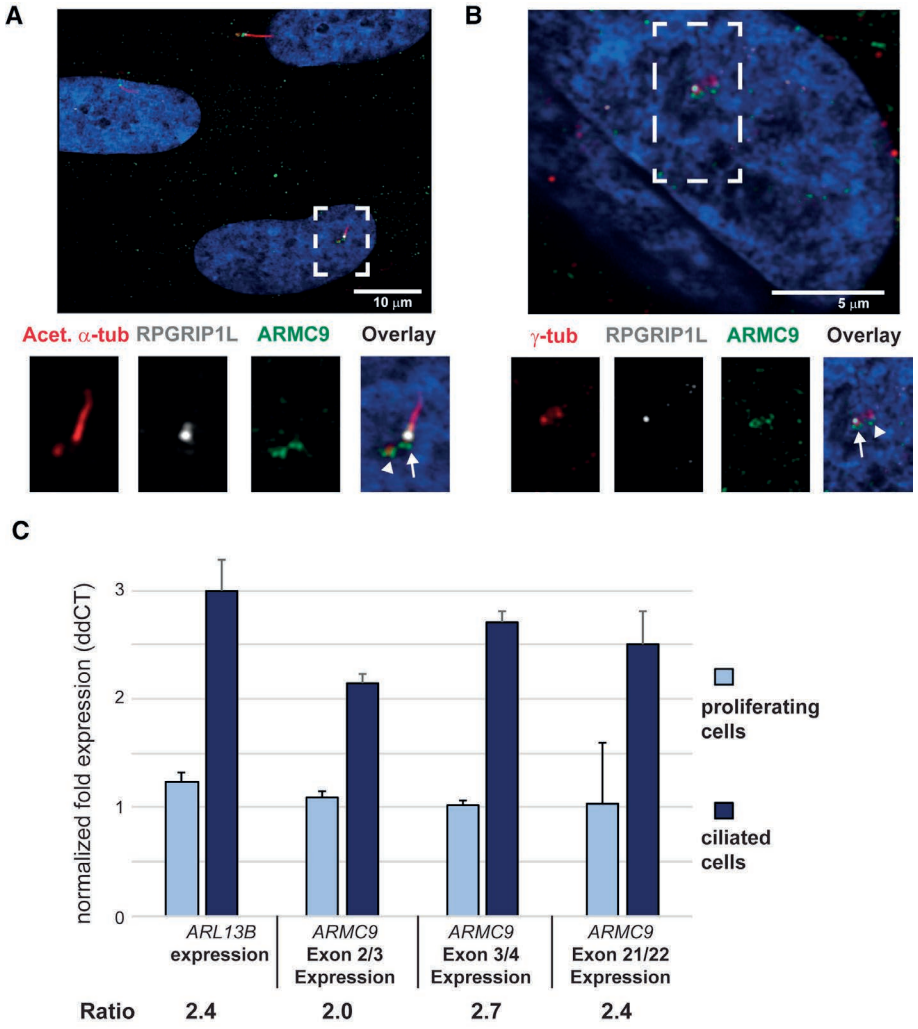

Figure 3. ARMC9 localization and ARMC9 expression in ciliated and proliferating cells (A) ARMC9 (green) localizes at the basal body (white arrow) and at the daughter centriole (white arrowhead) of the primary cilium in serum-starved hTERT RPE1 cells. The ciliary marker anti-RPGRIP1L (white), marks the ciliary transition zone and anti-acetylated α-tubulin (red) marks the ciliary axoneme. (B) ARMC9 (green) co-localizes with with γ-tubulin (red) at the ciliary basal body in serum-starved hTERT RPE1 cells. Anti-RPGRIP1L marks distal to the basal body (white) and DAPI (blue) stains the nuclei. (C) ARMC9 expression in control human fibroblasts grown with serum (proliferating cells) and without serum (ciliated cells), assessed using qPCR with GAPDH as a reference gene. ARL13B is used a positive control for a gene upregulated in ciliated cells.

Zebrafish armc9 mutants display typical ciliopathy phenotypes

To investigate the function of ARMC9 in vivo, we turned to the zebrafish model. Zebrafish have a single ARMC9 orthologue that has 58% identity and 72% similarity with the human protein. Based on database predictions and manual curation, both the LisH domain and the armadillo-fold domain are conserved in zebrafish at similar positions to the human protein (amino acids 7-39 and 375-600 respectively) (Figure S1). In adult zebrafish, armc9 is expressed in multiple CNS regions based on in situ hybridization, including the cerebellum (Figure S1), all periventricular regions (Figure 4A) and all layers of the retina (Figure 4B). To explore whether loss of armc9 function results in ciliopathy phenotypes, we engineered frameshift mutations in zebrafish using CRISPR/Cas9 (Figure S2). Co-injecting pairs of small guide RNAs targeting either exon 4 or exons 14-15 (the latter corresponding to the middle of the armadillo-fold domain), we generated mutations with very high efficiency (91% of sequenced clones from individual F0 larvae carried indels, the majority of which were out-of-frame; Figure S2). Of approximately 140 surviving F0 fish raised, 10 developed a curved body axis around six weeks of age (Figure 4C-D), including both exon 4 and exon 14-15 targeted animals. The body curvature phenotype correlated well with the presence of indels affecting the targeted exons; genotyping of 49 F0 fish by gel electrophoresis demonstrated various armc9 indels in 11 fish, only one of which did not have a curved body shape. Moreover, such body curvature was never observed in hundreds of raised F0 fish injected with sgRNA targeting non-ciliary genes (20 different sgRNAs). A recent study suggested body curvature in zebrafish caused by deficient ependymal cilia-generated cerebrospinal fluid (CSF) flow.[81] Indeed, using SEM we observed a substantial reduction of cilia numbers on the ventricular surface of adult zebrafish harboring armc9 mutations (Figure 4E-F). In addition, a subset of F0 fish with body curvature also displayed a retinal coloboma and had shortened photoreceptor outer segments, typical phenotypes observed with ciliary dysfunction (Figure 4G-J and Figure S2).[38] Taken together, these results confirm that armc9 loss-of-function in zebrafish causes typical ciliopathy phenotypes and strongly support a role for armc9 in ciliary function.

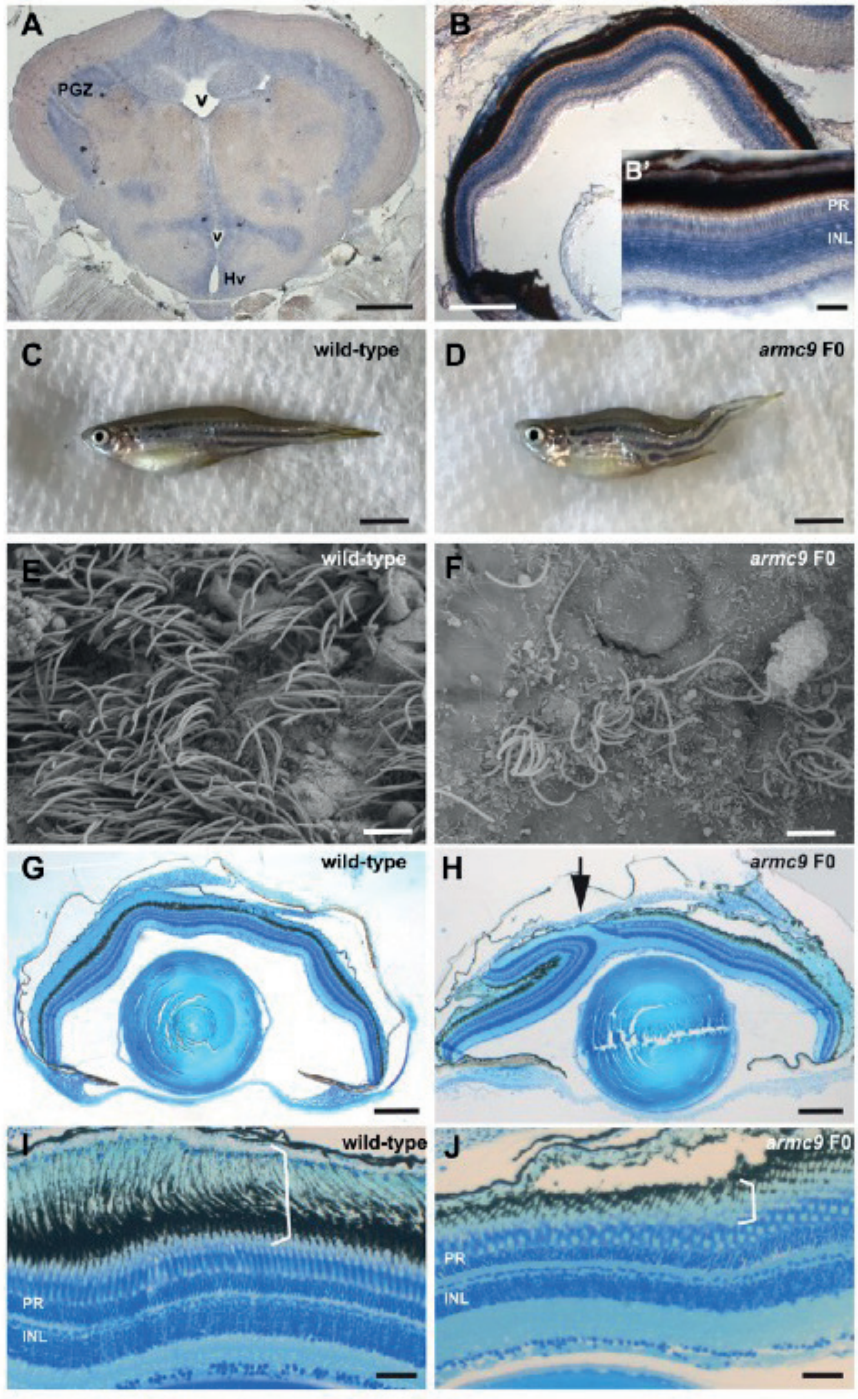
A
PGZ
V
v
Hv
B
B'
PR
INL
C
wild-type
D
armc9 F0
E
wild-type
F
armc9 F0
G
wild-type
H
armc9 F0
I
wild-type
PR
INL
J
armc9 F0
PR
INL

◀**Figure 4: armc9 loss-of-function in zebrafish leads to typical ciliopathy phenotypes** (A-B) Expression of armc9 in zebrafish adult brain (A) and retina (B) by in situ hybridization. Note the expression along ventricular surfaces in (A) and in all retinal layers, including the photoreceptor (PR) and the inner nuclear layer (INL) in (B-B'). (C-D) Adult zebrafish harboring armc9 mutations display a curved body shape (D) compared to wild-type controls (C). (E-F) Scanning electron microscopy image of the ventricular surface demonstrates bundles of cilia in wild-type (E) but substantial reduction of cilia numbers in F0 armc9 fish (F). (G-H) Histological sections through adult zebrafish eyes of wild-type (G) and F0 armc9 mutants (H) showing a coloboma (arrow). (I-J) Higher magnification images show the different retinal layers in wild-type fish (I) including the PRs and their long outer segments (OS, bracket) which represent highly specialized ciliary compartments. (J) Note the shortened OS in F0 armc9 mutants (bracket). Scale bars are 200 µm in (A-B), 50 µm in (B'), 5 mm in (C-D), 3 µm in (E-F), 250 µm in (G-H) and 50 µm in (I-J). v ventricle, PGZ periventricular grey zone of optic tectum, Hv ventral zone of periventricular hypothalamus, PR photoreceptors, INL inner nuclear layer.

DISCUSSION

Mutations in more than 35 genes have been identified in individuals with JS, explaining the genetic cause in 62% to 97% of cases, depending on the study.[47; 66; 82] In addition to these known causes, we now identify ARMC9 mutations as an additional cause of JS accounting for almost 1% of families in our cohort of >500. Substantial functional evidence supports ARMC9 as a ciliopathy-associated gene.

ARMC9 localizes to the basal body

We provide evidence that ARMC9 localizes to the ciliary basal body, similar to other JS-associated proteins (Figure 3A-B). The basal body originates from the mother centriole that docks at the cell membrane during interphase to nucleate the ciliary axoneme. The daughter centriole remains tethered to the basal body by an interconnecting fiber, and both structures often appear as juxtaposed puncta on immunofluorescence images. Basal bodies are composed of nine short triplet microtubules arranged in a circle, and two of the three microtubules in each basal body triplet extend as axonemal microtubules. Several other JS-associated proteins, OFD1, KIAA0586, and C2CD3, also localize to the basal body.[40; 45; 72-74; 83] Strikingly, ARMC9 and OFD1 both have an N-terminal LisH motif that is known to bind to microtubules (Figure 1A).[72; 84; 85] Two published proteomic studies in murine inner medullary collecting duct (IMCD3) cells also provide support for ARMC9 as a cilium-associated protein: 1) ARMC9 was detected a total of 31 times across ciliary fractions via MudPIT mass spectrometry of isolated cilia;[86] 2) Proximity labeling using a promiscuous biotinylating enzyme conjugated to the transition zone protein NPHP3 detected ARMC9-specific peptides (6 spectral counts), thus providing direct evidence for their adjacency.[87]

ARMC9 is present in ciliated organisms and upregulated in ciliated cells

The use of comparative genomics to compile genes exclusively present in ciliated organisms versus non-ciliated organisms is a common technique in identifying ciliary genes.[88; 89] ARMC9 homologs are present in ciliated eukaryotes from humans to unicellular flagellates such as Trochaic trifallax, but absent in plants, fungi, bacteria, viruses, and Archaea.[90] Expression of the ARMC9 C. elegans homolog, F59G1.4, is restricted to sensory neurons, the only ciliated cells in this organism.[91-93] Ciliary gene induction was first linked to ciliogenesis in classical experiments in unicellular flagellates, notably Chlamydomonas, a model system particularly well-suited to study ciliary biology. These experiments demonstrated that new protein synthesis was required for full cilia regeneration via use of protein synthesis inhibitors or enucleating cells.[75; 76] Later experiments show that ciliary genes are widely induced during ciliogenesis and maintained at high levels in ciliated cells.[77-79] Ciliary genes are similarly upregulated in higher organisms.[36; 94; 95] Similar to other ciliary genes, we demonstrate that ARMC9 expression is upregulated in human ciliated fibroblasts, as compared to cycling cells (Figure 3C).

Zebrafish harboring armc9 mutations display typical ciliopathy phenotypes

In a vertebrate model, zebrafish harboring CRISPR-engineered armc9 ^{mutations} display phenotypes similar to those seen with loss-of-function for zebrafish orthologs of other ciliopathy-associated genes (Figure 4).[38; 96; 97] The retinal dystrophy and/or curved body axis are also seen in loss-of-function models for the cc2d2a, ahi1, and ift genes.[38; 97-100] Furthermore, we show a strong reduction of cilia in the brain ventricles of zebrafish harboring armc9 mutations, suggesting the gene product may participate in early stages of ciliogenesis or be required for ciliary maintenance. The mosaic state of the animals analyzed in this work does not allow for discrimination between these two possibilities. Indeed, the presence of residual cilia on some ventricular cells may be explained by lack of armc9 mutations in those cells, or incomplete penetrance of the phenotype. Future analysis of stable lines will help address these possibilities. The identical phenotypes observed in multiple animals generated using guides targeting different armc9 regions, combined with the lack of these phenotypes with CRISPR/Cas9-generated deletions in 20 different non-ciliary genes, strongly supports the specificity of the observed phenotypes and argues against non-specific or off-target effects of CRISPR/Cas9.

In conclusion, we demonstrate that mutations in ARMC9 cause JS and show that ARMC9 localizes to the basal body. Given the LisH domain, ARMC9 likely binds microtubules there, but the details of its function remain to be elucidated. Delineating all of the genes involved in JS

will enable future work to determine how proteins that localize to the basal body, transition zone, cilium proper, and cilium tip all contribute to the molecular mechanism(s) underlying JS. Understanding the molecular mechanisms of JS will lead to more specific treatments in the future and further our understanding of basic ciliary biology in health and disease.

Table 1. Phenotypic features of individuals with ARMC9-related Joubert syndrome with mutations

ID#	UW132-3	UW132-4	UW348-3	UW116-3	UW335-3	UW335-4	UW349-3	LR09-023	SA1-3	SA2-3	SA2-4
Gene	ARMC9	ARMC9	ARMC9	ARMC9	ARMC9	ARMC9	ARMC9	ARMC9	ARMC9	ARMC9	ARMC9
Mutation 1	c.205G>A p.Gly69Arg	c.205G>A p.Gly69Arg	c.51+5G>T splice	c.1027C>T p.Arg343Cys	c.259C>T p.Arg87*	c.259C>T p.Arg87*	c.1474+1G>C splice	c.1474G>A p.Gly492Arg	c.1027C>T p.Arg343Cys	c.1559C>T p.Pro520Leu	c.1559C>T p.Pro520Leu
MAF	0.000025 (7/277212)	0.000025 (7/277212)	ND	ND	0.000018 (5/277214)	0.000018 (5/277214)	ND	ND	0.000053 (13/246244)	0.0000041 (1/246192)	0.0000041 (1/246192)
CADD v1.3	33	33	14.54	N/A	35	35	23.5	26	34	34	34
parent	paternal	paternal	unable	maternal	paternal	paternal	maternal	maternal	maternal	maternal	maternal
Mutation 2	c.1336C>T p.Arg446Cys	c.1336C>T p.Arg446Cys	c.51+5G>T splice	c.1211_1334del p.Arg405Afs*7	c.1027C>A p.Arg343Ser	c.1027C>A p.Arg343Ser	c.1027C>T p.Arg343Cys	c.1027C>T p.Arg343Cys	c.1027C>T p.Arg343Cys	c.1559C>T p.Pro520Leu	c.1559C>T p.Pro520Leu
AF	0.0000041 (1/246076)	0.0000041 (1/246076)	ND	0.000053 (13/246244)	0.0000041 (1/246244)	0.0000041 (1/246244)	0.000053 (13/246244)	0.000053 (13/246244)	0.000053 (13/246244)	0.0000041 (1/246192)	0.0000041 (1/246192)
CADD v1.3	34	34	14.54	34	34	34	34	34	34	34	34
parent	maternal	maternal	unable	paternal	maternal	maternal	paternal	paternal	paternal	paternal	paternal
Ethnicity/ country	white/ US	white/ US	white/ Israel	white/ US	white/ Australia	white/ Australia	>1 race/ US	white/ US	Arab/ Saudi	Arab/ Saudi	Arab/ Saudi
gender	F	M	F	F	F	M	M	M	M	F	M
age (years)	33	29	10	8	5	7	2	8	7	4	5
Dev Disability	Y	Y	Y	Y	Y	Y	Y	Y	Y	Y	Y
apnea/tachyp	N	N	unk	both	both	N	A	T	Y*	N	Y*
abnl eye mvts	Y	Y	Y	Y	Y	Y	Y	unk	Y	Y	N
retinal dystrophy	N	N	Y	N	N	N	N	unk	unk	Y	N
kidney	N	N	unk	unk	N	N	N	unk	N	N	N
liver	N	N	unk	unk	N	N	N	unk	N	N	N
polydactyly	N	Y	unk	N	N	N	N	N	N	Y	N

ID#	UW132-3	UW132-4	UW348-3	UW116-3	UW335-3	UW335-4	UW349-3	LR09-023	SA1-3	SA2-3	SA2-4
Gene	**ARMC9**	**ARMC9**	**ARMC9**	**ARMC9**	**ARMC9**	**ARMC9**	**ARMC9**	**ARMC9**	**ARMC9**	**ARMC9**	**ARMC9**
coloboma	N	N	unk	N	N	N	N	unk	unk	N	N
ptosis	N	Y	unk	Y	N	N	Y	Y	Y	Y	Y
seizures	Y	N	N	Y	N	N	N	N	N	N	N
other	Hysterectomy 2016 (heavy bleeding); worsening visual acuity; seizures	Lithium induced hypo-thyroidism L foot postaxial polydactyly	Abnormal ERG	G-tube	-	single heterotopia (left occipital horn)	Micrognathia; high palate; bifid uvula; bilateral optic nerve hypoplasia, GH deficiency; micropenis, eyelid implants; possible hearing loss; borderline HSM;	Dandy Walker malformation; Ventriculo- and cysto-peritoneal shunts; non-ambulatory; non- verbal at age 8 yr	-	Broad nasal bridge, thin upper lip, Y-shaped 2/3 toe syndactyly	-

A=apnea, AF= Allele Frequency based on gnomAD,[51] F=female, GH=Growth Hormone, HSM= heptosplenomegaly, ID=Identification, M=male, N=No, ND=not documented, T=tachypnea, unk=unknown, Y=Yes; *=transient neonata

MATERIALS AND METHODS

Subject ascertainment and phenotypic data

Informed consent was obtained for all participants were enrolled under approved human subjects research protocols at the University of Washington (UW), Seattle Children's Hospital, or King Faisal Specialist Hospital and Research Centre (KFSHRC). All participants have clinical findings of JS (intellectual impairment, hypotonia, ataxia and/or oculomotor apraxia) and diagnostic or supportive brain imaging findings (MTS or cerebellar vermis hypoplasia). Clinical data were obtained by direct examination of participants, review of medical records and structured questionnaires.

Variant identification

Samples from individuals affected by JS were previously screened using a Molecular Inversion Probes (MIPs) targeted capture[46] for AHI1 [OMIM: 608894], ARL13B [OMIM: 608922], B9D1 [OMIM: 614144], B9D2 [OMIM: 611951], C2CD3 [OMIM: 615944], C5ORF42 [OMIM: 614571], CC2D2A [OMIM: 612013], CEP290 [OMIM: 61042], CEP41 [OMIM: 610523], CSPP1 [OMIM: 611654], IFT172 [OMIM: 607386], INPP5E [OMIM: 613037], KIF7 [OMIM: 611254], MKS1 [OMIM: 609883], NPHP1 [OMIM: 607100], OFD1 [OMIM: 300170], RPGRIP1L [OMIM: 610937], TCTN1 [OMIM: 609863], TCTN2 [OMIM: 613846], TCTN3 [OMIM: 613847], TMEM138 [OMIM: 614459], TMEM216 [OMIM: 613277], TMEM231 [OMIM: 614949], TMEM237 [OMIM: 614423], TMEM67 [OMIM: 609884], TTC21B [OMIM: 612014] and ZNF423 [OMIM: 604557].[1-24; 47] In samples without causal variants, exome sequencing was performed as previously described [48] using Roche Nimblegen SeqCap EZ Human Exome Library v2.0 capture probes (36.5 Mb of coding exons) and paired-end 50 base pair reads on an Illumina HiSeq sequencer. In accordance with the Genome Analysis ToolKit's (GATK) best practices, we mapped sequence reads to the human reference genome (hg19) using the Burrows-Wheeler Aligner (v.0.6.2), removed duplicate reads (PicardMarkDuplicates v1.70), and performed indel realignment (GATK IndelRealigner v.1.6) and base-quality recalibration (GATK TableRecalibration v1.6). We called variants using the GATK UnifiedGenotyper and flagged with VariantFiltration to mark potential false positives that did not pass the following filters: Heterozygous Allele Balance (ABHet) > 0.75, Quality by Depth > 5.0, Quality (QUAL) _ 50.0, Homopolymer Run (Hrun) < 4.0, and low depth (<6x). We used SeattleSeq for variant annotation and the Combined Annotation Dependent Depletion (CADD) score to determine deleteriousness of identified missense variants.[49] Based on CADD score data for causal variants in other JS-associated genes, we used a CADD score cutoff of 15 to define deleterious variants.[47]

LR09-023 was ascertained as part of a larger study of genetic causes for Dandy-Walker malformation (DWM). Exome sequencing of this individual and his parents was performed by Beckman Coulter genomics as follows: genomic DNA isolated from peripheral blood was captured using the Agilent SureSelect V5 enrichment kit and sequenced on an Illumina HiSeq 2000 as 150-bp paired-end runs. Reads were aligned with BWA; variants were called with GATK and freebayes. Variants called by both GATK and freebayes were annotated using Gemini,[50] including data sets from the ExAc Exome,[51] NHLBI 6500 Exome,[52] and 1000 Genomes projects for variant frequencies, and amino-acid-change functional predictions from CADD scores.[49] Variants were filtered for de novo, recessive (compound heterozygous or homozygous), or X-linked inheritance, <0.001 frequency in public databases, predicted to be deleterious by CADD >10, and expressed in human fetal (BrainSpan[53]) or adult (GTex[54]) cerebellum.

For the two families in the Saudi Arabian cohort, DNA from the affected individuals, as well as their unaffected siblings and parents, were genotyped using the Axiom SNP Chip platform to determine the candidate autozygome.[55; 56] The previously described "Mendeliome" targeted sequencing assay was then performed on DNA from affected members to search for likely causal variants in the known JS genes followed by whole exome sequencing in samples without causal variants.[57] WES was performed using TruSeq Exome Enrichment kit (Illumina) following the manufacturer's protocol. Samples were prepared as an Illumina sequencing library, and in the second step, the sequencing libraries were enriched for the desired target using the Illumina Exome Enrichment protocol. The captured libraries were sequenced using an Illumina HiSeq 2000 Sequencer. The reads were mapped against UCSC hg19 by BWA. SNPs and Indels were detected by SAMTOOLS. Homozygous rare, predicted-deleterious, coding/splicing variants within the autozygome of the affected individual were considered as likely causal. We defined rare variants as those with frequency of <0.1% in publicly available variant databases (1000 Genomes, Exome Variant Server and gnomAD), as well as a database of 2,379 in-house ethnically-matched exomes, and deleterious if predicted to be pathogenic by PolyPhen, SIFT and CADD (score >15).

Array CGH

To assess copy number variation, we performed array comparative genomic hybridization using a custom 8x60K oligonucleotide array (Agilent Technologies, Santa Clara, CA)[58] targeting AHI1, ARL13B, ARMC9, B9D1, B9D2, C2CD3, C5orf42, CBY1 [OMIM: 607757], CC2D2A, CEP104 [OMIM: 616690], CEP120 [OMIM: 613446], CEP290, CEP41 [OMIM: 610523], CEP83 [OMIM:615847], CSPP1, DDX59 [OMIM: 615464], EXOC8 [OMIM: 615283], HYLS1 [OMIM:610693], IFT172,

INPP5E, KCTD10 [OMIM: 613421], KIAA0556 [OMIM: 616650], KIAA0586 [OMIM: 610178], KIAA0753 [OMIM: 617112], KIF7, MKS1, NPHP1, NPHP3 [OMIM: 608002], NPHP4 [OMIM: 607215], OFD1, PDE6D, PIBF1 [OMIM: 607532], POC1B [OMIM: 614784], RPGRIP1L, TBC1D32 [OMIM: 615867], TCTN1, TCTN2, TCTN3, TMEM107 [OMIM:616183], TMEM138, TMEM17 [OMIM: 614950], TMEM216, TMEM218, TMEM231, TMEM237, TMEM67, TTC21B, ZNF423. Probe spacing was a median of 11bp in the exons, and a median of 315bp throughout the intronic regions and 100kb on either side of each gene: Data were generated on an Agilent Technologies DNA Microarray Scanner with Surescan High-Resolution Technology using Agilent Scan Control software, and were processed and analyzed using Agilent Feature Extraction and Agilent Cytogenomics software.

RNA isolation and quantitative PCR

We cultured human fibroblasts from healthy controls in DMEM + 10 % fetal bovine serum (FBS) and 1% penicillin/streptomycin under standard conditions.[59-61] To induce ciliogenesis, we cultured in DMEM without FBS once the cells reached ~70% confluency. After treatment with 0.05% trypsin, cycling cells and serum-starved cells were harvested and RNA extracted using the Aurum Total RNA Mini Kit (Bio-rad, Hercules, CA). We generated cDNA from 2 μg of total RNA using the iScript Reverse Transcription Supermix for RT-qPCR (Biorad, Hercules, CA). The expression of ARL13B and ARMC9 mRNAs was determined using qPCR. Each cDNA sample was amplified using Power SYBR Green PCR Master Mix (Applied Biosystems, Thermo Fisher Scientific) on the C1000 Thermal Cycler CFX (Bio-rad, Hercules, CA). After an initial denaturation of 10 minutes at 95°C, each cycle (x39) consisted of denaturation at 95°C for 15 seconds and anneal/extend at 60°C for one minute with a plate read. The primers for ARL13B and ARMC9 are listed in Table S1. GAPDH was used as an endogenous control to normalize each sample. The experiment was performed in triplicate.

Cell lines, antibodies and microscopy

Human telomerase-immortalized retinal pigment epithelium (hTERT-RPE1) cells were grown in DMEM (PAA) supplemented with F12 in a 1:1 ratio with 10% fetal bovine serum and 1% penicillin/streptomycin. Cells were plated on glass cover slips for immunofluorescence imaging. Twenty-four hours after plating, cells were serum starved for 48 h in 0.2% FBS medium to induce cell cycle arrest and ciliogenesis. Cells were rinsed once with 1 x PBS at room temperature and then fixed in 2% paraformaldehyde for 20 min and permeabilized with 1% Triton-X for 5 min. Cells were blocked in freshly prepared 2% bovine serum albumin for 45

minutes and then incubated with the following antibodies for 1 hour: rabbit anti-ARMC9 (Atlas Antibodies, HPA019041; 1:200), guinea pig anti-RPGRIP1L (SNC040, 1:300), a monoclonal anti-acetylated tubulin (clone 6-11-B1, Sigma-Aldrich, T6793; 1:1000), and a mouse monoclonal anti-γ-tubulin (Sigma T5326, 1:500). Anti-ARMC9 recognizes an epitope at the N-terminal portion of the protein. Cells were stained with secondary antibodies for 45 min. The following secondary antibodies were used (all from Life Technologies/Thermo Fisher Scientific, Bleiswijk, The Netherlands; all diluted 1:500 in 2% BSA): anti-guinea pig IgG Alexa Fluor 647, anti-rabbit IgG Alexa Fluor 488, and anti-mouse IgG Alexa Fluor 568. DAPI (4',6-diamidino-2-phenylindole) stained the nucleus. Confocal imaging was done with the Zeiss LSM 880 Laser scanning microscope equipped with Airyscan technology.

Antibody validation with siRNA knock down

Reverse transfections on hTERT-RPE1 cells were performed with pre-designed Silencer Select siRNA to ARMC9 (Ambion from Life Technologies), as well as a positive control to knock down GAPDH (Ambion from Life Technologies) and a scrambled non-targeting negative control (Ambion from Life Technologies). Lyophilised siRNAs were re-constituted with RNase-free water (Thermo Scientific) to a final working concentration of 50 nM. Lipofectamine RNAiMax (LifeTechnologies) and Opti-MEM (LifeTechnologies) were used for siRNA transfection and done in accordance with the manufacturer's protocol. Cells were harvested and lysed with RIPA lysis buffer supplemented with Complete Protease Inhibitor Cocktail Tablets (Roche) 72 hours post transfection and western blotting was performed. Primary antibodies mouse monoclonal GAPDH (Thermo Scientific) and rabbit polyclonal ARMC9 (Human Protein Atlas Sigma Aldrich) were used at 1:1000 and 1:500 dilutions respectively and incubated overnight at 4 degrees. Secondary antibodies goat anti-rabbit IRDye800 (LI-COR Biosciences) and goat anti-mouse IRDye680 (LI-COR Biosciences) were used at a dilution of 1:10,000 and incubated with blots for 1 hour at room temperature. Imaging was done with the Odyssey CLx imaging system (LI-COR Biosciences). Protein quantification was performed using Image Studio Lite software (LI-COR Biosciences).

Zebrafish in situs, CRISPR, mutation assay, histology

Zebrafish were maintained at 28°C with a 14 h/10 h light/dark cycle as previously described.[62] All zebrafish protocols were in compliance with internationally recognized guidelines for the use of zebrafish in biomedical research, and the experiments were approved by local authorities (Veterinäramt Zürich TV4206).

In situ hybridization was performed following standard protocols with a probe spanning over 800 bp at the 3' end of armc9 generated using the primers 5'-AGCTCAACTCAGCGACCATC-3' and 3'-TGCTGTTACAGGAAGCTGGA-5'. sgRNAs for CRISPR/Cas9 mutagenesis were designed using the CHOPCHOP website: 3'-GGGATTGGGCACAAATGGCA-5' and 3'-GGAACAGCTCCTGAAAGGAC-5' for exon 4 and 5'-GGTCAAAGAGCTGAATGACT-3' and 3'-GGAGCTCCGTCAGGACTTTC-5' for exon 14/15. Pairs of sgRNAs for each target site were mixed with Cas9 protein (gift from Darren Gilmour) and injected into 1-cell stage embryos obtained through natural matings. Individual larvae were lysed for assessment of mutagenesis efficiency. Amplification of the target regions for genotyping was performed using primer pairs 5'-CAGCCAAACCACTGAGTTCC-3' and 3'-TGACCCTGTAGTGTGTGCGTA-5' for exon 4 and 5'-CACGCCTTGCACCACACT-3' and 3'-CACTCCCCTGTTTGAGCAAT-5' for exons 14/15. The PCR products were analyzed on gel electrophoresis, bands were cut out and subcloned before sequencing. The remaining F0 fish were raised. Brains of four F0 fish with curved bodies were dissected out at five months of age, halved and fixed in 2.5% Glutaraldehyde in 0.1M Cacodylate buffer and prepared for scanning electron microscopy (SEM) following standard protocols. SEM was performed on a ZEISS Supra VP 50 microscope. Cryosections were performed following standard protocols and IHC was performed as previously described,[37; 62] using the zpr1 antibody.[63] Vybrant® DiO (ThermoFisherScientific) and DAPI were used for counterstaining. Images were acquired on a Leica HCS LSI confocal microscope. Histological sections using Technovit were performed as previously described.[62] Images were acquired on an Olympus BX61 microscope.

ACKNOWLEDGEMENTS

We deeply thank the families who participated in this study. We also thank the Joubert syndrome and Related Disorder Foundation for referring families, Heather Mefford and her laboratory for help with arrays, the Center for Microscopy and Image Analysis, University of Zurich (ZMB), for their assistance with Scanning Electron Microscopy, in particular Gery Barmettler, the Genotyping and Sequencing Core Facilities at King Faisal Specialist Hospital & Research Centre for their technical help, and Darren Gilmour for the Cas9 protein. This work was supported by the following: NIH Eunice Kennedy Shriver National Institute of Child Health and Human Development U54HD083091 (Genetics Core and Sub-project 6849) to DD, NIH National Institute of Neurological Diseases and Stroke (R01NS064077 to DD, and R01NS050375 to WBD), private donations from families to DD, the Swiss National Science foundation (PZ00P3_163979) to RB-G, the Netherlands Organization for Scientific Research (NWO Vici-865.12.005) to RR, the King Salman Center for Disability Research to FSA, Dandy-Walker Alliance to WBD, and NIH National Human Genome Research Institute (U54HG006493) to MB and DN.

WEB RESOURCES

SeattleSeq, http://snp.gs.washington.edu/SeattleSeqAnnotation137/
Combined Annotation Dependent Depletion (CADD) score, http://cadd.gs.washington.edu/
UCSC hg19, http://genome.ucsc.edu/
BWA, http://bio-bwa.sourceforge.net/
SAMTOOLS, http://samtools.sourceforge.net/
CHOPCHOP website http://chopchop.cbu.uib.no/
exome variant server [EVS] database, http://evs.gs.washington.edu/EVS/
Online Mendelian Inheritance in Man, https://www.omim.org/

REFERENCES

1. Valente, E.M., Logan, C.V., Mougou-Zerelli, S., Lee, J.H., Silhavy, J.L., Brancati, F., Iannicelli, M., Travaglini, L., Romani, S., Illi, B., et al. (2010). Mutations in TMEM216 perturb ciliogenesis and cause Joubert, Meckel and related syndromes. Nat Genet 42, 619-625.
2. Tuz, K., Bachmann-Gagescu, R., O'Day, D.R., Hua, K., Isabella, C.R., Phelps, I.G., Stolarski, A.E., O'Roak, B.J., Dempsey, J.C., Lourenco, C., et al. (2014). Mutations in CSPP1 cause primary cilia abnormalities and Joubert syndrome with or without Jeune asphyxiating thoracic dystrophy. Am J Hum Genet 94, 62-72.
3. Thomas, S., Legendre, M., Saunier, S., Bessieres, B., Alby, C., Bonniere, M., Toutain, A., Loeuillet, L., Szymanska, K., Jossic, F., et al. (2012). TCTN3 mutations cause Mohr-Majewski syndrome. Am J Hum Genet 91, 372-378.
4. Srour, M., Schwartzentruber, J., Hamdan, F.F., Ospina, L.H., Patry, L., Labuda, D., Massicotte, C., Dobrzeniecka, S., Capo-Chichi, J.M., Papillon-Cavanagh, S., et al. (2012). Mutations in C5ORF42 cause Joubert syndrome in the French Canadian population. Am J Hum Genet 90, 693-700.
5. Srour, M., Hamdan, F.F., Schwartzentruber, J.A., Patry, L., Ospina, L.H., Shevell, M.I., Desilets, V., Dobrzeniecka, S., Mathonnet, G., Lemyre, E., et al. (2012). Mutations in TMEM231 cause Joubert syndrome in French Canadians. J Med Genet 49, 636-641.
6. Sayer, J.A., Otto, E.A., O'Toole, J.F., Nurnberg, G., Kennedy, M.A., Becker, C., Hennies, H.C., Helou, J., Attanasio, M., Fausett, B.V., et al. (2006). The centrosomal protein nephrocystin-6 is mutated in Joubert syndrome and activates transcription factor ATF4. Nat Genet 38, 674-681.
7. Sang, L., Miller, J.J., Corbit, K.C., Giles, R.H., Brauer, M.J., Otto, E.A., Baye, L.M., Wen, X., Scales, S.J., Kwong, M., et al. (2011). Mapping the NPHP-JBTS-MKS protein network reveals ciliopathy disease genes and pathways. Cell 145, 513-528.
8. Romani, M., Micalizzi, A., Kraoua, I., Dotti, M.T., Cavallin, M., Sztriha, L., Ruta, R., Mancini, F., Mazza, T., Castellana, S., et al. (2014). Mutations in B9D1 and MKS1 cause mild Joubert syndrome: expanding the genetic overlap with the lethal ciliopathy Meckel syndrome. Orphanet J Rare Dis 9, 72.
9. Parisi, M.A., Bennett, C.L., Eckert, M.L., Dobyns, W.B., Gleeson, J.G., Shaw, D.W., McDonald, R., Eddy, A., Chance, P.F., and Glass, I.A. (2004). The NPHP1 gene deletion associated with juvenile nephronophthisis is present in a subset of individuals with Joubert syndrome. Am J Hum Genet 75, 82-91.
10. Lee, J.H., Silhavy, J.L., Lee, J.E., Al-Gazali, L., Thomas, S., Davis, E.E., Bielas, S.L., Hill, K.J., Iannicelli, M., Brancati, F., et al. (2012). Evolutionarily assembled cis-regulatory module at a human ciliopathy locus. Science 335, 966-969.
11. Lee, J.E., Silhavy, J.L., Zaki, M.S., Schroth, J., Bielas, S.L., Marsh, S.E., Olvera, J., Brancati, F., Iannicelli, M., Ikegami, K., et al. (2012). CEP41 is mutated in Joubert syndrome and is required for tubulin glutamylation at the cilium. Nat Genet 44, 193-199.
12. Huang, L., Szymanska, K., Jensen, V.L., Janecke, A.R., Innes, A.M., Davis, E.E., Frosk, P., Li, C., Willer, J.R., Chodirker, B.N., et al. (2011). TMEM237 is mutated in individuals with a Joubert syndrome related disorder and expands the role of the TMEM family at the ciliary transition zone. Am J Hum Genet 89, 713-730.
13. Halbritter, J., Bizet, A.A., Schmidts, M., Porath, J.D., Braun, D.A., Gee, H.Y., McInerney-Leo, A.M., Krug, P., Filhol, E., Davis, E.E., et al. (2013). Defects in the IFT-B component IFT172 cause Jeune and Mainzer-Saldino syndromes in humans. Am J Hum Genet 93, 915-925.

14. Gorden, N.T., Arts, H.H., Parisi, M.A., Coene, K.L., Letteboer, S.J., van Beersum, S.E., Mans, D.A., Hikida, A., Eckert, M., Knutzen, D., et al. (2008). CC2D2A is mutated in Joubert syndrome and interacts with the ciliopathy-associated basal body protein CEP290. Am J Hum Genet 83, 559-571.
15. Garcia-Gonzalo, F.R., Corbit, K.C., Sirerol-Piquer, M.S., Ramaswami, G., Otto, E.A., Noriega, T.R., Seol, A.D., Robinson, J.F., Bennett, C.L., Josifova, D.J., et al. (2011). A transition zone complex regulates mammalian ciliogenesis and ciliary membrane composition. Nat Genet 43, 776-784.
16. Ferland, R.J., Eyaid, W., Collura, R.V., Tully, L.D., Hill, R.S., Al-Nouri, D., Al-Rumayyan, A., Topcu, M., Gascon, G., Bodell, A., et al. (2004). Abnormal cerebellar development and axonal decussation due to mutations in AHI1 in Joubert syndrome. Nat Genet 36, 1008-1013.
17. Edvardson, S., Shaag, A., Zenvirt, S., Erlich, Y., Hannon, G.J., Shanske, A.L., Gomori, J.M., Ekstein, J., and Elpeleg, O. (2010). Joubert syndrome 2 (JBTS2) in Ashkenazi Jews is associated with a TMEM216 mutation. Am J Hum Genet 86, 93-97.
18. Davis, E.E., Zhang, Q., Liu, Q., Diplas, B.H., Davey, L.M., Hartley, J., Stoetzel, C., Szymanska, K., Ramaswami, G., Logan, C.V., et al. (2011). TTC21B contributes both causal and modifying alleles across the ciliopathy spectrum. Nat Genet 43, 189-196.
19. Dafinger, C., Liebau, M.C., Elsayed, S.M., Hellenbroich, Y., Boltshauser, E., Korenke, G.C., Fabretti, F., Janecke, A.R., Ebermann, I., Nurnberg, G., et al. (2011). Mutations in KIF7 link Joubert syndrome with Sonic Hedgehog signaling and microtubule dynamics. J Clin Invest 121, 2662-2667.
20. Coene, K.L., Roepman, R., Doherty, D., Afroze, B., Kroes, H.Y., Letteboer, S.J., Ngu, L.H., Budny, B., van Wijk, E., Gorden, N.T., et al. (2009). OFD1 is mutated in X-linked Joubert syndrome and interacts with LCA5-encoded lebercilin. Am J Hum Genet 85, 465-481.
21. Cantagrel, V., Silhavy, J.L., Bielas, S.L., Swistun, D., Marsh, S.E., Bertrand, J.Y., Audollent, S., Attie-Bitach, T., Holden, K.R., Dobyns, W.B., et al. (2008). Mutations in the cilia gene ARL13B lead to the classical form of Joubert syndrome. Am J Hum Genet 83, 170-179.
22. Bielas, S.L., Silhavy, J.L., Brancati, F., Kisseleva, M.V., Al-Gazali, L., Sztriha, L., Bayoumi, R.A., Zaki, M.S., Abdel-Aleem, A., Rosti, R.O., et al. (2009). Mutations in INPP5E, encoding inositol polyphosphate-5-phosphatase E, link phosphatidyl inositol signaling to the ciliopathies. Nat Genet 41, 1032-1036.
23. Baala, L., Romano, S., Khaddour, R., Saunier, S., Smith, U.M., Audollent, S., Ozilou, C., Faivre, L., Laurent, N., Foliguet, B., et al. (2007). The Meckel-Gruber syndrome gene, MKS3, is mutated in Joubert syndrome. Am J Hum Genet 80, 186-194.
24. Arts, H.H., Doherty, D., van Beersum, S.E., Parisi, M.A., Letteboer, S.J., Gorden, N.T., Peters, T.A., Marker, T., Voesenek, K., Kartono, A., et al. (2007). Mutations in the gene encoding the basal body protein RPGRIP1L, a nephrocystin-4 interactor, cause Joubert syndrome. Nat Genet 39, 882-888.
25. Badano, J.L., Mitsuma, N., Beales, P.L., and Katsanis, N. (2006). The ciliopathies: an emerging class of human genetic disorders. Annu Rev Genomics Hum Genet 7, 125-148.
26. Dixon-Salazar, T., Silhavy, J.L., Marsh, S.E., Louie, C.M., Scott, L.C., Gururaj, A., Al-Gazali, L., Al-Tawari, A.A., Kayserili, H., Sztriha, L., et al. (2004). Mutations in the AHI1 gene, encoding jouberin, cause Joubert syndrome with cortical polymicrogyria. Am J Hum Genet 75, 979-987.
27. Doherty, D. (2009). Joubert syndrome: insights into brain development, cilium biology, and complex disease. Semin Pediatr Neurol 16, 143-154.
28. Chavez, M., Ena, S., Van Sande, J., de Kerchove d'Exaerde, A., Schurmans, S., and Schiffmann, S.N. (2015). Modulation of Ciliary Phosphoinositide Content Regulates Trafficking and Sonic Hedgehog Signaling Output. Dev Cell 34, 338-350.

29. Dyson, J.M., Conduit, S.E., Feeney, S.J., Hakim, S., DiTommaso, T., Fulcher, A.J., Sriratana, A., Ramm, G., Horan, K.A., Gurung, R., et al. (2017). INPP5E regulates phosphoinositide-dependent cilia transition zone function. J Cell Biol 216, 247-263.

30. Garcia-Gonzalo, F.R., Phua, S.C., Roberson, E.C., Garcia, G., 3rd, Abedin, M., Schurmans, S., Inoue, T., and Reiter, J.F. (2015). Phosphoinositides Regulate Ciliary Protein Trafficking to Modulate Hedgehog Signaling. Dev Cell 34, 400-409.

31. He, M., Subramanian, R., Bangs, F., Omelchenko, T., Liem, K.F., Jr., Kapoor, T.M., and Anderson, K.V. (2014). The kinesin-4 protein Kif7 regulates mammalian Hedgehog signalling by organizing the cilium tip compartment. Nat Cell Biol 16, 663-672.

32. Ko, H.W., Norman, R.X., Tran, J., Fuller, K.P., Fukuda, M., and Eggenschwiler, J.T. (2010). Broad-minded links cell cycle-related kinase to cilia assembly and hedgehog signal transduction. Dev Cell 18, 237-247.

33. Mariani, L.E., Bijlsma, M.F., Ivanova, A.I., Suciu, S.K., Kahn, R.A., and Caspary, T. (2016). Arl13b regulates Shh signaling from both inside and outside the cilium. Mol Biol Cell.

34. Qin, J., Lin, Y., Norman, R.X., Ko, H.W., and Eggenschwiler, J.T. (2011). Intraflagellar transport protein 122 antagonizes Sonic Hedgehog signaling and controls ciliary localization of pathway components. Proc Natl Acad Sci U S A 108, 1456-1461.

35. Clement, D.L., Mally, S., Stock, C., Lethan, M., Satir, P., Schwab, A., Pedersen, S.F., and Christensen, S.T. (2013). PDGFRalpha signaling in the primary cilium regulates NHE1-dependent fibroblast migration via coordinated differential activity of MEK1/2-ERK1/2-p90RSK and AKT signaling pathways. J Cell Sci 126, 953-965.

36. Schneider, L., Clement, C.A., Teilmann, S.C., Pazour, G.J., Hoffmann, E.K., Satir, P., and Christensen, S.T. (2005). PDGFRalphaalpha signaling is regulated through the primary cilium in fibroblasts. Curr Biol 15, 1861-1866.

37. Bachmann-Gagescu, R., Dona, M., Hetterschijt, L., Tonnaer, E., Peters, T., de Vrieze, E., Mans, D.A., van Beersum, S.E., Phelps, I.G., Arts, H.H., et al. (2015). The Ciliopathy Protein CC2D2A Associates with NINL and Functions in RAB8-MICAL3-Regulated Vesicle Trafficking. PLoS Genet 11, e1005575.

38. Bachmann-Gagescu, R., Phelps, I.G., Stearns, G., Link, B.A., Brockerhoff, S.E., Moens, C.B., and Doherty, D. (2011). The ciliopathy gene cc2d2a controls zebrafish photoreceptor outer segment development through a role in Rab8-dependent vesicle trafficking. Hum Mol Genet 20, 4041-4055.

39. Craige, B., Tsao, C.C., Diener, D.R., Hou, Y., Lechtreck, K.F., Rosenbaum, J.L., and Witman, G.B. (2010). CEP290 tethers flagellar transition zone microtubules to the membrane and regulates flagellar protein content. J Cell Biol 190, 927-940.

40. Hoover, A.N., Wynkoop, A., Zeng, H., Jia, J., Niswander, L.A., and Liu, A. (2008). C2cd3 is required for cilia formation and Hedgehog signaling in mouse. Development 135, 4049-4058.

41. Lancaster, M.A., Gopal, D.J., Kim, J., Saleem, S.N., Silhavy, J.L., Louie, C.M., Thacker, B.E., Williams, Y., Zaki, M.S., and Gleeson, J.G. (2011). Defective Wnt-dependent cerebellar midline fusion in a mouse model of Joubert syndrome. Nat Med 17, 726-731.

42. Plotnikova, O.V., Seo, S., Cottle, D.L., Conduit, S., Hakim, S., Dyson, J.M., Mitchell, C.A., and Smyth, I.M. (2015). INPP5E interacts with AURKA, linking phosphoinositide signaling to primary cilium stability. J Cell Sci 128, 364-372.

43. Singla, V., Romaguera-Ros, M., Garcia-Verdugo, J.M., and Reiter, J.F. (2010). Ofd1, a human disease gene, regulates the length and distal structure of centrioles. Dev Cell 18, 410-424.

44. Slaats, G.G., Saldivar, J.C., Bacal, J., Zeman, M.K., Kile, A.C., Hynes, A.M., Srivastava, S., Nazmutdinova, J., den Ouden, K., Zagers, M.S., et al. (2015). DNA replication stress underlies renal phenotypes in CEP290-associated Joubert syndrome. J Clin Invest 125, 3657-3666.
45. Ye, X., Zeng, H., Ning, G., Reiter, J.F., and Liu, A. (2014). C2cd3 is critical for centriolar distal appendage assembly and ciliary vesicle docking in mammals. Proc Natl Acad Sci U S A 111, 2164-2169.
46. O'Roak, B.J., Vives, L., Fu, W., Egertson, J.D., Stanaway, I.B., Phelps, I.G., Carvill, G., Kumar, A., Lee, C., Ankenman, K., et al. (2012). Multiplex targeted sequencing identifies recurrently mutated genes in autism spectrum disorders. Science 338, 1619-1622.
47. Bachmann-Gagescu, R., Dempsey, J.C., Phelps, I.G., O'Roak, B.J., Knutzen, D.M., Rue, T.C., Ishak, G.E., Isabella, C.R., Gorden, N., Adkins, J., et al. (2015). Joubert syndrome: a model for untangling recessive disorders with extreme genetic heterogeneity. J Med Genet 52, 514-522.
48. Chong, J.X., Buckingham, K.J., Jhangiani, S.N., Boehm, C., Sobreira, N., Smith, J.D., Harrell, T.M., McMillin, M.J., Wiszniewski, W., Gambin, T., et al. (2015). The Genetic Basis of Mendelian Phenotypes: Discoveries, Challenges, and Opportunities. Am J Hum Genet 97, 199-215.
49. Kircher, M., Witten, D.M., Jain, P., O'Roak, B.J., Cooper, G.M., and Shendure, J. (2014). A general framework for estimating the relative pathogenicity of human genetic variants. Nat Genet 46, 310-315.
50. Paila, U., Chapman, B.A., Kirchner, R., and Quinlan, A.R. (2013). GEMINI: integrative exploration of genetic variation and genome annotations. PLoS Comput Biol 9, e1003153.
51. Lek, M., Karczewski, K.J., Minikel, E.V., Samocha, K.E., Banks, E., Fennell, T., O'Donnell-Luria, A.H., Ware, J.S., Hill, A.J., Cummings, B.B., et al. (2016). Analysis of protein-coding genetic variation in 60,706 humans. Nature 536, 285-291.
52. Tennessen, J.A., Bigham, A.W., O'Connor, T.D., Fu, W., Kenny, E.E., Gravel, S., McGee, S., Do, R., Liu, X., Jun, G., et al. (2012). Evolution and functional impact of rare coding variation from deep sequencing of human exomes. Science 337, 64-69.
53. Miller, J.A., Ding, S.L., Sunkin, S.M., Smith, K.A., Ng, L., Szafer, A., Ebbert, A., Riley, Z.L., Royall, J.J., Aiona, K., et al. (2014). Transcriptional landscape of the prenatal human brain. Nature 508, 199-206.
54. Consortium, G.T. (2013). The Genotype-Tissue Expression (GTEx) project. Nat Genet 45, 580-585.
55. Alkuraya, F.S. (2010). Autozygome decoded. Genet Med 12, 765-771.
56. Alkuraya, F.S. (2012). Discovery of rare homozygous mutations from studies of consanguineous pedigrees. Curr Protoc Hum Genet Chapter 6, Unit6 12.
57. Saudi Mendeliome, G. (2015). Comprehensive gene panels provide advantages over clinical exome sequencing for Mendelian diseases. Genome Biol 16, 134.
58. Mefford, H.C., Yendle, S.C., Hsu, C., Cook, J., Geraghty, E., McMahon, J.M., Eeg-Olofsson, O., Sadleir, L.G., Gill, D., Ben-Zeev, B., et al. (2011). Rare copy number variants are an important cause of epileptic encephalopathies. Ann Neurol 70, 974-985.
59. Kane, M.S., Davids, M., Bond, M.R., Adams, C.J., Grout, M.E., Phelps, I.G., O'Day, D.R., Dempsey, J.C., Li, X., Golas, G., et al. (2017). Abnormal glycosylation in Joubert syndrome type 10. Cilia 6, 2.
60. Slaats, G.G., Isabella, C.R., Kroes, H.Y., Dempsey, J.C., Gremmels, H., Monroe, G.R., Phelps, I.G., Duran, K.J., Adkins, J., Kumar, S.A., et al. (2016). MKS1 regulates ciliary INPP5E levels in Joubert syndrome. J Med Genet 53, 62-72.
61. Stratigopoulos, G., Martin Carli, J.F., O'Day, D.R., Wang, L., Leduc, C.A., Lanzano, P., Chung, W.K., Rosenbaum, M., Egli, D., Doherty, D.A., et al. (2014). Hypomorphism for RPGRIP1L, a ciliary gene vicinal to the FTO locus, causes increased adiposity in mice. Cell Metab 19, 767-779.

62. Westerfield, M. (1993). The zebrafish book : a guide for the laboratory use of zebrafish (Brachydanio rerio).(Eugene, OR: M. Westerfield).

63. Zou, J., Lathrop, K.L., Sun, M., and Wei, X. (2008). Intact retinal pigment epithelium maintained by Nok is essential for retinal epithelial polarity and cellular patterning in zebrafish. J Neurosci 28, 13684-13695.

64. Hartmann, C., von Spiczak, S., Suls, A., Weckhuysen, S., Buyse, G., Vilain, C., Van Bogaert, P., De Jonghe, P., Cook, J., Muhle, H., et al. (2015). Investigating the genetic basis of fever-associated syndromic epilepsies using copy number variation analysis. Epilepsia 56, e26-32.

65. Mefford, H.C., Muhle, H., Ostertag, P., von Spiczak, S., Buysse, K., Baker, C., Franke, A., Malafosse, A., Genton, P., Thomas, P., et al. (2010). Genome-wide copy number variation in epilepsy: novel susceptibility loci in idiopathic generalized and focal epilepsies. PLoS Genet 6, e1000962.

66. Shaheen, R., Szymanska, K., Basu, B., Patel, N., Ewida, N., Faqeih, E., Al Hashem, A., Derar, N., Alsharif, H., Aldahmesh, M.A., et al. (2016). Characterizing the morbid genome of ciliopathies. Genome Biol 17, 242.

67. Poretti, A., Huisman, T.A., Scheer, I., and Boltshauser, E. (2011). Joubert syndrome and related disorders: spectrum of neuroimaging findings in 75 patients. AJNR Am J Neuroradiol 32, 1459-1463.

68. Friede, R.L., and Boltshauser, E. (1978). Uncommon syndromes of cerebellar vermis aplasia. I: Joubert syndrome. Dev Med Child Neurol 20, 758-763.

69. Juric-Sekhar, G., Adkins, J., Doherty, D., and Hevner, R.F. (2012). Joubert syndrome: brain and spinal cord malformations in genotyped cases and implications for neurodevelopmental functions of primary cilia. Acta Neuropathol 123, 695-709.

70. Poretti, A., Brehmer, U., Scheer, I., Bernet, V., and Boltshauser, E. (2008). Prenatal and neonatal MR imaging findings in oral-facial-digital syndrome type VI. AJNR Am J Neuroradiol 29, 1090-1091.

71. Yachnis, A.T., and Rorke, L.B. (1999). Neuropathology of Joubert syndrome. J Child Neurol 14, 655-659; discussion 669-672.

72. Romio, L., Fry, A.M., Winyard, P.J., Malcolm, S., Woolf, A.S., and Feather, S.A. (2004). OFD1 is a centrosomal/basal body protein expressed during mesenchymal-epithelial transition in human nephrogenesis. J Am Soc Nephrol 15, 2556-2568.

73. Kobayashi, T., Kim, S., Lin, Y.C., Inoue, T., and Dynlacht, B.D. (2014). The CP110-interacting proteins Talpid3 and Cep290 play overlapping and distinct roles in cilia assembly. J Cell Biol 204, 215-229.

74. Yin, Y., Bangs, F., Paton, I.R., Prescott, A., James, J., Davey, M.G., Whitley, P., Genikhovich, G., Technau, U., Burt, D.W., et al. (2009). The Talpid3 gene (KIAA0586) encodes a centrosomal protein that is essential for primary cilia formation. Development 136, 655-664.

75. Rosenbaum, J.L., Moulder, J.E., and Ringo, D.L. (1969). Flagellar elongation and shortening in Chlamydomonas. The use of cycloheximide and colchicine to study the synthesis and assembly of flagellar proteins. J Cell Biol 41, 600-619.

76. Tamm, S.L. (1969). The effect of enucleation on flagellar regeneration in the protozoon Peranema trichophorum. J Cell Sci 4, 171-178.

77. Chhin, B., Pham, J.T., El Zein, L., Kaiser, K., Merrot, O., and Bouvagnet, P. (2008). Identification of transcripts overexpressed during airway epithelium differentiation. Eur Respir J 32, 121-128.

78. Stolc, V., Samanta, M.P., Tongprasit, W., and Marshall, W.F. (2005). Genome-wide transcriptional analysis of flagellar regeneration in Chlamydomonas reinhardtii identifies orthologs of ciliary disease genes. Proc Natl Acad Sci U S A 102, 3703-3707.

79. Lefebvre, P.A., Nordstrom, S.A., Moulder, J.E., and Rosenbaum, J.L. (1978). Flagellar elongation and shortening in Chlamydomonas. IV. Effects of flagellar detachment, regeneration, and resorption on the induction of flagellar protein synthesis. J Cell Biol 78, 8-27.

80. Ocbina, P.J., and Anderson, K.V. (2008). Intraflagellar transport, cilia, and mammalian Hedgehog signaling: analysis in mouse embryonic fibroblasts. Dev Dyn 237, 2030-2038.

81. Grimes, D.T., Boswell, C.W., Morante, N.F., Henkelman, R.M., Burdine, R.D., and Ciruna, B. (2016). Zebrafish models of idiopathic scoliosis link cerebrospinal fluid flow defects to spine curvature. Science 352, 1341-1344.

82. Vilboux, T., Doherty, D.A., Glass, I.A., Parisi, M.A., Phelps, I.G., Cullinane, A.R., Zein, W., Brooks, B.P., Heller, T., Soldatos, A., et al. (2017). Molecular genetic findings and clinical correlations in 100 patients with Joubert syndrome and related disorders prospectively evaluated at a single center. Genet Med.

83. Keller, L.C., Romijn, E.P., Zamora, I., Yates, J.R., 3rd, and Marshall, W.F. (2005). Proteomic analysis of isolated chlamydomonas centrioles reveals orthologs of ciliary-disease genes. Curr Biol 15, 1090-1098.

84. Mateja, A., Cierpicki, T., Paduch, M., Derewenda, Z.S., and Otlewski, J. (2006). The dimerization mechanism of LIS1 and its implication for proteins containing the LisH motif. J Mol Biol 357, 621-631.

85. Delto, C.F., Heisler, F.F., Kuper, J., Sander, B., Kneussel, M., and Schindelin, H. (2015). The LisH motif of muskelin is crucial for oligomerization and governs intracellular localization. Structure 23, 364-373.

86. Ishikawa, H., Thompson, J., Yates, J.R., 3rd, and Marshall, W.F. (2012). Proteomic analysis of mammalian primary cilia. Curr Biol 22, 414-419.

87. Mick, D.U., Rodrigues, R.B., Leib, R.D., Adams, C.M., Chien, A.S., Gygi, S.P., and Nachury, M.V. (2015). Proteomics of Primary Cilia by Proximity Labeling. Dev Cell 35, 497-512.

88. Li, J.B., Gerdes, J.M., Haycraft, C.J., Fan, Y., Teslovich, T.M., May-Simera, H., Li, H., Blacque, O.E., Li, L., Leitch, C.C., et al. (2004). Comparative genomics identifies a flagellar and basal body proteome that includes the BBS5 human disease gene. Cell 117, 541-552.

89. Avidor-Reiss, T., Maer, A.M., Koundakjian, E., Polyanovsky, A., Keil, T., Subramaniam, S., and Zuker, C.S. (2004). Decoding cilia function: defining specialized genes required for compartmentalized cilia biogenesis. Cell 117, 527-539.

90. Coordinators, N.R. (2016). Database resources of the National Center for Biotechnology Information. Nucleic Acids Res 44, D7-19.

91. Bae, Y.K., and Barr, M.M. (2008). Sensory roles of neuronal cilia: cilia development, morphogenesis, and function in C. elegans. Front Biosci 13, 5959-5974.

92. Kunitomo, H., Uesugi, H., Kohara, Y., and Iino, Y. (2005). Identification of ciliated sensory neuron-expressed genes in Caenorhabditis elegans using targeted pull-down of poly(A) tails. Genome Biol 6, R17.

93. Vazquez-Manrique, R.P., Gonzalez-Cabo, P., Ortiz-Martin, I., Ros, S., Baylis, H.A., and Palau, F. (2007). The frataxin-encoding operon of Caenorhabditis elegans shows complex structure and regulation. Genomics 89, 392-401.

94. Lih, C.J., Cohen, S.N., Wang, C., and Lin-Chao, S. (1996). The platelet-derived growth factor alpha-receptor is encoded by a growth-arrest-specific (gas) gene. Proc Natl Acad Sci U S A 93, 4617-4622.

95. Yeh, S.D., Chen, Y.J., Chang, A.C., Ray, R., She, B.R., Lee, W.S., Chiang, H.S., Cohen, S.N., and Lin-Chao, S. (2002). Isolation and properties of Gas8, a growth arrest-specific gene regulated during male gametogenesis to produce a protein associated with the sperm motility apparatus. J Biol Chem 277, 6311-6317.

96. Kim, Y.H., Epting, D., Slanchev, K., Engel, C., Walz, G., and Kramer-Zucker, A. (2013). A complex of BBS1 and NPHP7 is required for cilia motility in zebrafish. PLoS One 8, e72549.

97. Sun, Z., Amsterdam, A., Pazour, G.J., Cole, D.G., Miller, M.S., and Hopkins, N. (2004). A genetic screen in zebrafish identifies cilia genes as a principal cause of cystic kidney. Development 131, 4085-4093.

98. Lessieur, E.M., Fogerty, J., Gaivin, R.J., Song, P., and Perkins, B.D. (2017). The Ciliopathy Gene ahi1 Is Required for Zebrafish Cone Photoreceptor Outer Segment Morphogenesis and Survival. Invest Ophthalmol Vis Sci 58, 448-460.

99. Krock, B.L., and Perkins, B.D. (2008). The intraflagellar transport protein IFT57 is required for cilia maintenance and regulates IFT-particle-kinesin-II dissociation in vertebrate photoreceptors. J Cell Sci 121, 1907-1915.

100. Sukumaran, S., and Perkins, B.D. (2009). Early defects in photoreceptor outer segment morphogenesis in zebrafish ift57, ift88 and ift172 Intraflagellar Transport mutants. Vision Res 49, 479-489.

SUPPLEMENTAL DATA

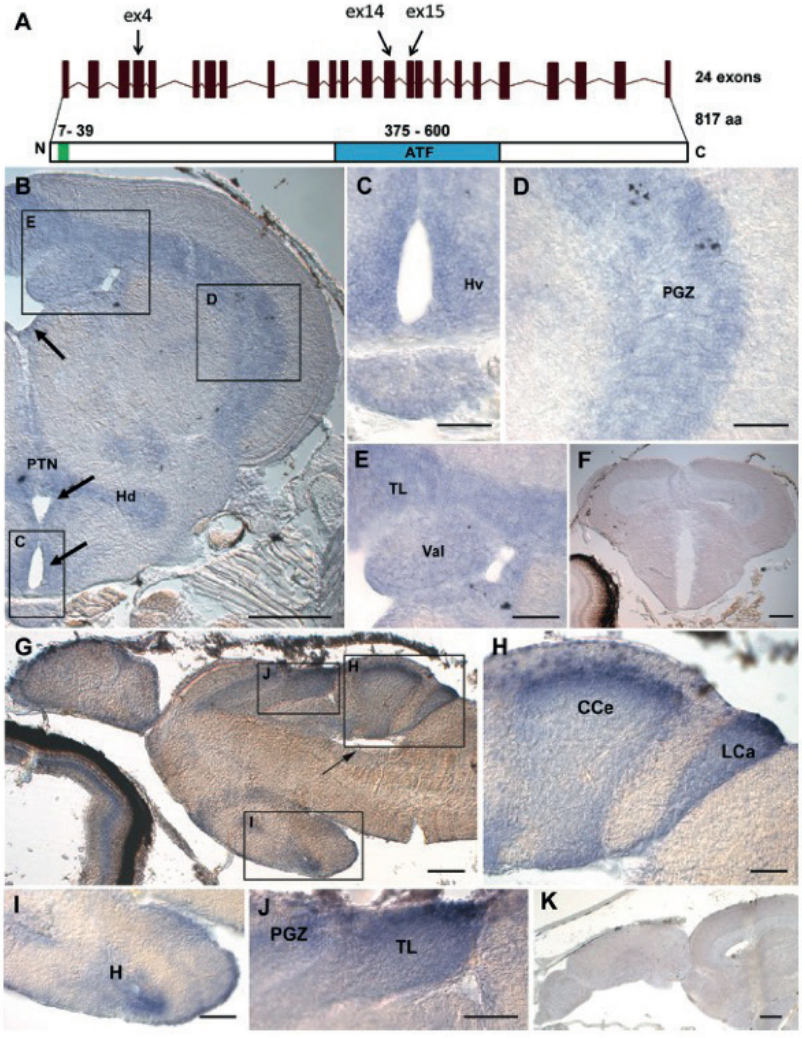

Figure S1: zebrafish armc9 gene structure and expression
(A) Schematic representation of the zebrafish armc9 gene (with exonic/intronic structure) and protein below, showing the predicted LisH domain (green, N-terminal) and the armadillo-type-fold (ATF) domain (blue). (B-K) In situ hybridization on brain cryosections from adult zebrafish (B-F transverse sections, G-K sagittal sections). (B) Note staining along the ventricles marked with the arrows. (C-E) Higher magnification views of the boxed areas in (B). (C) Ventral zone of periventricular hypothalamus Hv, (D) periventricular grey zone of optic tectum PGZ, (E) lateral division of valvula cerebelli Val and torus longitudinalis TL. (F) Absence of staining with the control sense probe. (G) Sagittal section through the brain and eye, showing signal in the cerebellum (boxed area H), the hypothalamus (boxed area I) and the optic tectum (boxed area J). CCe corpus cerebelli, LCa lobus caudalis cerebelli, H periventricular hypothalamus, PGZ periventricular grey zone of optic tectum, TL torus longitudinalis. (K) Absence of staining with the control sense probe. Scale bars: 200µm (B,F,G,K), 50µm (C-E), 100 µm (H-J).

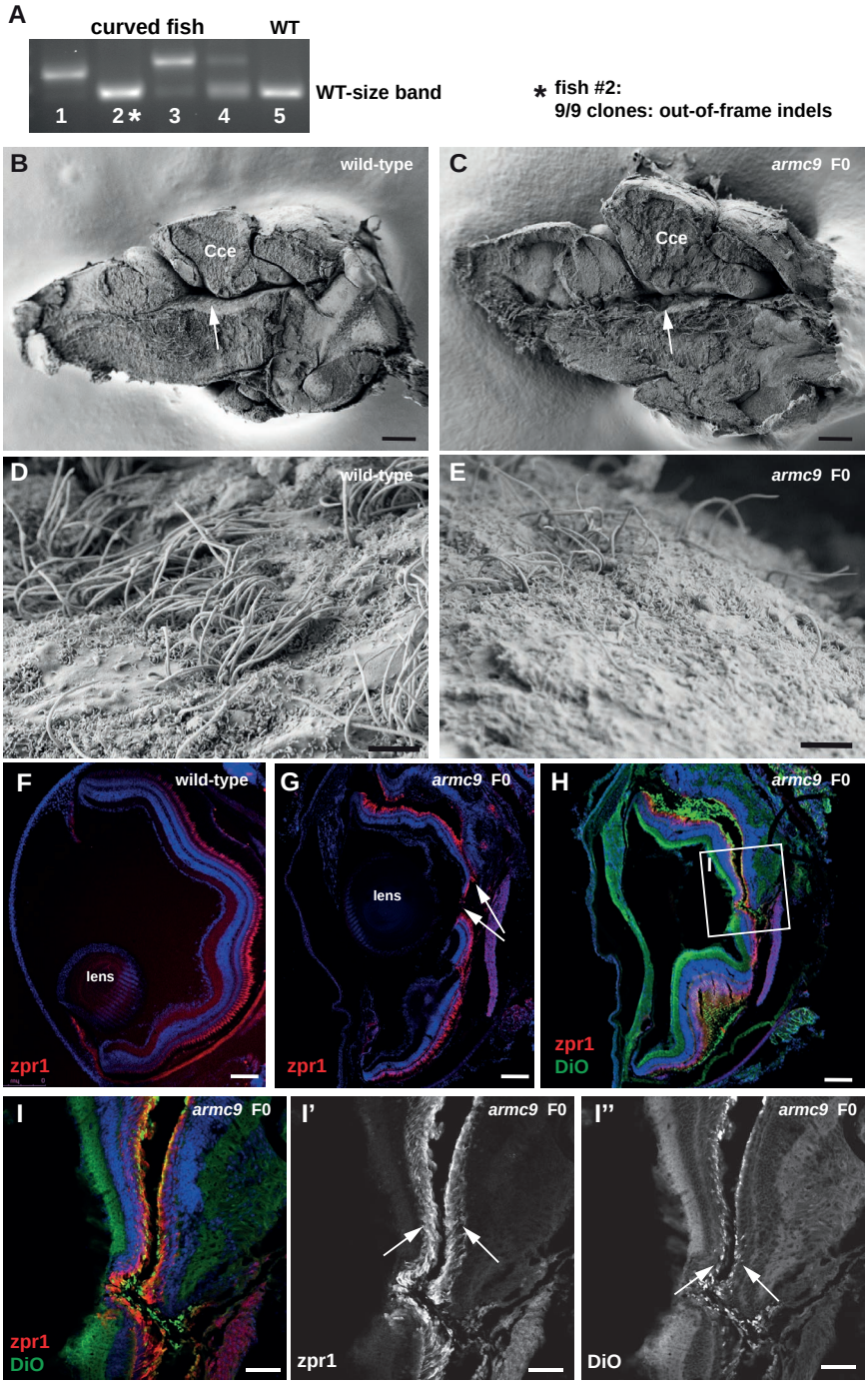
A
curved fish
WT
1
2*
3
4
5
WT-size band
* fish #2:
9/9 clones: out-of-frame indels
B
wild-type
Cce
C
armc9 F0
Cce
D
wild-type
E
armc9 F0
F
wild-type
lens
zpr1
G
armc9 F0
lens
zpr1
H
armc9 F0
I
zpr1
DiO
I
armc9 F0
zpr1
DiO
I'
armc9 F0
zpr1
I''
armc9 F0
DiO

◄Fig S2: CRISPR/Cas9 armc9 mutants
(A) Representative gel showing PCR amplification around the CRISPR target sites on finclips from adult F0 animals with body curvature. Note the presence of bands in addition to the WT-sized band in the curved fish. The PCR product from animal #2 was cloned and sequenced, revealing that 9 of 9 selected clones had small out-of-frame indels, indicating that this animal had a very high rate of mutations in armc9 despite a wild-type-sized band on the gel. (B-C) Scanning electron microscopy (SEM) overview images of dissected and halved brains from F0 armc9 animals with body curvature. The arrow points to the ventricular surfaces shown in (D-E). (D-E) Close up SEM images of the ventricular surface showing bundles of cilia in wild-type animals (D). In contrast, armc9 F0 mutant animals display a paucity of cilia (E). (F-I') Immunohistochemistry on cryosections through whole eyes of wild-type (F) and an F0 armc9 mutant (G-I') stained with the zpr1 antibody marking red-green cone cell bodies (red in F-I) and DiO highlighting photoreceptor (PR) outer segments (OS) (green in H-I). Note the thinner retinal layers and the coloboma (arrows in G and boxed area in H). (I-I'') represent the boxed area in (H). Note the discontinuity of the retinal layers and the presence of a second leaflet of retina folding back, with presence of PRs and OSs in a mirror image on either side of this aberrant second retinal layer (arrows). Scale bars are 100µm in (B-C), 3µm in (D-E), 100µm in (F-H), 50µm in (I'-I'').

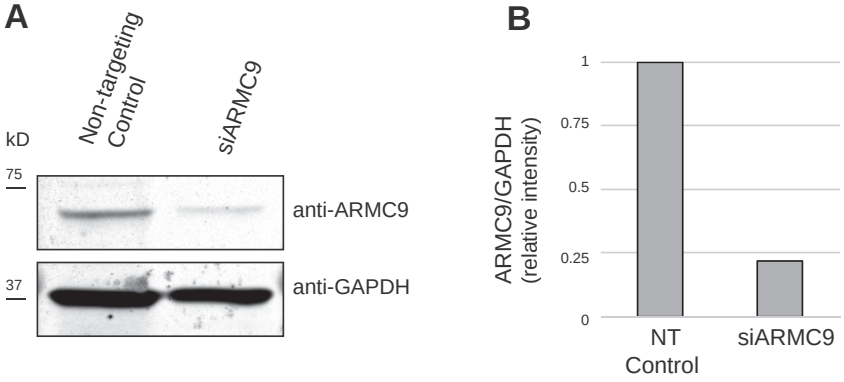

Fig S3: ARMC9 antibody validation
(A) Western blot analysis of hTERT-RPE cells transfected with non-targeting control siRNA and siARMC9. Cell lysates were probed with antibodies to ARMC9 and GAPDH as loading control. (B) Quantification of western blot signal in (A) quantified via densitometry normalized to GAPDH

Table S1. Oligonucleotide primers for qPCR

Target Gene	Primer ID	Sequence (5'-3')
ARL13B Exons 2/3	Forward:	AATGCTGGTAAAACCGCAAC
	Reverse:	TTCCCCGAATTCTTATTCCA
ARMC9 Exons 21/22	Forward:	GGAGTGACCACCAGGGAATG
	Reverse:	GGCCACACGAAGAGAACAGA
ARMC9 Exons 3/4	Forward:	GAGACCGGACAAAGAGGAGC
	Reverse:	CTCTGTGGTCTGGCTCAAGG
ARMC9 Exons 2/3	Forward:	TTCCATCCGAGATGGGGACT
	Reverse:	GCTCCTCTTTGTCCGGTCTC
GAPDH Exons 2/6	Forward:	AGGTGAAGGTCGGAGTCAAC
		TTCACACCCATGACGAACAT

Table S2. Brain imaging findings in individuals with *ARMC9*-related Joubert syndrome

UW#	UW132-3	UW132-4	UW348-3	UW116-3	UW335-3	UW335-4	UW349-3	LR09-023	SA1-3	SA2-3	SA2-4
Age at MRI	29 yr	18 yr	10 mo	6 mo	2 mo	16 mo	7 mo	1 mo	14 mo	2 yr	4 yr
Molar Tooth Sign	Y	Y	Y	Y	Y	Y	Y	Y	Y	Y	Y
Agenesis of the corpus callosum	N	N	N	N	N	N	N	N	N	N	N
Ventriculomegaly	N	N	mild	mild	N	N	N	N	mild	N	N
PMG	N	N	N	N	N	N	N	N	N	N	N
Heterotopia	N	N	N	Y	N	Y	N	Y	N	N	N
Pituitary bright spot	P	P	P	P	P	P	A	P	A	P	P
Superior cb dysplasia	Y	Y	Y	Y	Y	Y	Y	Y	Y	Y	Y
cb hemisphere dysplasia	N	N	N	N	N	Y	N	Y	N	Y	N
cb atrophy	Y	Y	N	N	N	N	N	N	N	N	N
cervicomedulary heterotopia	N	N	unk	N	N	N	Y	possible	N	N	N
Foramen magnum cephalcele	unk	N	N	N	N	N	Y	possible	Y	N	N
		moderate-size retro-cb fluid		single L occipital PVNH		single L occipital PVNH	kinked brainstem	large posterior fossa with retro-cb fluid, single L temporal PVNH			thick corpus callosum

A=Absent, cb=cerebellar, L=Left, mo=months, N=No, P=Present, PMG=PolyMicroGyria, PVNH=PeriVentricular Nodular Heterotopia, unk=unknown, Y=Yes, yr=years,

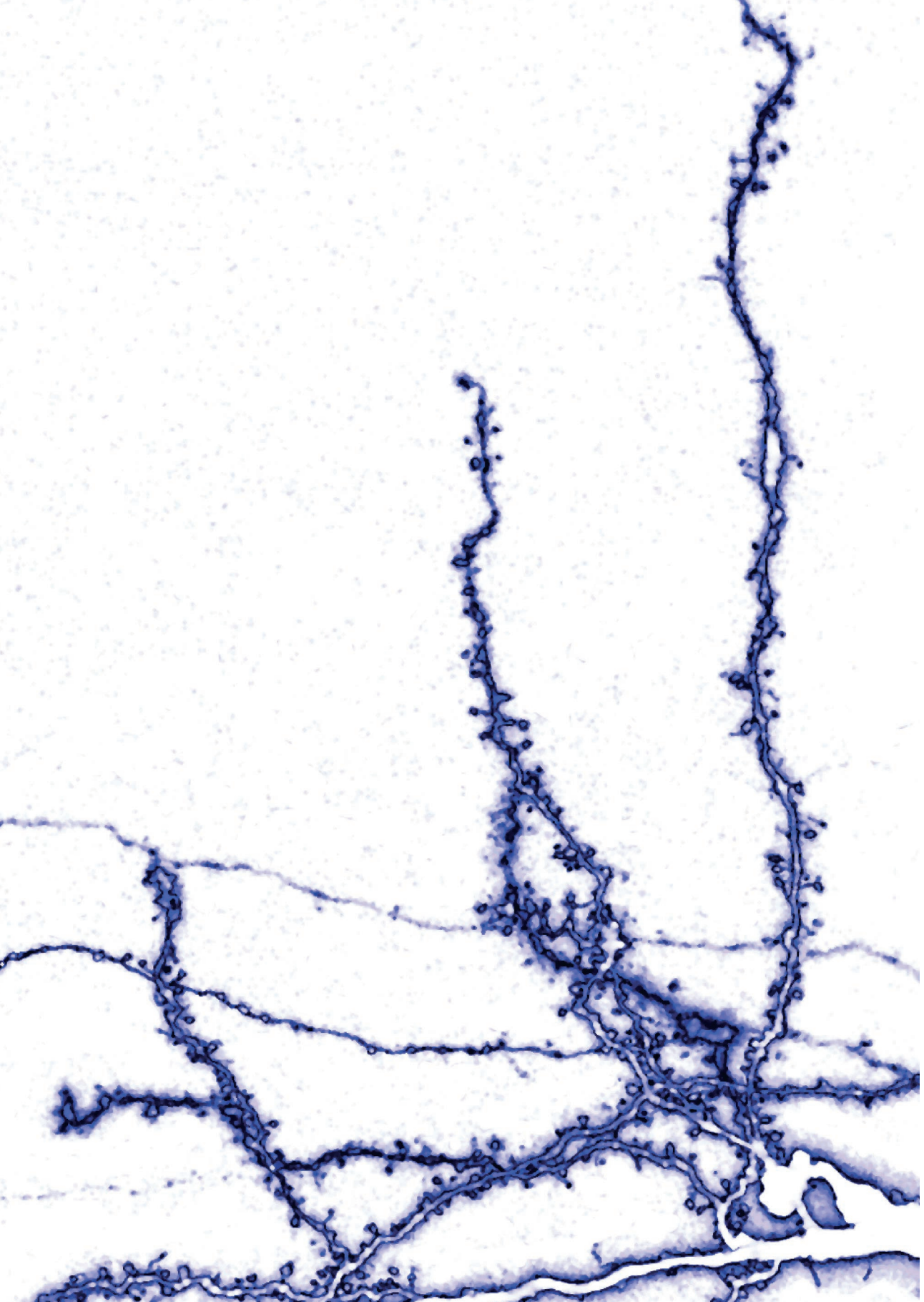

3

CHAPTER

Dysfunction of the ciliary ARMC9/ TOGARAM1 protein module causes Joubert syndrome

Brooke L. Latour (1)*, Julie C. Van De Weghe (2)*, Tamara D.S. Rusterholz (3,4)*, Stef J.F. Letteboer (1), Arianna Gomez (2), Ranad Shaheen (5), Matthias Gesemann (4), Arezou Karamzade (6), Mostafa Asadollahi (6), Miguel Barroso-Gil (7), Manali Chitre (8), Megan E. Grout (2), Jeroen van Reeuwijk (1), Sylvia E.C. van Beersum (1), Caitlin V. Miller(2), Jennifer C. Dempsey (2), Heba Morsy (9), University of Washington Center for Mendelian Genomics (10), Michael J. Bamshad (2,10,11), Genomics England Research Consortium (12), Deborah A. Nickerson (10,11), Stephan C.F. Neuhauss (4), Karsten Boldt (13), Marius Ueffing (13), Mohammad Keramatipour (6), John A. Sayer (7), Fowzan S. Alkuraya (5,14), Ruxandra Bachmann-Gagescu (3,4)*, Ronald Roepman (1)* & Dan Doherty (2,15)*

*These authors contributed equally to this work.

1. Department of Human Genetics and Radboud Institute for Molecular Life Sciences, Radboud University Medical Center, Geert Grooteplein Zuid 10, 6525 GA Nijmegen, The Netherlands
2. Department of Pediatrics, University of Washington, Seattle, WA, 98195 USA
3. Institute of Medical Genetics, University of Zurich, 8952 Schlieren, Switzerland
4. Department of Molecular Life Sciences, University of Zurich, 8057 Zürich, Switzerland
5. Department of Genetics, King Faisal Specialist Hospital and Research Center, Riyadh, Saudi Arabia
6. Department of Medical Genetics, Faculty of Medicine, Tehran University of Medical Sciences, Tehran 14179 13151, Iran
7. Translational and Clinical Research Institute, Faculty of Medical Sciences, Newcastle University, Newcastle Upon Tyne, UK
8. Department of Paediatric Neurology, Cambridge University Hospitals NHS Foundation Trust, Cambridge, UK.
9. Department of Human Genetics, Medical Research Institute, Alexandria University, Alexandria, Egypt
10. University of Washington Center for Mendelian Genomics, Seattle, WA 98195, USA
11. Department of Genome Sciences, University of Washington, Seattle, WA 98195, USA
12. Genomics England, London, EC1M 6BQ, United Kingdom
13. Medical Proteome Center, Institute for Ophthalmic Research, University of Tuebingen, 72074 Tuebingen, Germany
14. Department of Anatomy and Cell Biology, College of Medicine, Alfaisal University, Riyadh 11533, Saudi Arabia
15. Center for Integrative Brain Research, Seattle Children's Research Institute, Seattle, WA, 98101 USA

Published *J Clin Invest.* 2020;130(8):4423-4439. https://doi.org/10.1172/JCI131656

ABSTRACT

Joubert syndrome (JBTS) is a recessive neurodevelopmental ciliopathy, characterized by a pathognomonic hindbrain malformation. All known JBTS-genes encode proteins involved in the structure or function of primary cilia, ubiquitous antenna-like organelles essential for cellular signal transduction. Here, we used the recently identified JBTS-associated protein ARMC9 in tandem-affinity purification and yeast two-hybrid screens to identify a ciliary module whose dysfunction underlies JBTS. In addition to known JBTS-associated proteins CEP104 and CSPP1, we identified CCDC66 and TOGARAM1 as ARMC9 interaction partners. We found that *TOGARAM1* variants cause JBTS and disrupt TOGARAM1 interaction with ARMC9. Using a combination of protein interaction analyses and characterization of patient-derived fibroblasts, CRISPR/Cas9-engineered zebrafish and hTERT-RPE1 cells, we demonstrated that dysfunction of ARMC9 or TOGARAM1 result in short cilia with decreased axonemal acetylation and polyglutamylation, but relatively intact transition zone function. Aberrant serum-induced ciliary resorption and cold-induced depolymerization in ARMC9 and TOGARAM1 patient cell lines suggest a role for this new JBTS-associated protein module in ciliary stability.

INTRODUCTION

Ciliopathies are a heterogeneous class of disorders that arise from defects in the structure or function of the primary cilium (1, 2), a highly specialized microtubule-based sensory organelle that protrudes from the surface of most eukaryotic cell types (3). Joubert syndrome (JBTS) is a recessive, genetically heterogeneous, neurodevelopmental ciliopathy, defined by a distinctive brain malformation, recognizable as the “molar tooth sign” (MTS) (4) in axial magnetic resonance images through the midbrain-hindbrain junction. Affected individuals have hypotonia, ataxia, abnormal eye movements, and cognitive impairment. Additional features can occur, including retinal dystrophy, fibrocystic kidney disease, liver fibrosis, polydactyly, and coloboma (5). To date, variants in more than 35 genes have been causally linked to JBTS, but the genetic diagnosis cannot be identified in all patients, and the disease mechanisms remain unclear (6–8).

All JBTS-associated proteins identified thus far function in and around the primary cilium, but their dysfunction can affect a wide variety of cellular processes, including cilium formation, resorption, tubulin post-translational modifications, membrane phosphatidylinositol composition, ciliary signaling pathways, actin cytoskeleton dynamics, and DNA damage response signaling (9–14). Many JBTS proteins act together in complexes that localize to specific subdomains of the ciliary compartment. Disruption of the composition, architecture, or function of these ciliary subdomains causes disease (6).

The core of the cilium is composed of nine microtubule doublets forming the ciliary axoneme, which is anchored to the cell by the basal body, a modified centriole. The axonemal microtubules undergo a range of post-translational modifications including polyglutamylation and acetylation which are important for the structure and function of the cilium (15–17). The ciliary membrane has a distinct protein and lipid distribution that differs from the contiguous plasma membrane. This unique composition is achieved in part by the transition zone (TZ) that connects the axoneme to the membrane and acts as a partition. Approximately half of the known JBTS proteins, including RPGRIP1L (JBTS7) (18, 19) and CC2D2A (JBTS9) (20), assemble into multi-protein complexes at the ciliary TZ where they organize the molecular gate that regulates ciliary protein entry and exit (21); TZ dysfunction is thought to play a key role in JBTS (22). Another subset of JBTS-associated proteins, including ARL13B (JBTS8) (23) and INPP5E (JBTS1) (10), associate with the ciliary membrane distal to the TZ. These proteins are thought to regulate signaling pathways such as Hedgehog (Hh) by modulating ciliary protein and lipid composition (24, 25). Different JBTS-associated proteins have been found to function at the basal body or distal segment/tip (6). CSPP1 (JBTS 21) (26, 27) and CEP104 (JBTS25) (28) are mainly detected at the centrosomes and ciliary basal bodies; however, their exact molecular

function, and how defects in these proteins lead to JBTS, are less well understood. CEP104 localizes to the ciliary tip during ciliogenesis, where it is required for structural integrity in the motile cilia of Chlamydomonas and Tetrahymena (29, 30). Pathogenic variants in the gene encoding the ciliary tip kinesin KIF7 (JBTS12) also cause JBTS, and KIF7 dysfunction has been linked to defects in tubulin acetylation and Hh signaling (31).

Recently, we identified biallelic pathogenic ARMC9 (armadillo repeat motif containing 9) variants in individuals with JBTS (JBTS30). ARMC9 localizes to centrioles (32) and the proximal portion of the cilium (33) in mammalian cilia. ARMC9 transcript levels are upregulated with induction of ciliogenesis, and armc9 dysfunction in zebrafish yields typical ciliopathy phenotypes (32). ARMC9 has not been identified as a component of the ciliary JBTS-associated protein complexes mentioned above, so in this work, we used ARMC9 as bait in protein interaction screens. These screens identified a microtubule-associated ciliary protein module containing multiple other JBTS-associated proteins (CEP104, CSPP1, RPGRIP1L, and CEP290) and two other ciliary proteins (TOGARAM1 and CCDC66) not previously implicated in JBTS. Strikingly, we identified biallelic pathogenic TOGARAM1 variants as the cause of JBTS in five families. To decipher the function of the ARMC9-TOGARAM1 protein module and assess its role in the pathology of JBTS, we mapped the interaction domains and evaluated cellular defects in cultured human cells and zebrafish mutants. We find that these proteins, previously shown to associate with microtubules (29, 34–36), are required for appropriate post-translational modification of ciliary microtubules and cilium stability.

RESULTS

Identification of a novel protein module implicated in JBTS

We performed protein interaction screens to define the ARMC9-associated interactome. To identify direct binding partners, we employed full-length ARMC9 and four fragments (Figure 1A) as bait in a GAL4-based yeast two-hybrid (Y2H) interaction trap screen of two validated prey retinal cDNA libraries that were generated via random or oligo-dT primers (37). Using full-length ARMC9 as a bait, we identified four proteins previously implicated in ciliary function as binary interactors, including ARMC9 itself (suggesting a propensity to multimerize), TOGARAM1 (29, 34), CCDC66 (36, 38), and the JBTS-associated protein CSPP1 (39). Validation of these interactions and evaluation of the interacting domains was performed by Y2H co-expression. This assay indicated that the potential self-binding propensity of ARMC9 is mediated by fragment 2 containing the N-terminal 350 amino acid stretch containing the lissencephaly type-1-like homology motif (LisH) and coiled-coil domains, while TOGARAM1 and CSPP1 associated with fragment 4 (150-665 aa) containing the coiled-coil domain and the

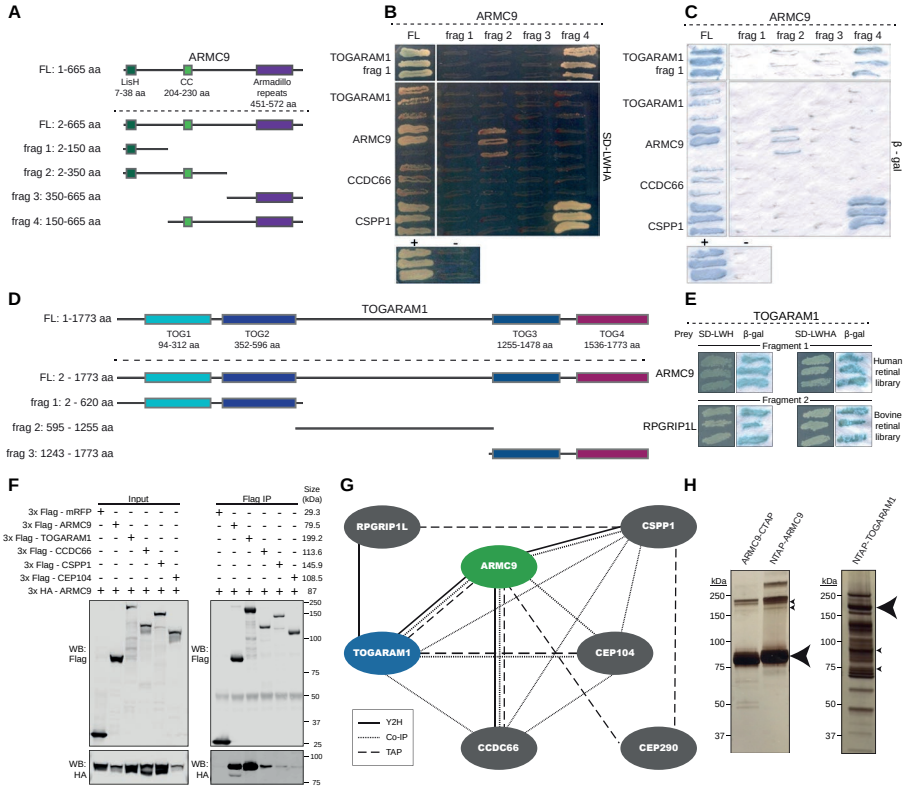

Figure 1 ARMC9 associates with TOGARAM1 in a ciliary module. (A) Schematic of full-length ARMC9 and fragments used as baits in Y2H bovine and human retinal cDNA library screens. Domains indicated are the predicted Lissencephaly type-1-like homology motif (LisH, dark green), coiled-coil domain (CC, light green) and the armadillo repeats-containing domain (armadillo, purple). (B) Direct interaction analysis grid using full length prey constructs. Selection of strains co-expressing bait and prey constructs was performed on quadruple knockout SD medium (SD-LWHA). The top row displays yeast colony growth when using fragment 1 of TOGARAM1 as prey. (C) β-Galactosidase activity assay confirming the interactions. (D) Schematic of full-length TOGARAM1 and fragments used in Y2H bovine and human retinal cDNA screens. (E) TOGARAM1 screen results validated in a Y2H directed interaction analysis on triple (SD-LWH) and quadruple (SD-LWHA) knockout media. (F) Flag co-IP of 3xFlag-ARMC9, 3xFlag-TOGARAM1, 3xFlag-CCDC66, 3xFlag-CSPP1, and 3xFlag-CEP104 with 3xHA-ARMC9. 3xFlag-mRFP served as a negative control. Western blot analysis post Flag-tag purification indicates the presence of 3xHA-ARMC9 confirming the interactions. 3xFlag-mRFP shows no interaction with 3xHA-ARMC9. (G) ARMC9 interacts with TOGARAM1 as confirmed by TAP, dashed lines, and Y2H screens, solid lines. Validation was subsequently performed using co-IP, dotted lines. (H) Silver stain gel of C-terminally and N-terminally SF-TAP tagged ARMC9 (left, large arrow, 80 kDa) and N-terminally SF-TAP tagged TOGARAM1 (right, large arrow, 200 kDa) post protein purification. The small arrows indicate the expected protein bands of two TOGARAM1 isoforms (195.6 kDa and 189.4 kDa) in the ARMC9 TAP purification, and two endogenous ARMC9 isoforms (91.8 kDa and 75.7 kDa) in the TOGARAM1 TAP purification.

armadillo repeats domain (Figure 1B, C). We also used full-length TOGARAM1 and three fragments (Figure 1D) in parallel screens which confirmed the direct interaction between TOGARAM1 and ARMC9 (Figure 1E), and yielded an additional candidate interactor, the JBTS-associated transition zone protein RPGRIP1L (JBTS7) (Figure 1E). The interaction with ARMC9 was mapped to the N-terminal portion of TOGARAM1 (fragment 1) containing the TOG1 and TOG2 domains, while RPGRIP1L bound to the linker region (fragment 2) between the TOG2 and TOG3 domain (Figure 1E).

To identify ARMC9-associated protein complexes, we expressed strep – FLAG epitope-tagged ARMC9 in HEK293T cells, followed by tandem affinity purification (TAP) and subsequent mass spectrometry. This identified 106 candidate ARMC9 interactors, including TOGARAM1 and the JBTS-associated protein CEP290 (Figure 1G, H; Supplemental table 1). Subsequent TAP experiments using tagged TOGARAM1, CCDC66, and CSPP1 confirmed the presence of ARMC9 in the TOGARAM1 and CCDC66 complexes, and extended the network to include several other ciliary proteins (Supplemental tables 2-4). For TOGARAM1, these additional candidate interactors included ciliary proteins ARMC9, CEP104, IFT74, IFT172, PLK1, and PRPF31, (Supplemental table 2), for CCDC66, they included ARMC9 and DYNLL1 (Supplemental table 3), and for CSPP1, they included RPGRIP1L and CEP290 (Supplemental table 4).

To further validate the ARMC9 interactors identified in TAP and Y2H experiments and evaluate their propensity to interact, we performed reciprocal co-IPs of all binary permutations of the module components ARMC9, TOGARAM1, CEP104, CCDC66, and CSPP1 (Figure 1F, Supplemental Figure 1A-I). The results confirmed the interaction of ARMC9 with TOGARAM1, CCDC66, CEP104, and CSPP1 (Figure 1G). Additionally, we performed PalmMyr-CFP mislocalization assays to further confirm the interaction of TOGARAM1 and ARMC9. The PalmMyr-CFP assay utilizes a PalmMyr tag which provides sites for palmitoylation and myristoylation. The palmitoylation and myristoylation forces the tagged protein to (mis) localize to the cell membrane (40). This mislocalization can be evaluated by fluorescence microscopy of CFP signal. We transfected PalmMyr-CFP tagged ARMC9 and mRFP-tagged TOGARAM1 into human telomerase reverse transcriptase retina pigmented epithelium (hTERT-RPE1) cells, alone and in combination, to assess the interaction between ARMC9 and TOGARAM1. Cells transfected with PalmMyr-CFP-ARMC9 alone showed diffuse localization across the cell membrane (Supplemental Figure 1B), while mRFP-TOGARAM1 alone localized to microtubule-like structures (Supplemental Figure 1C). Co-expression yielded complete co-localization along these structures despite the PalmMyr tag on ARMC9 (Supplemental Figure 1D), thereby indicating a direct interaction of the two proteins and a likely strong microtubule binding affinity of TOGARAM1.

TOGARAM1 variants cause JBTS in humans

Next, we investigated whether our interactome dataset could be used to identify new JBTS-associated genes. We cross-referenced the ARMC9-interactome data with DNA sequence data from our cohort of >600 families affected by JBTS (41). We first evaluated exome sequence data for 53 individuals in 51 families without variants in known JBTS genes. We identified biallelic, missense *TOGARAM1* variants in a fetus with cerebellar vermis hypoplasia and polydactyly (UW351-3 in Figure 2A and Table 1). These variants (c.1124T>C; p.Leu375Pro and c.3931C>T; p.Arg1311Cys) are rare in gnomAD v2.1 (42) and predicted to be deleterious by combined annotation dependent depletion (CADD) (43) (Table 1). To identify additional families, we sequenced all of the known JBTS genes using small-molecule molecular inversion probe capture (44) in 534 additional individuals from the same cohort and identified another individual (UW360-3 in Table 1 and Figure 2A) with the molar tooth sign (Figure 2B) and a nonsense variant (c.1084C>T; p.Gln362*) on one allele and low read depth indicating a possible multi-exon deletion event on the other allele. We confirmed a 12 kb deletion using a custom comparative genomic hybridization array, and fibroblast cDNA sequencing revealed deletion of exons 4-7 (Figure 2C). Genomic DNA sequencing of the proband and parents revealed that the 12,191 base pair deletion was inherited from the father (Figure 2C). In parallel, exome sequencing in several other cohorts of individuals with ciliopathy and neurodevelopmental conditions identified three other individuals with TOGARAM1-related JBTS (Table 1 and Figure 2A, B): 13DG1578 (consanguineous) with a homozygous rare, predicted-deleterious missense variant (c.1102C>T; p.Arg368Trp), WGL-1914 (consanguineous) with a rare, homozygous stop-gain variant (c.3248C>A; p.Ser1083*), and JAS-L50 (non-consanguineous) with rare, compound heterozygous missense and stop-gain variants (c.1112C>A; p.Ala371Asp and c.5023C>T; p.Arg1675*). Most variants identified in this work cluster around the TOG (tumor overexpressed gene) domains in the protein (Figure 2D). TOGARAM1 is also known as FAM179B and KIAA0423, with homologs CHE-12 in C.elegans and Crescerin1 in mouse. Segregation analysis for all affected families confirmed a recessive inheritance pattern (Figure 2A and Supplemental Figure 3).

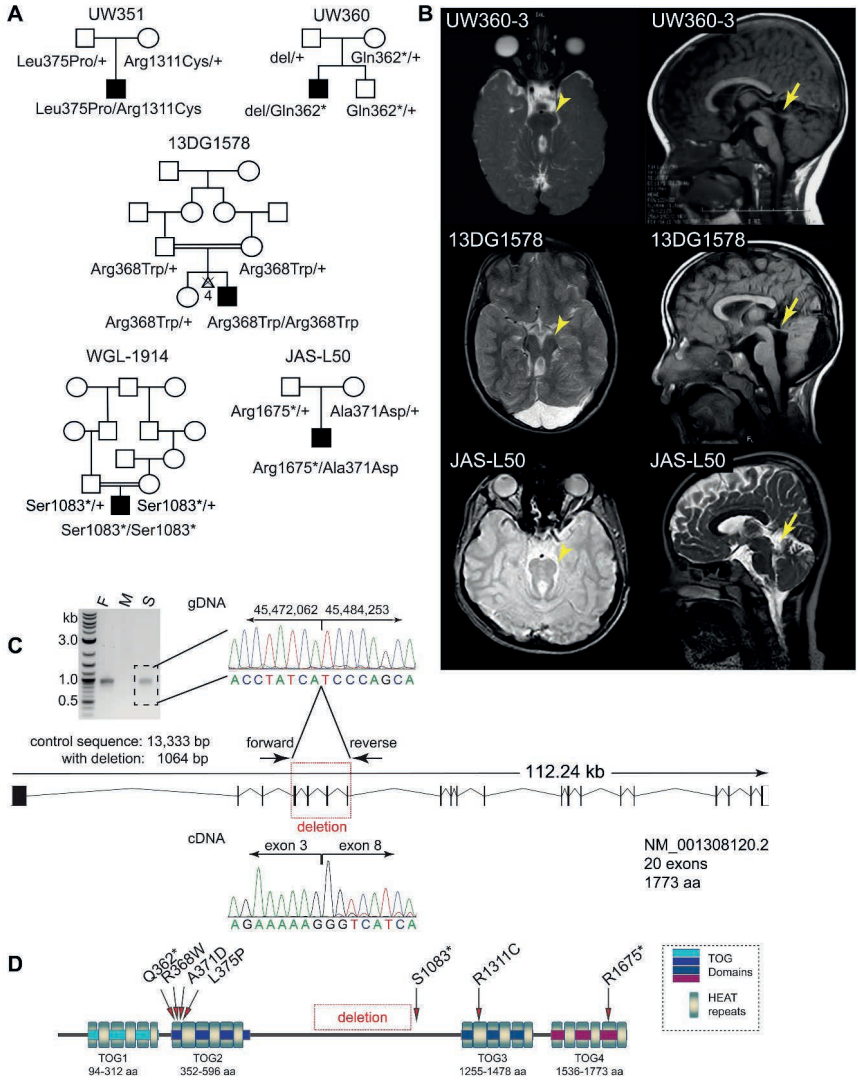

Figure 2 TOGARAM1 variants cause JBTS. (A) Pedigrees and segregation of TOGARAM1 variants. (B) Brain imaging features in individuals with TOGARAM1-related JBTS. Molar tooth sign (arrowheads in left column, axial T2-weighted images), and elevated roof of the 4th ventricle (arrows in right column, sagittal T1-weighted (top two) and T2-weighted (bottom) images). Much of the cerebellar tissue on the sagittal images (right column) is hemisphere based on axial and coronal views (not shown). (C) Multi-exon deletion in UW360. Primers flanking the predicted deletion amplify a 1064 base pair product in father (F) and affected son (S) due to a 12,191 base pair deletion, but not mother (M) because the predicted product is too large. Sanger sequencing of the breakpoint in gDNA (upper) and cDNA (lower) from the affected child, confirming deletion of exons 4-7. Coding genomic schematic of Homo sapiens TOG array regulator of axonemal microtubules 1, TOGARAM1. Transcript variant 1 is shown (NM_001308120, variant 2 NM_015091.2, not shown). (D) Protein schematic of TOGARAM1 with JBTS associated variants indicated, TOG domains 1-4 are shown with HEAT repeats indicated in gradient blue.

The five affected individuals had features consistent with JBTS, including classic brain imaging findings (absent cerebellar vermis and thick, horizontally oriented superior cerebellar peduncles, giving the appearance of the molar tooth sign) in the four children (Figure 2B), and cerebellar vermis hypoplasia in the fetus (UW351-3). This fetus also had bilateral postaxial foot polydactyly and abnormal craniofacial features at autopsy including broad nasal bridge and posteriorly rotated ears. The four living children have typical hypotonia, ataxia, cognitive delays and behavioral features associated with JBTS, while WGL-1914 and JAS-L50 had kidney involvement and WGL-1914 also had liver involvement. Uncommonly seen in individuals with JBTS, widely spaced nipples, male genital abnormalities (undescended testicles and possible micropenis in UW360-3, and small scrotum and testicle in 13DG1578), and somewhat similar dysmorphic features were noted in several of these individuals (Table 1).

JBTS-associated TOGARAM1 missense variants in the TOG2 domain disrupt the ARMC9-TOGARAM1 interaction

TOGARAM1 is a member of the highly conserved FAM179 protein family and is found across ciliated eukaryotes including Chlamydomonas reinhardtii, Tetrahymena thermophila, and Caenorhabditis elegans. TOGARAM1 has four conserved TOG domains that display similarity to the tubulin binding domains in ch-TOG and CLASP family proteins (34). Arg368Trp, Ala371Asp, and Leu375Pro, lie within the highly conserved TOG2 domain (Figure 2D, Supplemental Figure 2A) which has been found to promote microtubule polymerization in vitro (34). The TOG2 domain conforms to the canonical TOG domain architecture found in other TOG array containing proteins such as CLASP and Stu2 (Supplemental Figure 2A), therefore disruption of this domain is predicted to disturb microtubule binding (45). Using in silico analysis of the effects of point mutations, we found that Arg368Trp, Ala371Asp, and Leu375Pro, variants were predicted to be deleterious to protein structure (45). Residue 368 is highly conserved, modeling the wild-type and mutant TOG domains using HOPE (45) predicts that the larger and neutral tryptophan disrupts the normal hydrogen bonds with the aspartic acid residues at positions 361 and 405 (Supplemental Figure 2B, C). Position 371 is highly conserved, and due to the difference in size and hydrophobicity, aspartic acid at this position is predicted to disrupt the structure and function of the HEAT4 domain. Position 375 is located in a predicted α-helix, and is highly conserved; proline at this position is predicted to disrupt this α-helix as it introduces a bend in the polypeptide chain (Supplemental Figure 2D, E), likely affecting protein folding or interaction with other domains (45).

To assess the effects of JBTS-associated missense variants, we modeled two of the TOG2 domain variants (Arg368Trp, Leu375Pro) and the single TOG3 domain variant (Arg1311Cys) by

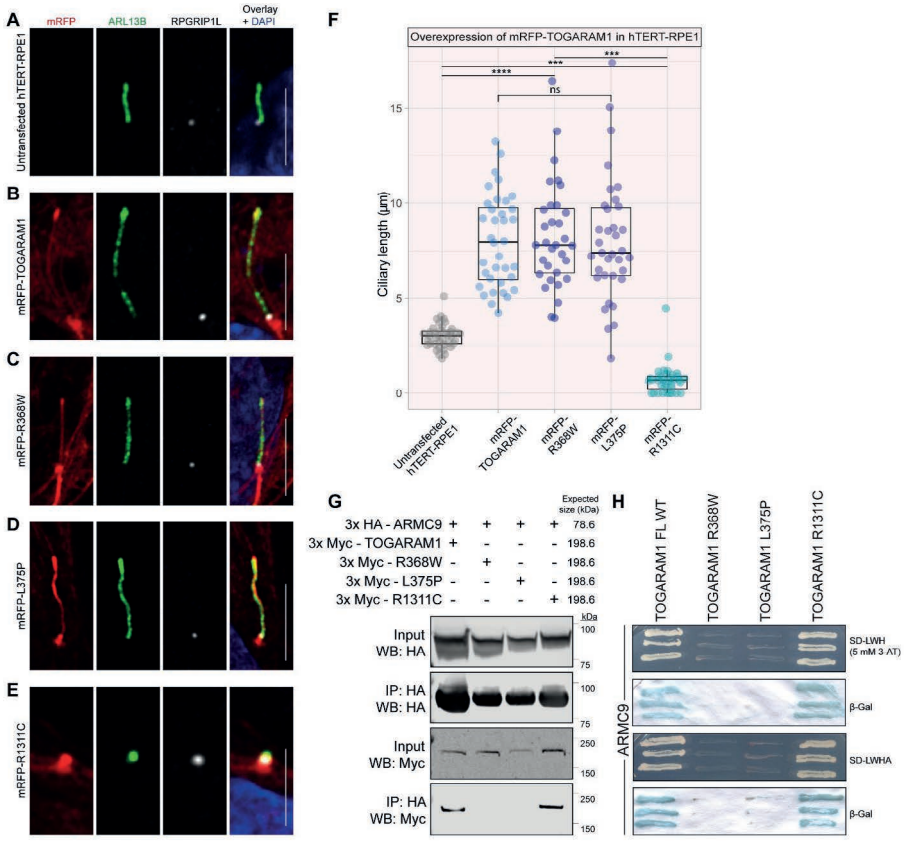

Figure 3 Overexpression of TOGARAM1 affects ciliary length and TOG2 domain variants reduce ARMC9 interaction. (A) Untransfected control hTERT-RPE1 cells, the cilium is shown with transition zone marker RPGRIP1L (white) and ciliary membrane marker ARL13B (green). (B-E) Transient mRFP-TOGARAM1 overexpression (red) in hTERT-RPE1 cells shown with transition zone marker RPGRIP1L (white) and ciliary membrane marker ARL13B (green): (B) mRFP-TOGARAM1-wild-type, (C) mRFP-TOGARAM1-Arg368Trp, (D) mRFP-TOGARAM1-Leu375Pro, and (E) mRFP-TOGARAM1-Arg1311Cys. Images are representative of >30 cilia assessed per condition over three experiments. Scale bars are 5µm. (F) Quantification of cilium lengths with overexpression of wild-type and variant forms of mRFP-TOGARAM1. (untransfected n=39, wild-type n=36, Arg368Trp n=32, Leu375Pro n=35, Arg1311Cys n=36). Box plot horizontal bars represent the median +/- 95CI. Significance was tested by one-way ANOVA and Tukey's multiple comparison test. No significant differences were found between cells overexpressing mRFP-TOGARAM1, mRFP-Arg368Trp, and mRFP-Leu375Pro. p=0.0004 for untransfected versus Arg1311Cys (G) Co-immunoprecipitation of HA-tagged ARMC9 and Myc-tagged TOGARAM1: Wild-type and Myc-tagged TOGARAM1-Arg1311Cys interact with ARMC9, while TOGARAM1 variants Arg368Trp and Leu375Pro do not. (H) Y2H direct interaction analysis assay with ARMC9 and TOGARAM1: Wild-type and TOGARAM1-Arg1311Cys interact with ARMC9 while the TOGARAM1 variants Arg368Trp and Leu375Pro do not. P-value symbols: ns p>0.05, ***p≤0.001, ****p≤0.0001.

expressing wild-type and mutant mRFP-tagged TOGARAM1 in control (Figure 3A-E) and genetically edited TOGARAM1 mutant hTERT-RPE lines (Supplemental Figure 4A, B). The genetically edited TOGARAM1 mutant hTERT-RPE line, TOGARAM1 mut 1, has a biallelic deletion of the ATG site of TOGARAM1 (Supplemental Figure 5A, B). Overexpressed wild-type TOGARAM1 localized along the ciliary axoneme and was associated with markedly longer cilia compared to untransfected wild-type cells (Figure 3A, B) and TOGARAM1 mut 1 cells (Supplemental Figure 4A,B). Exogenous TOGARAM1 harboring these three variants individually also localized to the cilium, but overexpression of TOG2-domain variants Arg368Trp and Leu375Pro resulted in longer cilia while overexpression of the TOG3-domain variant Arg1311Cys resulted in shorter cilia compared to untransfected cells (Figure 3A-E, quantification in Figure 3F). These data suggest that disruption of the TOG3 domain may have a dominant negative effect on the microtubule polymerization capacity of TOGARAM1 and disruption of the TOG3 domain has a different effect on TOGARAM1 localization and ciliary extension as compared to TOG2 domain variants.

We next investigated the effects of the TOGARAM1 variants on the interaction with ARMC9 using co-IP, binary yeast two-hybrid (Y2H) interaction analysis, and PalmMyr colocalization assays. We found that the variants in the TOG2 domain (Arg368Trp and Leu375Pro) abolished co-IP of HA-ARMC9 with Myc-TOGARAM1, while the Arg1311Cys variant in the TOG3 domain does not influence the interaction in these assays (Figure 3G). Y2H analysis confirmed these binary interactions (Figure 3H). In PalmMyr assays, the individually-expressed wild-type and mutant mRFP-tagged TOGARAM1 proteins localized along the length of cilia and along cytoplasmic microtubules (Supplemental Figure 4D). Co-expression of PalmMyr-CFP tagged ARMC9 with wild-type or Arg1311Cys mRFP-TOGARAM1 resulted in a pattern consistent with co-localization to cytoplasmic microtubules (Supplemental Figure 4E), indicating protein-protein interaction. In contrast, co-expression with the TOG2 variants resulted in PalmMyr-CFP tagged ARMC9 remaining localized to the plasma membrane, suggesting a lack of interaction with the TOGARAM1 mutants affecting the TOG2 domain (Supplemental Figure 4E). Taken together, these data indicate that variants in the TOG2 domain abrogate the ARMC9-TOGARAM1 interaction.

togaram1 mutations cause ciliopathy phenotypes in zebrafish

To further investigate the function of TOGARAM1 and the association between TOGARAM1 dysfunction and JBTS, we turned to zebrafish, an established model organism for ciliopathies. Indeed, zebrafish display a variety of ciliated cell types similar to humans, and pathogenic

variants in human ciliopathy genes result in typical ciliopathy phenotypes in zebrafish. Ciliated cells typically assessed in the zebrafish model include epithelial cells in pronephric (kidney) ducts, olfactory neurons in nose pits or neuronal progenitors on larval brain ventricular surfaces.

We identified a single zebrafish togaram1 ortholog displaying a highly conserved C-terminal region encompassing two TOG domains (similar to human TOG3 and 4) and a single N-terminal TOG domain corresponding to mammalian TOG2 domain (Supplemental Figure 6A). The three TOG domains are well-conserved between zebrafish and its corresponding human counterparts (50-58% amino acid identity and 72-77% similarity). As for the linker region between TOG domains, while it is more poorly conserved, it is enriched in serines and lysines (125 of 589 residues are Ser or Lys), similar to the proportion found in the human protein (165 of 657 residues are Ser or Lys); this is a common feature of TOG-domain containing proteins (46). Gene synteny analysis confirmed that the identified zebrafish sequence represents the ortholog of human TOGARAM1 (Supplemental Figure 6B). Importantly, on the paralogous chromosomal fragment generated by the teleost-specific whole genome duplication, no second togaram1 paralog could be identified. Moreover, synteny analysis also revealed that the zebrafish genome lacks a TOGARAM2 ortholog (Supplemental Figure 6C), leaving zebrafish with just one togaram ortholog. These findings support the utility of zebrafish as a model for TOGARAM1-associated human disease.

We next generated zebrafish mutants using CRISPR/Cas9. Two different pairs of sgRNAs targeting different regions of the gene (Supplemental Figure 6D) led to similar phenotypes in injected F0 larvae. 39% developed a curved body shape and 9% developed kidney cysts, both typical zebrafish ciliopathy-associated phenotypes (Supplemental Figure 6E). Single larvae genotyping revealed a very high mutation efficiency (94% of sequenced clones from 7 larvae had small insertions-deletions, the majority of which were frameshift mutations). Mutant F0 fish displayed a striking scoliosis phenotype as juveniles (Supplemental Figure 6E), reminiscent of other ciliopathy mutants including armc9 CRISPR-F0 fish (32). Taken together, these results confirm that loss of togaram1 causes ciliopathy phenotypes in zebrafish and supports a role for togaram1 in ciliary function.

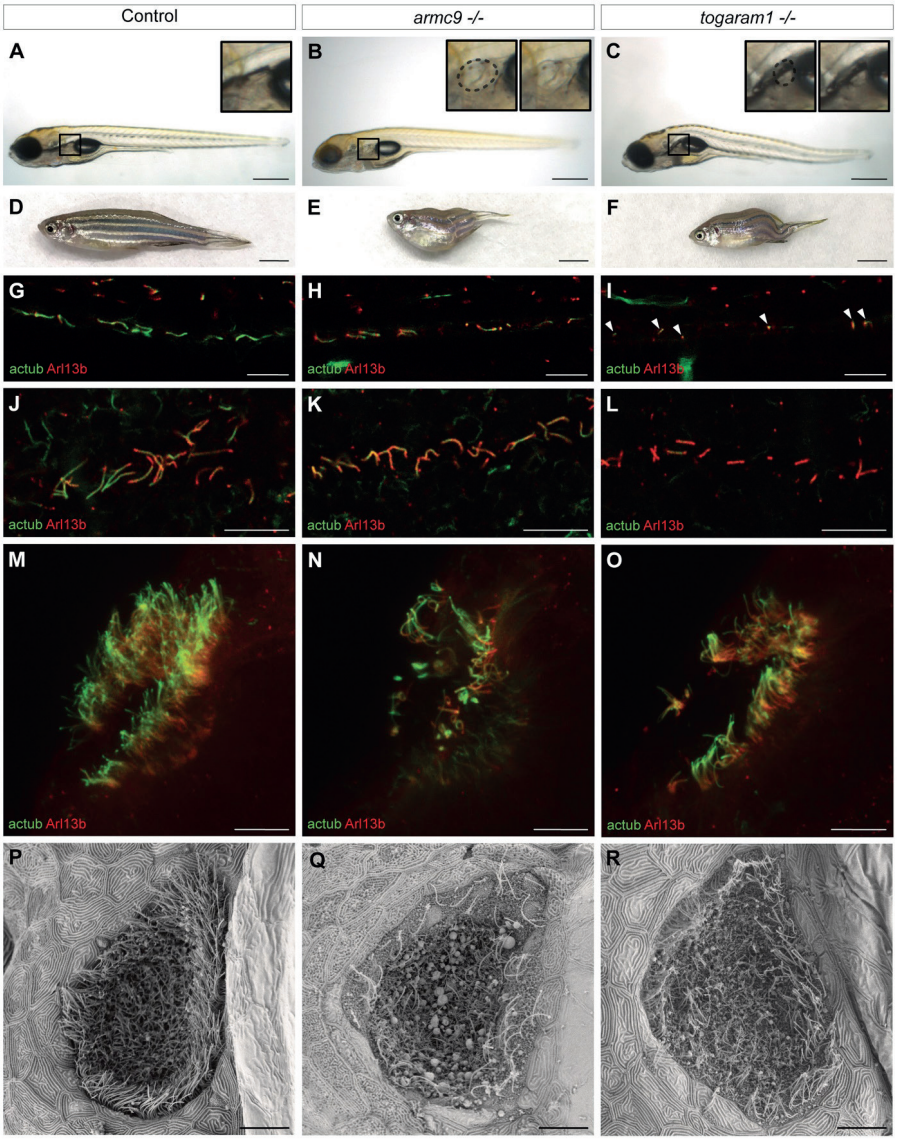

Figure 4 armc9 and togaram1 mutant zebrafish display ciliopathy associated phenotypes. (A-C) Larval phenotype demonstrating kidney cysts in armc9-/- (B) and kidney cysts and slightly curved body shape in togaram1-/- (C). Black boxes in (A-C) show magnification of glomerulus region in inset. Dashed lines highlight kidney cysts in (B, C). (D-F) Adult scoliosis phenotype in both mutants (E, F) compared to wild-type (D). (G-I) Immunofluorescence of the pronephric duct in 3 day post fertilization (dpf) larvae showing fewer cilia. White arrowheads in (I) point to the short remaining cilia in the togaram1 mutant. (J-L) Immunofluorescence of midbrain ventricles shows shortened cilia in 3 dpf armc9 and togaram1 mutant zebrafish larvae (K, L). (M-O) Immunofluorescence of 3 dpf zebrafish nose pits: decreased cilia number in both mutants (N, O) compared to wildtype (M). (P-R) Scanning electron microscopy of 5 dpf zebrafish nose pits confirming reduced cilia numbers in armc9-/- (Q) and togaram1-/- (R). Controls are wildtype, +/+ or +/- siblings of -/-. Scale bars are 500µm in (A-C), 5mm in (D-F) and 10µm in (G-R).

armc9 and *togaram1* mutant zebrafish display similar phenotypes

To further evaluate the link between TOGARAM1 and ARMC9, we compared zebrafish mutants in the two genes. Following up on our previous work (32), we raised several stable (>F2) zebrafish lines harboring frameshift insertion and deletion alleles of armc9 (Supplemental Figure 6F). Since homozygous mutants from all generated alleles have comparable phenotypes, we focused on the armc9^{zh505} allele for follow up experiments (Supplemental Figure 6F). This allele harbors a 110bp insertion in exon 14 that leads to exon skipping, causing a frameshift that inserts a stop codon at position 73 of exon 15. armc9-/- larvae have a straight body shape and an incompletely penetrant pronephric cyst phenotype affecting 44% of homozygous mutants (Figure 4A-B). In comparison, togaram1$^{zh509\ or\ zh510}$ mutant F2 larvae harboring frameshift mutations leading to stop codons in exons 21/22 have a slightly curved body shape and display a similar rate of kidney cysts compared to armc9-/- mutants (Figure 4C). Pronephric cysts and body curvature do not necessarily correlate with each other in togaram1 mutants, as each phenotype can be found in isolation or in combination, but overall, 85 % of togaram1-/- larvae have at least one ciliopathy phenotype. Neither mutant displayed heart laterality defects that are seen in some zebrafish ciliopathy models. In addition to frameshift mutations in exon 21/22, we also identified a 21 bp in-frame deletion leading to loss of 7 amino acids in the TOG4 domain, of which 6 are highly conserved (togaram1^{zh508}, Supplemental Figure 7). Homozygous in-frame mutant larvae are indistinguishable from the frameshift mutants, suggesting that the TOG4 domain may be critical for Togaram1 function.

In addition to the pronephric cysts, both armc9-/- and togaram1-/- fish develop scoliosis as juveniles compared to wild-type (Figure 4D-F), as previously described in other zebrafish ciliary mutants (47, 48). Given that pronephric cysts and curved bodies are typical ciliopathy phenotypes, we next analyzed the cilia in both mutants using immunofluorescence with anti-Arl13b and anti-acetylated α-tubulin antibodies. Compared to wild-type, larvae of both mutants have reduced numbers of shortened pronephric, ventricular, and nose pit cilia (Figure 4G-O), the latter being confirmed by scanning electron microscopy (Figure 4P-R). The reduced and shortened cilia in both mutants support a role for Armc9 and Togaram1 in zebrafish cilium formation and/or stability.

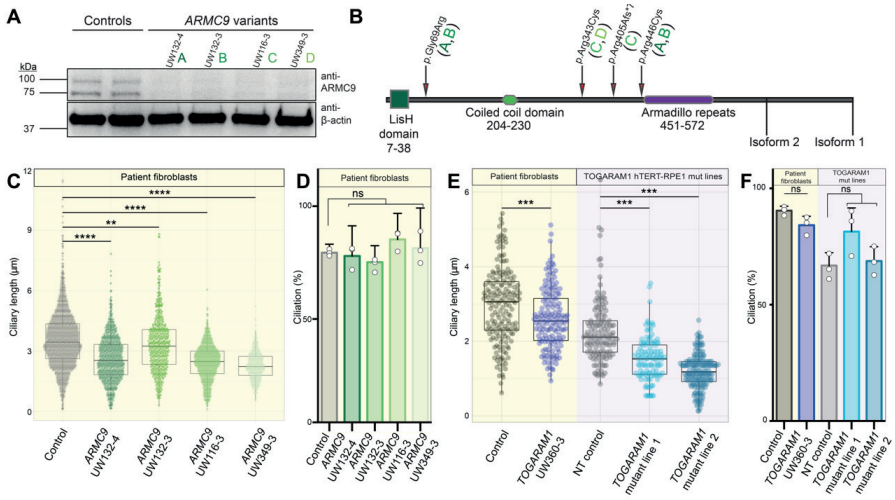

Figure 5 ARMC9 and TOGARAM1 dysfunction results in short cilia. (A) Immunoblot of endogenous ARMC9 in control and patient fibroblasts indicating trace amounts of ARMC9 isoforms 1 and 2 (92 and 75.5 kDa). Loading control is β-actin. (B) ARMC9 schematic indicating JBTS-associated patient variants (green letters represent variants found in patients as indicated in (A)). (C) Ciliary length in control and ARMC9 patient fibroblasts (control n=1395, UW132-4 n=699, UW132-3 n=437, UW116-3 n=656, and UW349-3 n=353). Significance was assessed by one-way ANOVA with Dunnett's multiple testing correction. (D) Ciliation percentage in ARMC9 fibroblast lines (control n=1723, UW132-4 n=898, UW132-3 n=584, UW116-3 n=764, and UW349-3 n=425). Results were not significant using the Kruskal-Wallis test. (E) Ciliary length in control and TOGARAM1 patient fibroblasts (yellow panel). p=0.0003 using unpaired Student's t-test. hTERT-RPE1 cilia length in wild-type and TOGARAM1 mut lines (purple panel) based on ARL13B staining. >100 cilia were pooled from 2 experiments (control n=137, TOGARAM1 mutant line 1 n=111, and TOGARAM1 mutant line 2 n=178). p<0.0001 per one-way ANOVA with Dunnett's multiple testing correction. (F) Ciliation percentage in TOGARAM1 patient fibroblasts (yellow panel: control n= 466 and UW360-3 n= 429 over 3 experiments), results were not significant using the Mann-Whitney test. Ciliation percentage in engineered TOGARAM1-mutant hTERT-RPE1 cells (purple panel: control n=330, TOGARAM1 mutant line 1 n=363, and TOGARAM1 mutant line 2 n=357 over 3 experiments) Results were not significant using the Kruskal-Wallis test. Open circles represent individual experiments in (D) and (F). Box and whiskers in (C) and (E) represent the median, the 95 CI is indicated by the notches. All ciliary length measurements were based on ARL13B staining. P-value symbols: ns p>0.05, **p≤0.01, ****p≤0.0001.

JBTS-associated *ARMC9* and *TOGARAM1* variants result in decreased ciliary length

To gain insight into the ciliary defects associated with JBTS in humans, we evaluated four fibroblast lines from patients with ARMC9-associated JBTS. Western blot analysis of total protein lysates revealed that all four cell lines express trace levels of the two major ARMC9 isoforms at 92kDa and 75.5kDa seen in control fibroblasts (32) (Figure 5A, B). To evaluate for ciliary phenotypes, we serum starved control and affected cells, and then stained with anti-acetylated α-tubulin and anti-ARL13B antibodies. All four patient lines displayed significantly

shorter mean ciliary length (2.3-3.3μm, standard deviation (SD) 0.7-1.4, n = 349-1395 cilia), versus controls (3.6μm, SD 1.4, n =1395 cilia) (Figure 5C). Ciliation rates 48 hours after serum starvation were similar in the patient lines (75-86%) compared to controls (80%), suggesting that ARMC9 does not play an integral role in ciliogenesis (Figure 5D).

Mean ciliary length was also shorter the one available patient cell line from UW360-3 with TOGARAM1-related JBTS (2.6μm, SD 0.8, n = 154 cilia) versus control (3.0μm, SD of 1.0, n = 179 cilia) (Figure 5E). This line had a slightly lower ciliation rate than control (85% versus 91% respectively) (Figure 5F). To generate additional data about the effects of loss of TOGARAM1 function on cilia in human cells, we turned to CRISPR/Cas9 genome-edited TOGARAM1 hTERT-RPE1 mutant cells. gRNAs targeting the translation start site of exon 1 resulted in two different lines harboring a disruption in the ATG site of both alleles of TOGARAM1 (Supplemental Figure 5). These lines make significantly shorter cilia (mut line 1: 1.5μm, SD 0.6, n= 111 cilia; mut line 2: 1.2μm, SD 0.5, n = 178 cilia) versus the isogenic control (2.3μm, SD 0.8, n = 137 cilia) (Figure 5E). Ciliation levels in the TOGARAM1 engineered lines (81% in mutant 1 and 69% in mutant 2) did not differ significantly from the isogenic control (67%) (Figure 5F). Taken together these results suggest that disruptions in TOGARAM1 and ARMC9 lead to shorter ciliary length but do not affect overall ciliation rates.

Transition zone integrity with *ARMC9* and *TOGARAM1* dysfunction

Given the well-described role of transition zone (TZ) dysfunction in JBTS (22), we evaluated whether the integrity of this compartment is affected by loss of TOGARAM1 or ARMC9 function. Since TZ dysfunction often results in loss of ciliary ARL13B, which secondarily causes loss of ciliary INPP5E (12, 49), we performed quantitative immunofluorescence (qIF) on control, ARMC9, and TOGARAM1 patient cell lines. Our data revealed mildly lower levels of ARL13B in three of four ARMC9 patient fibroblast lines and normal levels in the TOGARAM1 patient fibroblast line (Figure 6A; Supplemental Figure 8A, C). Importantly, the mildly lower ARL13B levels observed in three of four ARMC9 lines were not associated with lower ciliary INPP5E (Figure 6B; Supplemental Figure 8B), indicating that the lower ARL13B levels were still sufficient to properly localize INPP5E. Western blot analysis also revealed similar levels of ARL13B and INPP5E in patient fibroblast lysates compared to control cells (Figure 6C, D).

In zebrafish, Arl13b levels were not lower in either mutant (and even slightly increased in the armc9-/- fish) (Figure 6A, E, F). Together, these results are strikingly different from the marked ciliary ARL13B and INPP5E reduction observed in TZ mutants (12, 49). To evaluate the composition of the TZ directly, we performed immunostaining for canonical TZ proteins RPGRIP1L in human cell lines (Figure 6G, H) and Cc2d2a in zebrafish (Figure 6F). Both proteins

localized normally to the TZ of the respective cilia. Taken together, these findings suggest that the TZ is generally intact, despite dysfunction of the ARMC9-TOGARAM1 complex.

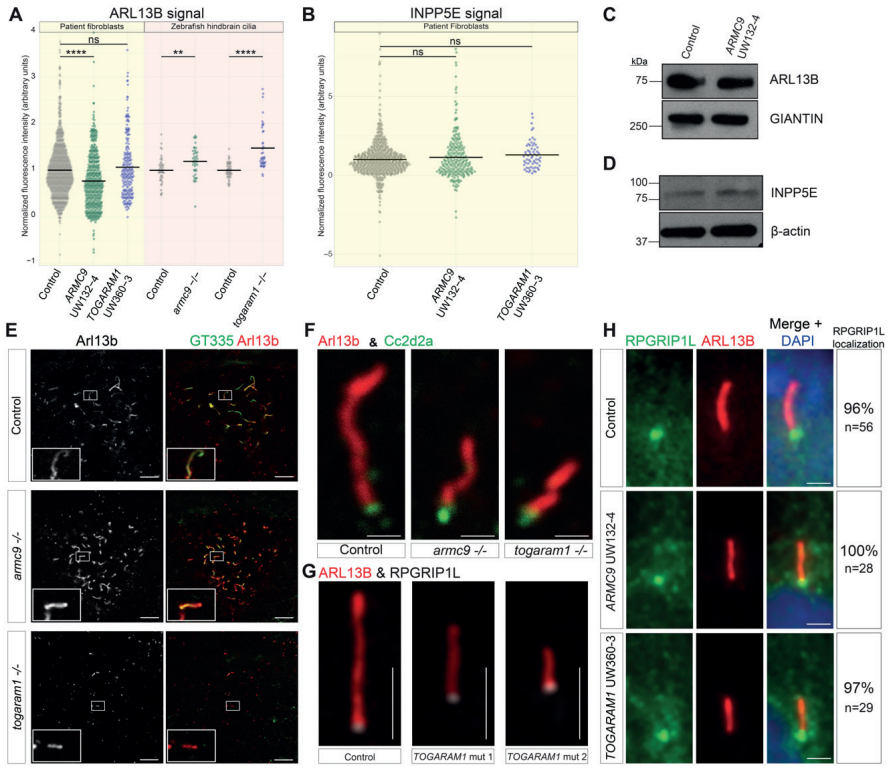

Figure 6 ARMC9 or TOGARAM1 dysfunction does not grossly affect the transition zone. (A) Normalized relative fluorescence intensity of ARL13B signal in human fibroblast cilia (yellow panel, pooled from 3 experiments, control: grey n=1089, ARMC9: green n=582, and TOGARAM1: blue n=126) and 3dpf zebrafish hindbrain cilia (pink panel: pooled data from 4 experiments, 10 cilia measured per larva, each data point represents one larva, grey: armc9 control n=42, green: armc9 -/- n=41, grey: togaram1 control n=45, blue: togaram1 -/- n=40). Bars represent the mean. Controls are wildtype, +/+ or +/- siblings of -/-. Statistical significance was assessed using a Student's t-test for both fibroblast (Bonferroni adjusted $p<0.025$) and zebrafish experiments ($p<0.05$). P-value symbols: **$p\leq0.01$, ****$p\leq0.0001$. (B) Normalized relative fluorescence intensity of INPP5E signal in human fibroblast cilia (pooled data from 3 experiments: control: grey n=620, ARMC9: green n=248, TOGARAM1: blue n=62). See Supplemental Figure 7 for ARL13B and INPP5E signal intensity across all ARMC9 fibroblast lines. Results were not significant (ns) using unpaired Student's t-test. (C-D) Western blot analysis of ARL13B (C) and INPP5E (D) in ARMC9 UW132-4 patient fibroblasts. GIANTIN and β-actin serve as loading controls respectively. (E) Representative immunofluorescence signal for Arl13b (red) and polyglutamylated (green) in 3dpf zebrafish hindbrain cilia quantified in (A). Scale bars are 10µm. (F) Single hindbrain cilia stained with Arl13b (red) and Cc2d2a (green) in 3dpf control, armc9-/- and togaram1-/- zebrafish. Scale bars are 1µm. (G) Representative immunofluorescence signal for RPGRIP1L (white) and ARL13B (red) in cilia from control and two TOGARAM1-mutant hTERT-RPE1 lines. Scale bars are 2µm. (H) Representative immunofluorescence for RPGRIP1L (green) and ARL13B (red) in ARMC9 and TOGARAM1 patient fibroblasts. Percentage of cilia with robust RPGRIP1L puncta are indicated. Scale bars are 2µm.

TOGARAM1 dysfunction results in attenuated SMO translocation

Recent work has reported Hedgehog (Hh) signaling defects in cell lines with dysfunction of the JBTS genes CEP104, CSPP1, and Armc9 (33, 39). Therefore, we tested whether TOGARAM1 dysfunction leads to attenuated ciliary SMO accumulation in response to Hh stimulation in the engineered TOGARAM1-mutant hTERT-RPE1 cells described above (Supplemental Figure 5). We starved the cells for 24 hours to promote ciliation and then exposed them to 100 nM Smoothened agonist (SAG) for an additional 24 hours before fixation and qIF (Supplemental Figure 9A). Upon pathway stimulation, the control and two TOGARAM1-mutant lines exhibited a significant induction of SMO translocation into the cilium as compared to their respective DMSO treatment condition; however, the ciliary enrichment of SMO was markedly lower in the two mutant lines compared to control cells (Supplemental Figure 9B-D). Overall, SMO intensity levels in both TOGARAM1-mutant lines were less than 50% of the control line, and mutant lines did not differ significantly in their response when compared to each other.

ARMC9 and *TOGARAM1* dysfunction affects tubulin post-translational modifications in patient fibroblasts and zebrafish mutants

During our experiments evaluating ciliary ARL13B and INPP5E, we noted that the acetylated α-tubulin and polyglutamylated tubulin signals appeared substantially less intense in patient cell lines versus controls (Figure 7A, B). Using qIF, mean acetylated tubulin levels were ~50% of control levels in the ARMC9 lines and ~70% of controls in the TOGARAM1 line (Figure 7E, F and Supplemental Figure 10A, B). Mean polyglutamylated signal levels were ~35% and ~45% of control levels in ARMC9 and TOGARAM1 lines respectively (Figure 7B, F and Supplemental Figure 10). Western blots of whole cell lysates also demonstrated substantially lower levels of both acetylated and polyglutamylated tubulin in ARMC9 fibroblast lines compared to controls (Figure 7A, B). In the zebrafish armc9 and togaram1 mutant lines, we observed similar reductions of ciliary acetylated and polyglutamylated tubulin in the remaining ventricular cilia (Figure 7C-F). Together, these results indicate that loss of either ARMC9 or TOGARAM1 results in decreased post-translational modifications of axonemal tubulin across multiple model systems.

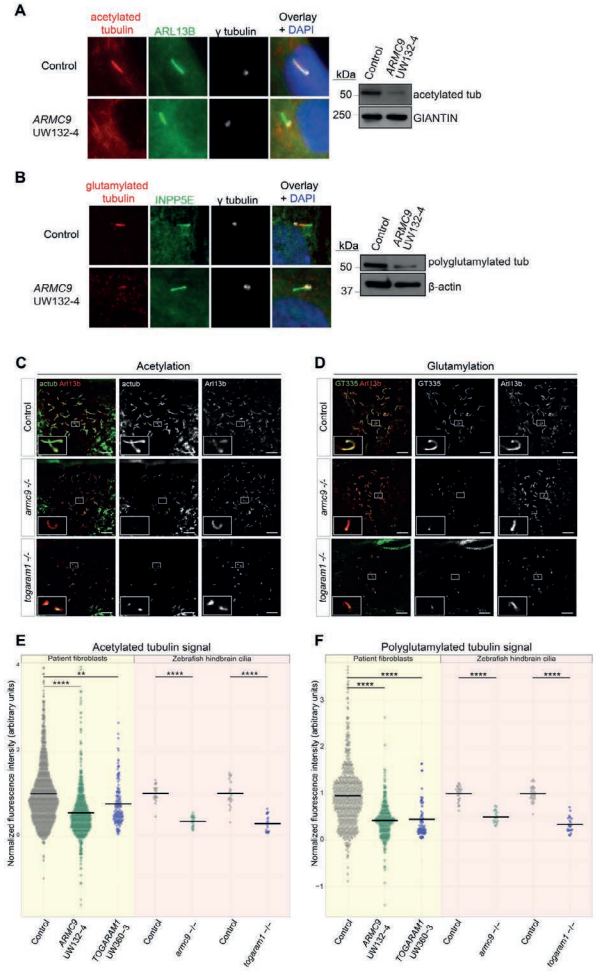

Figure 7 ARMC9 and TOGARAM1 mutant cilia display reduced tubulin posttranslational modifications in both patient fibroblasts and zebrafish ventricular cells. (A–B) Immunofluorescence and immunoblots of (A) acetylated and (B) polyglutamylated tubulin in ARMC9 patient fibroblasts versus control. In the immunoblots, GIANTIN and β-actin are used as loading controls. (C-D) Representative immunofluorescence of 3dpf zebrafish hindbrain cilia marked with Arl13b (red) and acetylated (green in (C)) or polyglutamylated (green in (D)) tubulin. Scale bars are 10µm. Note that acetylated tubulin also marks axons in the developing brain, visible at the edges of the image in (C). (E) Normalized relative fluorescence intensity for acetylated tubulin signal in human fibroblast cilia (yellow panel: control n=1106, ARMC9 n=532, and TOGARAM1 n=131) and zebrafish hindbrain cilia (pink panel: pooled data from 2 experiments, 10 cilia measured per larva, each data point represents one larva, grey: armc9 control n=20, green: armc9 -/- n=21, grey: togaram1 control n=20, blue: togaram1 -/- n=20). (F) Normalized relative fluorescence intensity for polyglutamylated tubulin assessed in human fibroblast cilia (yellow panel: pooled from 3 experiments, control n=602, ARMC9 n=298, and TOGARAM1 n=58) and zebrafish hindbrain cilia (pink panel: pooled data from 2 experiments, 10 cilia measured per larva, grey: armc9 control n=22, green: armc9 -/- n=20, grey: togaram1 control n=25, blue: togaram1 -/- n=20). Zebrafish controls are wt, +/+ or +/- siblings of -/-. In (E and F), data points >4 and <-2 are not displayed, but were included in the statistical analysis. For complete graph of all data points and a graphical summary of all ARMC9 lines, see Supplemental Figure 8 (A, B) and (C, D) respectively. Statistical significance (adjusted p<0.025) was assessed using a Bonferroni-corrected Student's t-test for both fibroblast and zebrafish experiments. P-value symbols: **p≤0.01, ****p≤0.0001.

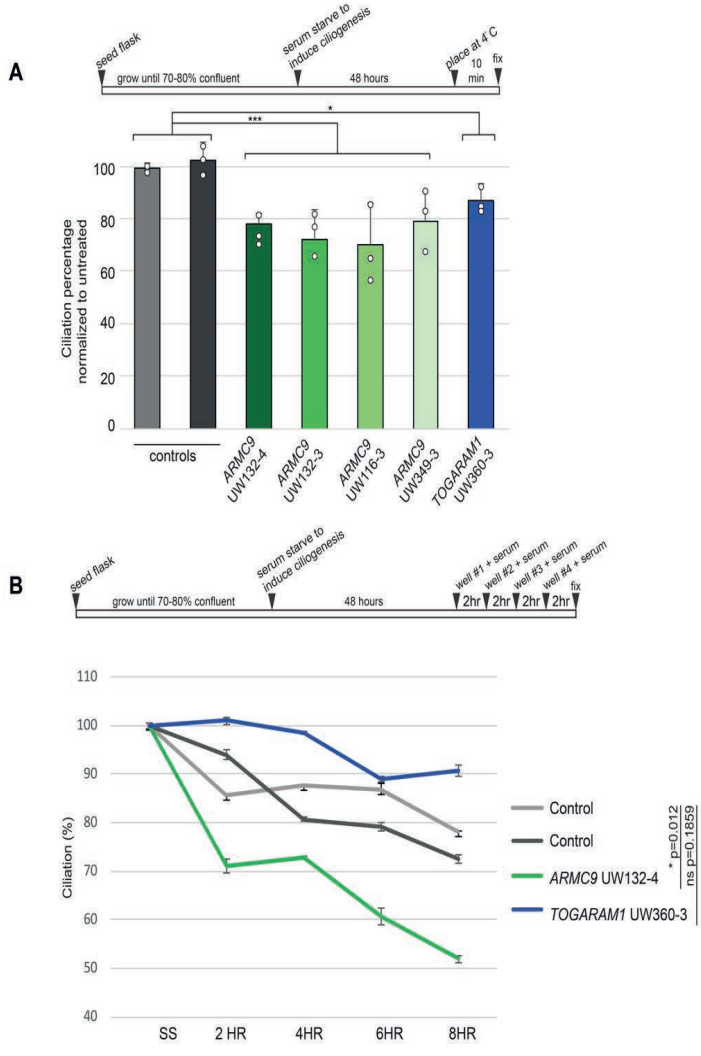

Figure 8 JBTS patient fibroblasts exhibit abnormal axonemal stability. (A) Cold-induced depolymerization assay schematic and ciliation percentages of treated cells normalized to non-treated controls. Statistical significance was assessed via Bonferroni-corrected Kruskal-Wallis test with p=0.0003, p=0.02 respectively. Open circles represent individual experiments. (B) Relative ciliation rates 2, 4, 6, and 8 hours after serum readdition in human fibroblasts previously serum starved for 48 hours. At t= 0, 2, 4, 6, 8 HR respectively, the following number of cells were assessed: Control 1: 455, 413, 350, 346, 395; Control 2: 595, 431, 351, 368, 279; ARMC9 UW132-4: 218, 193, 229, 195, 189; TOGARAM1 UW360-3: 496, 622, 513, 558, 492. Ciliation percentages were normalized to 100% at the time of serum readdition, percentages represent the amount of remaining cilia compared to time zero. Error bars represent 95% confidence intervals. See "Statistics and reproducibility" section for details of statistical testing for cilia stability assays.

ARMC9 and *TOGARAM1* dysfunction is associated with abnormal ciliary resorption

Post-translational modifications of microtubules such as acetylation and polyglutamylation are enriched in the ciliary compartment and play roles in ciliogenesis, axoneme stability, and cilium disassembly (17). To investigate the consequence of reduced ciliary microtubule post-translational modifications on axonemal stability, we evaluated cilia of control and ARMC9 patient cells for sensitivity to cold-induced microtubule depolymerization (50, 51). In control cells, a 10-minute treatment at 4°C was not associated with reduced numbers of cilia, while cold-treated ARMC9 patient cells had 20-30% fewer cilia than untreated cells (Figure 8A). TOGARAM1 patient cell cilia were also more susceptible to cold-induced depolymerization, with 15% fewer cilia after treatment compared to untreated cells (Figure 8A).

As a second measure of cilium stability, we evaluated the rate of cilium resorption after serum re-addition to serum-starved cells. Serum provides growth factors that quickly initiate ciliary resorption, so that cells can re-enter the cell cycle. In controls, the ciliation rate was ~85% of baseline 4 hours after serum re-addition. In contrast, the ciliation rate was 70% of baseline in ARMC9 patient fibroblasts only 2 hours after serum re-addition, and by 8 hours, it was down to 50%, compared to 75% in controls (Figure 8B). To determine whether the faster resorption was due to an overactive deacetylating enzyme in the ARMC9 cell lines, we repeated these experiments with and without the histone deacetylase 6 (HDAC6) inhibitor tubacin. Tubacin treatment did not rescue the faster resorption in ARMC9 cell lines to control levels (Supplemental Figure 11A-C). Intriguingly, the ciliation rate of the one TOGARAM1 patient fibroblast line available remained 90% of baseline even 8 hours after serum re-addition, substantially higher than controls (Figure 8B). To determine if this abnormal ciliary stability caused defects in cell cycle progression, we used a flow-cytometry based approach to quantify cell cycle reentry (Supplemental Figure 12A-B). ARMC9 and TOGARAM1 patient cell lines reentered the cell cycle closely with similar timing to control cells. These data suggest that the ARMC9-TOGARAM1 complex plays a role in regulation of axonemal stability.

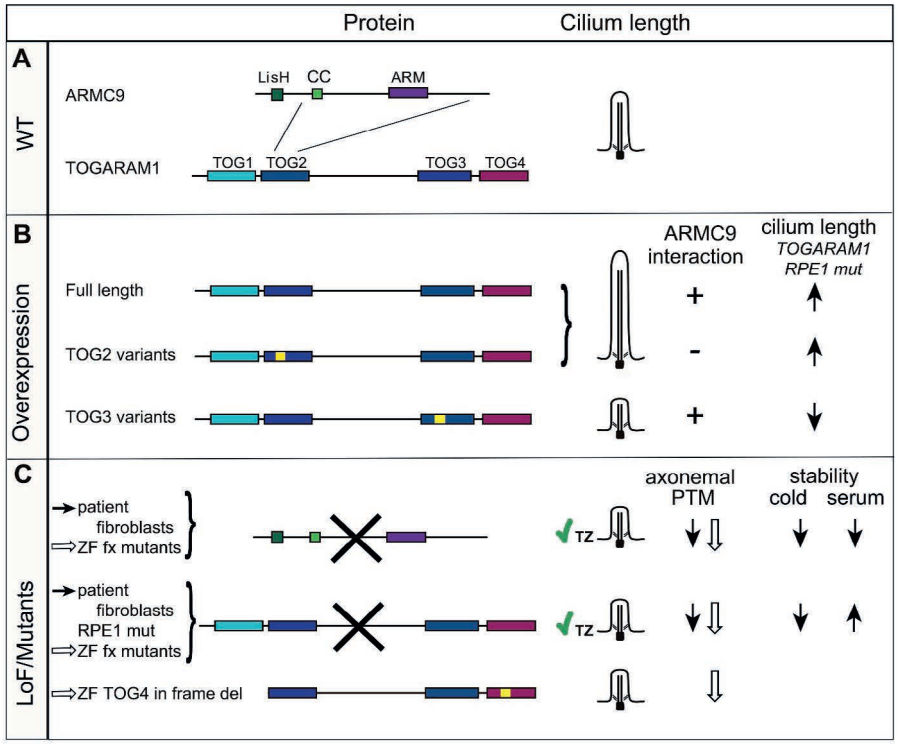

Figure 9 Graphical Summary: Disruptions of the ARMC9-TOGARAM1 module affect ciliary length, axonemal PTMs, and stability. (A) TOGARAM1 interacts with ARMC9 through its TOG2 domain. (B) Effects of TOGARAM1 overexpression (wild-type and with JBTS-associated variants) on ciliary length in TOGARAM1 mutant hTERT-RPE1 cells and consequences of JBTS-associated variants on the interaction with ARMC9. (C) Consequences of mutations in ARMC9 or TOGARAM1 on ciliary length and axonemal post-translational microtubule modifications (PTM) in patient fibroblast lines (black arrows) or zebrafish mutants (white arrows). Transition zone (TZ) integrity despite ARMC9 or TOGARAM1 dysfunction is indicated with a green checkmark. Consequences of TOGARAM1 and ARMC9 mutations on ciliary stability in response to cold or serum readdition in patient fibroblasts are indicated with black arrows. Yellow boxes represent pathogenic variants. Bold crosses indicate presumed loss-of-function mutations. del=deletion, fx=frameshift, LoF=loss of function, WT=wild-type, ZF=zebrafish. RPE1 mut=hTERT-RPE1 TOGARAM1 mutant lines. Protein domains: LisH=Lis-homology, CC=coiled-coil, ARM=armadillo, TOG=tumour overexpression gene.

DISCUSSION

In this study, we identified a new JBTS-associated protein module that can be distinguished physically and functionally from the previously described JBTS protein complex at the ciliary transition zone of primary cilia (52). Several components of this new module localize at the ciliary basal body (32) and at the proximal end of the ciliary axoneme (33, 53). Pathogenic variants in the genes encoding two directly interacting members of the module, ARMC9 and TOGARAM1, cause defects in cilium length, Hh signaling (SMO translocation), microtubule

post-translational modifications (acetylation and polyglutamylation), and ciliary stability in patient-derived fibroblasts, zebrafish mutants, and genetically edited hTERT-RPE1 cell lines (Summary Figure 9).

The ARMC9-TOGARAM1 complex in JBTS

Knowledge of the components and associations of the ciliary molecular machinery has been instrumental for relating ciliopathy genetic defects, associated pathomechanisms, and the wide spectrum of overlapping ciliopathy phenotypes. Several affinity and proximity proteomics approaches have been used to determine the topology of ciliary protein-protein interaction networks and generate molecular blueprints of the ciliary machinery, e.g. the entire ciliary organelle (54), of the human centrosome-cilium interface (53), or specific ciliopathy-associated protein modules (55, 56). The majority of the previously identified JBTS-associated proteins participate in specific sub-modules of complex ciliary protein networks that vary in sub-ciliary localization, concentrating at the transition zone to organize and regulate the ciliary gate (12, 57).

Using a combination of affinity proteomics (TAP) and Y2H protein interaction screens, we found that the newly JBTS-associated protein ARMC9 interacts with known JBTS-associated proteins CSPP1 and CEP290, confirming the importance of this complex to JBTS. We also identified two ciliary microtubule-associated proteins, TOGARAM1 and CCDC66, not previously associated with JBTS. A subsequent TAP screen using TOGARAM1 as bait pulled out ARMC9, further validating their interaction, and also identified another JBTS-associated protein, CEP104 (JBTS25). By Y2H screening we determined the direct interaction of TOGARAM1 with another JBTS-associated protein, RPGRIP1L (JBTS7), while a TAP experiment using CSPP1 as a bait again identified CEP290 as a complex member, and confirmed its previously identified interaction with RPGRIP1L (58). Our results are in agreement with the BioID proximity interactome of CEP104 that contained most of our module components, except for ARMC9 and RPGRIP1L (53). Co-IP and yeast two-hybrid analysis validated the core module, ARMC9, TOGARAM1, CCDC66, and CEP104 consisting of proteins important for cilium function and ciliopathy disease. For instance, CCDC66 was previously found to interact with CEP290 (36) and null mutations cause retinal degeneration in dogs (59) and mice (60). CEP104 localizes both to the daughter centriole as well as to the apical tip of a growing cilium (30) and, similar to TOGARAM1, interacts with tubulin through its TOG domain (61). Moreover, CEP104 has been shown to interact with NEK1 (61), which is associated with the ciliopathy “short-rib polydactyly syndrome Majewski type” (62), and with the JBTS-associated protein CSPP1 (39). This interaction, that we confirmed in our co-IP experiments, is required for the formation of Hedgehog signaling-competent cilia, as

mutations in CSPP1 and CEP104 significantly decreased ciliary SMO translocation (39), similar to what we observed with RPE1 TOGARAM1 mutant lines. Following the “guilt by association” paradigm, we next found biallelic TOGARAM1 variants in multiple individuals with JBTS, reiterating the relevance of the complex to JBTS, and moving us closer to identifying all genetic causes of this disorder. We did not find CCDC66 variants in >600 families affected by JBTS, indicating that variants in this gene are, at most, a very rare cause of JBTS.

Role of the ARMC9-TOGARAM1 complex in ciliary length and stability

The structure of TOG domains is highly conserved for microtubule binding, where the intra-HEAT loop in the discontinuous TOG domain binds tubulin (63–66). TOG domains are thought to regulate microtubule growth and dynamics (67). The TOG domains in TOGARAM1 have differential microtubule binding capacity and likely function in concert to coordinate microtubule polymerization (34). For example, the C-terminal TOG domains TOG3 and TOG4 promote microtubule lattice binding (34). Interestingly, we found that cilia are shorter in cells with ARMC9 or TOGARAM1 dysfunction. In contrast, we demonstrate that TOGARAM1 overexpression results in long cilia, and this effect requires an intact TOG3 domain, but not an intact TOG2 domain which is required for TOGARAM1 interaction with ARMC9. In fact, the TOG3 domain Arg1311Cys variant does not interfere with the ARMC9 interaction, but overexpression of this mutant protein results in severely shortened cilia. Since both long and short cilia have been identified in fibroblasts from patients with different genetic causes of JBTS, no simple correlation between cilium length and JBTS disease mechanism can be made (31, 32, 68, 69).

Recent work in Tetrahymena indicates that TOGARAM1 and ARMC9 orthologs may have opposite effects on B-tubule length (29). In mammalian cells, we found that dysfunction of either gene leads to shorter cilia, decreased post-translational modifications, and sensitivity to cold-induced ciliary microtubule depolymerization, suggesting reduced ciliary stability. Intriguingly, TOGARAM1 and ARMC9 dysfunction seem to have opposite effects on the kinetics of cilium resorption after serum re-addition in patient fibroblasts. This result suggests that different mechanisms may underlie ciliary resorption in the setting of serum re-addition versus cold-induced depolymerization. The latter may represent an acute stressor directly correlated with cilium stability, while the former is a regulated mechanism required for cell cycle reentry, for which TOGARAM1 and ARMC9 may indeed play opposing roles as suggested by the work in Tetrahymena (29).

Post-translational modifications of ciliary microtubules

ARMC9 and TOGARAM1 dysfunction also leads to significantly decreased axonemal post-translational modifications (PTMs, polyglutamylation and acetylation) in patient fibroblasts and zebrafish, supporting the relevance of altered PTMs in JBTS. Tubulin PTMs are indispensable for proper microtubule function, affecting their mechanical properties, stability, and binding of microtubule-associated proteins (MAPs) to influence protein trafficking and signaling (17).

Polyglutamylation decorates the surface of axonemal microtubules. This reversible modification ranges from 1-17 glutamyl residues in vivo (70), and plays a role in intraflagellar transport activity and MAP binding (71–74). Decreased ciliary polyglutamylation interferes with kinesin2-mediated anterograde transport, also on the B-tubule, and subsequently negatively impacts Hedgehog signaling (72, 73). Some MAPs are sensitive to the amount of glutamylation. For example, spastin has optimal microtubule-severing activity in vitro with moderate polyglutamylation, while both hypo- and hyper-glutamylation suppresses severing activity (75). In the context of JBTS, decreased axonemal polyglutamylation was reported in fibroblasts from patients with CEP41-related JBTS (11). More recent work found decreased axonemal glutamylation with ARL13B, FIP5 and TTLL5 knockdown in immortalized cells, associated with impacts on polycystin localization and Hh signaling (71).

While most PTMs are added to the C-terminus of tubulin on the microtubular surface, acetylation uniquely occurs on the luminal surface of α-tubulin. Ciliary resorption requires removal of this modification by HDAC6 (76). It has been long observed that the hyperstabilized ciliary microtubules are acetylated, but until recently it was not known if the modification confers stability or if long-lived stable microtubules accumulate this modification. Recent work using cryo-EM confirmed that acetylation causes a stabilizing conformational change (77). This is in line with our findings of decreased axonemal microtubule acetylation and stability with ARMC9 and TOGARAM1 dysfunction, as well as previously published findings with Kif7 and Armc9 dysfunction (33, 68). In particular, Armc9 null NIH3T3 cells had short cilia and decreased acetylation and glutamylation. The more rapid ciliary resorption with ARMC9 dysfunction is unlikely due to excessive deacetylation since cilia were not stabilized by HDAC6 inhibition. Interestingly, Kif7 mutant mouse embryonic fibroblasts (MEFs) exhibited reduced glutamylation, making it the only other JBTS model with decreases in both of these PTMs (31, 68). Fibroblasts from patients with INPP5E-related JBTS also display decreased cilium stability (78). Notably, these models of KIF7- and INPP5E-related ciliary dysfunction disrupt Hh signaling, likely due to GLI/SUFU mislocalization and aberrant phosphatidylinositol composition respectively, while emerging evidence indicates that reduced polyglutamlyation may indirectly alter translocation of Hh pathway components by perturbing anterograde intraflagellar transport (71, 72).

The observed reduction of PTMs with ARMC9 and TOGARAM1 dysfunction could therefore affect ciliary function through loss of stability and/or direct disruption of signaling pathways. In fact, Armc9 and Togaram1 (FAM179B) were identified as positive regulators of the Hh pathway in a genome-wide screen for Hh signaling components (33). That study also demonstrated that over-expressed ARMC9 translocates from the ciliary base to the tip upon Hh pathway stimulation (33). In Tetrahymena, orthologs of ARMC9 and TOGARAM1 are seen at both the base and tip, with tip enrichment during cilia regeneration (29). Taken together, these results suggest a dynamic localization of the complex members, and likely changes in protein complex composition at each locale. Further work will be required to determine the details of dynamic ARMC9-TOGARAM1 localization during ciliogenesis, resorption, and signaling.

CONCLUSIONS

The biological mechanisms underlying JBTS remain incompletely understood. This work brings us one step closer to the complete catalog of JBTS genetic causes, and highlights the role of a new JBTS-associated protein complex including ARMC9 and TOGARAM1. Approximately half of JBTS-associated genes are implicated in transition zone function which is required for ciliary ARL13B and INPP5E localization. In contrast, the ARMC9-TOGARAM1 complex is not required for INPP5E localization, and instead, appears to regulate the post-translational modification of ciliary microtubules, ciliary length and ciliary stability. Future work will need to reconcile how the diverse array of cellular defects associated with loss of function for the JBTS genes relate to this important human disorder.

Table 1. Variants and Clinical Features in individuals with TOGARAM1-related Joubert syndrome

	UW351-3	UW360-3	13DG1578	WGL-1914	JAS-L50
Variant 1[1]	c.1124T>C; p.(Leu375Pro)	c.1084C>T; p.(Gln362*)	c.1102C>T; p.(Arg368Trp)	c.3248C>A; p.(S1083*)	c.1112C>A; p.(Ala371Asp)
Allele frequency 1[2]	8/276914	0/251328	0/251284	0	5/282580
CADD v1.3[3]	25.5	35	28.7	38	26.6
Parent	father	Mother	NA	NA	mother
Variant 2[1]	c.3931C>T; p.(Arg1311Cys)	del14q21.2: g.45472062-45484253	c.1102C>T; p.(Arg368Trp)	c.3248C>A; p.(Ser1083*)	c.5023C>T; p.(Arg1675*)
Allele frequency 2	0/218738	NA	0/251284	0	1/251414
CADD v1.3[3]	35	NA	28.7	38	NA
Parent	mother	father	NA	NA	NA
Ethnicity/country	Mixed European (Australia)	Mixed European (US)	Middle Eastern (Egypt)	Middle Eastern (Iran)	White British
Gender	male	male	male	male	female
Age	21 wk fetus	16 yr	11 yr, 5 mo	6 yr	14 yr
Molar tooth	VH	Y	Y	Y	Y
Dev disability	NA	Y	Y	Y	Y
Apnea/tachypnea	NA	N	Y	NA	NA
Abnl eye mvts	NA	Y (and strabismus)	Y	NA	Y
Retinal	NA	N	N	NA	N
Kidney	NA	N	N	Y	Y
Liver	NA	N	N	Y	N
Polydactyly	Y (B post-ax foot)	N	N	Y (B post-ax hand)	N

	UW351-3	UW360-3	13DG1578	WGL-1914	JAS-L50
Coloboma	NA	N	N	Y	N
Craniofacial	broad nasal bridge, post rotated ears, thickened neck	low set ears, high arched palate	broad nose, anteverted alae, deep set eyes, hypertelorism, metopic ridge, frontal bossing, low set ears	broad nasal bridge, anteverted alae, deep set eyes, hypertelorism, frontal bossing	Oculomotor apraxia, Bilateral ptosis, left jaw/ wink ptosis
Other		widely spaced nipples, undescended testes, possible micropenis	widely spaced nipples, small scrotum and testes	corpus callosum hypoplasia, neonatal metabolic acidosis and jaundice, hepatomegaly, cholestasis, bilateral hydronephrosis hypotrichosis, small scrotum and testes, possible micropenis, microphthalmia, coloboma	short stature, generalized hypotonia, lumbar hyperlordosis, obesity, joint hypermobility, nonverbal, autistic behaviors, small scarred left kidney

[1]NM_015091.2
[2]gnomAD reference
[3]CADD reference
Abbreviations: Abnl=Abnormal, B=bilateral, mo=months, mvts=movements, N=No, NA=Not Available, post-ax=post-axial, US=United States, VH=Vermis Hypoplasia, wk=weeks, Y=Yes, yr=years

MATERIALS AND METHODS

A detailed description of cell culturing conditions, cloning, immunofluorescence and microscopy, cell cycle assay, zebrafish experiments, Palm-Myr assay, tandem affinity purification, yeast two-hybrid interaction analysis, coimmunoprecipitation, statistical analysis, microtubule cold assay, cilia stability assay, subject ascertainment and phenotypic data, variant identification, and array CGH can be found in the supplemental material and methods file.

WEB RESOURCES

http://chopchop.cbu.uib.no
http://gnomad.broadinstitute.org
https://www.ensembl.org/index.html
http://www.cmbi.umcn.nl/hope/
https://huygens.science.uva.nl/PlotsOfData/ (79)
http://www.phylogeny.fr/
http://syntenydb.uoregon.edu/synteny_db/

ACKNOWLEDGEMENTS

We thank the patient and parents for their participation in this research. We thank Dr David Breslow (Yale University) and Dr Max Nachury (University of California San Francisco) for providing the ARMC9-3xFlag IMCD3 FlpIn lines and NIH-3T3 ARMC9 mutant lines. The research leading to these results has received funding from the Netherlands Organisation for Scientific Research (NWO Vici-865.12.005 to R.R.), the Netherlands Organisation for Health Research and Development (ZonMW, #91216051 to R.R.), the Foundation Fighting Blindness (PPA-0717-0719-RAD to M.U. and R.R.), the Tistou & Charlotte Kerstan Stiftung (to M.U.), the Swiss National Science Foundation SNF (PP00P3_170681 to R.B.G and 31003A_173083 to S.C.F.N.), the Zurich Neuroscience Center (to R.B.G), the NIH Eunice Kennedy Shriver National Institute of Child Health and Human Development (U54HD083091 Genetics Core and sub-project 6849 to D.D. and F32 HD095599 to J.V.D.W.), private donations (to D.D.), Watson Genetic Laboratory (Tehran, Iran) for WGL-1914 sequencing (to M.K.), NIH National Human Genome Research Institute (U54HG006493 to M.B. and D.N.), Kidney Research UK, the Northern Counties Kidney Research Fund (joint studentship ST_001_20171120 to M.B.-G. and 18/01 to J.A.S.), and the King Salman Center for Disability Research (FSA). Part of the data presented here was provided through access to the data and findings generated by the 100,000 Genomes Project, which is funded by the NIHR and NHS England.

AUTHOR CONTRIBUTIONS

R.B.-G., R.R. and D.D. conceived the overall project. B.L., J.V.D.W., T.D.S.R., J.C.D., S.C.F.N., K.B., M.U., M.K., J.A.S., F.S.A., R.B.-G., R.R., & D.D. designed experiments and led the data generation and processing. B.L., J.V.D.W., T.D.S.R., S.J.F.L., A.G., A.K., M.A, M.E.G., S.E.C.v.B., C.V.M., and U.W.C.M.G. performed experiments. R.S., M.C., H.M., & J.C.D acquired clinical phenotype data. B.L., J.V.D.W., T.D.S.R., M.G., M.E.G., C.M., R.B.-G., R.R., & D.D. analyzed and interpreted data. B.L., J.V.D.W., T.D.S.R., R.B.-G., R.R., & D.D. wrote the paper with input from all authors.

REFERENCES

1. Hildebrandt F, Benzing T, Katsanis N. Ciliopathies. N. Engl. J. Med. 2011;364(16):1533–1543.
2. van Reeuwijk J, Arts HH, Roepman R. Scrutinizing ciliopathies by unraveling ciliary interaction networks. Hum. Mol. Genet. 2011;20(R2):R149–57.
3. Satir P, Pedersen LB, Christensen ST. The primary cilium at a glance. J. Cell Sci. 2010;123(Pt 4):499–503.
4. Maria BL et al. "Joubert Syndrome" Revisited: Key Ocular Motor Signs With Magnetic Resonance Imaging Correlation. J. Child Neurol. 2016;12(7):423–430.
5. Sattar S, Gleeson JG. The ciliopathies in neuronal development: a clinical approach to investigation of Joubert syndrome and Joubert syndrome-related disorders. Dev. Med. Child Neurol. 2011;53(9):793–798.
6. Reiter JF, Leroux MR. Genes and molecular pathways underpinning ciliopathies. Nat. Rev. Mol. Cell Biol. 2017;18(9):533–547.
7. Shamseldin HE et al. The morbid genome of ciliopathies: an update. Genet. Med. 2020;1–10.
8. Bachmann-Gagescu R et al. Healthcare recommendations for Joubert syndrome. Am. J. Med. Genet. Part A 2019;182(1):229–249.
9. Chaki M et al. Exome capture reveals ZNF423 and CEP164 mutations, linking renal ciliopathies to DNA damage response signaling. Cell 2012;150(3):533–548.
10. Bielas SL et al. Mutations in INPP5E, encoding inositol polyphosphate-5-phosphatase E, link phosphatidyl inositol signaling to the ciliopathies. Nat. Genet. 2009;41(9):1032–1036.
11. Lee JE et al. CEP41 is mutated in Joubert syndrome and is required for tubulin glutamylation at the cilium. Nat. Genet. 2012;44(2):193–199.
12. Garcia-Gonzalo FR et al. A transition zone complex regulates mammalian ciliogenesis and ciliary membrane composition. Nat. Genet. 2011;43(8):776–784.
13. Valente EM et al. Mutations in TMEM216 perturb ciliogenesis and cause Joubert, Meckel and related syndromes. Nat. Genet. 2010;42(7):619–625.
14. Garcia-Gonzalo FR et al. Phosphoinositides Regulate Ciliary Protein Trafficking to Modulate Hedgehog Signaling. Dev. Cell 2015;34(4):400–409.
15. Piperno G, Fuller MT. Monoclonal antibodies specific for an acetylated form of alpha-tubulin recognize the antigen in cilia and flagella from a variety of organisms. J. Cell Biol. 1985;101(6):2085–2094.
16. Bré MH, de Néchaud B, Wolff A, Fleury A. Glutamylated tubulin probed in ciliates with the monoclonal antibody GT335. Cell Motil. Cytoskeleton 2005;27(4):337–349.
17. Wloga D, Joachimiak E, Louka P, Gaertig J. Posttranslational Modifications of Tubulin and Cilia. Cold Spring Harb. Perspect. Biol. 2017;9(6):a028159–16.
18. Arts HH et al. Mutations in the gene encoding the basal body protein RPGRIP1L, a nephrocystin-4 interactor, cause Joubert syndrome. Nat. Genet. 2007;39(7):882–888.
19. Delous M et al. The ciliary gene RPGRIP1L is mutated in cerebello-oculo-renal syndrome (Joubert syndrome type B) and Meckel syndrome. Nat. Genet. 2007;39(7):875–881.
20. Gorden NT et al. CC2D2A is mutated in Joubert syndrome and interacts with the ciliopathy-associated basal body protein CEP290. Am. J. Hum. Genet. 2008;83(5):559–571.

21. Williams CL et al. MKS and NPHP modules cooperate to establish basal body/transition zone membrane associations and ciliary gate function during ciliogenesis. J. Cell Biol. 2011;192(6):1023–1041.
22. Shi X et al. Super-resolution microscopy reveals that disruption of ciliary transition-zone architecture causes Joubert syndrome. Nat. Cell Biol. 2017;19(10):1178–1188.
23. Cantagrel V et al. Mutations in the Cilia Gene ARL13B Lead to the Classical Form of Joubert Syndrome. Am. J. Hum. Genet. 2008;83(2):170–179.
24. Chávez M et al. Modulation of Ciliary Phosphoinositide Content Regulates Trafficking and Sonic Hedgehog Signaling Output. Dev. Cell 2015;34(3):338–350.
25. Caspary T, Larkins CE, Anderson K V. The Graded Response to Sonic Hedgehog Depends on Cilia Architecture. Dev. Cell 2007;12(5):767–778.
26. Tuz K et al. Mutations in CSPP1 cause primary cilia abnormalities and Joubert syndrome with or without Jeune asphyxiating thoracic dystrophy. Am. J. Hum. Genet. 2014;94(1):62–72.
27. Shaheen R et al. Mutations in CSPP1, Encoding a Core Centrosomal Protein, Cause a Range of Ciliopathy Phenotypes in Humans. Am. J. Hum. Genet. 2014;94(1):73–79.
28. Srour M et al. Joubert Syndrome in French Canadians and Identification of Mutations in CEP104. Am. J. Hum. Genet. 2015;97(5):744–753.
29. Louka P et al. Proteins that control the geometry of microtubules at the ends of cilia. J. Cell Biol. 2018;217(12):4298–4313.
30. Satish Tammana T V, Tammana D, Diener DR, Rosenbaum J. Centrosomal protein CEP104 (Chlamydomonas FAP256) moves to the ciliary tip during ciliary assembly. J. Cell Sci. 2013;126(21):5018–5029.
31. Dafinger C et al. Mutations in KIF7 link Joubert syndrome with Sonic Hedgehog signaling and microtubule dynamics. J. Clin. Invest. 2011;121(7):2662–2667.
32. Van De Weghe JC et al. Mutations in ARMC9, which Encodes a Basal Body Protein, Cause Joubert Syndrome in Humans and Ciliopathy Phenotypes in Zebrafish. Am. J. Hum. Genet. 2017;101(1).
33. Breslow DK et al. A CRISPR-based screen for Hedgehog signaling provides insights into ciliary function and ciliopathies. Nat. Genet. 2018;50(3):460–471.
34. Das A, Dickinson DJ, Wood CC, Goldstein B, Slep KC. Crescerin uses a TOG domain array to regulate microtubules in the primary cilium. Mol. Biol. Cell 2015;26(23):4248–4264.
35. Jiang K et al. A Proteome-wide Screen for Mammalian SxIP Motif-Containing Microtubule Plus-End Tracking Proteins. Curr. Biol. 2012;22(19):1800–1807.
36. Conkar D et al. The centriolar satellite protein CCDC66 interacts with CEP290 and functions in cilium formation and trafficking. J. Cell Sci. 2017;130(8):1450–1462.
37. Letteboer SJF, Roepman R. Versatile screening for binary protein-protein interactions by yeast two-hybrid mating. Methods Mol. Biol. 2008;484:145–159.
38. Conkar D, Bayraktar H, Firat-Karalar EN. Centrosomal and ciliary targeting of CCDC66 requires cooperative action of centriolar satellites, microtubules and molecular motors. Sci. Rep. 2019;9(1):14217–14250.
39. Frikstad K-AM et al. A CEP104-CSPP1 Complex Is Required for Formation of Primary Cilia Competent in Hedgehog Signaling. Cell Rep. 2019;28(7):1907–1922.e6.
40. Zacharias DA, Violin JD, Newton AC, Tsien RY. Partitioning of lipid-modified monomeric GFPs into membrane microdomains of live cells. Science. 2002;296(5569):913–916.

41. Bachmann-Gagescu R et al. Joubert syndrome: a model for untangling recessive disorders with extreme genetic heterogeneity. J. Med. Genet. 2015;52(8):514–522.

42. Karczewski KJ et al. Variation across 141,456 human exomes and genomes reveals the spectrum of loss-of-function intolerance across human protein-coding genes [Preprint]. https://doi.org/10.1101/531210. Posted on bioRxiv August 13, 2019.

43. Rentzsch P, Witten D, Cooper GM, Shendure J, Kircher M. CADD: predicting the deleteriousness of variants throughout the human genome. Nucleic Acids Res. 2018;47(D1):D886–D894.

44. O'Roak BJ et al. Exome sequencing in sporadic autism spectrum disorders identifies severe de novo mutations. Nat. Genet. 2011;43(6):585–589.

45. Venselaar H, Te Beek TAH, Kuipers RKP, Hekkelman ML, Vriend G. Protein structure analysis of mutations causing inheritable diseases. An e-Science approach with life scientist friendly interfaces. BMC Bioinformatics 2010;11:548.

46. Nithianantham S et al. Structural basis of tubulin recruitment and assembly by microtubule polymerases with tumor overexpressed gene (TOG) domain arrays. Elife 2018;7:1–60.

47. Grimes DT et al. Zebrafish models of idiopathic scoliosis link cerebrospinal fluid flow defects to spine curvature. Science. 2016;352(6291):1341–1344.

48. Bachmann-Gagescu R et al. The ciliopathy gene cc2d2a controls zebrafish photoreceptor outer segment development through a role in Rab8-dependent vesicle trafficking. Hum. Mol. Genet. 2011;20(20):4041–4055.

49. Slaats GG et al. MKS1 regulates ciliary INPP5E levels in Joubert syndrome. J. Med. Genet. 2015;53(1):62–72.

50. Piperno G, LeDizet M, Chang XJ. Microtubules containing acetylated alpha-tubulin in mammalian cells in culture. J. Cell Biol. 1987;104(2):289–302.

51. LeDizet M, Piperno G. Cytoplasmic microtubules containing acetylated alpha-tubulin in Chlamydomonas reinhardtii: spatial arrangement and properties. J. Cell Biol. 1986;103(1):13–22.

52. Reiter JF, Blacque OE, Leroux MR. The base of the cilium: roles for transition fibres and the transition zone in ciliary formation, maintenance and compartmentalization. EMBO Rep. 2012;13(7):608–618.

53. Gupta GD et al. A Dynamic Protein Interaction Landscape of the Human Centrosome-Cilium Interface. Cell 2015;163(6):1484–1499.

54. Boldt K et al. An organelle-specific protein landscape identifies novel diseases and molecular mechanisms. Nat. Commun. 2016;7:1–13.

55. Toriyama M et al. The ciliopathy-associated CPLANE proteins direct basal body recruitment of intraflagellar transport machinery. Nat. Genet. 2016;48(6):648–656.

56. Sang L et al. Mapping the NPHP-JBTS-MKS Protein Network Reveals Ciliopathy Disease Genes and Pathways. Cell 2011;145(4):513–528.

57. Garcia-Gonzalo FR, Reiter JF. Scoring a backstage pass: Mechanisms of ciliogenesis and ciliary access. J. Cell Biol. 2012;197(6):697–709.

58. Patzke S et al. CSPP is a ciliary protein interacting with Nephrocystin 8 and required for cilia formation. Mol. Biol. Cell 2010;21(15):2555–2567.

59. Dekomien G et al. Progressive retinal atrophy in Schapendoes dogs: mutation of the newly identified CCDC66 gene. Neurogenetics 2009;11(2):163–174.

60. Gerding WM et al. Ccdc66 null mutation causes retinal degeneration and dysfunction. Hum. Mol. Genet. 2011;20(18):3620–3631.

61. Al-Jassar C et al. The Ciliopathy-Associated Cep104 Protein Interacts with Tubulin and Nek1 Kinase. Structure 2017;25(1):146–156.

62. Thiel C et al. NEK1 mutations cause short-rib polydactyly syndrome type majewski. Am. J. Hum. Genet. 2011;88(1):106–114.

63. Howard AE, Fox JC, Slep KC. Drosophila melanogaster mini spindles TOG3 utilizes unique structural elements to promote domain stability and maintain a TOG1- and TOG2-like tubulin-binding surface. J. Biol. Chem. 2015;290(16):10149–10162.

64. Leano JB, Rogers SL, Slep KC. A cryptic TOG domain with a distinct architecture underlies CLASP-dependent bipolar spindle formation. Structure 2013;21(6):939–950.

65. Slep KC. A Cytoskeletal Symphony: Owed to TOG. Dev. Cell 2018;46(1):5–7.

66. Al-Bassam J et al. CLASP promotes microtubule rescue by recruiting tubulin dimers to the microtubule. Dev. Cell 2010;19(2):245–258.

67. Leano JB, Slep KC. Structures of TOG1 and TOG2 from the human microtubule dynamics regulator CLASP1. PLoS One 2019;14(7).

68. He M et al. The kinesin-4 protein Kif7 regulates mammalian Hedgehog signalling by organizing the cilium tip compartment. Nat. Cell Biol. 2014;16(7):663–672.

69. Srivastava S et al. A human patient-derived cellular model of Joubert syndrome reveals ciliary defects which can be rescued with targeted therapies. Hum. Mol. Genet. 2017;26(23):4657–4667.

70. Geimer S, Teltenkötter A, Plessmann U, Weber K, Lechtreck KF. Purification and characterization of basal apparatuses from a flagellate green alga. Cell Motil. Cytoskeleton 1997;37(1):72–85.

71. He K et al. Axoneme polyglutamylation regulated by Joubert syndrome protein ARL13B controls ciliary targeting of signaling molecules. Nat. Commun. 2018;9(1):3310–3314.

72. Hong S-R et al. Spatiotemporal manipulation of ciliary glutamylation reveals its roles in intraciliary trafficking and Hedgehog signaling. Nat. Commun. 2018;9(1):1713–1732.

73. OHagan R et al. Glutamylation Regulates Transport, Specializes Function, and Sculpts the Structure of Cilia. Curr. Biol. 2017;27(22):3430–3441.e6.

74. Orbach R, Howard J. The dynamic and structural properties of axonemal tubulins support the high length stability of cilia. Nat. Commun. 2019;1–11.

75. Valenstein ML, Roll-Mecak A. Graded Control of Microtubule Severing by Tubulin Glutamylation. Cell 2016;164(5):911–921.

76. Pugacheva EN, Jablonski SA, Hartman TR, Henske EP, Golemis EA. HEF1-Dependent Aurora A Activation Induces Disassembly of the Primary Cilium. Cell 2007;129(7):1351–1363.

77. Eshun-Wilson L et al. Effects of α-tubulin acetylation on microtubule structure and stability. Proc. Natl. Acad. Sci. U. S. A. 2019;116(21):10366–10371.

78. Hardee I et al. Defective ciliogenesis in INPP5E-related Joubert syndrome. Am. J. Med. Genet. Part A 2017;173(12):3231–3237.

79. Postma M, Goedhart J. PlotsOfDataA web app for visualizing data together with their summaries. PLoS Biol. 2019;17(3):e3000202–8.

SUPPLEMENTAL MATERIALS AND METHODS

Patient Fibroblast Culture

Patient fibroblasts were cultured at 37°C, 5% CO_2 in DMEM (Gibco, 11995-065) supplemented with 10% FBS, 1% penicillin/streptomycin. Fibroblasts are seeded at 5x10^5 and allowed to reach 70-80% confluency prior to passages. For experiments, cells are serum starved in DMEM only for 48 hours to induce ciliogenesis. All cell lines used were within 1 passage number of each other and ≤10 total passages. All cell lines were routinely tested for mycoplasma.

CRISPR/Cas9 generation of *TOGARAM1* mut hTERT-RPE1 cell lines

hTERT-RPE1 were maintained in culture according to ATCC specifications. Cells were plated in 1 well of a 6 well plate. At ~70-80% confluency, cells were co-transfected with the Cas9 backbone px459v2 containing gRNAs to TOGARAM1. Transfections were performed with lipofectamine 2000 (Thermo Fisher). Sequencing primers for genotyping targeted the 5'UTR CTGAAGCTGTTCTTTTGCCTCT (forward) and exon 1 CTACCTCCTTCCACAAGCACTC (reverse). Both TOGARAM1 mut clone 1 and 2 have compound heterozygous mutations which result in large deletions including the ATG site and a portion of exon 1. *TOGARAM1* mut line 1: NM_001308120.2:c.[2_269del;270dup]; [2_269inv]. TOGARAM1 mut line 2: NM_001308120.2:c.[-33_314del]; [2_269inv; 269_270insTC] (Supplemental Figure 5 A, B). Cloning was performed as previously described (1). gRNAs to the 5'UTR and ATG site, 5'-CACCTGACAACCCTGCATGG-3' and exon 1, 5'-TCTGGAGGCGGTTTGTCAGG-3', were designed utilizing the web-based tool CHOPCHOP. pSpCas9(BB)-2A-Puro (PX459) V2.0 from Feng Zhang (Addgene plasmid # 62988) was purchased from Addgene.

hTERT-RPE1 Immunofluorescence and microscopy

Human telomerase-immortalized retinal pigment epithelium (hTERT-RPE1) cells were cultured according to ATCC specifications. For immunofluorescence imaging, cells were plated on glass coverslips. At 24 hr after plating, cells were serum starved for 48 hr in 0.2% FBS medium to induce cell cycle arrest and ciliogenesis. Transfections were performed where indicated at 48 hours post plating using lipofectamine 2000 (Thermo Fisher) in accordance with the manufacturer's protocol. 72 hours after plating, cells were rinsed once with 1X PBS, fixed with 2% paraformaldehyde for 20 min and permeabilized with 1% Triton-X for 5 min. All steps were performed at room temperature. Cells were blocked in freshly prepared 2% BSA for 45 min and then incubated with the following antibodies for 1 hr: rabbit polyclonal anti-ARL13B

(Proteintech, cat. no. 17711-1-AP; 1:500), guinea pig polyclonal anti-RPGRIP1L (in house; SNC040, 1:300), monoclonal anti-acetylated tubulin antibody (clone 6-11-B1, Sigma-Aldrich, cat. no. T6793; 1:1,000), monoclonal anti-GT335 (a kind gift from Carsten Janke; 1:2000), rabbit polyclonal anti-SMO (Abcam, cat. no. ab38686; 1:200), and mouse monoclonal anti-ARL13B (NeuroMab, cat. no. 75-287; 1:500). Cells were stained with secondary antibodies for 45 min. The following secondary antibodies were used (all from Life Technologies/Thermo Fisher Scientific; all diluted 1:500 in 2% BSA): anti-guinea pig IgG Alexa Fluor 647, anti-rabbit IgG Alexa Fluor 488, and anti-mouse IgG Alexa Fluor 568. Fluoromount-G mounting solution with DAPI (ThermoFisher) was used to mount the coverslips to slides. Non-confocal imaging was performed with the Zeiss Axio Imager Z2 Microscope. Confocal imaging was done with the Zeiss LSM 880 Laser scanning microscope equipped with Airyscan technology.

Fixation and staining for patient fibroblast immunofluorescence

Patient fibroblasts were grown on coverslips (Neuvitro, GG-12-1.5.pdl, 0.3mg/mL Poly-D-lysine coating, 1.5mm thickness), serum-starved for 48 hours, then fixed in ice cold 2% paraformaldehyde in PBS for 20 minutes. After a PBS wash, cells were permeablized with 1% Trition-X in PBS or ice-cold Methanol for 5 minutes. Cells were blocked in 2% BSA in PBS for 1 hour at room temperature, then incubated with the following antibodies (in 2% BSA/PBS) for 1.5 hours at room temperature: mouse anti-polyglutamylated tubulin, GT335, (Adipogen, AG- 20B-0020-C100, 1:2000), mouse anti-acetylated tubulin (clone 6-11-B1, Sigma-Aldrich, T6793; 1:1,000), mouse anti-ARL13B (UC Davis NeuroMab 75-287 clone N295B/66, 1:2000), goat anti-γ-tubulin (Santa Cruz, SC-7396 1:200), rabbit anti-ARL13B (Proteintech, 17711-1-AP, 1:200), or rabbit anti-INPP5E (Proteintech, 17797-1-AP, 1:100). Cells were washed thrice with PBS and stained with secondary antibodies (in 2% BSA/PBS) for 1 hour at room temperature (all Invitrogen at 1:2000, anti-goat-647, A21447, anti-rabbit-488, A11008). After three PBS washes, coverslips were mounted on slides using Fluoromount-G with DAPI (Invitrogen, 00-4959-52) and sealed with nail polish.

Patient Fibroblast Microscopy & Immunofluorescence Quantification

Wide-field fluorescent images were acquired on an 3i imaging workstation (3i, Denver, CO) with Axio inverted microscope with Definite Focus (Zeiss). For each experiment, optimal exposures were determined for each fluorophore to ensure that we used the full dynamic range of our CoolSnap HQ2 camera (Photometrics, Inc., Tuscon, AZ) without saturating any pixels. Dark field correction was applied to each channel to remove artifacts generated from

the camera and electronics due to non-uniformities in illumination. Z-stack images with 0.3 μm steps were acquired at ≥10 distinct locations on each slide with a 40x objection using identical scope settings for all slides in an experiment. Sum projected images were analyzed in FIJI (NIH). A reference ciliary mask was drawn atop the reference signal for each cilium by standardized methods. A skeleton measurement of this mask extracted ciliary length data. The average fluorescence intensity was measured within the cilium mask in the channel of interest. To correct for antibody background, the background from a region directly adjacent to each cilium was measured and subtracted.

Patient Fibroblast Cell Cycle Reentry Analysis

Near confluent cells were serum starved for 48 hours, then serum was added back for 0, 4, 8, 16, or 24 hours. Cells were tryspinzed, concentrated, then triturated in 10mg/mL DAPI and 0.1% nonident P-40 solution with a 25 gauge needle to release intact nuclei. Nuclear DNA content was measured with a 405 nm laser on a LSRII (BD Bioscience) flow cytometer, then data was analyzed in FCS Express 6 (De Novo Software) (2).

Zebrafish experiments: Phylogeny and Synteny Analysis, CRISPR gene editing, Scanning electron microscopy and Immunofluorescence

Phylogeny and Synteny analyses were performed as previously described (3), using the Phylogeny.fr platform (http://www.phylogeny.fr/) and the synteny database (http://syntenydb.uoregon.edu/ synteny_db/). Briefly, for Phylogeny, length of input sequences varied between 256 (*xenopus* truncated version) and 516 amino acids, and after curation 487 amino acids were used for further analysis. For Synteny analysis, parameters were adjusted to sliding window sizes between 25 and 100, and several genes in the vicinity of TOGARAMs were used for additional syntenic comparison. Zebrafish (*Danio rerio*) were maintained at 28 °C with a 14 h/10 h light/dark cycle as previously described (4). All zebrafish protocols were in compliance with internationally recognized guidelines for the use of zebrafish in biomedical research, and the experiments were approved by local authorities (Veterinäramt Zürich TV150). Generation and genotyping of the *armc9* mutant zebrafish was previously described (5). sgRNAs for *togaram1* CRISPR/Cas9 mutagenesis were designed with the website CHOPCHOP: 3'-GGGGTCTCCTCTGCTGGGCC-5' and 5'-GGACGAGATGCTGGACCGAG-3' for exon 6/7 and 3'-GGCTGCCGATGACCAGAGCT-5' and 5'-GGTGAATCTGCGCGCTCTGG-3' for exon 21/22 in *togaram1.* sgRNAs were mixed with Cas9 protein (gift from Darren Gilmour, M0646M NEB, or B25641 invitrogen) and co-injected into 1-cell stage embryos using a microinjector

(Eppendorf). Amplification of the target regions for genotyping was performed using primer pairs 5'-AGACGCTCCTCAACTCCAGA-3' and 5'-GCCGTGTAGACGAGTGTGTT-3' for exon 21/22 in *togaram1.* The PCR products were analyzed with gel electrophoresis and subcloned before sequencing. Experiments were performed using the *armc9*^{zh505} (WIK background) and the *togaram1*^{zh509} or *togaram1*^{zh510} (Tü background) mutants from generation F2+ (Supplemental Figure 6F). Zebrafish larvae were fixed in 2.5 % Glutaraldehyde in 0.1 M Cacodylate buffer and prepared for scanning electron microscopy (SEM) following standard protocols. SEM was performed on a ZEISS Supra VP 50 microscope. Whole-mount immunohistochemistry was performed on zebrafish larvae fixed in 4% paraformaldehyde or 80% MeOH in DMSO according to standard protocols. The following primary antibodies were used: acetylated tubulin (1:400, Sigma 7451), GT335 (1:400, Enzo Life Sciences A20631002), arl13b (1:100, gift from Z.Sun (6)), cc2d2a (7). Images were taken with a Leica HCS LSI confocal microscope. Acetylated tubulin and glutamylated tubulin mean fluorescence intensity was quantified using FIJI: fluorescence intensity of 10 cilia from each larvae were measured and averaged, so that each datapoint in graphs Fig 6A, 7E and 7F represents one individual larva. The background was subtracted from each measurement.

Cloning of constructs

All expression constructs were generated using Gateway Technology (Life Technologies) and according to manufacturer's instructions. The constructs generated encoded TOGARAM1 (and JBTS associated variants), ARMC9 (NM_025139.2),, pENTR223-CCDC66 (NM_001141947.3), CEP104 (NM_014704.4) and CSPP1 (NM_024790.6) in the following destination vectors: 3xHA, 3xFlag, TAP, myc, mRFP, GAL4-BD, and PalmMyr-CFP. The entry clone of human TOGARAM1 (NM_001308120.2) was synthesized and purchased from VectorBuilder. Constructs encoding TOGARAM1 and variants were generated by site directed mutagenesis PCR. All entry clone sequences were verified using Sanger sequencing.

PalmMyr Assay

hTERT-RPE1 cells were plated on glass slides, 24 hours later when cells reached approximately 80% confluency they were transfected using lipofectamine 2000 (ThermoFisher) with either mRFP-tagged TOGARAM1 / TOGARAM1 variants or PalmMyr-CFP-tagged ARMC9 or both. 24 hours post transfection, cells were starved for an additional 24 hours, fixed with 2% PFA at room temperature and prepared for analysis. Imaging was performed with the Zeiss Axio Imager Z2 Microscope.

Tandem affinity purification and mass spectrometry

HEK293Tcells were grown in DMEM (PAA) supplemented with 10% fetal bovine serum and 1% penicillin/streptomycin. Cells were seeded and expanded for 16 – 24 hours, then transfected with the corresponding SF-TAP-tagged DNA constructs using PEI reagent (Polysciences) according to the manufacturer's protocol. 48 hours later, cells were harvested in lysis buffer containing 0.5% Nonidet-P40 (NP-40), protease inhibitor cocktail (Roche), and phosphatase inhibitor cocktails II and III (Sigma-Aldrich) in TBS (30mM Tris-HCl, pH 7.4 and 150mM NaCl) for 20 min at 4°C. Cell debris and nuclei were removed by centrifugation at 10,000g for 10 min. For SF-TAP analysis, the cleared supernatant was incubated for 1 hour at 4°C with Strep-Tactin superflow (IBA). Subsequently, the resin was washed three times in wash buffer (TBS containing 0.1% NP-40 and phosphatase inhibitor cocktails II and III, Sigma-Aldrich). Protein baits were eluted with Strep-elution buffer (2mM desthiobiotin in TBS). For the second purification step, the eluates were transferred to anti-Flag M2 agarose beads (Sigma-Aldrich) and incubated for 1 hour at 4°C. The beads were washed three times with wash buffer and proteins were eluted with FLAG peptide (200 mg/ml, Sigma-Aldrich) in TBS. After purification, the protein samples were precipitated with chloroform and methanol and subjected to in-solution tryptic cleavage. Mass spectrometry and subsequent analysis were performed as previously described (8).

Yeast two-hybrid interaction analysis

The GAL4-based yeast two-hybrid system was used to screen for binary protein–protein interactions. Yeast two-hybrid constructs were generated according to manufacturer's instructions using Gateway cloning technology (Thermo Fisher Scientific) by LR recombination of GAL4-BD Gateway destination vectors with sequence verified Gateway entry vectors containing the cDNAs of selected bait proteins ARMC9, TOGARAM1, and CCDC66. Fragments thereof were generated by Gateway adapted PCR and subsequent cloning. Constructs encoding full-length or fragments of bait proteins fused to a DNA binding domain (GAL4-BD) were used as baits to screen human oligo-dT primed and bovine random hexamer primed retinal cDNA libraries, prey proteins are fused to a GAL4 activation domain (GAL4-AD). The yeast strain PJ96-4A, which carries the HIS3 (histidine), ADE2 (adenine), MEL1 (α-galactosidase) and LacZ (β-galactosidase) reporter genes, was used as a host. Interactions were analyzed by assessment of reporter gene (HIS3 and ADE2) activation via growth on selective media and β-galactosidase colorimetric filter lift assays (*LacZ* reporter gene). cDNA inserts of clones containing putative interaction partners were confirmed by Sanger sequencing.

Coimmunoprecipitation assay

HEK293T cells were plated in 6 well plates and transfected using Effectene Transfection Reagent (Qiagen) according to the manufacturer's protocol. Cells were subsequently incubated at 37°C for 24 hours and then lysed in 200 μL per well of ice cold IP lysis buffer and collected for centrifugation. Lysates were centrifuged at 4 °C for 10 minutes at 11,000 rpm, supernatant was subsequently collected and incubated in new Eppendorf tubes with HA affinity matrix beads (Roche). Lysates were nutated for 2 hours at 4°C. The beads were spun down for 30 seconds at 4000 rpm. Beads were washed 3 times in 1 ml of ice cold IP lysis buffer, then all liquid was removed from the beads using a syringe with 0.5 mm needle. 50 μL of NuPAGE loading dye plus 100 mM DTT was added to the samples and they were heated at 95°C for 10 minutes. Western blotting was performed using the standard protocol for the NuPAGE system and visualized on the Odyssey. c-myc (Roche, 11667149001; 1:500), HA (Sigma; H9658; 1:1000), and Flag (Sigma; F3165-0.2MG; 1:1000) primary antibodies were used. The secondary antibody used was goat anti-Mouse IRDye800 (Licor biosciences; 926-32210; 1:20,000).

Western blotting

Trypsinized and concentrated cells were lysed with NP-40 cell lysis buffer (ThermoFisher, FNN0021). Cellular proteins were denatured using Laemmli sample buffer supplemented with 2-Mercaptoethanol (both BioRad, #1610747, #1610710) and heated at 95°C for 10 minutes. Cellular proteins were separated by SDS-PAGE and transferred to a PVDF membrane (Millipore IPVH00010) using standard protocols. The following primary antibodies were used: mouse anti-acetylated tubulin (clone 6-11-B1, Sigma-Aldrich, T6793; 1:1,000), mouse-anti beta-actin (Sigma, A5441, 1:5000), rabbit anti-ARL13B (Proteintech, 17711-1-AP, 1:1000), rabbit anti-INPP5E (Proteintech, 17797-1-AP, 1:1000), rabbit anti-Giantin (Abcam, ab24586, 1:5000) or rabbit anti-ARMC9 (Atlas Antibodies cat# HPA019041, RRID: AB_1233489; 1:2000). Anti-ARMC9 recognizes an epitope at the N-terminal portion of the protein. Western blots were developed using anti-mouse or anti-rabbit secondary antibodies conjugated to horseradish peroxidase (anti-rabbit-HRP, Novex A16029 1:2000, anti-mouse-HRP, Invitrogen G21040 1:2000) and chemiluminescent substrate (BioRad Clarity Max 1705062). A ChemiDoc MP imaging system with ImageLab software was used for imaging (both BioRad).

Statistics and reproducibility

Statistical analyses were performed in Excel and Graphpad / Prism 6. Graphical data presented as percentages include 95% confidence intervals, but otherwise represent standard deviations.

Quantitative immunofluorescence statistics were calculated with Student's t-test with unequal variances. Fluorescence intensity measurements from multiple experiments were combined for statistical analysis. Experiments were independently performed thrice. In cilia stability assays, linear regression of ciliary loss over time yielded the slope, and we used Student's t-test with unequal variances for singular comparisons and a one-way ANOVA to assess significance for multiple samples. N values are stated in the figures and either represent cilia or cells (as indicated in each Figure). P values are stated in the figure legends, and symbols indicate the following P values: ns, $P > 0.05$; *, $P \leq 0.05$; **, $P \leq 0.01$; ***, $P \leq 0.001$; ****, $P \leq 0.0001$, *****, $P \leq 0.00001$.

Microtubule cold depolymerization assay

For microtubule cold depolymerization assays, cells were grown until near-confluent on coverslips in 24-well plates, serum starved for 48 hours, then placed at either room temperature or 4°C for 10 minutes. Cells were then fixed as described and processed for immunofluorescence to determine ciliation percentage.

Cilia stability assay

For cilia stability assays, cells were grown until near-confluent on coverslips in 24-well plates, serum starved for 48 hours, then media was replaced with DMEM 10% FBS at hourly time points for 4-8 hours (9). Cells were then fixed as described and processed for immunofluorescence to determine ciliation percentage. In a subset of these experiments, we blocked histone deacetylase 6 (HDAC6) activity, with a specific inhibitor, tubacin (Sigma, SML0065). Cells were either treated with 1 μM tubacin in DMSO or in DMSO only as a vehicle control.

Subject Ascertainment and Phenotypic Data

The UW351 and UW360 families were enrolled under approved human subjects research protocols at the University of Washington (UW). The 13DG1578 family was enrolled King Faisal Specialist Hospital and Research Centre KFSHRC RAC# 2070023, 2080006 and 2121053. The JAS-L50 family was enrolled in the 100,000 Genomes Project. All participants in the 100KGP have provided written consent to provide access to their anonymised clinical and genomic data for research purposes. The 100KGP research and clinical project model and its informed consent process has been approved by the National Research Ethics Service Research Ethics Committee for East of England – Cambridge South Research Ethics Committee. The WGL-191

family consented under a human subjects research protocol approved by the Ethics Committee at Tehran University of Medical Sciences.

All participants or their legal guardians provided written informed consent. All participants have clinical findings of JBTS (intellectual impairment, hypotonia, ataxia, and/or oculomotor apraxia) and diagnostic or supportive brain imaging findings (MTS or cerebellar vermis hypoplasia). Clinical data were obtained by direct examination of participants, review of medical records, and structured questionnaires.

Variant Identification

To identify the UW351 and UW360 families, samples from individuals affected by JBTS were previously screened using a molecular inversion probes (MIPs) targeted capture (10). See Supplemental Table 4 for the target gene list (11-35). In samples without causal variants, exome sequencing was performed as previously described (36) using Roche Nimblegen SeqCap EZ Human Exome Library v2.0 capture probes (36.5 Mb of coding exons) and paired-end 50 base pair reads on an Illumina HiSeq sequencer. In accordance with the Genome Analysis ToolKit's (GATK) best practices, we mapped sequence reads to the human reference genome (hg19) using the Burrows-Wheeler Aligner (v.0.7.8), removed duplicate reads (PicardMarkDuplicates v.1.113), and performed indel realignment (GATK IndelRealigner v.3.1) and base-quality recalibration (GATK TableRecalibration v.3.1). We called variants using the GATK UnifiedGenotyper and flagged with VariantFiltration to mark potential false positives that did not pass the following filters: Heterozygous Allele Balance (ABHet) > 0.75, Quality by Depth > 5.0, Quality (QUAL) > 50.0, Homopolymer Run (Hrun) < 4.0, and low depth (< 8x). We used SeattleSeq for variant annotation and the Combined Annotation Dependent Depletion (CADD) score to determine deleteriousness of identified missense variants (37). Based on CADD score data for causal variants in other JBTS-associated genes, we used a CADD score cutoff of 15 to define deleterious variants (26). In Supplemental Figure 3E, we used the Integrated Genome Viewer for visualization of next-generation sequencing data (38).

For family 13DG1578, DNA from the affected individual, unaffected siblings, and parents were genotyped using the Axiom SNP Chip platform to determine the candidate autozygome (39, 40). WES was performed using TruSeq Exome Enrichment kit (Illumina) following the manufacturer's protocol. Samples were prepared as an Illumina sequencing library, and then the sequencing libraries were enriched for the desired target using the Illumina Exome Enrichment protocol. The captured libraries were sequenced using an Illumina HiSeq 2000 Sequencer. The reads were mapped against UCSC hg19 by BWA. SNPs and indels were detected by SAMTOOLS.

Homozygous rare, predicted-deleterious, and coding/splicing variants within the autozygome of the affected individual were considered as likely causal. We defined rare variants as those with frequency of <0.1% in publicly available variant databases (1000 Genomes, Exome Variant Server, and gnomAD) as well as a database of 2,379 in-house ethnically matched exomes, and defined deleterious if predicted to be pathogenic by PolyPhen, SIFT, and CADD (score > 15).

For family JAS-L50, whole genome sequencing was performed by Genomics England via the 100,000 Genomes Project using the Illumina TruSeq DNA PCR-Free sample preparation kit (Illumina, Inc.) and an Illumina HiSeq 2500 sequencer, generating a mean depth of 45x 10 (range from 34x to 72x) and greater than 15x for at least 95% of the reference human genome. WGS reads were aligned to the Genome Reference Consortium human genome build 37 (GRCh37) using Isaac Genome Alignment Software (version 01.14; Illumina, Inc.). Sequence data was analysed using bcftools scripts designed to search vcf.gz files and individual BAM files were viewed using IGV.

For family WGL-1914, genomic DNA was extracted from whole blood. Human whole exome enrichment was performed using Twist Human Core Exome Plus Kit and the library was sequenced on an Illumina NovaSeq platform. Data analysis was performed using a standard clinical pipeline, and the homozygous TOGARAM1 variant was the only likely pathogenic variant identified that was consistent with the phenotype. The variant was validated by Sanger sequencing and confirmed heterozygous in parents.

Array CGH

To assess copy-number variation, we performed array comparative genomic hybridization using a custom 8x60K oligonucleotide array (Agilent Technologies) (41). For gene list see supplemental table 5. Probe spacing was a median of 11 bp in the exons, and a median of 315 bp throughout the intronic regions and 100 kb on either side of each gene. Data were generated on an Agilent Technologies DNA Microarray Scanner with Surescan High-Resolution Technology using Agilent Scan Control software and were processed and analyzed using Agilent Feature Extraction and Agilent Cytogenomics software. To determine the effect of the deletion in UW360-3, we extracted RNA (BioRad, Aurum Total RNA kit, 7326820) from the associated cell line and converted it to cDNA (Biorad, iScript Reverse Transcription Supermix, 1708840) for downstream Sanger sequencing. To determine segregation of this deletion in family UW360 and to determine the precise breakpoints, we amplified the deletion-flanking region from genomic DNA and Sanger sequenced.

REFERENCES

1. Ran FA et al. Genome engineering using the CRISPR-Cas9 system. *Nat. Protoc.* 2013;8(11):2281–2308.
2. Rabinovitch PS. Chapter 18 DNA Content Histogram and Cell-Cycle Analysis. *Methods Cell Biol.* 1994;41(C):263–296.
3. Ojeda Naharros I et al. Loss-of-function of the ciliopathy protein Cc2d2a disorganizes the vesicle fusion machinery at the periciliary membrane and indirectly affects Rab8-trafficking in zebrafish photoreceptors. *PLoS Genet.* 2017;13(12):e1007150–32.
4. Mullins MC, Hammerschmidt M, Haffter P, Nüsslein-Volhard C. Large-scale mutagenesis in the zebrafish: in search of genes controlling development in a vertebrate. *Curr. Biol.* 1994;4(3):189–202.
5. Van De Weghe JC et al. Mutations in ARMC9, which Encodes a Basal Body Protein, Cause Joubert Syndrome in Humans and Ciliopathy Phenotypes in Zebrafish. *Am. J. Hum. Genet.* 2017;101(1).
6. Duldulao NA, Lee S, Sun Z. Cilia localization is essential for in vivo functions of the Joubert syndrome protein Arl13b/Scorpion. *Development* 2009;136(23):4033–4042.
7. Bachmann-Gagescu R et al. The ciliopathy gene cc2d2a controls zebrafish photoreceptor outer segment development through a role in Rab8-dependent vesicle trafficking. *Hum. Mol. Genet.* 2011;20(20):4041–4055.
8. Boldt K et al. An organelle-specific protein landscape identifies novel diseases and molecular mechanisms. *Nat. Commun.* 2016;7:1–13.
9. Postma FR et al. Serum-induced membrane depolarization in quiescent fibroblasts: activation of a chloride conductance through the G protein-coupled LPA receptor. *EMBO J.* 1996;15(1):63–72.
10. O'Roak BJ et al. Multiplex targeted sequencing identifies recurrently mutated genes in autism spectrum disorders. *Science.* 2012;338(6114):1619–1622.
11. Bielas SL et al. Mutations in INPP5E, encoding inositol polyphosphate-5-phosphatase E, link phosphatidyl inositol signaling to the ciliopathies. *Nat. Genet.* 2009;41(9):1032–1036.
12. Lee JE et al. CEP41 is mutated in Joubert syndrome and is required for tubulin glutamylation at the cilium. *Nat. Genet.* 2012;44(2):193–199.
13. Halbritter J et al. Defects in the IFT-B component IFT172 cause Jeune and Mainzer-Saldino syndromes in humans. *Am. J. Hum. Genet.* 2013;93(5):915–925.
14. Ferland RJ et al. Abnormal cerebellar development and axonal decussation due to mutations in AHI1 in Joubert syndrome. *Nat. Genet.* 2004;36(9):1008–1013.
15. Valente EM et al. Mutations in TMEM216 perturb ciliogenesis and cause Joubert, Meckel and related syndromes. *Nat. Genet.* 2010;42(7):619–625.
16. Edvardson S et al. Joubert syndrome 2 (JBTS2) in Ashkenazi Jews is associated with a TMEM216 mutation. *Am. J. Hum. Genet.* 2010;86(1):93–97.
17. Davis EE et al. TTC21B contributes both causal and modifying alleles across the ciliopathy spectrum. *Nat. Genet.* 2011;43(3):189–196.
18. Coene KLM et al. OFD1 is mutated in X-linked Joubert syndrome and interacts with LCA5-encoded lebercilin. *Am. J. Hum. Genet.* 2009;85(4):465–481.
19. Cantagrel V et al. Mutations in the Cilia Gene ARL13B Lead to the Classical Form of Joubert Syndrome. *Am. J. Hum. Genet.* 2008;83(2):170–179.
20. Arts HH et al. Mutations in the gene encoding the basal body protein RPGRIP1L, a nephrocystin-4 interactor, cause Joubert syndrome. *Nat. Genet.* 2007;39(7):882–888.

21. Baala L et al. The Meckel-Gruber syndrome gene, MKS3, is mutated in Joubert syndrome. *Am. J. Hum. Genet.* 2007;80(1):186–194.

22. Gorden NT et al. CC2D2A is mutated in Joubert syndrome and interacts with the ciliopathy-associated basal body protein CEP290. *Am. J. Hum. Genet.* 2008;83(5):559–571.

23. Tuz K et al. Mutations in CSPP1 cause primary cilia abnormalities and Joubert syndrome with or without Jeune asphyxiating thoracic dystrophy. *Am. J. Hum. Genet.* 2014;94(1):62–72.

24. Srour M et al. Joubert Syndrome in French Canadians and Identification of Mutations in CEP104. *Am. J. Hum. Genet.* 2015;97(5):744–753.

25. Dafinger C et al. Mutations in KIF7 link Joubert syndrome with Sonic Hedgehog signaling and microtubule dynamics. *J. Clin. Invest.* 2011;121(7):2662–2667.

26. Bachmann-Gagescu R et al. Joubert syndrome: a model for untangling recessive disorders with extreme genetic heterogeneity. *J. Med. Genet.* 2015;52(8):514–522.

27. Garcia-Gonzalo FR et al. A transition zone complex regulates mammalian ciliogenesis and ciliary membrane composition. *Nat. Genet.* 2011;43(8):776–784.

28. Sang L et al. Mapping the NPHP-JBTS-MKS Protein Network Reveals Ciliopathy Disease Genes and Pathways. *Cell* 2011;145(4):513–528.

29. Thomas S et al. TCTN3 mutations cause Mohr-Majewski syndrome. *Am. J. Hum. Genet.* 2012;91(2):372–378.

30. Srour M et al. Mutations in C5ORF42 cause Joubert syndrome in the French Canadian population. *Am. J. Hum. Genet.* 2012;90(4):693–700.

31. Sayer JA et al. The centrosomal protein nephrocystin-6 is mutated in Joubert syndrome and activates transcription factor ATF4. *Nat. Genet.* 2006;38(6):674–681.

32. Romani M et al. Mutations in B9D1 and MKS1 cause mild Joubert syndrome: expanding the genetic overlap with the lethal ciliopathy Meckel syndrome. *Orphanet J. Rare Dis.* 2014;9(1):72.

33. Parisi MA et al. The NPHP1 gene deletion associated with juvenile nephronophthisis is present in a subset of individuals with Joubert syndrome. *Am. J. Hum. Genet.* 2004;75(1):82–91.

34. Lee JH et al. Evolutionarily assembled cis-regulatory module at a human ciliopathy locus. *Science.* 2012;335(6071):966–969.

35. Huang L et al. TMEM237 is mutated in individuals with a Joubert syndrome related disorder and expands the role of the TMEM family at the ciliary transition zone. *Am. J. Hum. Genet.* 2011;89(6):713–730.

36. Chong JX et al. The Genetic Basis of Mendelian Phenotypes: Discoveries, Challenges, and Opportunities. *Am. J. Hum. Genet.* 2015;97(2):199–215.

37. Kircher M et al. A general framework for estimating the relative pathogenicity of human genetic variants. *Nat. Genet.* 2014;46(3):310–315.

38. Robinson JT et al. Integrative Genome Viewer. *Nat. Biotechnol.* 2011;29(1):24–6.

39. Alkuraya FS. Autozygome decoded. *Genet. Med.* 2010;12(12):765–771.

40. Alkuraya FS. Discovery of Rare Homozygous Mutations from Studies of Consanguineous Pedigrees. *Curr. Protoc. Hum. Genet.* 2012;75(1):6.12.1–6.12.13.

41. Mefford HC et al. Rare copy number variants are an important cause of epileptic encephalopathies. *Ann. Neurol.* 2011;70(6):974–985.

SUPPLEMENTAL FIGURES

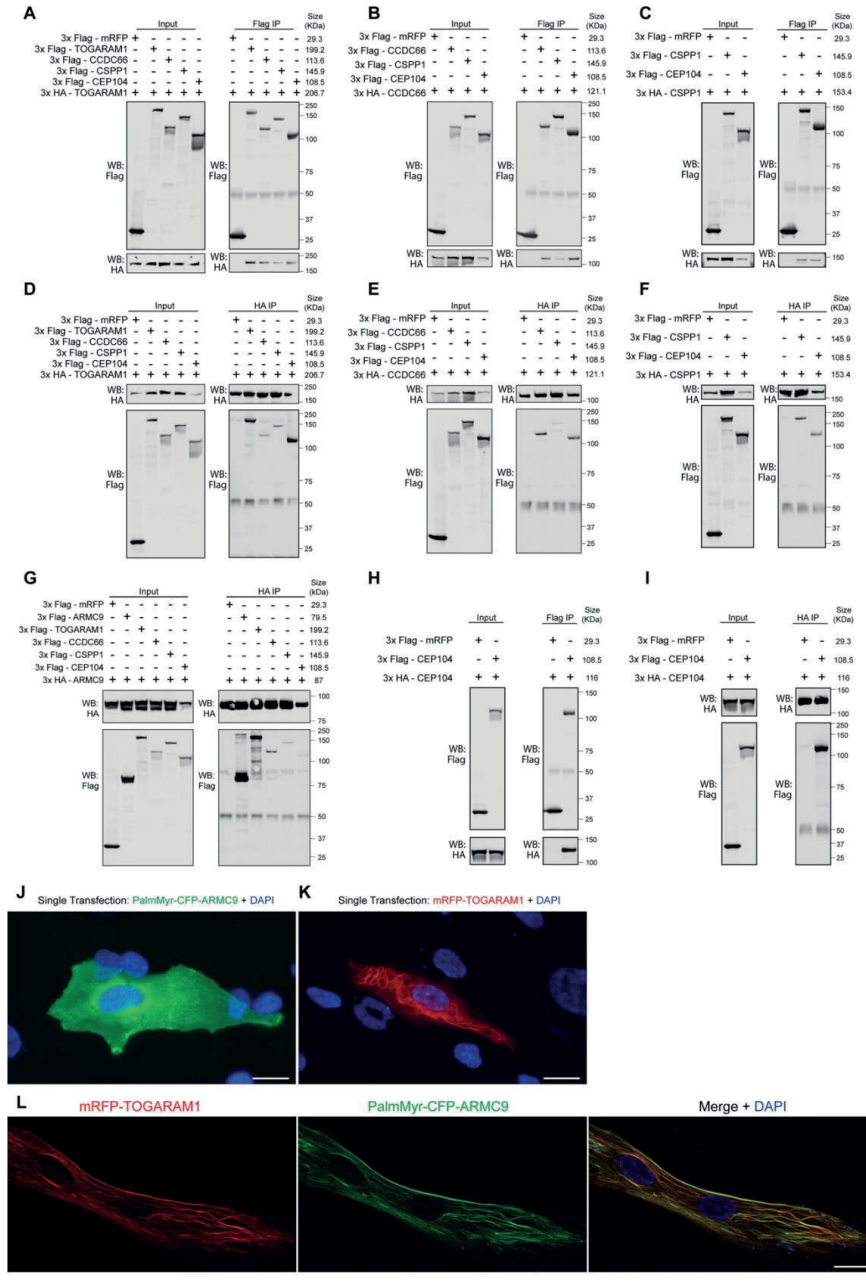

◀**Supplemental Figure 1 Validation of ARMC9 interactome. (A-I)** Reciprocal co-IPs of 3xFlag-ARMC9, 3xFlag-TOGARAM1, 3xFlag-CCDC66, 3xFlag-CSPP1, and 3xFlag-CEP104 with 3xHA-ARMC9, 3xHA-TOGARAM1, 3xHA-CCDC66, 3xHA-CSPP1, and 3xHA-CEP104. 3xFlag-mRFP was used as a negative control in each experiment. Pairs of Flag and HA tagged constructs were co-transfected into HEK293T cells, which were then lysed and subjected to pull down with either Flag or HA beads. Western blots of the pulldowns were probed with Flag and HA antibodies to visualize the interaction partners. The experiments were performed in triplicate. The reciprocal experiment of **(G)**, the Flag co-IP, is shown in Figure 1F. **(J-K)** Single transfections of PalmMyr-CFP-ARMC9 (green in **(J)**) and mRFP-TOGARAM1 (red in **(K)**) shows the localization of each tagged proteins in the absence of the other. **(L)** Co-expression of mRFP-TOGARAM1 and PalmMyr-CFP-ARMC9 shows localization consistent with a subset of cytoplasmic microtubules. Scale bar indicates 20 µm.

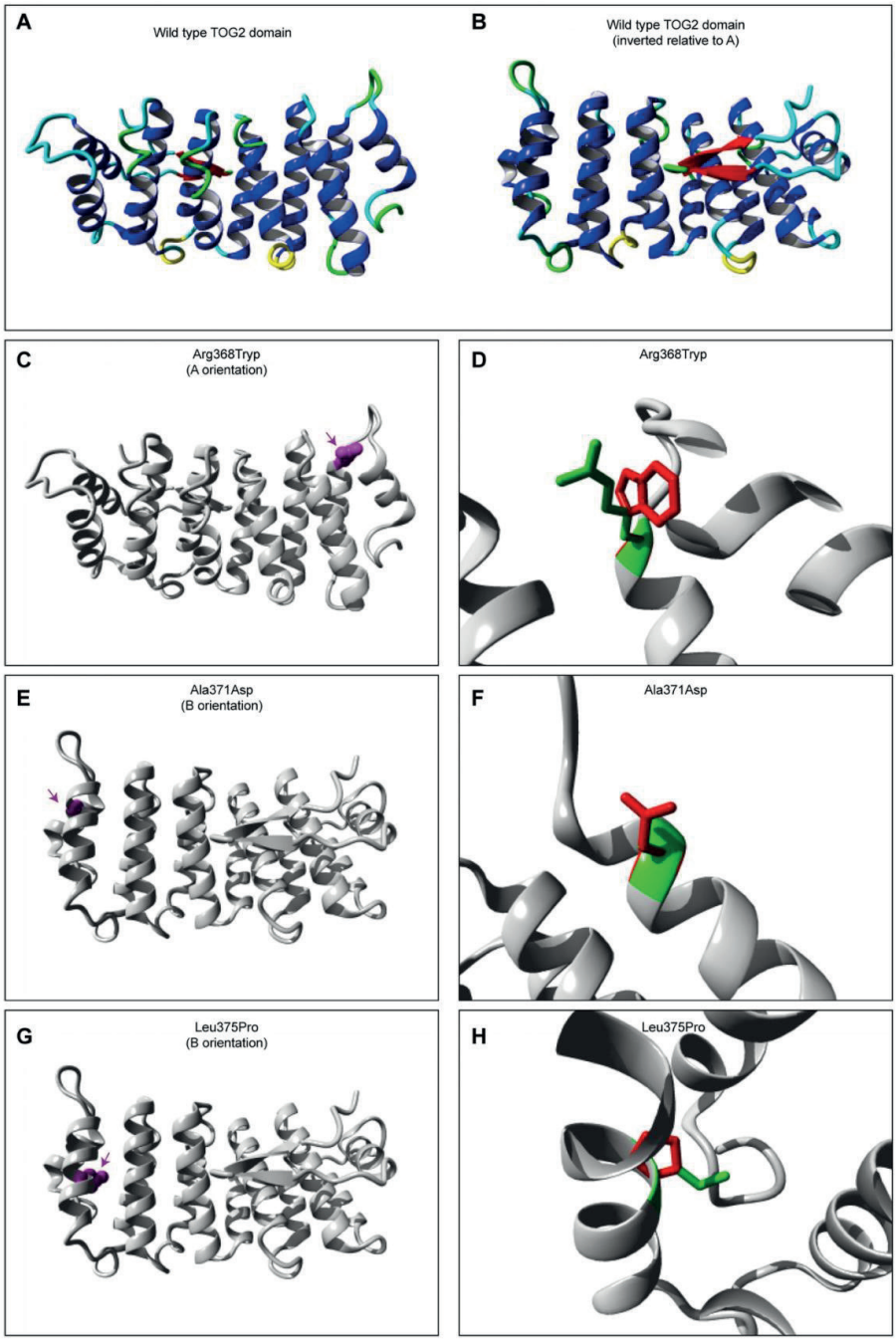
A
Wild type TOG2 domain
B
Wild type TOG2 domain
(inverted relative to A)
C
Arg368Tryp
(A orientation)
D
Arg368Tryp
E
Ala371Asp
(B orientation)
F
Ala371Asp
G
Leu375Pro
(B orientation)
H
Leu375Pro

◀**Supplemental Figure 2 *In silico* modeling of the TOG2 variants. (A-B)** Ribbon model (two views) of the wild-type TOGARAM1 TOG2 domain generated using HOPE. Alpha-helices are blue, beta-strand is red, turns are green, 3/10 helix is yellow, and random coil is cyan. (B) view is the inversion of wild-type TOGARAM1 TOG2 domain structure of as compared to (A) view **(C)** p. Arg368Trp missense variant in the TOG2 domain in ribbon-presentation generated using HOPE. **(D)** Close up of the side chain with wild-type arginine (green) and variant tryptophan (red). **(E)** p. Ala371Asp missense variant in the TOG2 domain. **(F)** Close up of the side chain with wild-type alanine (green) and variant aspartic acid (red). **(G)** p.Leu375Pro missense variant modeled in the TOG2 domain. **(H)** Close up of the side chain of both wild-type leucine (green) and variant proline (red). For (C, E, F) the TOG2 is shown in grey, the side chain of the mutated residue is shown in magenta. A magenta arrow indicates the location of the variant.

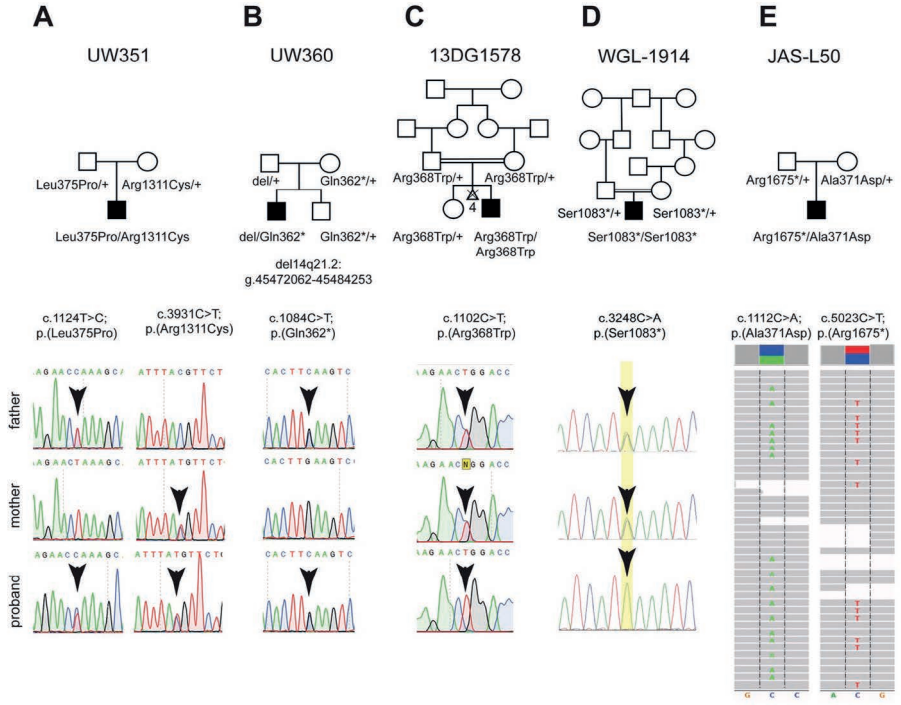

Supplemental Figure 3 Segregation and Sanger confirmation of *TOGARAM1* variants. (A) In UW351, Leu375Pro is inherited from father and Arg1311Cys is inherited from mother. **(B)** In UW360, Gln362* is inherited from mother and a multi-exon deletion is inherited from father. See Figure 2C for validation and paternal segregation of the deletion. **(C)** In 13DG1578, both parents are heterozygous for Arg368Trp and the proband is homozygous at this position. **(D)** In WGL-1914, both parents are heterozygous for Ser1083* and the proband is homozygous at this position. **(E)** In JAS-L50, Ala371Asp is inherited from the mother and the father was not available. Visualization of the next-generation sequencing data for the proband in the Integrated Genome Viewer confirms that the proband carries both pathogenic variants. Grey bars indicate individual reads with pathogenic variants in green and red; nucleotides at the bottom are the reference allele. Variants are indicated with arrows on the electropherograms.

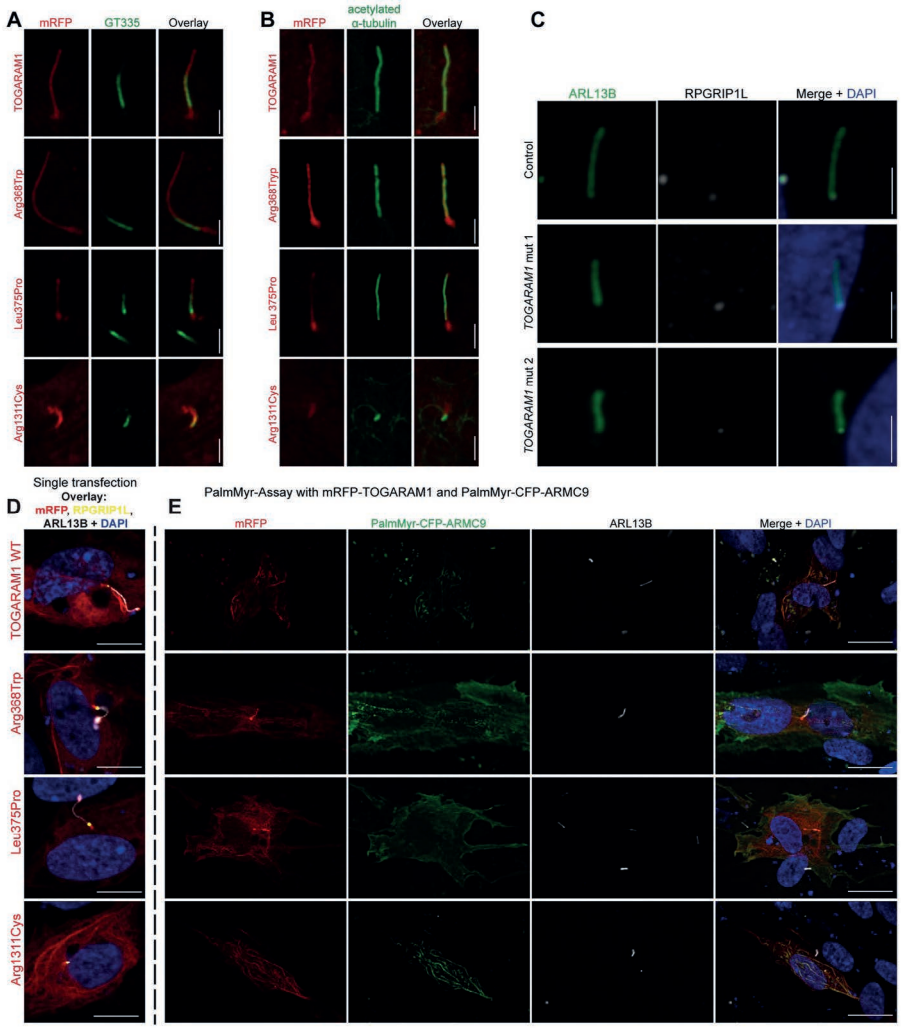

Supplemental Figure 4 Impact of *TOGARAM1* variants on localization, transition zone, and ARMC9 interaction. (A-B) Wild-type and variant mRFP-tagged TOGARAM proteins co-localize with polyglutamylated (A) and acetylated tubulin (B) in transfected hTERT-RPE1 *TOGARAM1* mutant cells. GT335 antibody (green in (A)) marks the glutamylated portion of the ciliary axoneme and acetylated alpha-tubulin antibody (green in (B)) marks the entire ciliary axoneme. All images are representative of 3 independent imaging experiments. Scale bars are 2µm. **(C)** Images of cilia from control and engineered *TOGARAM1* mutant hTERT-RPE1 cell lines marked with ARL13B antibody (green, ciliary membrane) and RPGRIP1L antibody (white, transition zone). Scale bars are 2µm. **(D)** PalmMyr assay with PalmMyr-CFP-ARMC9 and mRFP-TOGARAM1 expressed in control hTERT-RPE1 cells. Single transfections of mRFP-TOGARAM1 wild-type and variants show characteristic localization in the absence of PalmMyr-CFP-ARMC9 (mRFP (red), ARL13B (white), RPGRIP1L (yellow), and DAPI (blue)). Scale bar is 10µm. **(E)** Co-expression of mRFP-TOGARAM1 and PalmMyr-CFP-ARMC9 (mRFP (red), ARL13B (white), CFP (green), and DAPI (blue)). Wild-type and Arg1311Cys TOGARAM1 colocalize with PalmMyr-CFP-ARMC9, indicating an interaction, while Arg368Trp and Leu375Pro show little to no specific colocalization. Scale bar is 20µm.

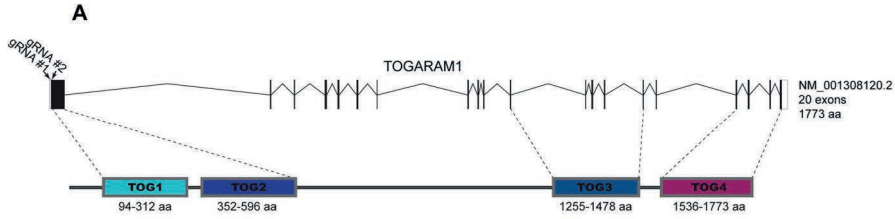

B

hTERT-RPE1 mut lines

NM_001308120.2	allele 1	allele 2
TOGARAM1 mut 1	c.[2_269del;270dup]	c.[2_269inv]
TOGARAM1 mut 2	c.[-33_314del]	c.[2_269inv; 269_270insTC]

Supplemental Figure 5 CRISPR/Cas9 edited *TOGARAM1* hTERT-RPE1 mutant lines. (A) Schematic representation of the TOG array aligned with the genomic region encoding *TOGARAM1*. The target sites of gRNA 1 and gRNA 2 are indicated by arrows in exon 1. They are predicted to cut at cDNA position 2 and 269 respectively. This portion of exon 1 encodes the region of the protein immediately before the TOG1 domain. **(B)** *TOGARAM1* mutant 1 harbors a 267 base pair deletion with a single base pair duplication in one allele and a 267 base pair inversion in the other allele, both occurring in exon 1: NM_015091.2:c.[2_269del;270dup]; [2_269inv]. *TOGARAM1* mutant line 2 harbors a 347 base pair deletion in one allele and a 267 base pair inversion with 2 base pair insertion in the other allele, both occurring in exon 1: NM_015091.2:c.[-33_314del]; [2_269inv; 269_270insTC].

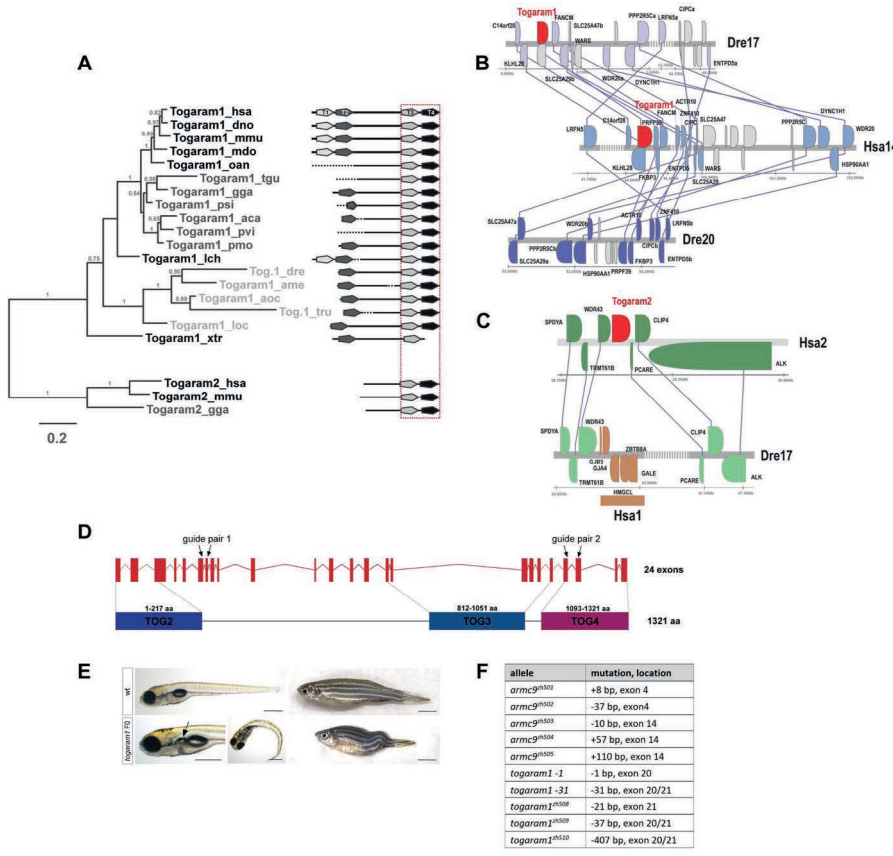

allele	mutation, location
armc9^{ih501}	+8 bp, exon 4
armc9^{ih502}	-37 bp, exon4
armc9^{ih503}	-10 bp, exon 14
armc9^{ih504}	+57 bp, exon 14
armc9^{ih505}	+110 bp, exon 14
togaram1 -1	-1 bp, exon 20
togaram1 -31	-31 bp, exon 20/21
togaram1^{ih508}	-21 bp, exon 21
togaram1^{ih509}	-37 bp, exon 20/21
togaram1^{ih510}	-407 bp, exon 20/21

Supplemental Figure 6 Togaram1 phylogeny, synteny and zebrafish F0 phenotypes. (A) Phylogenetic analysis of the C-terminal part (red box) of *TOGARAMs* in different vertebrate species revealed a clear phylogenetic separation of *TOGARAM1* and *TOGARAM2*. The following species were used for phylogeny: *Anolis carolinensis* (aca), *Astyanax mexicanus* (ame), *Amphiprion ocellaris* (aoc), *Dasypus novemcinctus* (dno), *Danio rerio* (dre), *Gallus gallus* (gga), *Homo sapiens* (hsa), *Latimeria chalumnae* (lch), *Lepisosteus oculatus* (loc), *Monodelphis domestica* (mdo), *Mus musculus* (mmu), *Ornithorhynchus anatinus* (oan), *Pelodiscus sinensis* (psi), *Pogona vitticeps* (pvi), *Taeniopygia guttata* (tgu), *Takifugu rubripes* (tru), *Xenopus tropicalis* (xtr). Dotted lines in the domain representation represent sequence strings so far not covered in the corresponding genome assemblies. In the phylogenetic tree mammals are given in black, amphibians, birds, turtles and reptiles in dark gray and teleosts in light gray. The scale bars represent the distance where 20% of the amino acids are changed. **(B)** Synteny analysis confirms orthology between human and zebrafish *TOGARAM1*. The human *TOGARAM1* gene is located on chromosome 14. Corresponding chromosomal regions to the human chromosome 14 are located on zebrafish chromosomes 17 and 20. In contrast to the zebrafish chromosome 17 where a *TOGARAM1* gene can be readily identified, zebrafish chromosome 20 lacks a corresponding ortholog, suggesting that in the case of *TOGARAM1* no zebrafish duplicate of this gene has been retained. **(C)** Synteny analysis of human *TOGARAM2* shows no corresponding gene in zebrafish. Interestingly, no ortholog of human *TOGARAM2* (located on human chromosome 2) is present in the zebrafish genomic region where the genes flanking *TOGARAM2* are located. **(D)** Zebrafish *togaram1* exons and corresponding protein with domains. Red dashed lines represent unknown intron size. Location of sgRNAs for genome editing are indicated: two different sgRNAs per target region were co-injected to generate larger deletions. **(E)** Phenotype of *togaram1* F0 mosaic zebrafish: Larvae have kidney cysts (arrow) and body curvature. Adults develop scoliosis. Scale bars are 500µm for larvae and 5mm for adults. **(F)** Alleles generated with CRISPR/Cas9 for *armc9* and *togaram1*.

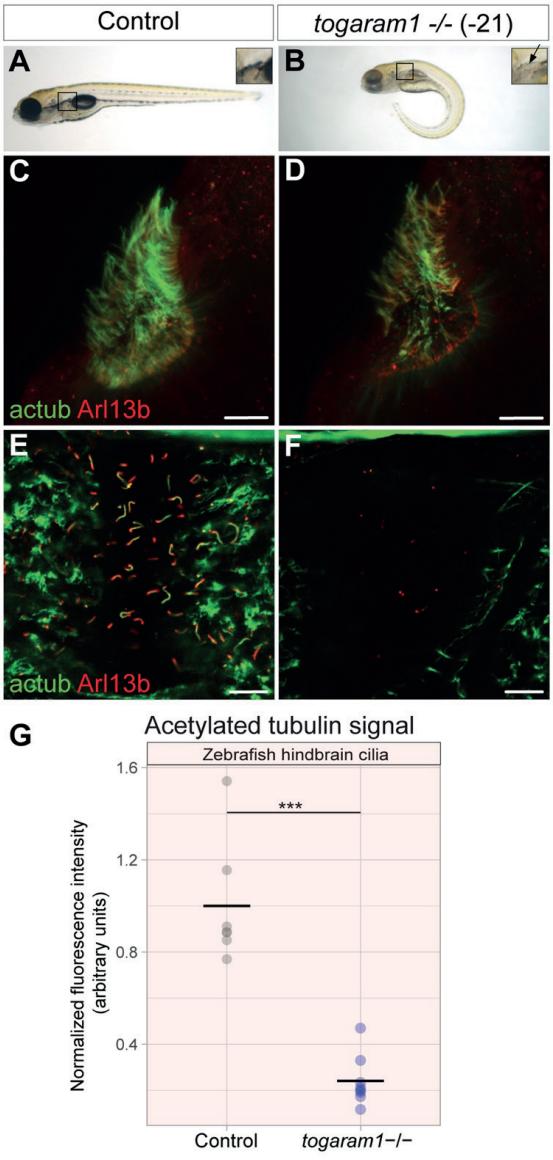

◀**Supplemental Figure 7 Phenotypes of *togaram1*^{zh508} in-frame mutant zebrafish. (A-B)** *togaram1*-/- (-21) larvae have kidney cysts and curved body shape compared to wild-type (A). Scale bars are 500µm. **(C-D)** Wild-type and **(D)** Acetylated tubulin (green) and Arl13b (red) immunofluorescence of 3 dpf *togaram1*-/- (-21) zebrafish nose pits shows decreased numbers of both motile and primary cilia compared to wild-type (C). **(E-F)** Acetylated tubulin (green) and Arl13b (red) immunofluorescence of hindbrain ventricles show a clear decrease in cilia number and acetylation in *togaram1*-/- (-21) compared to wild-type (E). Scale bars for (C-F) are 10µm. **(G)** Quantification of acetylated tubulin of cilia in hindbrain ventricles, $p<0.001$ using Student's t-test. Zebrafish controls are wt, +/+ or +/- siblings of -/-.

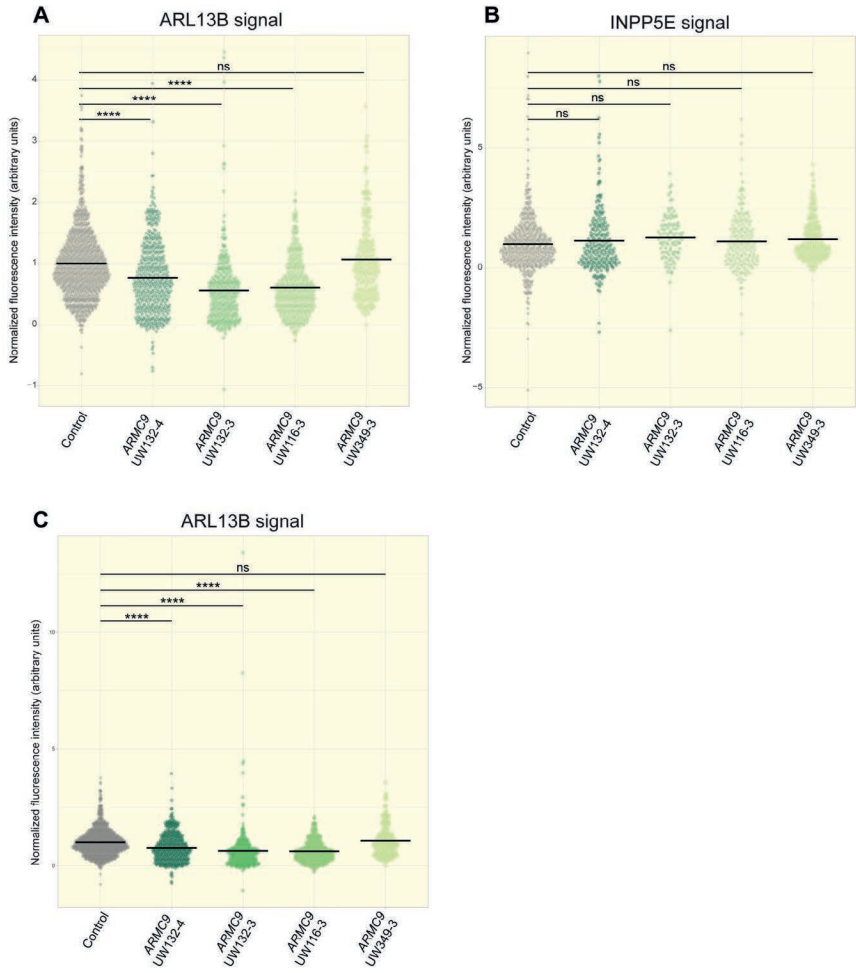

Supplemental Figure 8 Ciliary INPP5E levels are maintained across *ARMC9* patient fibroblast lines. (A) Normalized ciliary ARL13B fluorescence intensity in control and *ARMC9* patient fibroblasts. >200 cilia were assessed per line for measurements. (control = 935 cilia, UW132-4 = 472 cilia, UW132-3 = 337 cilia, UW116-3= 477 cilia, and UW349-3= 208 cilia). p<0.0001 between control and *ARMC9* patient cilia UW132-4, UW132-3, UW116-3, by one-way ANOVA and Dunnett's multiple comparison test. Results were not significant for control versus UW349-3 by one-way ANOVA. **(B)** Normalized ciliary INPP5E fluorescence intensity in control and *ARMC9* patient fibroblasts. >99 cilia were assessed per line for measurements. (control = 471 cilia, UW132-4 = 248 cilia, UW132-3 = 100 cilia, UW116-3= 180 cilia, and UW349-3= 194 cilia). Results were not significant as assessed by one-way ANOVA. Dunett's multiple comparison test yielded the following p values: control versus UW132-4 p= 0.4373, UW132-3 p=0.1701, UW116-3 p=0.7163, UW349-3 p=0.2038. **(C)** ARL13B intensity dataset including outlier data points that are not included in the other graphs, but are included in the statistical analyses. P-value symbols: ns p>0.05, ****p≤0.0001. Bars represent the mean.

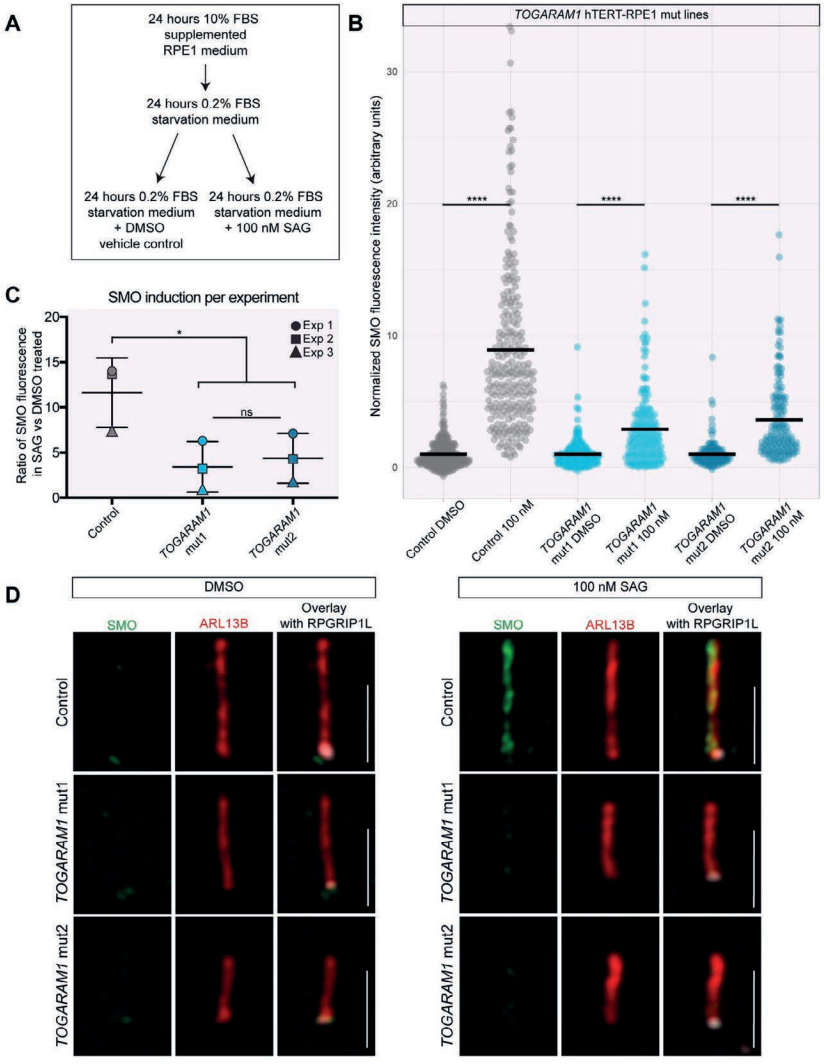

Supplemental Figure 9 SMO ciliary translocation is impaired in TOGARAM1 mutant cell lines. (A) Hh assay schematic. **(B)** Intensity values of SMO localization in the ciliary compartment between DMSO and 100 nM SAG treated control and TOGARAM1 mutant cell lines. >150 cilia were assessed for each condition and pooled from 3 independent experiments (For the control line, N=300 for DMSO and N=248 for SAG treatment, for TOGARAM1 mut1 N=210 for DMSO and N=165 for SAG treatment, and for TOGARAM1 mut2 N=157 for DMSO and N=162 for SAG treatment). Results were statistically significant as assessed by the Kruskal-Wallis test, multiple comparisons were corrected for using Dunn's test. $p<0.0001$ for DMSO versus 100 nM SAG treatment in all lines. **(C)** The median ratios of SMO induction levels in response to SAG treatment across experiments. The central bar represents the mean of 3 independent experiments, the error bars display the standard deviation. Results were statistically assessed by the Kruskal-Wallis test with Dunn's test for multiple testing correction. $p=0.02$ for induction of TOGARAM1 mut 1 line and TOGARAM1 mut 2 line versus induction in the control. No significant difference between the two *TOGARAM1* mutant lines was observed. **(D)** Representative immunofluorescence images of SMO (green) localization in DMSO and 100 nM SAG treated cells. ARL13B is shown in red (ciliary membrane) and RPGRIP1L is shown in white (transition zone). Scale bar is 2µm.

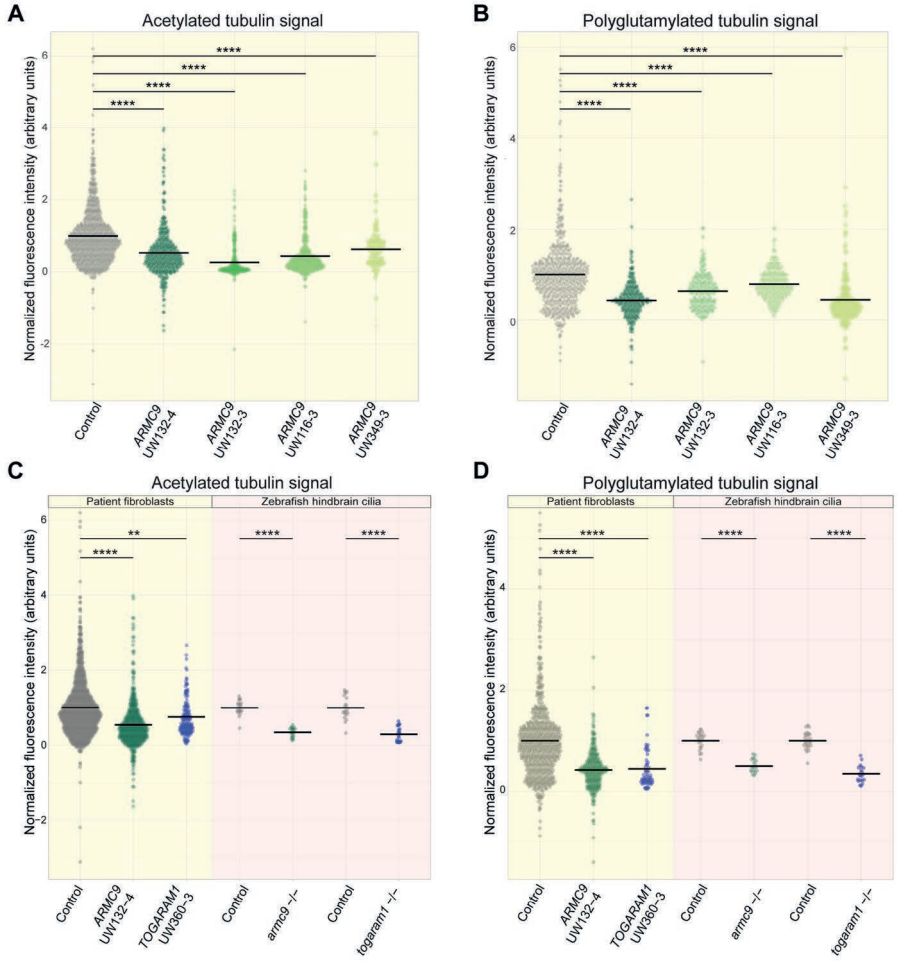

Supplemental Figure 10 Aberrant post-translational modifications across *ARMC9* patient fibroblast lines. (A) Normalized acetylated alpha-tubulin fluorescence intensity in control and *ARMC9* patient fibroblasts. >80 cilia were assessed per line for measurements. (control = 848 cilia, UW132-4 = 397 cilia, UW132-3 = 258 cilia, UW116-3= 399 cilia, and UW349-3= 84 cilia). p<0.0001 between control and patient cilia using one-way ANOVA and Dunnett's multiple comparison test. **(B)** Normalized polyglutamylated tubulin fluorescence intensity in control and *ARMC9* patient fibroblasts. >150 cilia were assessed per line for measurements. (control = 557 cilia, UW132-4 = 262 cilia, UW132-3 = 179 cilia, UW116-3= 253 cilia, and UW349-3= 194 cilia). p<0.0001 between control and patient cilia using one-way ANOVA and Dunnett's multiple comparison test. **(C)** Full graphs of the dot plots shown in Figure 7E-F showing all data points. P-value symbols: **p≤0.01, ****, p≤ 0.0001. Bars represent the mean.

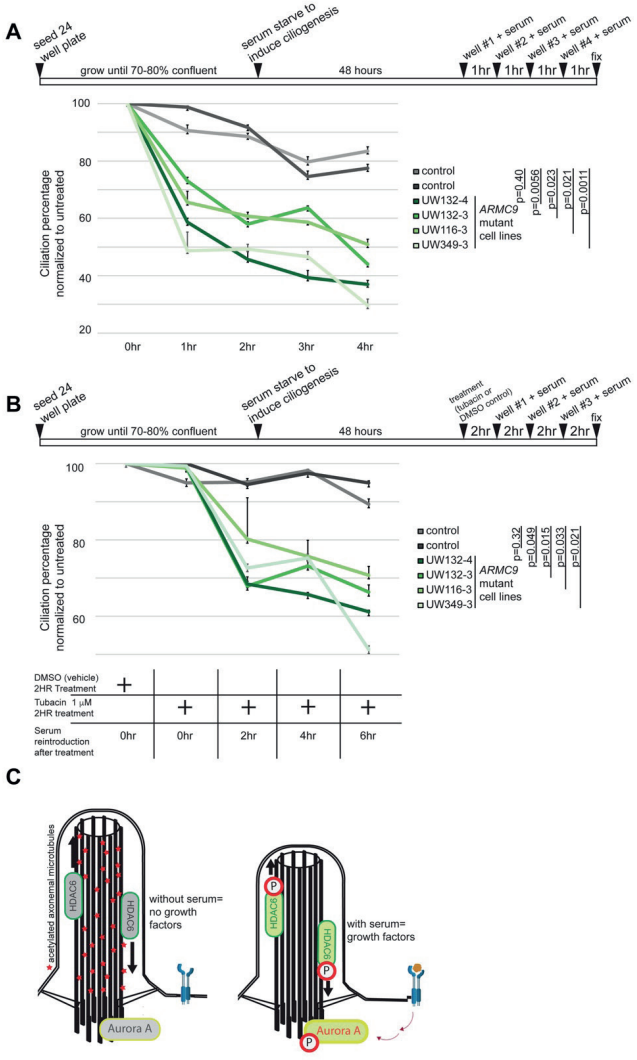

Supplemental Figure 11 *ARMC9* patient fibroblasts exhibit reduced cilium stability. (A) Serum readdition assay schematic and time course showing ciliation percentages normalized to serum-starved cells for each cell line. Note accelerated loss of cilia in all *ARMC9* lines. **(B)** Serum readdition assay schematic with HDAC6 inhibitor (Tubacin) treatment to block HDAC6 activity (to test whether the faster resorption observed in ARMC9 lines observed in A is caused by overactive deacetylation) and time course showing ciliation percentages normalized to vehicle-treated serum-starved cells for each cell line. For (A) and (B), error bars represent 95% confidence intervals and Student's t-test with unequal variance was used to test for differences in slope modeled by linear regression. Note that HDAC6-inhibition does not rescue the accelerated loss of cilia in *ARMC9* lines, but does inhibit resorption in controls. **(C)** Schematic model of HDAC6 activity in ciliary disassembly. Upon initiation of resorption, histone deacetylase 6 (HDAC6) becomes activated and deacetylates ciliary microtubules, a required step for resorption.

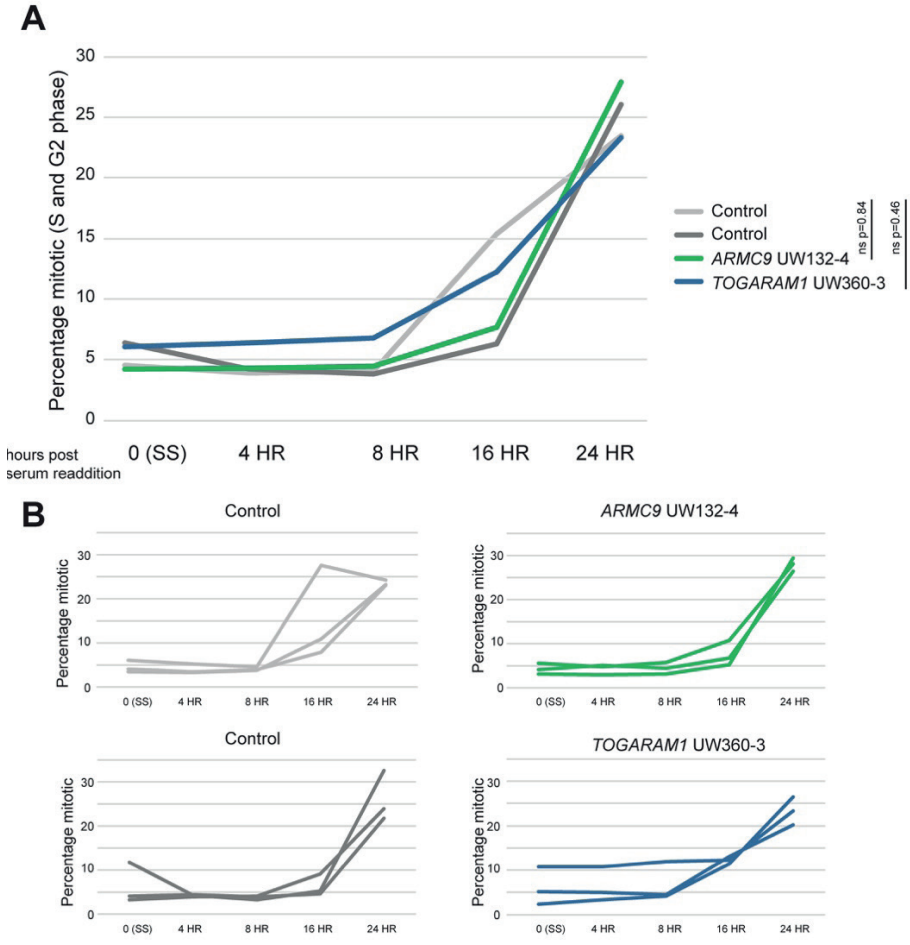

Supplemental Figure 12 *ARMC9* and *TOGARAM1* patient fibroblasts cells reenter the cell cycle normally after serum readdition. (A) Average of three experiments assessing cell cycle stage after serum readdition. 10,000 DAPI-stained nuclei were assessed at each time point by flow cytometry. **(B)** Individual experiments for each cell line.

University of Washington Center for Mendelian Genomics (UW-CMG)

Michael J. Bamshad[1,2]; Suzanne M. Leal[3]; and Deborah A. Nickerson[1]; Peter Anderson[1]; Tamara J. Bacus[1]; Elizabeth E. Blue[1]; Kati J. Buckingham[1]; Jessica X. Chong[1]; Colleen P. Davis[1]; Christopher Frazar[1]; Danielle Giroux[1]; William W. Gordon[1]; Martha Horike-Pyne[1]; Jameson R. Hurless[1]; Gail P. Jarvik[1]; Eric Johanson[1]; Tom Kolar[1]; Melissa P. MacMillan[1]; Colby T. Marvin[1]; Sean McGee[1]; Daniel J. McGoldrick[1]; Betselote Mekonnen[1]; Patrick M. Nielsen[1]; Karynne Patterson[1]; Ben Pelle[1]; Aparna Radhakrishnan[1]; Matthew A. Richardson[1]; Peggy D. Robertson[1]; Erica L. Ryke[1]; Aimee M. Schantz[1]; Isabelle Schrauwen[3]; Kathryn M. Shively[1]; Joshua D. Smith[1]; Monica Tackett[1]; Machiko S. Threlkeld[1]; Marc Wegener[1]; Jeffrey M. Weiss[1]; Marsha M. Wheeler[1]; Janson J. White[1]; Qian Yi[1]; Di Zhang[3]; and Xiaohong Zhang[1]

1. University of Washington, Seattle, Washington, USA
2. Seattle Children's Hospital, Seattle, Washington, USA
3. Columbia University, New York City, New York, USA

Genomics England Research Consortium

Ambrose, J. C. [1]; Arumugam, P.[1]; Baple, E. L. [1]; Bleda, M. [1]; Boardman-Pretty, F. [1,2]; Boissiere, J. M. [1]; Boustred, C. R. [1]; Brittain, H.[1]; Caulfield, M. J.[1,2]; Chan, G. C. [1]; Craig, C. E. H. [1]; Daugherty, L. C. [1]; de Burca, A. [1]; Devereau, A. [1]; Elgar, G. [1,2]; Foulger, R. E. [1]; Fowler, T. [1]; Furió-Tarí, P. [1]; Hackett, J. M. [1]; Halai, D. [1]; Hamblin, A.[1]; Henderson, S.[1,2]; Holman, J. E. [1]; Hubbard, T. J. P. [1]; Ibáñez, K.[1,2]; Jackson, R. [1]; Jones, L. J. [1,2]; Kasperaviciute, D. [1,2]; Kayikci, M. [1]; Kousathanas, A. [1]; Lahnstein, L. [1]; Lawson, K. [1]; Leigh, S. E. A. [1]; Leong, I. U. S. [1]; Lopez, F. J. [1]; Maleady-Crowe, F. [1]; Mason, J. [1]; McDonagh, E. M. [1,2]; Moutsianas, L. [1,2]; Mueller, M. [1,2]; Murugaesu, N. [1]; Need, A. C. [1,2]; Odhams, C. A. [1]; Patch, C. [1,2]; Perez-Gil, D. [1]; Pereira, M. B.[1]; Polychronopoulos, D. [1]; Pullinger, J. [1]; Rahim, T. [1]; Rendon, A. [1]; Riesgo-Ferreiro, P.[1]; Rogers, T. [1]; Ryten, M. [1]; Savage, K. [1]; Sawant, K. [1]; Scott, R. H. [1]; Siddiq, A. [1]; Sieghart, A. [1]; Smedley, D. [1,2]; Smith, K. R. [1,2]; Smith, C. S. [1]; Sosinsky, A. [1,2]; Spooner, W. [1]; Stevens, H. E. [1]; Stuckey, A. [1]; Sultana, R. [1]; Thomas, E. R. A. [1,2]; Thompson, S. R. [1]; Tregidgo, C. [1]; Tucci, A. [1,2]; Walsh, E. [1]; Watters, S. A. [1]; Welland, M. J. [1]; Williams, E. [1]; Witkowska, K. [1,2]; Wood, S. M. [1,2]; Zarowiecki, M.[1]

1. Genomics England, London, UK
2. William Harvey Research Institute, Queen Mary University of London, London, UK.

Full uncut gels and blots

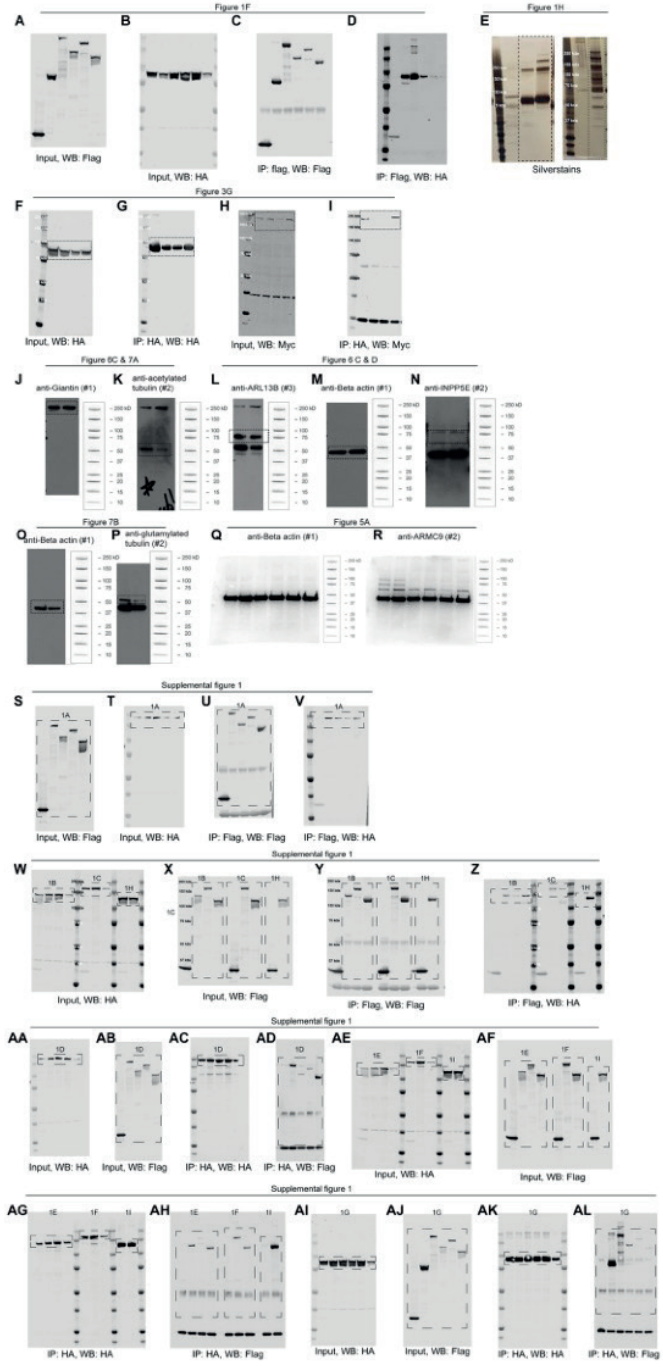

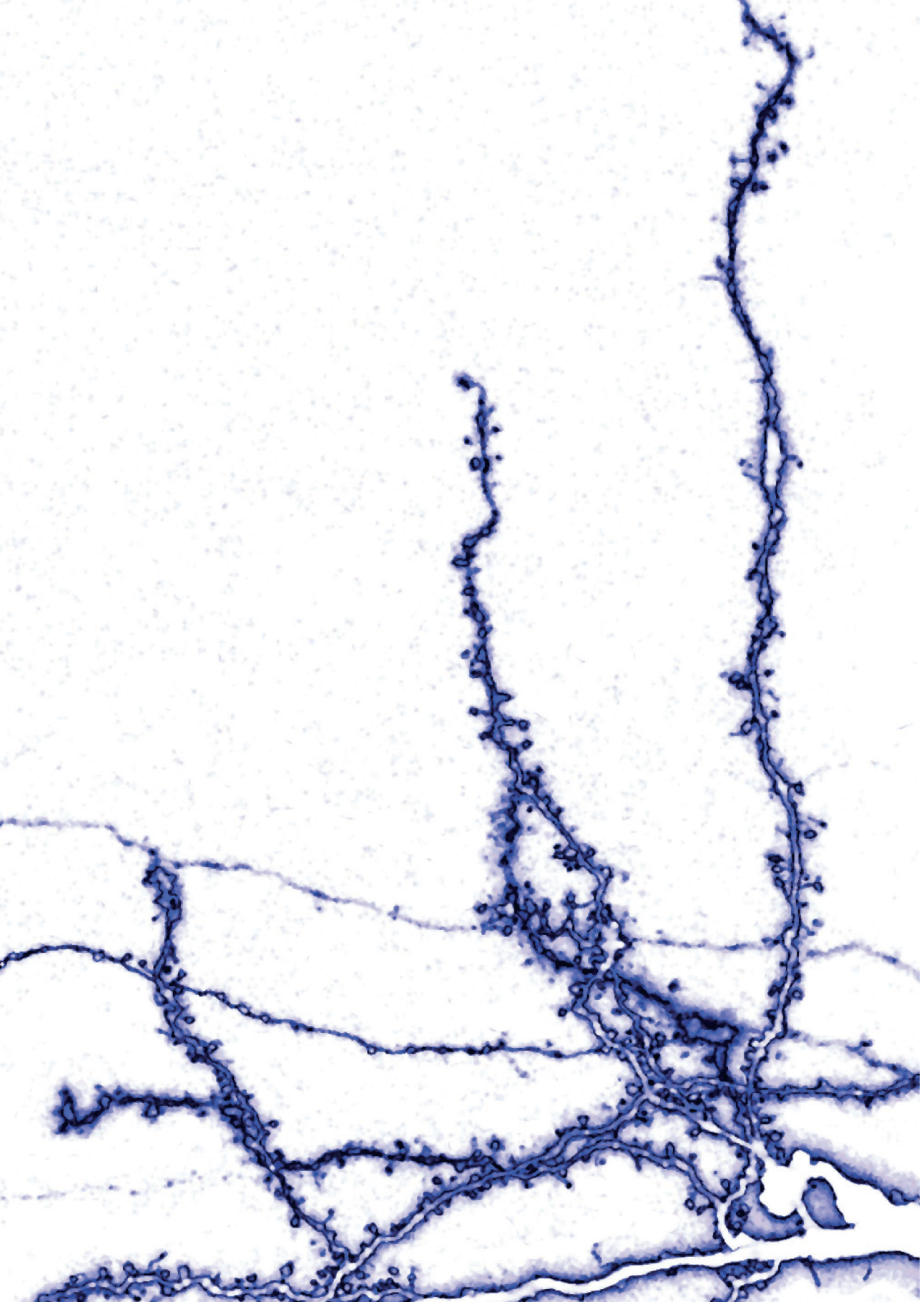

CHAPTER 4

De novo loss of function mutations in USP9X cause a female specific recognizable syndrome with developmental delay and distinct congenital malformations

Margot R.F. Reijnders[1,21], Vasilios Zachariadis[2,21], **Brooke Latour**[1,3,21], Lachlan Jolly[4,21], Grazia M. Mancini[5], Rolph Pfundt[1], Ka Man Wu[1], Conny M.A. van Ravenswaaij-Arts[6], Hermine E. Veenstra-Knol[6], Britt-Marie M. Anderlid[2,7], Stephen A. Wood[8], Sau Wai Cheung[9], Angela Barnicoat[10], Frank Probst[9], Pilar Magoulas[9], Alice S. Brooks[5], Helena Malmgren[2,7], Arja Harila-Saari[11], Carlo M. Marcelis[1], Maaike Vreeburg[12], Emma Hobson[13], V. Reid Sutton[9], Zornitza Stark[14], Julie Vogt[15], Nicola Cooper[16], Jiin Ying LIM[17], Sue Price[18], Angeline Hwei Meeng LAI[17], Deepti Domingo[19], Bruno Reversade[20], the DDD study, Jozef Gecz[4], Christian Gilissen[1], Han G. Brunner[1,12], Usha Kini[18,22], Ronald Roepman[1,22]*, Ann Nordgren[2,7,22], Tjitske Kleefstra[1,22]*

[22] These authors contributed equally

1. Department of Human Genetics, Radboud University Medical Center, 6500 HB Nijmegen, The Netherlands.
2. Department of Molecular Medicine and Surgery and Centre for Molecular Medicine, Karolinska Institutet, 171 76 Stockholm, Sweden
3. Radboud Institute for Molecular Life Sciences, Radboud University Medical Center, 6500 HB Nijmegen, The Netherlands.
4. Neurogenetics, School of Medicine and the Robinson Research Institute, SA 5005 the University of Adelaide, Adelaide, Australia
5. Department of Clinical Genetics, Erasmus MC, Sophia Children's Hospital, 3000 CA Rotterdam, The Netherlands
6. University of Groningen, University Medical Center of Groningen, 9700 RB Department of Genetics, Groningen, The Netherlands
7. Departement of Clinical Genetics, Karolinska University Hospital, 171 76 Stockholm, Sweden
8. The Eskitis Institute for Drug Discovery, Griffith University, QLD 4111 Brisbane, Australia
9. Department of Molecular and Human Genetics, Baylor College of Medicine, One Baylor Plaza, Houston, TX, 77030, USA
10. Great Ormond Street Hospital for Children NHS Foundation Trust, London WC1N 3JH, UK
11. Department of Women's and Children's Health, Karolinska University Hospital, 171 76 Stockholm
12. Department of Clinical Genetics, Maastricht University Medical Center, 6202 AZ Maastricht, The Netherlands
13. Department of Clinical Genetics, Chapel Allerton Hospital, Leeds, LS7 4SA, UK
14. Victorian Clinical Genetics Services, Murdoch Children's Research Institute, Melbourne, VIC 3052 Australia
15. West Midlands Regional Genetics Service, Clinical Genetics Unit, Birmingham Women's Hospital, Birmingham, B15 2TG, UK
16. Clinical Genetics Unit, Birmingham Women's NHS Foundation Trust, Mindelsohn Way, Edgbaston, Birmingham, B15 2G, UK
17. KK Women's and Children's Hospital, 229899 Singapore, Singapore
18. Department of Clinical Genetics, Oxford University Hospitals NHS Foundation Trust, Oxford OX3 7LE, UK
21. These authors contributed equally
19. School of Biological Sciences, The University of Adelaide, Adelaide 5000, Australia
20. Institute of Medical Biology, A(*)STAR, 138648 Singapore, Singapore

Published: Am J Hum Genet. 2016 Feb 4;98(2):373-81. doi: 10.1016/j.ajhg.2015.12.015

ABSTRACT

Mutations in over a hundred genes have been reported to cause X-linked recessive intellectual disability (ID) mainly in males. In contrast, the number of identified X-linked genes in which de novo mutations specifically cause ID in females is limited. Here, we report seventeen females with de novo loss of function mutations in USP9X, encoding a highly conserved deubiquitinating enzyme. The females in our study have a specific phenotype that includes ID/developmental delay (DD), characteristic facial features, short stature and distinct congenital malformations comprising choanal atresia, anal abnormalities, post-axial polydactyly, heart defects, hypomastia, cleft palate/bifid uvula, progressive scoliosis and structural brain abnormalities. Four females from our cohort were identified by targeted genetic testing as their phenotype was suggestive for USP9X mutations. In several females pigment changes along Blaschko lines and body asymmetry were observed which is likely related to differential (escape from) X-inactivation between tissues. Expression studies on both mRNA and protein level in affected female-derived fibroblasts showed significant reduction of USP9X level, confirming the loss of function effect of the identified mutations. Given that some features of affected females are also reported in known ciliopathy syndromes, we examined the role of USP9X in the primary cilium and found that endogenous USP9X localizes along the length of the ciliary axoneme, indicating that its loss of function could indeed disrupt cilium-regulated processes. Absence of dysregulated ciliary parameters in affected female-derived fibroblasts however points towards spatiotemporal specificity of ciliary USP9X (dys-)function.

REPORT

X-linked intellectual disability (ID) with presumed recessive inheritance pattern is shown to be caused by mutations in over a hundred genes [1; 2] Most families display a clear X-linked segregation pattern, in which males are affected while females are unaffected or mildly affected carriers.[3-5] In contrast, the number of identified X-linked genes in which de novo mutations cause ID specifically in females is limited.

Using whole exome sequencing (WES), SNP array, CGH array and CytoScan HD array in a diagnostic setting as described before[6-11], we identified thirteen de novo loss of function mutations in USP9X [Ubiquitin-specific protease 9, MIM 300072, RefSeq: NM_001039590.2] in females with ID/developmental delay (DD) and multiple congenital malformations (Figure 1A, B; Table S1). Female 7 was previously reported as part of a large study sequencing individuals with ID, congenital anomalies and/or autism with a targeted gene panel.[9] Written consent was obtained from the legal guardians for all females and the study was given IRB approval. We recognized a similar pattern of facial characteristics, congenital malformations and brain abnormalities in these females. Four additional affected females were identified as their phenotype was suggestive for USP9X mutations. Subsequently, de novo protein-truncating mutations and intragenic USP9X deletions were duly demonstrated by Sanger sequencing, WES or CytoScan HD array (Figure 1A, B, Table S1), illustrating the clinical recognizability of this new syndrome. All females (age ranging 2 years 7 months – 23 years) with de novo mutations shared a distinct phenotype. They showed mild to moderate ID with motor and language delay, short stature, hearing loss and distinct congenital malformations, notably choanal atresia, asymmetric hypomastia, cleft palate/bifid uvula, heart defects, progressive scoliosis, post-axial polydactyly and anal abnormalities (Table 1, Table S2, supplemental case reports). Shared facial characteristics included prominent forehead, low nasal bridge, prominent nose with flared alae nasi, thin upper lip, smooth and long philtrum and low set, posteriorly rotated and dysplastic ears (Figure 2A). In addition to the USP9X variant, female 5 also harbored a de novo variant in PTPN11 [MIM 176876], which has previously been reported to cause Noonan syndrome [MIM 163950].[12] Though all features that were observed in this female could potentially be explained by the USP9X variant itself (Table S2), a contribution of aberrant PTPN11 to phenotypic features such as intellectual disability, short stature and heart defect in this female is likely. Neuroimaging reports were available for thirteen out of seventeen females (Table S2). Detailed evaluation of brain images of five of these females (female 1,2,3, 7 and 16) showed asymmetric hypoplasia of the cerebellar vermis and hemisphere with a retrocerebellar cyst, short and thin corpus callosum, thin brainstem and mildly abnormal frontal gyration pattern (Figure 3). Notably, we observed thyroid hormone abnormalities in six of the females, requiring medical treatment in three of them.

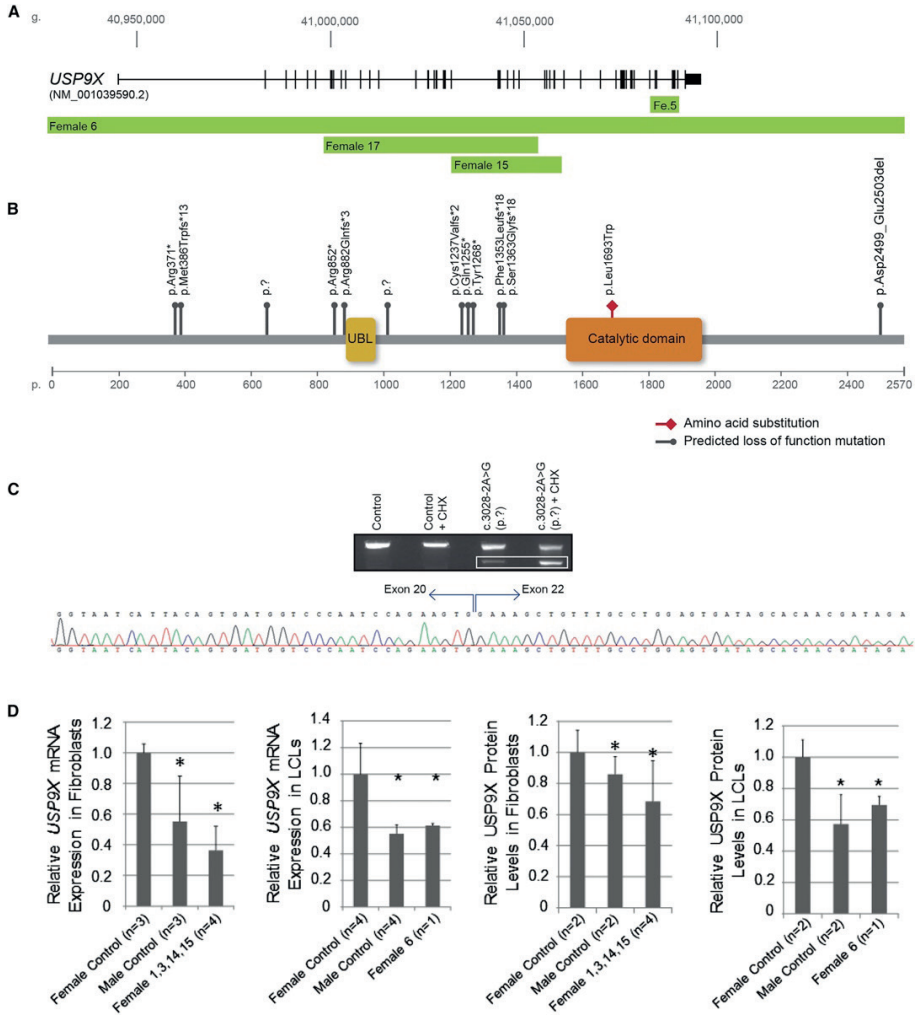

Figure 1: Identified de novo USP9X loss of function mutations (A) Detailed view of the USP9X (NM_001039590.2) region and the reported deletions. (B) Overview of USP9X including UBL- and catalytic domain and the location of reported mutations according to their relative position at the protein level. The reported amino acid substitution is located within the catalytic domain. (C) RNA was extracted from both control and affected female (c.3028-2A>G) fibroblasts cultured under normal conditions or in the presence of cycloheximide (CHX) to inhibit NMD. After cDNA synthesis and PCR, agarose gel analysis showed two different product sizes generated from the c.3028-2A>G transcript but only one from the control fibroblast transcript. Excision and sequencing of the additional band revealed that the aberrant USP9X transcript lacked exon 21. The level of the aberrant transcript was increased fourfold when fibroblasts were treated with cycloheximide confirming that the aberrant transcript was indeed subjected to NMD. (D) USP9X expression is depleted in female cell lines harbouring loss of function alleles. Relative qPCR analysis of USP9X mRNA and relative quantification of immunoblot analysis of USP9X protein derived from female and male control cell lines and from affected female cell lines. n=the number of individual cell lines analysed. Each cell line analysed in quadruplicate. Error bars represent standard deviations. *significantly different to female controls, $p<0.05$ by Student's t-test.

The X-linked USP9X encodes a structurally and functionally highly conserved deubiquitinating enzyme, containing a UBL (ubiquitin-like) and a catalytic ubiquitin specific protease (USP) domain.[13-15] It is known to play an important role in neural development of both humans and mice and is required for fetal development[16-18]. USP9X is highly expressed during embryogenesis and expression declines as cell fates become restricted.[18] The USP9X orthologue in Drosophila, fat facets (faf), has been shown to be important in cell polarity and cell fate of the developing eye in Drosophila.[19] A range of signaling proteins involved in different neurodevelopmental pathways including Notch, Wnt, TGF-β and mTOR have been shown to interact with USP9X.[14; 20-27] USP9X also has been described to act as both an oncogene and tumor suppressor gene and is frequently found to be dysregulated in human cancer.[14; 28; 29] Two of the affected females developed malignancy at a young age (22 and 8 years). Both acute lymphoblastic leukemia and osteosarcoma were treated successfully and have not reoccurred. To determine the risk and nature of particular malignancies in this new syndrome, further studies are required.

We observed pigment abnormalities along Blaschko lines and facial asymmetry, asymmetric abnormalities of the brain and breast and asymmetric length of the legs (Figure 2A, 2D, 3), all suggestive for a pattern of post-zygotic mosaicism or differential X-inactivation (XCI) between tissues (functional mosaicism).[30] USP9X is one of the genes shown to escape XCI.[31; 32]However, it is known that most of the genes that escape from XCI are not fully expressed from the inactivated X chromosome and rather show a partial escape.[33-35] Moreover, there is accumulating evidence for tissue-specific and developmental stage dependent differences in XCI and variability of escape of USP9X.[34; 36-39] In the partial escaping genes, non-random XCI or skewing, as observed often in female carriers of an X-linked mutation, will only partially restore a normal phenotype.[35] Consistent with this hypothesis, XCI was found to be skewed >90% in fibroblasts in three of the five of the tested females, but skewing was not related to disease severity (Table S3). We note that a similar skewing pattern of XCI was observed recently in females with de novo mutations in DDX3X [MIM 300160], another X-chromosomal gene that has been suggested to escape XCI and in which de novo mutations cause ID specifically in females.[40]

Figure 2: Clinical characteristics of females with de novo USP9X loss of function mutations (A) Frontal and lateral photographs of females with de novo mutations in USP9X. Shared facial characteristics include facial asymmetry, prominent forehead, bitemporal narrowing, short palpebral fissures, low nasal bridge, prominent nose with flared alae nasi from adolescence age, thin upper lip, smooth and long philtrum, hanging full cheeks in early childhood and low set, posteriorly rotated and dysplastic ears with attached lobule. (B) Photographs of the hands of seven affected females. Shared characteristics include ulnar deviation of 5th digit, tapered fingers, short 4th and 5th metacarpals and post-axial polydactyly (Simian crease present but not shown). (C) Photographs of the feet of five affected females. Shared characteristics include hallux valgus and sandal gap (pes cavus present but not shown). (D) Observed Blaschko lines of female 3, indicative for 11 of the affected females, suggestive for different X-inactivation pattern between tissues (functional mosaicism).

In one of the affected females a predicted splice site mutation was identified. To evaluate if this mutation indeed results in an aberrant transcript, we synthesized cDNA from RNA extracted from primary skin fibroblasts of both the affected female and a control. We amplified a fragment of 576 basepairs covering exon 20 to exon 22 by PCR. Electrophoretic separation showed two products of 576 and 455 basepairs in the sample from the affected female, and a single 576 basepairs product in the control. Sequencing of the smaller product revealed that this cDNA transcript from the affected female indeed lacked exon 21, confirming the truncating effect of the splice site mutation. Importantly, the level of the transcript was increased four-fold when fibroblasts were treated with cycloheximide, strongly suggesting that the aberrant transcript was subjected to nonsense mediated mRNA decay and as such leads to loss of function of this USP9X allele (Figure 1C). To study the effect of the heterozygous loss-of-function USP9X alleles on their mRNA expression and protein levels, we performed both qRT-PCR and immunoblot blot analysis of fibroblasts (n=4) and lymphoblastoid cell lines (LCLs; n=1) derived from affected females and both female and male controls (Figure 1D and Figure S1). We found that expression of USP9X in affected females was reduced compared to control females in both fibroblasts and LCLs at both mRNA expression and protein levels. Although some cellular variability was evident, on average this decrease was significant ($p<0.05$ by

Student's t-test) (Figure 1D and Figure S1). There was no correlation between skewing of XCI and expression of mRNA and protein level. Whether the cells in affected tissue have benefit from the skewed XCI remains uncertain. The escape from XCI was supported by the fact that the average expression of USP9X mRNA in both control male fibroblasts and control male LCLs was ~50% of that in female controls. After quantification of protein levels in male control LCLs, similar levels were observed. The USP9X protein level in male control fibroblasts was increased to ~80% of that in female controls, but was still significantly less than the protein level in female controls. Intriguingly these data thus reveal that affected females displayed reduced levels of USP9X compared to female controls, but comparable levels to that in healthy control males. It will be important to expose whether these trends extend more to other tissues, where the level of escape from XCI may not comparable. Furthermore, characterization of different expression patterns between sexes (described for USP9X in brain thus far[41]) and/or that of protein levels of USP9X substrates, will be important to ascertain as well.

In contrast to the severely disruptive de novo mutations in females, three milder mutations in USP9X have been reported in males without multiple congenital malformations. The mutations were transmitted by phenotypically normal females and resulted in ID, hypotonia, and behavioral problems in the males.[42] An additional 2 missense mutations were identified after resequencing of USP9X in a cohort of 284 males with epilepsy.[43] For 2 de novo mutations reported in large autism cohorts, no specific gender information was described.[44] The phenotype of the males differs notably from the observed phenotype in the affected females described here. They had ID and short stature, but lacked the multiple congenital malformations observed in affected females. Besides four missense mutations, one frameshift mutation has been reported in the males. This single frameshift mutation occurred within the last 50 nucleotides upstream of the last 3'-exon-exon junction, presumably escaping nonsense-mediated mRNA decay (NMD) and therefore results in a truncated protein lacking the last exon.[45; 46] Since no truncating variants have been described in healthy controls in the ExAC database and no mutations causing loss of function of USP9X have been reported in males, we suspect that loss of function mutations could be lethal in males. This hypothesis is further supported by the fact that the absence of Usp9X in male mice is embryonically lethal.[47] In contrast, all but one of the affected females we report here have protein truncating mutations and deletions. In one female, we identified a de novo missense mutation, located in the catalytic domain of the protein. Given the fact that this female was phenotypically comparable with the other females, it is likely that this specific missense mutation leads to loss of function of the protein. We hypothesize that in addition to complete loss of function mutations, such as protein truncating mutations and deletions, also a small subset of specific missense mutations, will lead to disease in females.

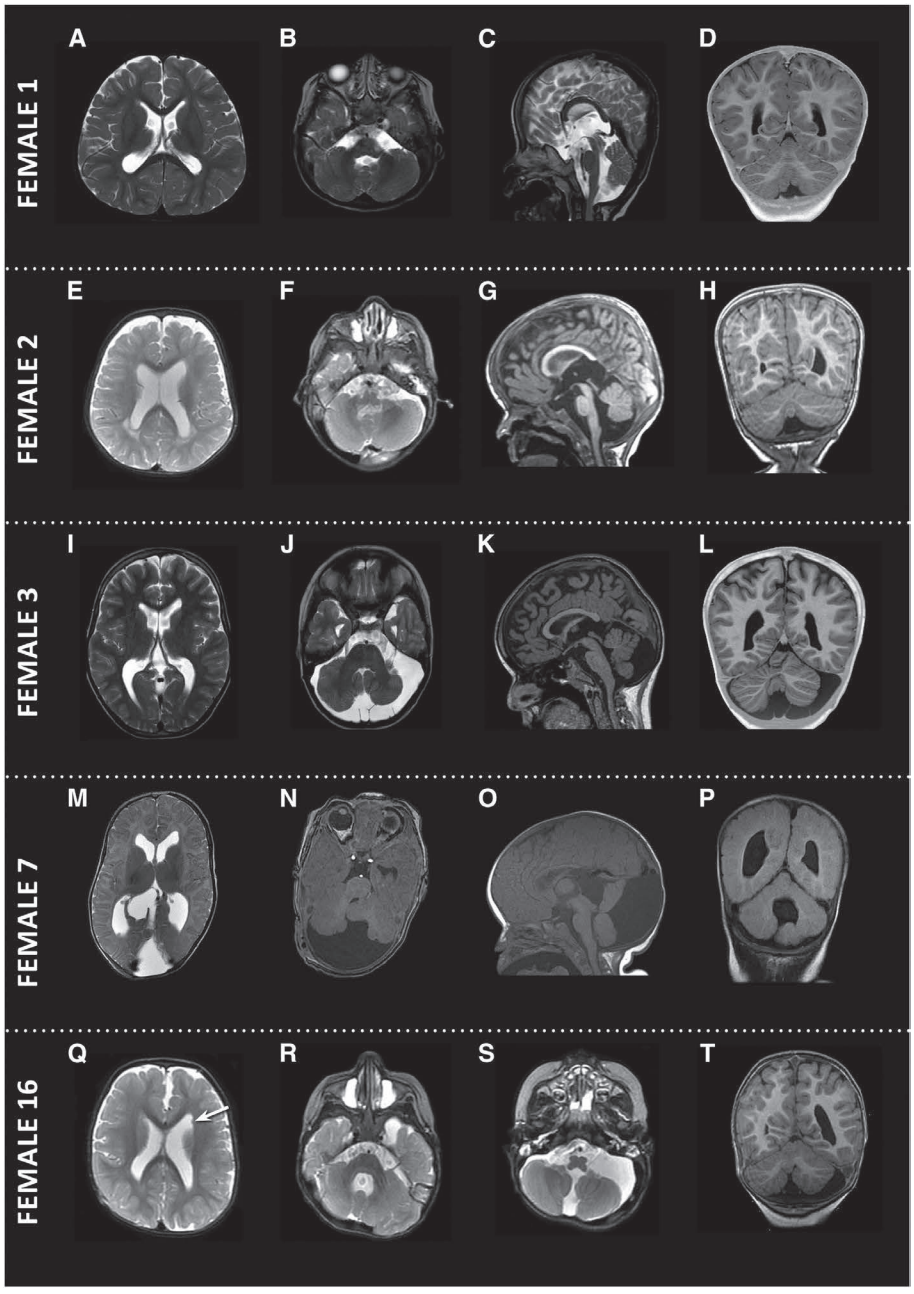
FEMALE 1
A
B
C
D
FEMALE 2
E
F
G
H
FEMALE 3
I
J
K
L
FEMALE 7
M
N
O
P
FEMALE 16
Q
R
S
T

◀**Figure 3: Representative MRI images from females (female 1, 2,3 and 7 and 16) with de novo USP9X loss of function mutations. Female 1** (2 years): MRI T2 axial (A, B), and sagittal (C), T1 axial (D) sections show brachycephaly, mild enlargement of the lateral and 3rd ventricles; mild hypoplasia of cerebellar vermis and left cerebellar hemisphere; enlarged IV ventricle and cisterna magna with small retrocerebellar cyst; thin brain stem and mesencephalon; relatively small frontal lobes with somewhat simplified gyration; short hypoplastic corpus callosum (both rostrum and splenium). **Female 2** (1.5 years): MRI T2 axial (E, F), T1 sagittal (G) and coronal (H) sections show enlargement of the lateral ventricles, mild hypoplasia of cerebellar vermis and left cerebellar hemisphere; enlarged cistern magna; thin corpus callosum, pons, mesencephalon and brain stem; broader and underdeveloped frontal gyri. **Female 3** (11 years): MRI T2 axial (I, J), T1 sagittal (K) and axial (L) sections show asymmetric enlargement of the lateral ventricles; simplified convolutions of the frontal lobes gyri; hypoplasia of cerebellar vermis and left hemisphere; large cisterna magna and retrocerebellar cyst; thin corpus callosum with hypoplasia of the rostrum. **Female 7**: MRI T2 axial (M), T1 axial (N), T1 sagittal (O), coronal FLAIR (P) sections show macrocephaly; enlargement of the lateral and 3rd ventricles with an interhemispheric cyst; dysplastic cerebellar hemispheres; dysplasia of the cerebellar vermis which is uplifted, with a high position of the tentorium and a large posterior fossa, typical of Dandy-Walker malformation; thin and hypoplastic corpus callosum. **Female 16** (2 years): MRI T2 axial (Q, R, S) and T1 coronal (T) sections show enlarged lateral ventricles; irregular gyri of the cerebral cortex with irregular depth of the sulci in frontal and perisylvian areas; small heterotopic nodule of grey matter (arrow) and thin and hypoplastic corpus callosum (both rostrum and splenium); hypoplasia of the anterior cerebellar vermis and left cerebellar hemisphere; enlarged cisterna magna and arachnoidal cyst surrounding the cerebellum, especially at the left side; mild hypoplasia of pons and brain stem. This female was identified with Sanger sequencing based on these brain abnormalities in combination with ID, dysmorphic features and congenital abnormalities.

Affected females presented with symptoms that overlap with CHARGE syndrome [MIM 214800] (CHD7 [MIM 608892] tested in 4 of the females) and with the clinical spectrum of some known ciliopathy syndromes, such as Bardet-Biedl, Meckel-Gruber and Joubert syndrome.[48] Therefore, we investigated whether heterozygous protein truncating mutations result in the disruption of ciliary structure, formation or trafficking in fibroblasts of four of the affected females we had available (female 1,3,14 and 15). First, we determined subcellular localization of endogenous USP9X in both controls and affected female derived fibroblasts under serum starvation to induce ciliogenesis, as well as in serum rich conditions. [49; 50] USP9X showed diffuse cytoplasmic staining with areas enriched with puncta consistent with its described association with protein and vesicle trafficking.[51] Importantly, upon ciliogenesis of the fibroblasts, USP9X was indeed found to localize to the cilium. This ciliary localization was observed along the length of the ciliary axoneme of most fibroblasts, and comparable in cells from affected females and from age and gender matched controls (Figure 4). This localization was significantly decreased with siRNA knock down of USP9X indicating specificity of the signal (Figure S2). We were unable to observe any significant differences in ciliogenesis, ciliary length or ciliary trafficking between fibroblasts from affected females when compared to controls (Figure S3), and siRNA knock down of USP9X did not impair ciliogenesis in fibroblasts. This suggests that USP9X dosage is not critical to the generation of primary cilia in these fibroblasts, despite localization of USP9X in their cilia. It is therefore more likely, that USP9X-regulated signal transduction pathways mediated by the primary cilium are more subtly disturbed, and/

or that this disturbance is spatiotemporally restricted to the tissues affected in this specific phenotype, possibly due to tissue-specific and developmental stage dependent differences in XCI and variability of escape of USP9X. Future studies utilizing dedicated cell-based or animal models will be necessary to evaluate these mechanisms.

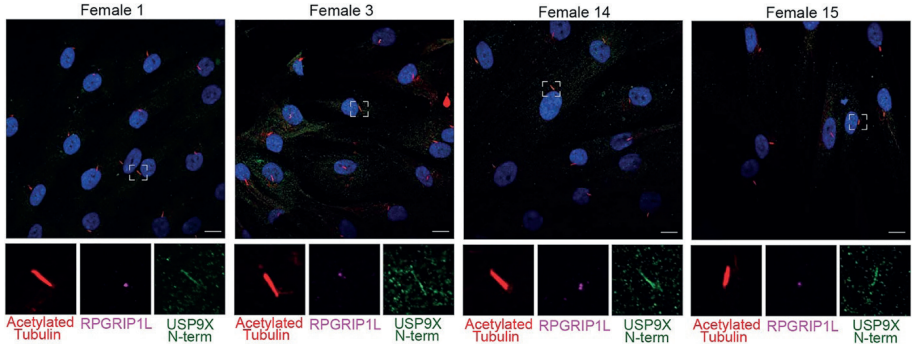

Figure 4: USP9X localizes to the primary cilium. To induce ciliogenesis, control and affected female fibroblasts, matched for gender and age, were starved for 48 hours prior to immunofluorescence labeling. Endogenous USP9X is detected along the length of the axoneme of primary cilia, using an antibody against its N-terminus (N-Term, shown in green) as compared to the ciliary markers RPGRIP1L (pink, denoting the ciliary transition zone at the base of the cilium), and acetylated alpha-tubulin (red, marking the ciliary axoneme). DAPI (blue) stains the nucleï; scale bars represent 10 µm. Ciliated fibroblasts derived from affected females are shown here, USP9X localization in control fibroblasts is shown in Figure S2.

In conclusion, this study defines a recognizable X-linked ID/DD syndrome with associated multiple congenital malformations and brain abnormalities specific to females, caused by de novo loss of function mutations in USP9X, a gene known to escape X-inactivation. The phenotypic characteristics overlap with ciliopathy conditions and USP9X localization along the length of the ciliary axoneme of fibroblasts indicates a role in de-ubiquitination of ciliary proteins, which could contribute to the disease pathogenesis of this specific syndrome.

Table 1: Clinical features of females with de novo USP9X loss of function mutations

	Percentage	Number
Development		
Intellectual disability / developmental delay	100%	17/17
Growth		
Short stature	53%	9/17
Congenital abnormalities		
Eye abnormality	59%	10/17
Choanal atresia	35%	6/17
Cleft palate/bifid uvula	29%	5/17
Dental abnormality	71%	12/17
Asymmetric hypomastia	29%	5/17
Heart defect	44%	7/16
Urogenital abnormality	29%	5/17
Sacral dimple	29%	5/17
Scoliosis	65%	11/17
Hip dysplasia	47%	8/17
Post-axial polydactyly	53%	9/17
Abdominal wall abnormality	12%	2/17
Anal atresia	53%	9/17
Neurology		
Seizures	24%	4/17
Hypotonia	47%	8/17
Brain abnormalities		
Dandy walker malformation (variant)	38%	5/13
Hypoplastic corpus callosum	62%	8/13
(Asymmetric) cerebellar hypoplasia	55%	6/11
(Asymmetric) enlarged ventricles	73%	8/11
Thin brain stem	30%	3/10
Abnormal gyration pattern frontal lobe	50%	5/10
Other		
Hearing loss	65%	11/17
(Blaschko) pigment abnormality	65%	11/17
Hypertrichosis	29%	5/17
Leg length discrepancy	41%	7/17
Malignancy	12%	2/17
Recurrent respiratory tract infections	53%	9/17
Thyroid hormone abnormality	35%	6/17

ACKNOWLEDGMENTS

We thank all the families for their contribution. We thank J. Hehir-Kwa, N. de Leeuw and N. Nadif-Kasri, for providing data and useful discussions. The DDD study presents independent research commissioned by the Health Innovation Challenge Fund [grant number HICF-1009-003], a parallel funding partnership between the Wellcome Trust and the Department of Health, and the Wellcome Trust Sanger Institute [grant number WT098051]. The views expressed in this publication are those of the author(s) and not necessarily those of the Wellcome Trust or the Department of Health. The study has UK Research Ethics Committee approval (10/H0305/83, granted by the Cambridge South REC, and GEN/284/12 granted by the Republic of Ireland REC). The research team acknowledges the support of the National Institute for Health Research, through the Comprehensive Clinical Research Network. This work was supported by grants from The Netherlands Organization for Health Research and Development, ZonMw (grant 907-00-365 to T.K), and the Netherlands Organization for Scientific Research (NWO Vici-865.12.005 to R.R.). A.N., A.H.S., H.M., B.M.A. and V.Z. were supported through the regional agreement on medical training and clinical research (ALF) between Stockholm County Council and Karolinska Institutet, by grants from Frimurare Barnhuset i Stockholm, The Cancer Research Foundations of Radiumhemmet, The Swedish Childhood Cancer Foundation and the Karolinska Institutet research funds. JG was supported by Australian National Health and Medical Research Council (NHMRC) Program Grant (628952) and Research Fellowship (1041920). B.Reversade is a fellow of the Branco Weiss Foundation, an EMBO Young Investigator and a recipient of the A*STAR Investigatorship. This work was partly funded by a Strategic Positioning Fund on Genetic Orphan Diseases from the Biomedical Research Council, A*STAR, Singapore. The authors declare no conflict of interest.

WEB RESOURCES

UCSC Genome Browser, http://genome.ucsc.edu/
Ensembl Genome Browser, http://www.enseml.org/
EXAC database, http://exac.broadinstitute.org/
OMIM, http://www.omim.org/
DECIPHER, https://decipher.sanger.ac.uk

REFERENCES

1. Lubs, H.A., Stevenson, R.E., and Schwartz, C.E. (2012). Fragile X and X-linked intellectual disability: four decades of discovery. Am J Hum Genet 90, 579-590.
2. Piton, A., Redin, C., and Mandel, J.L. (2013). XLID-causing mutations and associated genes challenged in light of data from large-scale human exome sequencing. Am J Hum Genet 93, 368-383.
3. Tarpey, P.S., Smith, R., Pleasance, E., Whibley, A., Edkins, S., Hardy, C., O'Meara, S., Latimer, C., Dicks, E., Menzies, A., et al. (2009). A systematic, large-scale resequencing screen of X-chromosome coding exons in mental retardation. Nat Genet 41, 535-543.
4. Hu, H., Haas, S.A., Chelly, J., Van Esch, H., Raynaud, M., de Brouwer, A.P., Weinert, S., Froyen, G., Frints, S.G., Laumonnier, F., et al. (2015). X-exome sequencing of 405 unresolved families identifies seven novel intellectual disability genes. Mol Psychiatry.
5. Whibley, A.C., Plagnol, V., Tarpey, P.S., Abidi, F., Fullston, T., Choma, M.K., Boucher, C.A., Shepherd, L., Willatt, L., Parkin, G., et al. (2010). Fine-scale survey of X chromosome copy number variants and indels underlying intellectual disability. Am J Hum Genet 87, 173-188.
6. de Ligt, J., Willemsen, M.H., van Bon, B.W., Kleefstra, T., Yntema, H.G., Kroes, T., Vulto-van Silfhout, A.T., Koolen, D.A., de Vries, P., Gilissen, C., et al. (2012). Diagnostic exome sequencing in persons with severe intellectual disability. N Engl J Med 367, 1921-1929.
7. Vulto-van Silfhout, A.T., Hehir-Kwa, J.Y., van Bon, B.W., Schuurs-Hoeijmakers, J.H., Meader, S., Hellebrekers, C.J., Thoonen, I.J., de Brouwer, A.P., Brunner, H.G., Webber, C., et al. (2013). Clinical significance of de novo and inherited copy-number variation. Hum Mutat 34, 1679-1687.
8. Stevens-Kroef, M.J., van den Berg, E., Olde Weghuis, D., Geurts van Kessel, A., Pfundt, R., Linssen-Wiersma, M., Benjamins, M., Dijkhuizen, T., Groenen, P.J., and Simons, A. (2014). Identification of prognostic relevant chromosomal abnormalities in chronic lymphocytic leukemia using microarray-based genomic profiling. Mol Cytogenet 7, 3.
9. Brett, M., McPherson, J., Zang, Z.J., Lai, A., Tan, E.S., Ng, I., Ong, L.C., Cham, B., Tan, P., Rozen, S., et al. (2014). Massively parallel sequencing of patients with intellectual disability, congenital anomalies and/or autism spectrum disorders with a targeted gene panel. PLoS One 9, e93409.
10. Wright, C.F., Fitzgerald, T.W., Jones, W.D., Clayton, S., McRae, J.F., van Kogelenberg, M., King, D.A., Ambridge, K., Barrett, D.M., Bayzetinova, T., et al. (2014). Genetic diagnosis of developmental disorders in the DDD study: a scalable analysis of genome-wide research data. Lancet 385, 1305-1314.
11. Wiszniewska, J., Bi, W., Shaw, C., Stankiewicz, P., Kang, S.H., Pursley, A.N., Lalani, S., Hixson, P., Gambin, T., Tsai, C.H., et al. (2014). Combined array CGH plus SNP genome analyses in a single assay for optimized clinical testing. Eur J Hum Genet 22, 79-87.
12. Lepri, F.R., Scavelli, R., Digilio, M.C., Gnazzo, M., Grotta, S., Dentici, M.L., Pisaneschi, E., Sirleto, P., Capolino, R., Baban, A., et al. (2014). Diagnosis of Noonan syndrome and related disorders using target next generation sequencing. BMC Med Genet 15, 14.
13. Faesen, A.C., Luna-Vargas, M.P., and Sixma, T.K. (2012). The role of UBL domains in ubiquitin-specific proteases. Biochem Soc Trans 40, 539-545.
14. Murtaza, M., Jolly, L.A., Gecz, J., and Wood, S.A. (2015). La FAM fatale: USP9X in development and disease. Cell Mol Life Sci 72, 2075-2089.
15. Khut, P.Y., Tucker, B., Lardelli, M., and Wood, S.A. (2007). Evolutionary and expression analysis of the zebrafish deubiquitylating enzyme, usp9. Zebrafish 4, 95-101.

16. Jolly, L.A., Taylor, V., and Wood, S.A. (2009). USP9X enhances the polarity and self-renewal of embryonic stem cell-derived neural progenitors. Mol Biol Cell 20, 2015-2029.

17. Jones, M.H., Furlong, R.A., Burkin, H., Chalmers, I.J., Brown, G.M., Khwaja, O., and Affara, N.A. (1996). The Drosophila developmental gene fat facets has a human homologue in Xp11.4 which escapes X-inactivation and has related sequences on Yq11.2. Hum Mol Genet 5, 1695-1701.

18. Wood, S.A., Pascoe, W.S., Ru, K., Yamada, T., Hirchenhain, J., Kemler, R., and Mattick, J.S. (1997). Cloning and expression analysis of a novel mouse gene with sequence similarity to the Drosophila fat facets gene. Mech Dev 63, 29-38.

19. Fischer-Vize, J.A., Rubin, G.M., and Lehmann, R. (1992). The fat facets gene is required for Drosophila eye and embryo development. Development 116, 985-1000.

20. Dupont, S., Mamidi, A., Cordenonsi, M., Montagner, M., Zacchigna, L., Adorno, M., Martello, G., Stinchfield, M.J., Soligo, S., Morsut, L., et al. (2009). FAM/USP9x, a deubiquitinating enzyme essential for TGFbeta signaling, controls Smad4 monoubiquitination. Cell 136, 123-135.

21. Friocourt, G., Kappeler, C., Saillour, Y., Fauchereau, F., Rodriguez, M.S., Bahi, N., Vinet, M.C., Chafey, P., Poirier, K., Taya, S., et al. (2005). Doublecortin interacts with the ubiquitin protease DFFRX, which associates with microtubules in neuronal processes. Mol Cell Neurosci 28, 153-164.

22. Xie, Y., Avello, M., Schirle, M., McWhinnie, E., Feng, Y., Bric-Furlong, E., Wilson, C., Nathans, R., Zhang, J., Kirschner, M.W., et al. (2013). Deubiquitinase FAM/USP9X interacts with the E3 ubiquitin ligase SMURF1 protein and protects it from ligase activity-dependent self-degradation. J Biol Chem 288, 2976-2985.

23. Agrawal, P., Chen, Y.T., Schilling, B., Gibson, B.W., and Hughes, R.E. (2012). Ubiquitin-specific peptidase 9, X-linked (USP9X) modulates activity of mammalian target of rapamycin (mTOR). J Biol Chem 287, 21164-21175.

24. Taya, S., Yamamoto, T., Kanai-Azuma, M., Wood, S.A., and Kaibuchi, K. (1999). The deubiquitinating enzyme Fam interacts with and stabilizes beta-catenin. Genes Cells 4, 757-767.

25. Taya, S., Yamamoto, T., Kano, K., Kawano, Y., Iwamatsu, A., Tsuchiya, T., Tanaka, K., Kanai-Azuma, M., Wood, S.A., Mattick, J.S., et al. (1998). The Ras target AF-6 is a substrate of the fam deubiquitinating enzyme. J Cell Biol 142, 1053-1062.

26. Mouchantaf, R., Azakir, B.A., McPherson, P.S., Millard, S.M., Wood, S.A., and Angers, A. (2006). The ubiquitin ligase itch is auto-ubiquitylated in vivo and in vitro but is protected from degradation by interacting with the deubiquitylating enzyme FAM/USP9X. J Biol Chem 281, 38738-38747.

27. Al-Hakim, A.K., Zagorska, A., Chapman, L., Deak, M., Peggie, M., and Alessi, D.R. (2008). Control of AMPK-related kinases by USP9X and atypical Lys(29)/Lys(33)-linked polyubiquitin chains. Biochem J 411, 249-260.

28. Luise, C., Capra, M., Donzelli, M., Mazzarol, G., Jodice, M.G., Nuciforo, P., Viale, G., Di Fiore, P.P., and Confalonieri, S. (2011). An atlas of altered expression of deubiquitinating enzymes in human cancer. PLoS One 6, e15891.

29. Schwickart, M., Huang, X., Lill, J.R., Liu, J., Ferrando, R., French, D.M., Maecker, H., O'Rourke, K., Bazan, F., Eastham-Anderson, J., et al. (2010). Deubiquitinase USP9X stabilizes MCL1 and promotes tumour cell survival. Nature 463, 103-107.

30. Firth, H.V., Hurst, J.A., and Hall, J.G. (2009). Clinical genetics.(New york: Oford University Press).

31. Deng, X., Berletch, J.B., Nguyen, D.K., and Disteche, C.M. (2014). X chromosome regulation: diverse patterns in development, tissues and disease. Nat Rev Genet 15, 367-378.

32. Cotton, A.M., Price, E.M., Jones, M.J., Balaton, B.P., Kobor, M.S., and Brown, C.J. (2015). Landscape of DNA methylation on the X chromosome reflects CpG density, functional chromatin state and X-chromosome inactivation. Hum Mol Genet 24, 1528-1539.

33. Berletch, J.B., Yang, F., Xu, J., Carrel, L., and Disteche, C.M. (2011). Genes that escape from X inactivation. Hum Genet 130, 237-245.

34. Yang, C., Chapman, A.G., Kelsey, A.D., Minks, J., Cotton, A.M., and Brown, C.J. (2011). X-chromosome inactivation: molecular mechanisms from the human perspective. Hum Genet 130, 175-185.

35. Morleo, M., and Franco, B. (2008). Dosage compensation of the mammalian X chromosome influences the phenotypic variability of X-linked dominant male-lethal disorders. J Med Genet 45, 401-408.

36. Carrel, L., and Willard, H.F. (2005). X-inactivation profile reveals extensive variability in X-linked gene expression in females. Nature 434, 400-404.

37. Talebizadeh, Z., Simon, S.D., and Butler, M.G. (2006). X chromosome gene expression in human tissues: male and female comparisons. Genomics 88, 675-681.

38. Zweier, C., Kraus, C., Brueton, L., Cole, T., Degenhardt, F., Engels, H., Gillessen-Kaesbach, G., Graul-Neumann, L., Horn, D., Hoyer, J., et al. (2013). A new face of Borjeson-Forssman-Lehmann syndrome? De novo mutations in PHF6 in seven females with a distinct phenotype. J Med Genet 50, 838-847.

39. Peeters, S.B., Cotton, A.M., and Brown, C.J. (2014). Variable escape from X-chromosome inactivation: Identifying factors that tip the scales towards expression. Bioessays 36, 746-756.

40. Snijders Blok, L., Madsen, E., Juusola, J., Gilissen, C., Baralle, D., Reijnders, M.R., Venselaar, H., Helsmoortel, C., Cho, M.T., Hoischen, A., et al. (2015). Mutations in DDX3X Are a Common Cause of Unexplained Intellectual Disability with Gender-Specific Effects on Wnt Signaling. Am J Hum Genet 97, 343-352.

41. Xu J, T.S., Kaibuchi K, Arnold AP. (2005). Sexually dimorphic expression of Usp9x is related to sex chromosome complement in adult mouse brain. Eur J Neurosci 21, 3017-3022.

42. Homan, C.C., Kumar, R., Nguyen, L.S., Haan, E., Raymond, F.L., Abidi, F., Raynaud, M., Schwartz, C.E., Wood, S.A., Gecz, J., et al. (2014). Mutations in USP9X are associated with X-linked intellectual disability and disrupt neuronal cell migration and growth. Am J Hum Genet 94, 470-478.

43. Paemka, L., Mahajan, V.B., Ehaideb, S.N., Skeie, J.M., Tan, M.C., Wu, S., Cox, A.J., Sowers, L.P., Gecz, J., Jolly, L., et al. (2015). Seizures Are Regulated by Ubiquitin-specific Peptidase 9 X-linked (USP9X), a De-Ubiquitinase. PLoS Genet 11, e1005022.

44. Iossifov, I., O'Roak, B.J., Sanders, S.J., Ronemus, M., Krumm, N., Levy, D., Stessman, H.A., Witherspoon, K.T., Vives, L., Patterson, K.E., et al. (2014). The contribution of de novo coding mutations to autism spectrum disorder. Nature 515, 216-221.

45. Nagy, E., and Maquat, L.E. (1998). A rule for termination-codon position within intron-containing genes: when nonsense affects RNA abundance. Trends Biochem Sci 23, 198-199.

46. Lewis, B.P., Green, R.E., and Brenner, S.E. (2003). Evidence for the widespread coupling of alternative splicing and nonsense-mediated mRNA decay in humans. Proc Natl Acad Sci U S A 100, 189-192.

47. Stegeman, S., Jolly, L.A., Premarathne, S., Gecz, J., Richards, L.J., Mackay-Sim, A., and Wood, S.A. (2013). Loss of Usp9x disrupts cortical architecture, hippocampal development and TGFbeta-mediated axonogenesis. PLoS One 8, e68287.

48. Ware, S.M., Aygun, M.G., and Hildebrandt, F. (2011). Spectrum of clinical diseases caused by disorders of primary cilia. Proc Am Thorac Soc 8, 444-450.

49. Tucker, R.W., Pardee, A.B., and Fujiwara, K. (1979). Centriole ciliation is related to quiescence and DNA synthesis in 3T3 cells. Cell 17, 527-535.

50. Vorobjev, I.A., and Chentsov Yu, S. (1982). Centrioles in the cell cycle. I. Epithelial cells. The Journal of cell biology 93, 938-949.

51. Murray, R.Z., Jolly, L.A., and Wood, S.A. (2004). The FAM deubiquitylating enzyme localizes to multiple points of protein trafficking in epithelia, where it associates with E-cadherin and beta-catenin. Mol Biol Cell 15, 1591-1599.

The American Journal of Human Genetics Supplemental Data

De Novo Loss-of-Function Mutations in USP9X Cause a Female-Specific Recognizable Syndrome with Developmental Delay and Congenital Malformations

Margot R.F. Reijnders, Vasilios Zachariadis, Brooke Latour, Lachlan Jolly, Grazia M. Mancini, Rolph Pfundt, Ka Man Wu, Conny M.A. van Ravenswaaij-Arts, Hermine E. Veenstra-Knol, Britt-Marie M. Anderlid, Stephen A. Wood, Sau Wai Cheung, Angela Barnicoat, Frank Probst, Pilar Magoulas, Alice S. Brooks, Helena Malmgren, Arja Harila- Saari, Carlo M. Marcelis, Maaike Vreeburg, Emma Hobson, V. Reid Sutton, Zornitza Stark, Julie Vogt, Nicola Cooper, Jiin Ying Lim, Sue Price, Angeline Hwei Meeng Lai, Deepti Domingo, Bruno Reversade, the DDD Study, Jozef Gecz, Christian Gilissen, Han G. Brunner, Usha Kini, Ronald Roepman, Ann Nordgren, and Tjitske Kleefstra

Supplemental Acknowledgements

The DDD study presents independent research commissioned by the Health Innovation Challenge Fund (grant number HICF-1009-003), a parallel funding partnership between the Wellcome Trust and the Department of Health, and the Wellcome Trust Sanger Institute (grant number WT098051). The views expressed in this publication are those of the author(s) and not necessarily those of the Wellcome Trust or the Department of Health. The study has UK Research Ethics Committee approval (10/H0305/83, granted by the Cambridge South REC, and GEN/284/12 granted by the Republic of Ireland REC). The research team acknowledges the support of the National Institute for Health Research, through the Comprehensive Clinical Research Network.

Supplemental Note: Case Reports

Female 1 is the second child of nonconsanguineous parents of Swedish and Thai ancestry. She has mild intellectual disability, short stature, hypotonia, PDA, aortic insufficiency, inguinal herniation, diaphragmatic herniation, a double collecting system of the kidney, bilateral hip dislocation, patellar dislocation, thoracolumbar scoliosis, abnormal teeth eruption, stenosis of lacrimary ducts and abnormal middle ears. She has hearing and visual impairment. She has dysmorphic features including; transverse palmar creases, a square face, brachycephaly (large fontanel in infancy), high palate, almond shaped eyes, long philtrum, thin upper lip, low set and posteriorly rotated ears, depressed nasal root and depressed nasal tip. Brain MRI showed brachycephaly, mild hypoplasia of cerebellar vermis and left hemisphere, small retrocerebellar cyst, ventricular enlargement, thin brain stem, relatively small frontal lobes with enlarged gyri and less deep sulci, short hypoplastic corpus callosum (both rostrum and splenium), malrotated hippocampi and thin commisura anterior. CT scan of the temporal bones showed dense middle ears, suspected stapes malformation and narrow auditory canals. She suffers from frequent upper respiratory infections and pneumonias. At 18 months she developed seizures. She has a percutaneous endoscopic gastrostomy (PEG) and she requires intermittent home oxygen therapy due to chronic respiratory insufficiency. At age 7 she was diagnosed with B- cell precursor acute lymphoblastic leukemia (BCP ALL).

Female 2 is the second of two children of nonconsanguineous parents of Dutch ancestry. Family history was non-contributory. She was born after 41+3 weeks of gestation with a birth weight of 3530 gram (0 SD), APGAR scores were 7 and 3 after respectively 1 and 5 minutes. Prenatal ultrasound showed bilateral hydronephrosis, postaxial polydactyly of the left hand and ventriculomegaly. Due to severe hypotonia, ventilatory support was necessary. Besides

post-axial polydactyly other congenital abnormalities, including bilateral choanal atresia, ventral position of the anus, atrial septum defect type II, and congenital vertical talus were diagnosed. Renal ultrasound showed no hydronephrosis, however nephrocalcinosis was evident and unilateral double renal collecting system was suspected. Auditory Brainstem Response Audiometry showed no abnormalities, however conductive hearing loss was measured due to recurrent middle ear infections. At the age of 2 years, there was no speech development and at currently age 3 years she learns to use sign language and she is able to speak a few single words. Hyperlaxity and hypotonia hampered her motor development; she started walking at the age of 2 years and 8 months. Physical examination at the age of 2 years and 11 months showed a height of 86 cm (-3 SD), a weight of 11.4 kg (-1.1 SD) and a head circumference of +1 SD. Facial dysmorphism, including a widows peak, posteriorly rotated, dysplastic ears, hypertelorism and a broad nasal bridge were noted. Hypoplastic nipple and a sacral dimple were present. She had hypertrichosis of both arms. Brain MRI showed mild hypoplasia of cerebellar vermis and left hemisphere, enlarged cistern magna, ventricular enlargement, thin pons and brain stem, broader and underdeveloped frontal gyri. Previous investigations consisting of a CytoSNP 12v2.1 array (Illumina), Asperchip BBS analysis, and Sanger sequencing of SETBP1, OFD1, CHD7, SALL1, BBS6, POR were normal. Blood analysis showed an increased TSH with normal FT4 values.

Female 3 is the second of five children of non-consanguineous parents. There was no family history of developmental delay. She was born after 41 weeks of gestation with a birth weight of 3500 gram (-0.5 SD). Delivery was uncomplicated. Physical examination after birth revealed several abnormalities: large frontal fontanel, post-axial polydactyly, single choanal atresia and a ventral position of the anus. With neonatal heel prick screening, no abnormalities were measured.

Nevertheless, at the age of 1 year hypothyroidism was detected. Both motor and language development were delayed. She walked without support at the age of 27 months and she spoke her first words at the age of 25 months. Psychological assessment when she was teenager showed mild intellectual disability. As child, surgery was required to correct strabism. She had recurrent middle ear infections. Puberty development was normal. However, she had remarkable asymmetric growth of her breasts. She needed dental braces to position her teeth. However, there was no growing of her canine teeth. Because of progressive pedes cavus, she required special shoes. She had diminished sensitivity in her hands, suspicious for polyneuropathy. However, this was not confirmed with electromyography. There was mild thoracal kyphosis. Physical examination at the age of 11 years showed macrocephaly, with a head circumference of 57 cm (+2.0 SD) and also present in her father. Her height was 157 cm

(0 SD) and her weight was 40.5 kg (-1 SD). She had an asymmetric face with deep set eyes, long nose, smooth philtrum and bifid uvula. She had small hands with tapering fingers. There was hypermobility of her joints. Inspection of the skin revealed Blaschko lines on her left arm, hyperpigmentation in her neck and hypertrichosis. A brain MRI at the age of 11 years showed hypoplasia of cerebellar vermis and left hemisphere, large retrocerebellar cyst, ventricular enlargement with left frontal horn of lateral ventricle more than right, simplified convolutions of the frontal lobes gyri and thin corpus callosum with hypoplasia of the rostrum. Previous investigations, consisting of 250k SNP-array and analysis of BBS6 were normal.

Female 4 is the first child of nonconsanguineous parents who had a prior first trimester miscariage. Two maternal uncles have intellectual disability of unknown etiology. She was born at 40 weeks gestation to a 17-year-old African-American by scheduled Cesearan section for poor fetal growth, with a birth weight of 2727 grams (-2 SD) and length 48 cm (-1 SD). Prenatal ultrasound had revealed a Dandy Walker variant. Delivery was uncomplicated. At birth she was noted to have a large fontanel, congenital scoliosis and pale skin with red streaks (but no blisters) that darkened with age. Brain MRI confirmed the Dandy Walker variant as well as bilateral temporal, frontal and insular hypomyelination. Renal ultrasound and echocardiogram were normal. She was discharged at 10 days of age. She was subsequently diagnosed with hypothyroidism and treated with synthroid. She developed febrile seizures but was not treated with antiepileptic medications. Fontanel was late to close. She was evaluated at 7 years of age for intellectual disability and skin pigmentary abnormalities. Physical examination revealed weight 2%, height 21% and head circumference at 50%. She had a narrow face with prominent forehead. Palpebral fissures were upslanting, lateral eyebrows were flared and the philtrum was smooth. She had diffuse Blaschkolinear hyperpigmentation. Array comparative genomic hybridization (oligonucleotide + SNP) was normal. Whole exome sequencing revealed a de novo mutation in exon 19 of USP9X: ChrX(GRCh37):g.41029255_41029256insA; NM_001039590.2: c.2644_2645insA(p.(Arg822Glnfs)).

Female 5 is the first child of non-consanguineous parents. There was no family history of developmental delay. She was born at full term with a birth weight of 3064 gram. Delivery was via Caesarean section due to abnormal fetal positioning. As neonate, she had failure to thrive due to feeding difficulties, requiring tube feeding. Left congenital hip dislocation and persistent ductus arteriosus were noticed. Her development was severely delayed with both motor and language delay. She walked her first steps at the age of 3 years and at the age of 9 years, she was essentially non-verbal. There were moderate to severe behavioral abnormalities with Obsessive-Complusive- Disorder symptoms. She had repetitive signing or verbalizations, tantrums, self injury, aggressiveness and sleeping problems, requiring

treatment with clonidine. Her forward vision was impaired due to severe ptosis. No other visual problems were present. Scoliosis and leg length discrepancy were observed, the latter required surgery. There were genu valgum and severe pes planus for which she has been prescribed special shoes. She had a history of easy bruising and episodes of epistaxis, but there is not a known deficiency in clotting factors. Renal ultrasound at the age of 7 years showed mild left hydronephrosis. Physical examination at the age of 11 years showed short stature with a height of 131 cm (-3 SD), weight of 28.4 kg (-2 SD) and head circumference of 53 cm (0 SD). She had facial dysmorphisms consisting of low posterior hairline, posteriorly rotated and low set ears with thickened helices and bilateral ptosis, diamond shaped eyebrows, down slanting palpebral fissures, thin nasal bridge, pinched nasal root and tip, prominent nasolabial folds, thin upper lip, bifid uvula, crowded teeth and pointed chin. Inspection of the hair showed a 1 cm lesion of atrophic skin on occiput where hair follicles were lacking, suspect for aplasia cutis congenital. The right eye lid had a kereatotic lesion and evidence of mild abrasion. Pectus excavatum and upper thoracic wide scoliosis were present. Brain MRI showed Dandy Walker malformation. Previous genetic tests, including Prader-Willi syndrome methylation, showed no abnormalities. Analysis of PTPN11 [MIM 176876] revealed a mutation c.1282 G>T (p.(V428L)) which was not present in the mother. CGH array showed a deletion in USP9X: Xp11.4 (Minimum: 41082619-41090198; maximum: ChrX:41082474-41092226), not present in mother.

Female 6 is the first child to non-consanguineous Caucasian parents. She has a younger sister who is well. The female was delivered at term following an uncomplicated pregnancy, with a birth weight of 3.17kg (25-50th centile). There were feeding difficulties in infancy, requiring a brief period of nasogastric tube feeding. She had developmental dysplasia of the hips, requiring treatment with a brace, and generalized hypotonia and joint hypermobility. She crawled at 14 months, and walked at 27 months of age. Currently, at the age of 2 years and 7 months, she has around 50 spoken words, and over 100 signs. She is putting short sentences together. She has moderate hearing loss and has hearing aids bilaterally. There is hypermetropia, and minor cataract in the right eye not requiring treatment. Her current weight is 10.3kg (3rd centile), height is 84.5cm (3rd centile) and head circumference is 50.5cm (75th centile). The anterior fontanelle was large and closed late. She has a prominent forehead, and low-set, posteriorly rotated ears, but is otherwise not dysmorphic. Echocardiogram is normal. SNP microarray (Illumina HumanCytoSNP-12 v2.1) showed a female molecular karyotype with an interstitial deletion of 0.2 megabases on Xp11.4 (40,811,713- 41,033,450), encompassing a single gene USP9X (interpretation based on hg18). Parental testing has confirmed this to be de novo.

Female 7 is the eldest of three daughters of healthy nonconsanguineous parents of Asian (Chinese) ancestry. There was no significant family history. Her two younger sisters are well. She was born at 33 weeks 5 days of gestation with a birth weight of 1964 grams (25th-50th centile). Prenatal ultrasound showed borderline ventriculomegaly and suspected Dandy-Walker malformation. At birth, facial dysmorphism (prominent forehead, low-set ears), bilateral post-axial polydactyly of the hands, hypoplastic nipples, omphalocoele minor, anteriorly placed anus with anal stenosis, sacral dimple and ventricular septal defect were observed. Renal and lumbosacral ultrasound scans were normal. Hip ultrasound scans showed right hip dislocation and left developmental dysplasia of the hip. Brain MRI done at 1 month of age showed Dandy-Walker malformation, hydrocephalus and a small arachnoid cyst of the 3rd ventricle on the right. She was also reported to have dysgenesis of the posterior body and splenium of the corpus callosum on brain CT. Auditory Brainstem Response Audiometry showed bilateral conductive hearing loss and she has had several procedures for myringotomy and Gromet tube insertion. She also underwent omphalocoele repair at 3 days old, insertion of a posterior fossa cysto-peritoneal shunt at 2 months old, right hip surgery at 9 months old. She has global developmental delay and intellectual disability. At the age of 8 years 10 months, she can sit independently and stand with support, but cannot stand or walk independently yet. She communicates by pointing to pictures or letters, but is still non-verbal. Physical examination at the age of 8 years and 10 months showed a height of 98 cm (18 cm < 3rd centile), a weight of 15.0 kg (3.5 kg < 3rd centile) and a head circumference of 49 cm (1 cm < 3rd centile). Facial dysmorphism, including facial asymmetry, prominent forehead, smooth and long philtrum, hanging full cheeks, low-set and posteriorly rotated ears, were noted. Hypoplastic nipples and a sacral dimple were present. She has a severe propensity to keloid formation, requiring multiple steroid injections and excisions, as well as corneal scarring, occurring without any obvious trauma. Previous investigations consisting of serum transferrin isoforms, and chromosomal microarray analysis (Agilent 400K array) were normal. Blood analysis showed an increased TSH with normal fT4 values.

Female 8 (DECIPHER ID 258511) is the first child of non-cansanguineous Caucasian couple. There is no significant family history of note. She was born at term weighing 2.8kgs, following a fairly smooth pregnancy. She was admitted to SCBU for 48 hours due to poor feeding and facial asymmetry. She was noted to have bilateral hip dysplasia and a vertical talus, which were treated with a harness for 6 months and splints for her feet respectively. She was noted to be hypotonic with significant joint laxity. She also developed scoliosis which was treated surgically at the age of 8 years. The scoliosis has been progressive. Seizures developed from 8 years of age and were in the form of absence seizures. The epilim was stopped recently

as she had been seizure-fee for a few years. A recurrence of seizures has been noted since. Global developmental delay was noted - she walked at 30 months and her first words came at 4 years. She was able to use the makaton before that prior to speech development. She has a hypernasal quality to her voice and has some sounds missing. She has been reported to have moderate intellectual disability. She was diagnosed with autism at the age of 8 years. Her behaviour can be very challenging and has been described as Pathological Demand Avoidance. Physical examination showed brachycephaly, plagiocephaly, very curly hair, a prominent nose with flared nostrils, hirsuite back, scoliosis and pes cavus. Skull X-rays showed wormian bones. MRI brain and spine were reported to be normal. Previous investigations including microarrays and basic metabolic screen were normal.

Female 9 (DECIPHER ID 267427) is the only child of nonconsanguineous parents of UK ancestry. Family history noted a male first cousin (the childrens' fathers are brothers) with a laryngeal abnormality, congenital heart disease and preaxial polydactyly. Pregnancy was complicated by polyhydramnios and serology positive for Toxoplasmosis at the time of birth. Antenatal ultrasound had revealed enlarged cerebral ventricles. She was born after 36 weeks of gestation with a birth weight of 2600 gram (50%), by emergency Caesarean section after premature rupture of the membranes with meconium stained liquor. She required ventilatory support at birth and was noted to have bilateral choanal atresia which was surgically repaired. A subglottic stenosis was subsequently noted. Additional problems in the neonatal period were a small ASD which closed spontaneously, peripheral cataracts and an anteriorly placed anus (which did not require intervention). Renal ultrasound was normal. In infancy there were considerable feeding problems with reflux and repeated episodes of aspiration and recurrent chest infections. A gastrostomy was placed until the age of 7 years. She has had recurrent episodes of blepharitis and was noted to have astigmatism. Conductive hearing loss was noted due to recurrent middle ear infections. Developmental milestones were delayed. At age 7 years she attends special school, she is able to talk in simple sentences and demonstrates simple understanding. She has little abstract thinking and poor attention. Her motor skills remain delayed and she is still hypotonic. She has mirror movements. Physical examination at the age of 7 years and 7 months showed a height of 119.6 cm (10-25%) and a head circumference of 50 cm (2%). Facial features include a broad nose with a depressed, grooved nasal tip. She has mildly posteriorly rotated ears with absent lobes. She has small hands and feet with tapering fingers and poorly opposable thumbs. She has recently been noted to have some missing secondary dentition and deficient enamel. She was noted to have a narrow chest and asymmetry of gait and posture. There is generalized joint laxity. Limb length discrepancy has been documented and a mild scoliosis convex to the right with apex at

L2 has been radiologically observed, hypoplasia of clavicles was noted. Her left side is weaker than right including a mild facial nerve weakness and there is asymmetry of hair growth with sparser hair on the left side. She has mild skin streaking along Blaschko lines visible mostly on limbs. Brain MRI showed non-specific underdevelopment of white matter with a slightly larger lateral ventricle on the left with focal dilation and gliosis around the left frontal horn. Previous investigations consisting of a Nimblegen 135K HG18 WG CGH v.3.1 which documented a 430 Kb copy number gain at 13q14.11 shared with her normal father and other paternal relatives. Sanger sequencing of CHD7 shows a change c8339C>T (p Ala2780Val) which is also shared with her normal father and other relatives in his family. Skin chromosomes were normal 46XX.

Female 10 (DECIPHER ID 281586) is the second of two children of nonconsanguineous parents of mixed Jamaican / White British ancestry. Her older sister had hydronephrosis in infancy which resolved, and an autistic spectrum diagnosis made in her teens. The patient also inherited Familial Hypercholesterolaemia from her father. There is no other family history of structural anomalies. A right multicystic dysplastic kidney and left hydronephrosis were detected at 20 weeks. She was felt to be a large baby so delivered by elective section at term weighing 3500g. There was abdominal distension with bilious aspirates and pylostomy was required at birth, and later double J stenting. No other anomalies were detected at birth. Early developmental milestones were all mildly delayed, and she was monitored in the Child Development Centre. She moved from mainstream school to special school for her secondary education. At around 5 years of age during investigations for persistent cough, lower thoracic scoliosis was noted, and found to be related to a hemivertebra at T10, requiring hemivertebrectomy at age 8. She has 13 pairs of ribs. There is also a suspicion of a leg length discrepancy due to a pelvic tilt. The scoliosis has continued to worsen below the operated area, requiring a brace and a second operation will be necessary. She has required investigation and monitoring for persistent neutropaenia, including bone marrow aspirate which was mildly hypocellular, but no clear cause has been identified. She requires tonsillectomy and grommet insertion for glue ear. Problems with frequent gall stones were present. At 8 years breast and pubic hair development led to investigations. The uterus was found to be absent on MRI, but both ovaries are present. Bone age was advanced at 11.5years at 9y chronological age. She has a persistently high Free T4 with normal TSH, without thyroid symptoms. On examination in the genetics clinic she was also found to have a shortening of the 4th metacarpals, most pronounced on the right. There are only 3 lower incisors, and the teeth are of poor quality and pitted. There are areas of hyperpigmentation on the skin, not typical of Café-au-lait patches. Eye examination was unremarkable. Microarray analysis was also normal.

Female 11 (DECIPHER ID 271249) is the first child of non-consanguineous parents of

English ancestry. She has an older healthy maternal half-sister. There is no significant family history. She was born after 39 weeks of gestation with a birth weight of 2877g (-0.9 SD). She was well at birth. Prenatal ultrasound showed unilateral hydronephrosis. Fetal echocardiography was normal. At birth she was noted to have bilateral post-axial polydactyly of the hands and congenital dislocation of the hips. She fed well. She had motor and speech developmental delay. She walked just before 2 years. Her first words were from 3 years. She had recurrent urinary tract infections and had a pyeloplasty aged 3 years. At 6 years she was diagnosed with a submucous cleft palate and bifid uvula. She has amylopia, astigmatism and bilateral cortical cataracts were diagnosed at 7 years. Abdominal ultrasounds shows a bicornuate uterus. She is entering puberty at 11.5 years. She has a school educational statement. Facial dysmorphism, includes low posteriorly rotated dysplastic ears. Her earlobes are attached. High nasal bridge with hypoplastic nasal alae, an overhanging colomella and smooth philtrum. Her right eyebrow is interrupted. She has wiry hair which is considered familial. She holds her 5th fingers in abduction at the MCP joint. She has wasting of the muscles of the hands and legs distally, with high arches to her feet. There is bilateral hallux valgus. She has faint streaks of hypopigmentation following the lines of Blaschko over her trunk and arms. Spine MRI scan was normal. Previous investigations consisted of a normal 0.5Mb BAC array (2007), normal blood and skin (wrist, ankle, groin samples) karyotype analysis.

Female 12 (DECIPHER ID 258617)is the first child of non consanguineous parents of Middle East/Maltese and white UK ancestry. The family history was non-contributory. Her birth was induced because of prolonged rupture of membrane and decreased fetal movements. The proband was born by normal vaginal delivery at 36 weeks of pregnancy with a birth weight of 2260 gram (-1 to -2 SD) and a head circumference of 32cm (0 SD). She was in good condition and did not require resuscitation. She was self-ventilating in air and established bottle feeding. Postnatally she was noted to have bilateral postaxial polydactyly of the hands and an anteriorly placed anus. Other congenital abnormalities included left choanal atresia and right choanal stenosis. A moderate patent ductus arteriosis, patent foramen ovale, tricuspid regurgitation and aortic regurgitation detected early on have resolved and she has required spinal bracing because of a marked thoracic scoliosis. She suffered with recurrent upper respiratory tract and middle ear infections. She had grommets and now wears hearing aids because of moderate conductive hearing loss. She had left sided strabismus, a pinpoint anterior subcapsular lens opacity on the left side and peripheral retinal pigment epithelial pigment changes bilaterally, and she has glasses because of mild myopia. More recently treatment has been required for hypertension of unknown cause. Developmentally she has severe intellectual disability with motor and speech delay. She had 3 words by the age of 2 ½ years and at the age of 7 years

she is able to speak in short phrases, however her speech can be difficult to understand. She also points and uses some Makaton signs. She has hypotonia and mobilises on her knees or hopping using her hands and knees. She can stand with support with her knees flexed. Physical examination at the age of 7 years and 4 months showed a height of 109 cm (-3 SD), a weight of 25.5 kg (0 SD) and a head circumference of 49.9 cm (-3 SD). Facial dysmorphism, including a widows peak, posteriorly rotated, dysplastic ears, arched eyebrows, a broad nasal bridge with a flattened nasal tip and a midline tongue depression were noted. A sacral dimple was present. She had hypertrichosis of her arms and back and patchy pigmentation over her back and the right side of her chest. A brain MRI showed a Dandy walker complex with a partially developed cerebellar vermis and a communication between the 4th ventricle and the cisterna magna, and a small posterior fossa with a hypoplastic cerebellum. A renal ultrasound scan was normal. Previous investigations included blood and skin karyotyping, 22q11.2 FISH, Sanger sequencing of CHD7 and microarray analysis. Endocrinology assessment was normal.

Female 13 (DECIPHER ID 261847)is the first of two children of nonconsanguineous British parents with no family history of relevance. She was born at 39 weeks gestation by normal delivery weighing 2.65kg. She had surfactant deficiency and was ventilated for 2 days. At birth she was in an extended breech position, and hip and knee abnormalities were noted. She had a dislocated right hip and subluxed left hip. There was bilateral absence of patellae with knee subluxation. Her feet were held in fixed flexion. She had torticollis with narrow sloping shoulders but other joints were hypermobile. In her early years she had hypotelorism with a bulbous nasal tip, pronounced nasolabial fold, slightly sagging cheeks and small jaw. Her dental eruption pattern was unusual and she has gingival hyperplasia. She had a streak of increased pigmentation on her inner left calf. Investigations included a normal cranial MRI scan and spinal X-rays. She has a normal metabolic screen and chromosome array. Her early EMG suggested mild axonal loss but she subsequently now has normal power and reflexes. She has a mild intellectual disability and is emotionally immature. Female 14 is the younger of two children of non-consanguineous parents. Her older brother is healthy. There was no family history of developmental delay. She was born after 35 weeks of gestation with a birth weight of 2510 gram (+0.5 SD). During the last weeks of pregnancy a polyhydramnion was noted. Delivery was uncomplicated. Physical examination after birth revealed several abnormalities: a large anterior fontanel, bilateral choanal atresia (neonatal surgically corrected neonatally), a rectovaginal fistula with anus perinealis (corrected at the age of 5 months), sacral dimple, short clavicles and left-sided post-axial polydactyly (without osseous structures). Both motor and language development were delayed with walking without support at the age of 2½ years. There was a history of balance problems, for which no cause could be found (normal CT mastoid

and normal electronystagmogram). Psychological assessment when she was a teenager showed a low- normal IQ of 85. In childhood she developed a progressive scoliosis due to asymmetry of her legs. She had mild conductive hearing loss caused by recurrent middle ear infections and tympanic membrane defects. Puberty development was normal with menarche at the age of 11 years. However, she had a remarkable asymmetric growth of her breasts. She was referred to the clinical genetics department for reevaluation at the age of 16 years. As part of the work-up a large ASD was found and surgically closed. At the age of 19 she underwent a bilateral cataract surgery. At the age of 22 years she was diagnosed with an osteosarcoma in her distal right femur. After surgery and chemotherapy, she is now without relapse for 1 year. Physical examination at the age of 16 years showed a height of 158.6 cm (-1.5 SD, target height 171.6 cm) and a head circumference of 55 cm (0 SD). She had an asymmetric face with short palpebral fissures, low-set and dysplastic ears, broad nasal bridge, bulbous tip of the nose and a thin upper lip. The left breast was smaller than the right breast. She had Simian creases on both hands with short 4th and 5th metacarpals. She had a scoliosis and her legs were asymmetric in length. Inspection of the skin revealed Blaschko lines. A brain MRI at the age of 6 months showed slightly enlarged ventricles, a thin corpus callosum and a variant Dandy Walker malformation. Previous genetic investigations, consisting of 105k oligo-array (Agilent AMADID-nr. 019015) on DNA extracted from blood and fibroblasts, and CHD7 analysis were normal. Using whole exome sequencing a de novo mutation in USP9X was identified: USP9X; ChrX(GRCh37):g.41047269del; NM_001039590.2:c.3709del(p.(Cys1237fs))

Female 15 is the 4th child of 4 children of nonconsanguineous parents. There was no family history of developmental delay. The first child was born hydropic and died postnatally due to intrauterine infections. The proband was born after 39 weeks of gestation with a birth weight of 2610 gram (-2 SD). Delivery was uncomplicated. After birth, several congenital abnormalities were noticed, including bilateral choanal atresia, anorectal malformation, post-axial polydactyly, single umbilical artery, a bifid uvula with submucosal cleft palate. Later on a hip dysplasia was noted. Both motor and language development were delayed. Psychological assessment at the age of 5,5 years showed mild intellectual disability with an IQ of 65. In childhood she developed progressive scoliosis and hypodontia. She had mild sensorineural hearing loss and hypermetropia (+2,25D OD/+3,75D OS). Physical examination at the age of 16 years showed a height of 152 cm (-3 SD), a weight of 50 kg (0 SD) and a head circumference of 52 cm (- 2 SD). Inspection of the skin revealed Blaschko lines. She had facial dysmorphic features, including a bitemporal narrow face, low set ears, short palpebral fissures, down slant eyes and a bulbous nasal tip. Her legs were asymmetric in length. She had short clavicles and no axillary hair and amastia. Previous investigations consisting of chromosome analysis

and oligo array (105K) were normal. CT brain (at age of 2 days) showed no abnormalities. Using CNV analysis on exome data, a de novo intragenic deletion in USP9X was identified and confirmed with array: Xp11.4(41,001,431-41,059,516)x1.

Female 16 presented with IUGR and maternal hypertension. She was born by caesarian section in the 36th week of gestation with a birth weight of 2205 grams, as first child of healthy unrelated Dutch parents. At birth a bilateral postaxial polydactyly (post-minimum), open ductus arteriosus and dysmorphic features were present: broad nasal bridge, low set ears with over folded helix, high palate, prominent heels and small labia majora. Hearing tests showed bilateral mixed conductive and sensorineural deafness and small ear meatus. She was temporarily treated with thyroid hormone because of high TSH titers. The psychomotor development is delayed: she walked unassisted at the age of 5 years, the speech is very nasal and limited to single words. At the age of 6 years she developed absences and short focal seizures, requiring treatment with levetiracetam. The EEG showed multifocal generalized peak-waves abnormalities. Height and head circumference follow the -1/-1.5 SD line. She never was toilet trained. At the age of 6 years she presented with short palpebral fissures, periorbital fullness, broad high forehead, broad and flattened nose bridge and nose tip, small nostrils, short columella, prognathism, rotated ears and underdeveloped ear lobes. The shoulders are hanging, the neck and distance between nipples is broad; the sternum is short. There is brachydactyly of the fingers with a bilateral cutaneous syndactyly of digits II-V. The toes are short with cutaneous syndactyly of digits II-III. She has flat feet and walks with bowed knees, but she cannot run, the tendon reflexes are brisk. At the age of 7 years she suffered from a major head trauma after falling from the stairs, which worsened her motor impairment. Brain MRI showed hypoplasia of the anterior cerebellar vermis and left cerebellar hemisphere, large retrocerebellar cyst, enlarged cistern magna, ventricular enlargement, mild hypoplasia of pons and brain stem, irregular gyri of the cerebral cortex with irregular depth of the sulci in frontal and perisylvian areas, small heterotopic nodule of grey matter and thin and hypoplastic corpus callosum (both rostrum and splenium).

Female 17 is the one of 3 children of non-consanguineous parents. There was no family history of developmental delay. Delivery was possibly complicated with hypoxia. Physical examination after birth revealed bilateral post-axial polydactyly and anal atresia with fistula requiring surgery at later age. Moreover, she had brachycephaly, general hypotonia and facial dysmorphisms, by the clinical geneticist suspicious found for Kaufman-McKusick, but no definitive diagnosis could be made. Her development was delayed with both motor and language delay. She walked her first steps at the age of 2.5 years and her speech started at normal age but developed slow. She followed special education. Psychological assessment

showed mild to moderate ID with an IQ of 50. The first four years of life, she had frequent respiratory infections. Small auditory canals were present. At later age, she was again referred to the pediatrician for the development of hirsutism, mainly at the back, chest and face. Her mensis started normal at the age of 12 years, but was irregular. She had severe pedes planus and shortening of both Achilles tendons, requiring surgery. There was general hypotonia present. Until adolescence, her growth was normal, but from the age of 12 she was shorter than expected. Physical examination at the age of 16 years showed a height of 156 cm (-2 SD) with target height of 175 cm (+1 SD), weight of 59.8 kg (+2 SD) and head circumference of 55 cm (0 SD). She had some facial dysmorphisms including narrow palpebral fissures, hypotelorism, bilateral ptosis and extra canine tooth. Her chest was broad and showed hirsutism, as well as her back. Both hands and feet were short with shortening of the fourth digit and Simean crease of the right hand. She had a sandal gap at her left foot. There was hyperlaxity of her wrists and fingers, but no general hyperlaxity. Evaluation of her skin revealed Blaschko lines at both arms. Previous SNP array revealed no abnormalities. After identification of the first females she was, based on her phenotype, found suspicious to have a USP9X mutations or deletion. Sanger sequencing showed no abnormalities, but re-evaluation of the SNP array data showed three negative probes in the USP9X region. The deletion Xp11.4(41,032,491-41,059,516)x1 was confirmed with CytoScan HD array, which had better coverage of the X-chromosome.

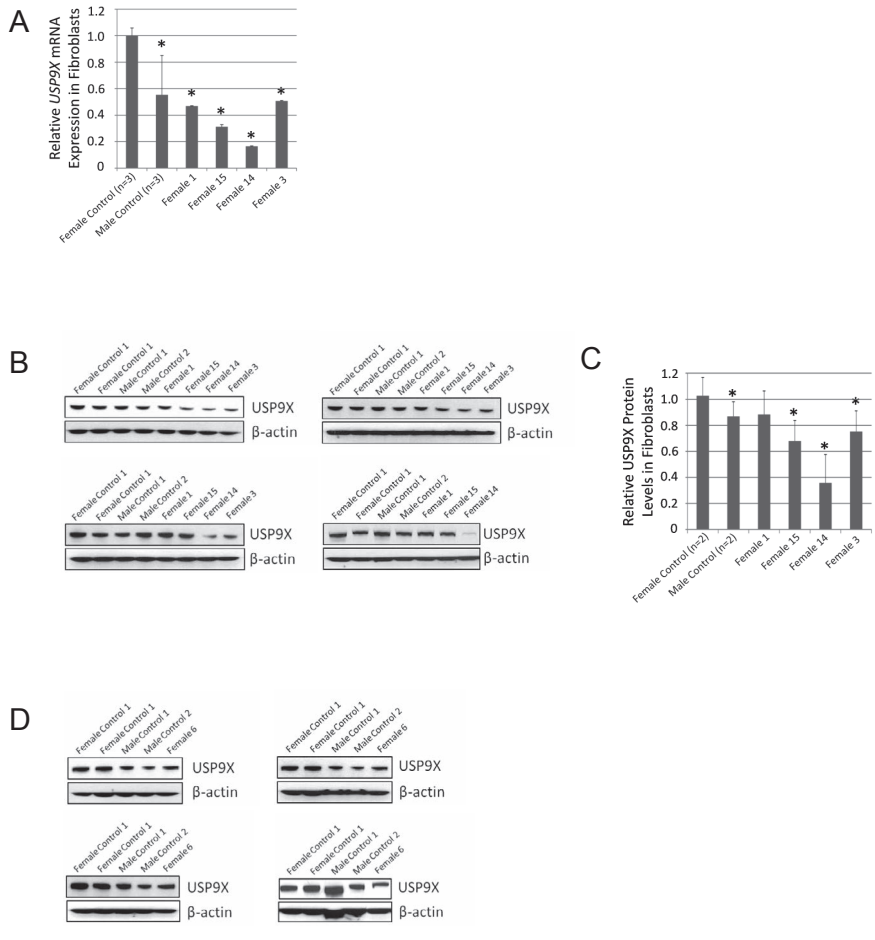

Figure S1: USP9X expression is depleted in female cell lines harbouring loss of function alleles.
Fibroblast and LCL cell lines from control female and male individuals, and females with heterozygous loss of function USP9X alleles were derived and cultured under established conditions.1; 2Isolation of mRNA, and protein was conducted as previously described. 3

(A) Relative qPCR analysis of USP9X mRNA in individual fibroblast cell lines. cDNA synthesis, qPCR conditions and ACTNB primers were as previously described.1; 4 USP9X primers used were F: TTGTGAACTCTGTCCAGAGG and R: GTTCATCTGGAGCATCTTGG.

(B) Immunoblot analysis of USP9X protein levels in fibroblast cell lines. SDS-PAGE and immunoblots were performed as previously described.5 Each panel represents a replicate experiment.

(C) Quantification of immunoblots in B using ImageJ software (NIH).

(D) Immunoblot analysis of USP9X protein levels in LCL cell lines. Each panel represents a replicate experiment.*$p<0.05$ by Student's t-test.

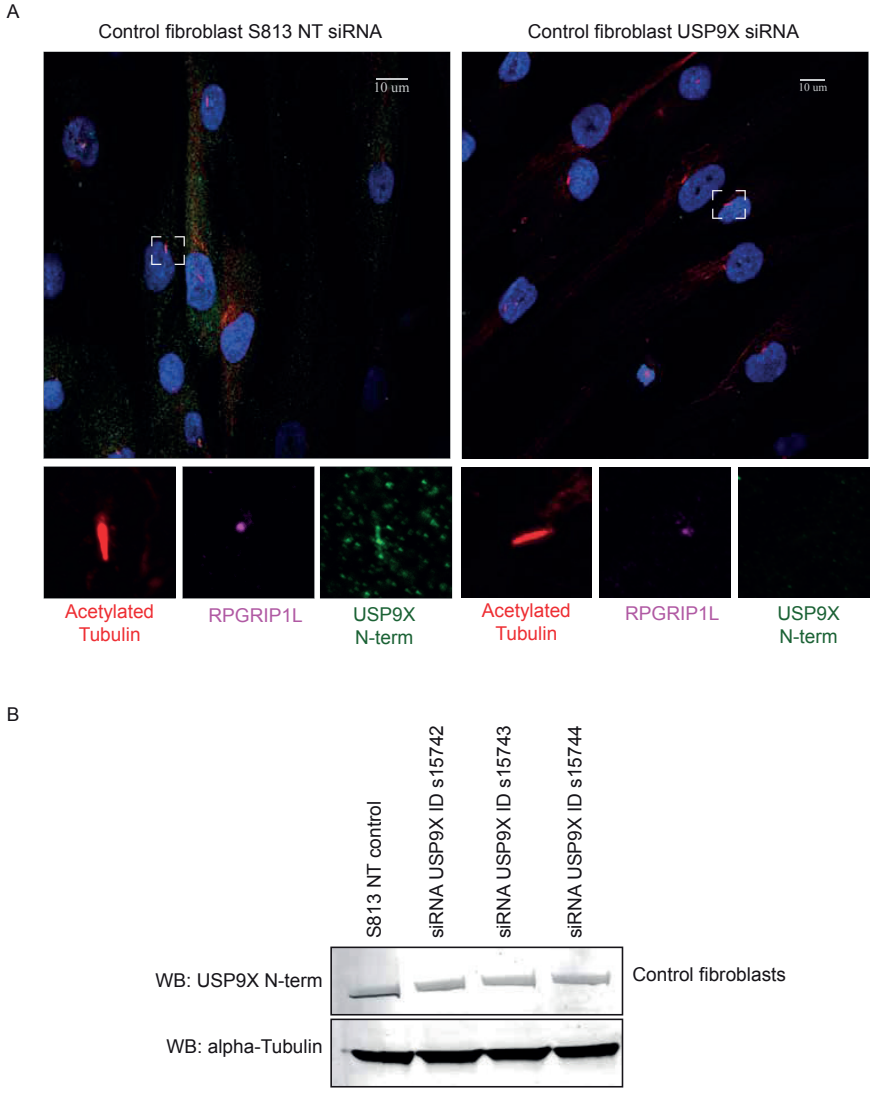

Figure S2: Decreased levels of USP9X in response to siRNA knock down

(A) Immunofluorescence imaging of control fibroblasts transfected with either S813 non-targeting siRNA or USP9X siRNA

(B) Western blotting of control fibroblasts demonstrating a decrease in USP9X protein levels in response to 3 different USP9X targeting siRNAs when compared with the control S813 nontargeting siRNA. Scale bars represent 10 µm.

A

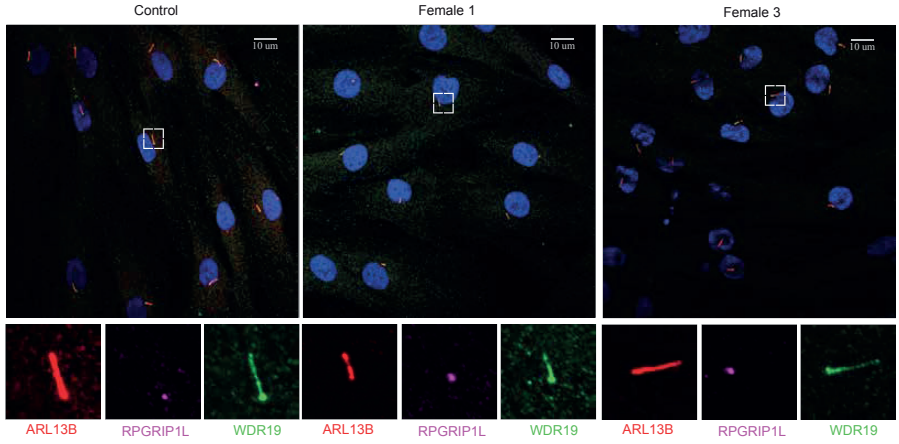
Control
Female 1
Female 3
10 um
10 um
10 um
ARL13B
RPGRIP1L
WDR19
ARL13B
RPGRIP1L
WDR19
ARL13B
RPGRIP1L
WDR19

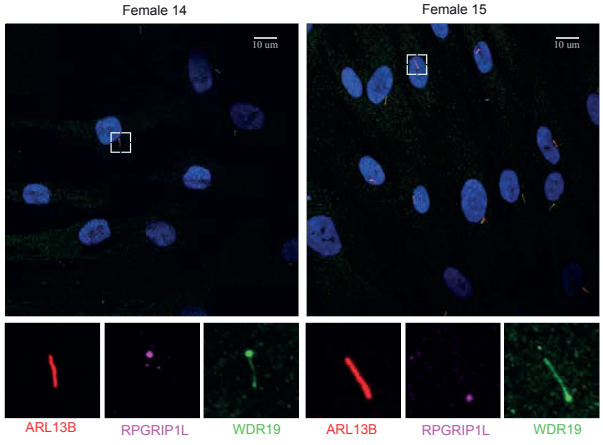
Female 14
Female 15
10 um
10 um
ARL13B
RPGRIP1L
WDR19
ARL13B
RPGRIP1L
WDR19

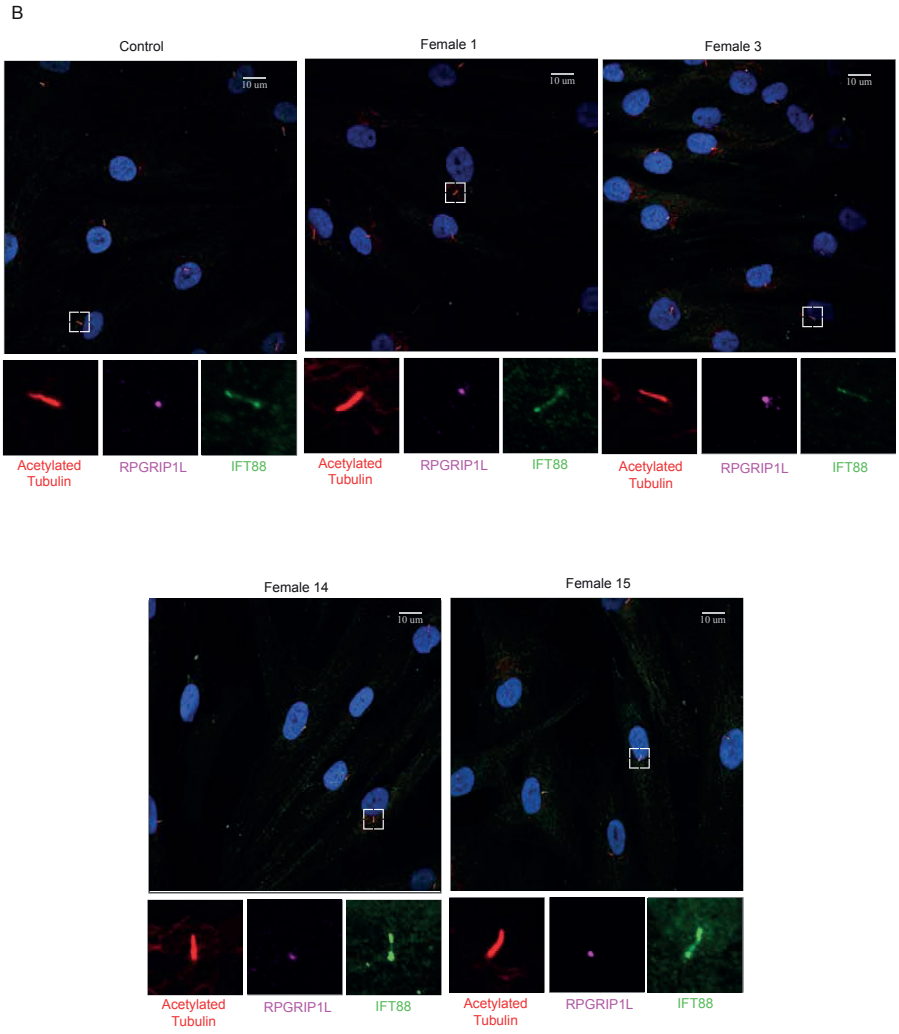

Figure S3: Ciliary architecture and ciliary trafficking are normal in affected female fibroblasts
(A) Immunofluorescence imaging of control fibroblasts and USP9X female fibroblasts. To induce ciliogenesis, fibroblasts were starved for 48 hours prior to immunofluorescence labeling. DAPI is used for nuclear staining and is shown in blue, RPGRIP1L denotes the ciliary transition zone at the base of the cilium and is shown in pink, acetylated alpha-tubulin marks the primary cilium and is shown in red, and WDR19, used as a IFT-A marker, is shown in green and (B) IFT88, used as a IFT-B marker, is shown in green. Scale bars represent 10 µm.

Table S1: Mutations in *USP9X*

Female	Deletion breakpoints (Hg19)	Nucleotide change (NM_001039590.2)	Amino acid change	Mosaic in blood
1	-	c.2554C>T	p.(Arg852*)	no
2	-	c.3804T>A	p.(Tyr1268*)	Yes[a]
3	-	c.3028-2A>G	p.(?)	no
4	-	c.2644_2645insA	p.(Arg882Glnfs*3)	no
5	Minimum: ChrX:41082619-41090198; Maximum: ChrX:41082474-41092226	-	-	no
6	ChrX: 40926769-41148506	-	-	no
7	-	c.1986-1G>T	p.(?)	no
8	-	c.5078T>G	p.(Leu1693Trp)	no
9	-	c.4082delTinsTGG	p. (Ser1363Glyfs*18)	no
10	-	c.7492_7507delCAAGATGC TCCAGATGinsC	p.(Asp2499_Glu2503del)	no
11	-	c.3763C>T	p.(Gln1255*)	no
12	-	c.1111C>T	p.(Arg371*)	no
13	-	c.1154_1155delGAinsG	p.(Met386Trp fs*13)	no
14	-	c.3709del	p.(Cys1237Valfs*2)	no
15	ChrX: 40998091-41057271	-	-	no
16	-	c.4055dup	p.(Phe1353Leufs*18)	no
17	ChrX: 41032491-41059516	-	-	no

[a] Visualization of Sanger sequencing results on next page

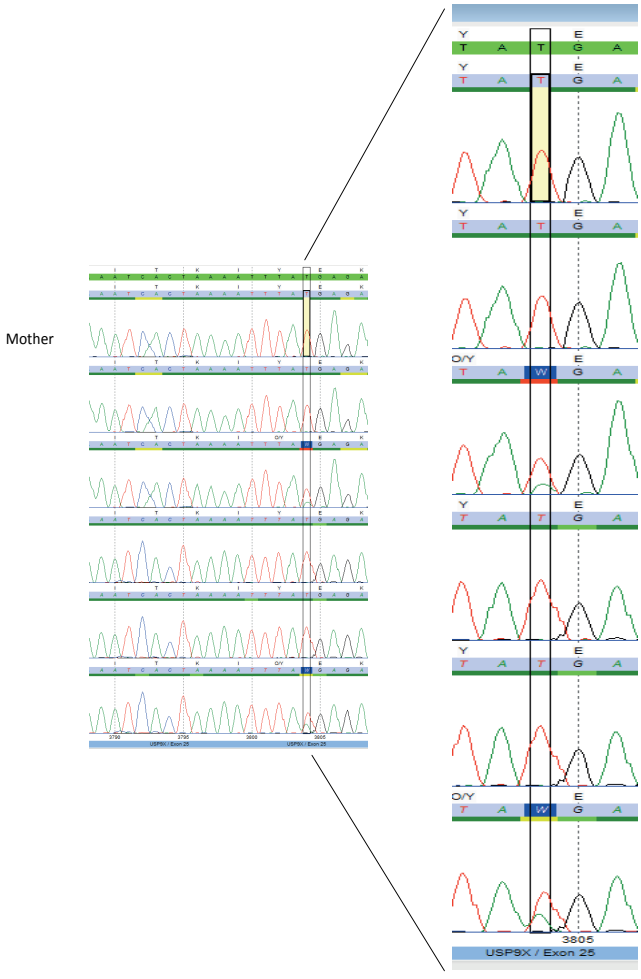
Mother
3805
USP9X / Exon 25

Table S2: clinical details of females with *de novo USP9X* defects

	Female 1	Female 2	Female 3	Female 4	Female 5[a]	Female 6	Female 7[b]	Female 8[c]	Female 9	Female 10	Female 11	Female 12[c]	Female 13[c]	Female 14	Female 15	Female 16	Female 17
Identification	WES	WES	WES	WES	Array CGH	SNP array	WES	WES	WES	WES	WES	WES	WES	WES	CSHD	Sanger	CSHD
Age of examination	9y3m	2y11m	14y	7y	9y	2y7m	9y5m	8y10m	7y7m	9y	16y	7y	6y	23y	22y	8y	16y
Growth																	
Short stature	+	+	-	-	+	+	+	-	-	-	+	+	NR	-	+	-	+
Development																	
Intellectual disability	+	TBA	+	+	+	TBA	+	+	+	+	+	+	+	- (IQ 85)	+ (IQ 65)	+	+ (IQ 50)
Language and motor delay	+	+	+	+	+	+	+	+	+	+	+	+	+	+	+	+	+
Congenital abnormalities																	
Eye abnormality	+	+	+	-	-	+	+	-	+	-	+	+	-	+	+	-	-
Choanal atresia	-	+	+	-	-	-	-	-	+	-	-	+	-	+	+	-	-
Cleft/bifid uvula	-	-	+	-	+	-	-	-	+	-	-	+	-	-	+	-	-
Dental abnormalities	+	+	+	-	+	-	+	-	+	+	+	+	+	-	+	-	+
Hearing loss	+	+	-	-	-	+	+	-	+	-	+	+	+	+	+	+	-
(Asymmetric) Hypomastia	-	+	+	-	-	-	+	-	-	-	-	-	-	+	+	-	-
Heart abnormality	+	-	-	-	+	-	+	-	+	NR	-	+	-	+	-	+	-
Kidney abnormality	+	+	-	-	+	-	-	-	-	+	+	-	-	-	-	-	-
Genital abnormality	-	-	-	-	-	-	-	-	-	+	+	-	-	-	-	+	-
Sacral dimple	-	+	-	-	+	-	+	-	-	-	-	+	-	+	-	-	-
Scoliosis	+	-	+	+	+	-	+	+	+	+	-	+	-	+	+	-	-
Hip dysplasia	+	-	-	-	+	+	+	+	-	-	+	-	+	-	+	-	-
Post-axial polydactyly	-	+	+	-	-	-	+	-	-	-	+	+	-	+	+	+	+
Abdominal wall abnormalities	+	-	-	-	-	-	+	-	-	-	-	-	-	-	-	-	-
Anal atresia/ventral anus	-	+	+	-	-	-	+	-	+	-	-	+	-	+	+	+	+
Other																	
Seizures	+	-	-	+	-	-	-	+	-	-	-	-	-	-	-	+	-
Hypotonia	+	+	-	-	-	+	+	+	+	-	-	+	-	-	-	-	+
(Blaschko) pigment abnormalities	+	-	+	+	-	-	-	-	+	+	+	+	+	+	+	-	+
Hypertrichosis	-	+	+	-	-	-	-	+	-	-	-	+	-	-	-	-	+
Leg length discrepancy	-	-	-	-	+	-	+	+	+	+	-	-	-	+	+	-	-
Malignancy	+	-	-	-	-	-	-	-	-	-	-	-	-	+	-	-	-
Recurrent URT infections	+	+	+	-	-	-	-	-	+	+	-	+	-	+	-	+	+
Hypothyreoidism	-	+/-[d]	+	+	-	-	+/-[d]	-	-	+/-[d]	-	-	-	-	-	+	-
MRI																	
DWM (variant)	-	-	-	+	+	NP	+	-	-	NP	NP	+	-	+	-	-	NP
Hypoplastic corpus callosum	+	+	+	-	+	NP	+	-	-	NP	NP	+	-	+	-	+	NP
Cerebellar hypoplasia	+	+	+	-	NR	NP	+	-	-	NP	NP	+	-	NR	-	+	NP
Enlarged ventricles	+	+	+	+	NR	NP	+	-	+	NP	NP	+	-	NR	-	+	NP
Thin brain stem	+	+	-	-	NR	NP	NR	-	-	NP	NP	-	-	NR	-	+	NP
Frontal lobe abnormality	+	+	+	+	NR	NP	NR	-	-	NP	NP	-	-	NR	-	+	NP

List of abbreviations: CSHD = CytoScan HD; DWM = Dandy Walker Malformation; IQ = intelligence quotient; M = month; NP = not performed; NR = not reported; URT = Upper Respiratory Tract; TBA = To Be Assessed; WES = whole exome sequencing; Y = years

[a] This female has also a *de novo PTPN11* [MIM 176876] mutation; [b] Previously reported in Brett et al, 2014[6]; [c] Previously reported in Wright et al, 2014[7]; [d] Abnormal TSH with normal FT4 levels or Normal TSH with abnormal FT4 levels

Table S3: X-inactivation in fibroblasts or LCL of *USP9X* affected females

Female	Mutation	Cell line Type	Skewing	Test
1	c.2554C>T (p.Arg852*)	Fibroblast	52.7%	FRAXA
3	c.3028-2A>G	Fibroblast	92.9%	AR
6	ChrX:40926769-41148506 del	LCL	96.6%	FRAXA
14	c.3709del (p.Cys1237fs)	Fibroblast	68,4%	FRAXA
15	ChrX:40998091-41057271 del	Fibroblast	93.6%	AR

Abbreviation: LCL = lymphoblastoid cell line

SUPPLEMENTAL REFERENCES

1. Nguyen LS, J.L., Shoubridge C, Chan WK, Huang L, Laumonnier F, Raynaud M, Hackett A, Field M, Rodriguez J, Srivastava AK, Lee Y, Long R, Addington AM, Rapoport JL, Suren S, Hahn CN, Gamble J, Wilkinson MF, Corbett MA, Gecz J. (2012). Transcriptome profiling of UPF3B/NMD- deficient lymphoblastoid cells from patients with various forms of intellectual disability. Mol Psychiatry 17, 1103-1115.
2. Tan, C., Shard, C., Ranieri, E., Hynes, K., Pham, D.H., Leach, D., Buchanan, G., Corbett, M., Shoubridge, C., Kumar, R., et al. (2015). Mutations of protocadherin 19 in female epilepsy (PCDH19-FE) lead to allopregnanolone deficiency. Hum Mol Genet 24, 5250-5259.
3. Jolly, L.A., Taylor, V., and Wood, S.A. (2009). USP9X enhances the polarity and self-renewal of embryonic stem cell-derived neural progenitors. Mol Biol Cell 20, 2015-2029.
4. Stegeman, S., Jolly, L.A., Premarathne, S., Gecz, J., Richards, L.J., Mackay-Sim, A., and Wood, S.A. (2013). Loss of Usp9x disrupts cortical architecture, hippocampal development and TGFbeta-mediated axonogenesis. PLoS One 8, e68287.
5. Homan, C.C., Kumar, R., Nguyen, L.S., Haan, E., Raymond, F.L., Abidi, F., Raynaud, M., Schwartz, C.E., Wood, S.A., Gecz, J., et al. (2014). Mutations in USP9X are associated with X-linked intellectual disability and disrupt neuronal cell migration and growth. Am J Hum Genet 94, 470-478.
6. Brett, M., McPherson, J., Zang, Z.J., Lai, A., Tan, E.S., Ng, I., Ong, L.C., Cham, B., Tan, P., Rozen, S., et al. (2014). Massively parallel sequencing of patients with intellectual disability, congenital anomalies and/or autism spectrum disorders with a targeted gene panel. PLoS One 9, e93409.
7. Wright, C.F., Fitzgerald, T.W., Jones, W.D., Clayton, S., McRae, J.F., van Kogelenberg, M., King, D.A., Ambridge, K., Barrett, D.M., Bayzetinova, T., et al. (2014). Genetic diagnosis of developmental disorders in the DDD study: a scalable analysis of genome-wide research data. Lancet.

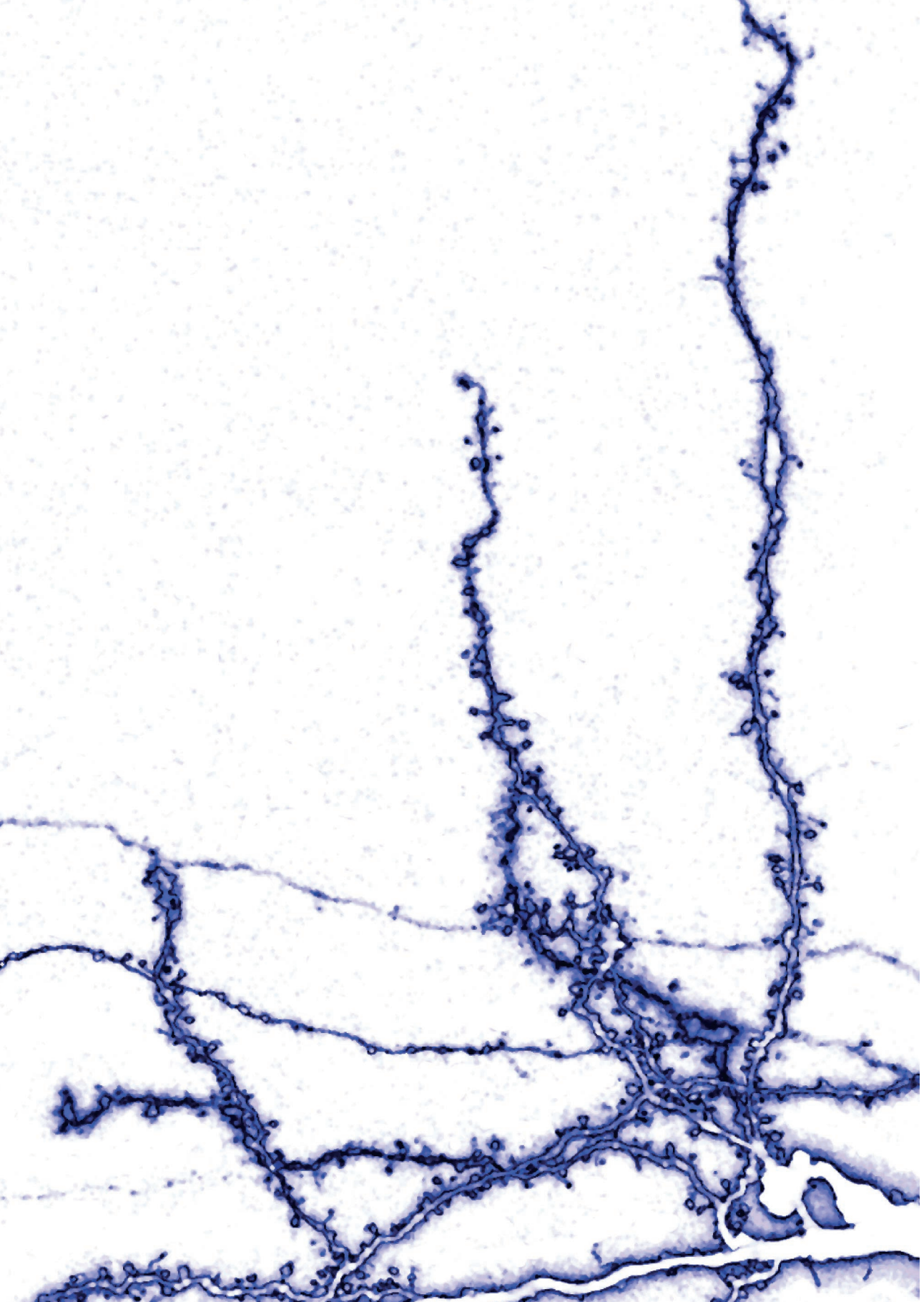

5

CHAPTER

Loss-of-function mutations in *USP9X* disrupt ciliary architecture in iPSC-derived neural progenitors

B. Latour (1,2), T.M. Klein Gunnewiek (1,3,4),
R. Roepman (1,2), N. Nadif Kasri (1,4), P. Antony (5)

1. Department of Human Genetics, Radboud University Medical Center, Nijmegen, The Netherlands.
2. Radboud Institute for Molecular Life Sciences, Radboud University Medical Center, Nijmegen, The Netherlands.
3. Department of Anatomy, Radboudumc, Donders Institute for Brain, Cognition, and Behaviour, Nijmegen, The Netherlands.
4. Department of Cognitive Neuroscience, Radboudumc, Donders Institute for Brain, Cognition and Behavior, Nijmegen, The Netherlands.
5. Luxembourg Centre for Systems Biomedicine (LCSB), University of Luxembourg, Esch-sur-Alzette, Luxembourg.

ABSTRACT

USP9X is an X-linked deubiquitinase essential for neural development in humans and mice. In female patients, heterozygous *USP9X* loss-of-function (LOF) mutations present with a stereotypical brain phenotype characterized by enlarged asymmetrical ventricles, agenesis of the corpus callosum, and variable manifestation of Dandy Walker malformation. This neural phenotype closely resembles those observed in neuronal ciliopathies. To understand the tissue-specific role of USP9X in cilia and brain development, we studied the effects of LOF patient mutations on early stages of neurogenesis. Neural rosettes are a morphologically identifiable niche for neural progenitor cells that can be produced *in vitro* and recapitulate early neural tube formation in 2D. We observed that during early differentiation circa day 6, cilia are ubiquitously found on most cell types throughout the 2D culture, and by day 10 of differentiation, cells display a polarized morphology and cilia are primarily localized to the apical lumens at the center of the neural rosettes. Using a segmentation analysis protocol for analyzing 3D organelle structures, we found that the rosettes of the USP9Xdel individual had volumetrically larger cilia than control rosettes. 3D rendering of the lumenal cilia demonstrated that the lumenal cilia in the USP9Xdel line were more disperse and loosely packed, while the counts and surface area of the lumenal cilia are comparable. Additionally, extra-lumenal cilia, defined as cilia outside the lumen of the rosettes, differed significantly in number and surface area. Specifically, USP9Xdel rosettes have significantly larger, longer and more extra-luminal cilia as compared to the control. This phenotype observed in the USP9Xdel line is reminiscent of the ciliary distribution observed in early rosettes. Our results indicate that LOF mutations in *USP9X* potentially affect neural development via the disruption of ciliary architecture.

INTRODUCTION

There is accumulating evidence that the ubiquitin machinery, involved in both ubiquitination and de-ubiquitination, plays an important role in the structure and function of the primary cilium. This is an antenna-like, sensory organelle that projects from the cell surface and plays an indispensable role in organogenesis via its role in cellular signaling. USP9X, an X-linked ubiquitin specific protease, has been described to play a role in ciliary and centrosomal biology [1,2] and is involved in a myriad of cellular functions from chromatin reprograming [3] to ribosomal stalling [4] and post-translation regulation of the ubiquitin precursors UBA52, UBA80, UBB and UBC [5]. In the brain, USP9X is indispensable for proper development and cortical architecture [6–8]. Missense mutations in *USP9X* are associated with intellectual disability in males and LOF mutations lead to a ciliopathy-like syndrome in females [9,10]. LOF mutations in *USP9X* manifest as a severe heterogeneous congenital disorder that affects multiorgan systems and results in a stereotypical brain phenotype characterized by enlarged asymmetrical ventricles, agenesis of the corpus callosum, and Dandy Walker malformation in approximately a third of individuals, [9,10] all of which are symptoms observed in neuronal ciliopathies [11–14].

Characterizing ciliary abnormalities in ciliopathies is often hindered by access to proper cell- and tissue types and analysis platforms. Differentiation protocols that give rise to neural progenitor and neuronal cell types are invaluable system for modeling brain development in ciliopathies that cannot be comprehensively assessed in other commonly used cell types such as patient-derived fibroblasts and immortalized cell lines. Three-dimensional segmentation analysis allows the visualization of organelle structure and localization. Morphological and positional changes in organelles can occur in response to for instance cell cycle state, nutrient deprivation [27,28] and disease-associated mutations [29]. Inducible pluripotent stem cells (iPS cells) allow researchers to model these effects in human cell types, such as neurons or neuronal progenitors. These polarized cell types contain complex and dynamic subdomains, that can require resolutions beyond the capacity of classical confocal microscopy for comprehensive analysis.

The use of *in vitro* modeling systems to investigate neural development, evolution, and disease has been a breakthrough for understanding the human brain. 2D and 3D culture systems can be used to model inherited and acquired diseases of the brain and understanding the spatial coordination of cellular processes that drive these trajectories represents a fundamental goal in biology. Advances in *in vitro* modeling systems that allow for the study of neuronal development and maturation further the need for tools to visualize and quantify dynamic changes in intracellular structures. Intracellular structure and localization patterns of organelles can be robustly assessed and biologically characterized using automated

segmentation analysis. Herein we assess cilia in neural rosettes with a segmentation analysis protocol previously validated in the assessment of mitochondria in neurons [15]. Due to the similarities in the overall shape and structure of cilia and mitochondria, we found that the translational segmentation platform could be used to assess both organelle types.

Neural rosettes are a morphologically identifiable, polarized epithelial niche for neural progenitor cells that can be generated in vitro via the dual SMAD inhibition neural induction protocol 16–19. Cilia, found in the central lumen, play a fundamental role in coordinating cellular responses to differentiation cues. Dual SMAD inhibition, involving the inhibition of BMP and TGFβ signaling pathways using Noggin or dorsomorphin and SB431542 respectively. Inhibition of BMP and TGFβ signaling inhibits the formation of the endodermal and mesodermal germ layers, thereby allowing for neuroectoderm differentiation. During early differentiation, neuroectoderm gives rise to neuroepithelium as seen in embryogenesis during neurulation, when the neural plate closes to form the neural tube 16.

During differentiation neuronal cell type specification is dependent on signal transduction via the primary cilium [20]. Cilia are enriched in multiple signaling receptors that transduce a variety of extracellular cues essential for cellular differentiation. During embryogenesis the cilium plays an indispensable role in neuroepithelial formation and patterning [21–25] Cilia are essential transducers of hedgehog (Hh) and Wnt signaling, which plays an indispensable role in ventral and dorsal patterning respectively in the neural tube [21,23,26].

Volumetric analysis of cilia in neuroepithelial rosettes has the potential to provide insight into ciliary formation patterns and organization. Advances in imaging methods such as Airyscan confocal imaging or super resolution stochastic optical reconstruction microscopy (STORM), provide ways of visualizing the tiniest of structures with increasing detail [29–31]. This creates a need for automated analysis- and quantification methods, that are open source for use and community scrutiny and improvement. Current protocols aimed at analyzing fluorescent imaging data, for instance specifically for mitochondria [32–34], are more often suited for larger, flat cell types (i.e. fibroblasts). In these cases, medium-to-high-throughput image analysis is either incomplete, in case of 2D images resulting from maximum projections, or time-consuming, when using image stacks. Specifically, our goal is to provide a simple-to-use protocol for automated medium-to-high throughput analysis of tubular/round organelle morphology and organization over multiple image stacks, which can be applied or adapted to any structural imaging experiment. We use this protocol to characterize the effects of *USP9X* loss-of-function mutations [9] on the polarization of neuroepithelial rosettes, as well as defects in ciliary volume, surface area, and position.

RESULTS

Ciliary structure and function are interdependent, and the architecture and number of cilia found in various tissues affects their capacity to transduce signal [35]. To determine potential ciliary defects, we analyzed neuroepithelial rosettes from various time points during neuronal differentiation and assessed lumenal and extra-lumenal cilia that form in neural rosette structures. Because LOF mutations in USP9X cause severe congenital malformation of the brain reminiscent of defects observed in neuronal ciliopathies, we utilized iPSCs derived from an individual female patient with a large chromosomal deletion in USP9X (ChrX 40998091-41057271) [9] (hereafter referred to as USP9Xdel) to characterize the absence of USP9X on cilia. No MRI data was available for the USP9Xdel individual, however they presented with mild intellectual disability (IQ of 65), motor and speech delay, mild sensorineural hearing loss, and multiple congential abnormalities including bilateral choanal atresia, anorectal malformation, post axial polydactyly, and a bifid uvula with submucosal cleft palate [9].

We generated neural rosettes using a dual SMAD inhibition protocol [18] starting from USP9Xdel- and control-derived IPSCs. The control used for all experiments was an age and gender matched healthy individual. This protocol [18] employs the inhibition of BMP and TGF-beta signaling pathways using dorsomorphin and SB431542 respectively (FIGURE 1A). For protocol validation, we assessed the expression of various neurogenesis markers in control rosettes on day 24. Day 24 was choose as it corresponded passage 1 in cell culture where the neuroepithelial rosettes should express markers of neural progenitor cells and early born neurons. Our analytical approach requires high axial resolution involving large z stacks with small inter-plane intervals, therefore we imaged 3D stacks using the Airyscan confocal. To process the large amount of resulting image data, we used a custom MATLAB image analysis algorithm for medium-to-high throughput automatic analysis, limiting the bias inherent to manual analysis [15]. The expression of PAX6 and CTIP2, Nestin and GFAP, and SOX2 and ARL13B (FIGURE 1B) were confirmed via immunofluorescent analysis of rosettes, demonstrating the presence of neuroepithelium (Nestin, SOX2), radial glial-like progenitors (PAX6, SOX2, GFAP, Nestin), and early born, post mitotic neurons (CTIP2). A time course analysis over the first 16 days of differentiation using qPCR demonstrated that transcripts associated with pluripotency were down regulated upon differentiation and neuroepithelium / radial glial associated transcripts such as PAX6 were upregulated visibly by day 8 (FIGURE 1C). The expression and efficiency of induction was correlated with the degree of cell confluence at the time of induction (FIGURE 1C). Due to expression profiles of neuroepithelial markers and patterns of cilia dispersion (FIGURE 1B-D), days 31 and 43 were selected for further analysis.

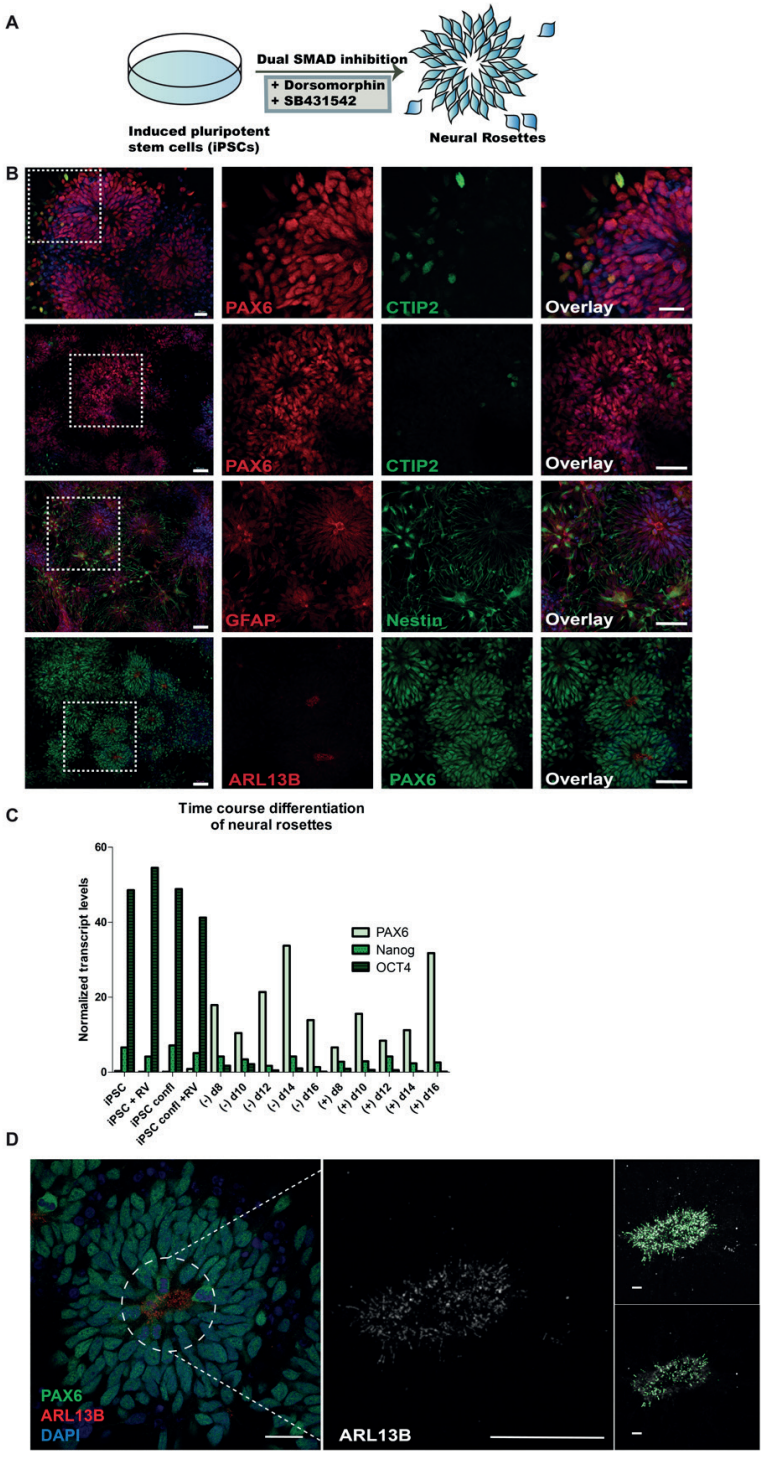
A
Dual SMAD inhibition
+ Dorsomorphin
+ SB431542
Induced pluripotent stem cells (iPSCs)
Neural Rosettes
B
PAX6
CTIP2
Overlay
PAX6
CTIP2
Overlay
GFAP
Nestin
Overlay
ARL13B
PAX6
Overlay
C
Time course differentiation of neural rosettes
Normalized transcript levels
60
40
20
0
PAX6
Nanog
OCT4
iPSC
iPSC + RV
iPSC confl
iPSC confl +RV
(-) d8
(-) d10
(-) d12
(-) d14
(-) d16
(+) d8
(+) d10
(+) d12
(+) d14
(+) d16
D
PAX6
ARL13B
DAPI
ARL13B

◀**FIGURE 1: Neural rosettes induction** (A) neural rosettes can be produced via the dual SMAD inhibition neural induction protocol shown here schematically. (B). Rosettes (DIV24) are positive for in vivo markers of neurogenesis, including PAX6, SOX2, nestin, GFAP, and CTIP2. Scale bar top row: 20 mm, all other scale bars: 50 mm. (C) qPCR analysis of samples collected during pre- and post-neural induction at days 8, 10, 12, 14, and 16. The minus sign indicates the iPSCs were plated at subconfluent levels at the time of induction. The plus sign indicates that the iPSCs were at 100% confluence at the time of neural induction. RV is Revita Cell (rock inhibitor). Performed in technical triplicate. N=1 (D) The lumens of each rosette (DIV24) are ciliated, recapitulating the architecture of the neural tube, shown here with ARL13B (red). Lumenal cilia can be assess in 3D via segmentation analysis, shown here as a compressed z-stack (middle panel). 3D (top) compression and 2D (bottom) single plane analysis of the right panel shows the automated segmentation assessment of ciliary shape and positioning, outlined in green. Scale bars are 20 microns in the left and middle panel, and 5 microns in the 2D and 3D compression analysis.

During early differentiation at day 6 and day 10, cilia are ubiquitously found on most cell types through the 2D culture (Figure 1D, Supplemental figure 2). By day 10, in control conditions, the cilia, though present on other cells, are primarily localized to the lumenal center of the neural rosettes where they protrude into the lumen (Supplemental figure 2). Over the course of differentiation, observable on days 24, 31, and 43, there is a loss of polarization in neural epithelial rosettes, demonstrated by the decrease in number of apical cilia and the rounded nuclei (Figure 1D, Supplemental figure 3).

We generated 3D imaging stacks at high magnification, using a Zeiss confocal microscope with Airyscan module (Supplemental figure 4A-B). The Airyscan detector on the LSM880 is able to deliver increased resolution and signal to noise ratio by utilizing a 32-channel GaAsP photomultiplier tube (PMT) array detector combined with linear devolution thereby achieving a resolution of 120 nm laterally (XY) and 350 nm axially (Z) (Supplemental figure 3B).

Utilizing this automated segmentation analysis, day 31 and 43 neuroepithelial cells from control and the USP9Xdel individual were fixed and analyzed for ciliary abnormalities. Lumenal and extra-lumenal ciliary were assessed for ciliary number, volume, shape, and distribution. To derive analytical data points from 3D Z-stacks of the cilia in neuroepthelial rosettes, first a median filter is applied to the Z plane images of the stacks, followed by background subtraction of the 3D rendering to determine which voxels represent cilia. After background subtraction, a global mask was defined via thresholding. In addition to the global mask, a local mask was defined via a difference of Gaussians, and subsequent thresholding. For computing the difference of Gaussians, the local background image was defined by convolution of the median filtered ARL13B channel with a Gaussian filter of size 11 and standard deviation 1.25. This local background image was subtracted from a foreground image defined by convolution of the median filtered mitochondrial channel with a Gaussian kernel of size 11 and standard deviation 1. The local ARL13B mask was defined by thresholding of the difference of Gaussians (>4). The final ARL13B mask was defined by Boolean AND operation on the local and global mitochondrial masks and subsequent removal of objects with less than 7 pixels (Supplemental figure 4A-C).

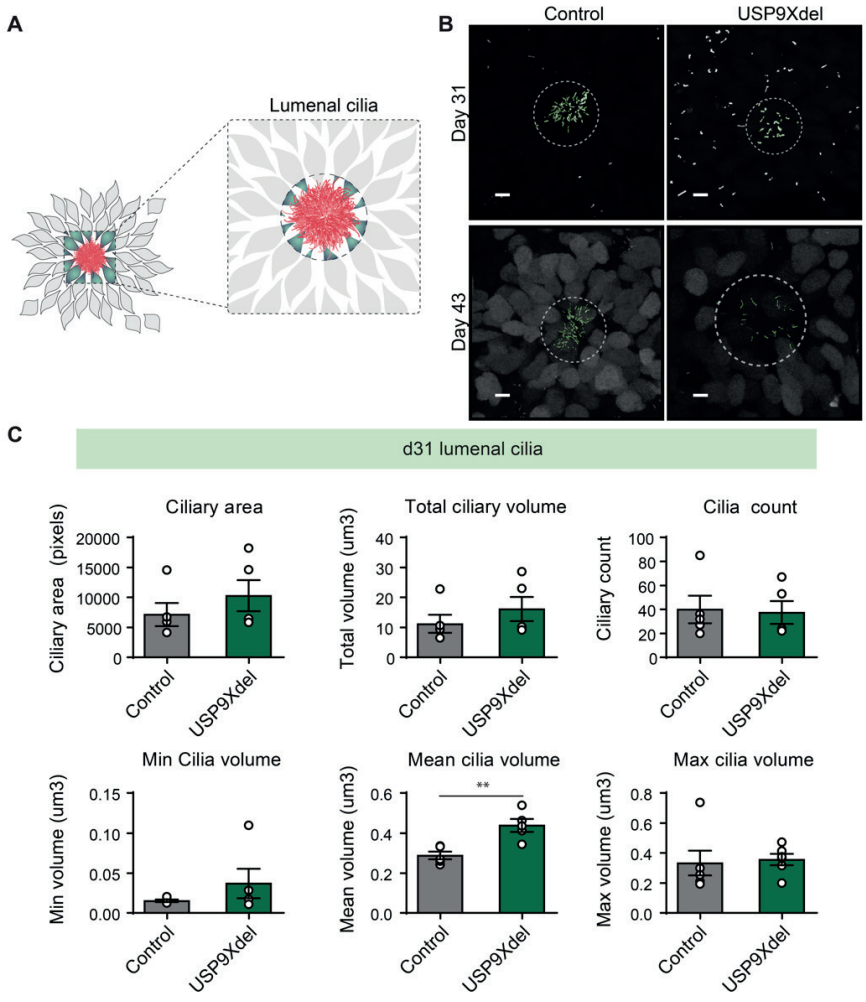
A
Lumenal cilia
B
Control
USP9Xdel
Day 31
Day 43
C
d31 lumenal cilia
Ciliary area
Ciliary area (pixels)
Total ciliary volume
Total volume (um3)
Cilia count
Ciliary count
Min Cilia volume
Min volume (um3)
Mean cilia volume
Mean volume (um3)
**
Max cilia volume
Max volume (um3)
Control
USP9Xdel

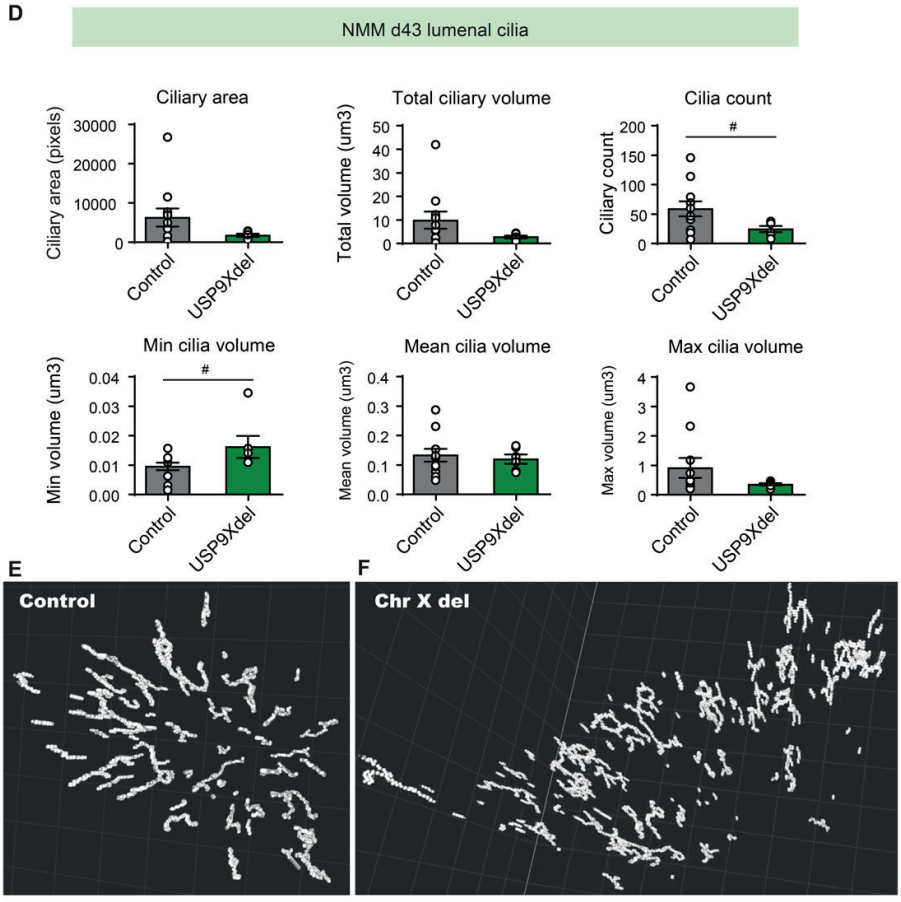

FIGURE 2: **The effects of LOF mutations in USP9X on neuroepithelial lumenal cilia morphology and organization.** (A) Schematic representation of the area selected for lumenal ciliary analysis. (B) Wide field view of cilia within control and USP9X rosettes. Specifically indicated are the lumenal cilia recognized for segmentation analysis (outlined in green) at day 31 and day 43 in control versus USP9Xdel rosettes. Scale bar indicates 5 microns. (C) Quantification of the differences in d31 lumenal cilia (Control n = 3; USP9Xdel n = 3). (D) Quantification of the differences in day 43 lumenal cilia (Control n = 3; USP9Xdel n = 3). NMM is neural maintenance medium without the growth factors necessary to maintain the cells in a primate state (E) 3D rendering of ARL13B stained lumenal cilia in the control line rosette on day 31. (F) 3D rendering of ARL13B stained lumenal cilia in the USP9Xdel line rosette on day 31. #P0.1-0.05, *P<0.05, **P<0.01, ***P<0.001, ****P<0.0001, a two-tailed student's T-test.

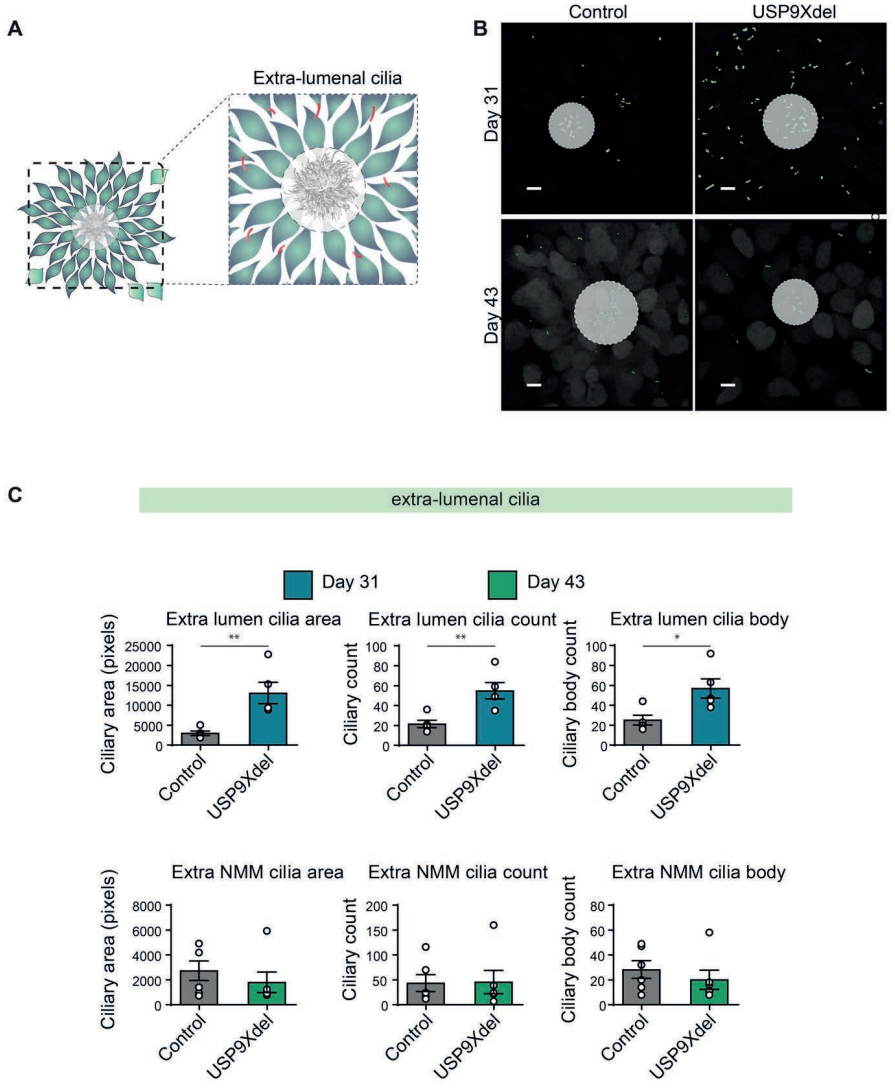

FIGURE 3: **The effects of LOF mutations in USP9X on neuroepithelial extra lumenal cilia morphology and organization during differentiation.** (A) Schematic representation of the area selected for extra lumenal ciliary analysis. The lumenal cilia count is subtracted from the selected area to obtain the extra-lumenal cilia count. (B) Wide field view of cilia within control and USP9X rosettes. Specifically indicated are the extra-lumenal cilia recognized for segmentation analysis (outlined in green) at day 31 and day 43 in control versus USP9Xdel rosettes. Scale bars are equal to 5 mincrons. (C) Quantification of the differences in day 31 and day 43 extra-lumenal cilia (Control n = 3; USP9Xdel n = 3). #P0.1-0.05, *P<0.05, **P<0.01, ***P<0.001, ****P<0.0001, a two-tailed student's T-test.

At day 31, the mean volume of lumenal cilia (FIGURE 2A-B) was found to be significantly greater in the USP9Xdel individual as compared to the control, indicating that the rosettes of the USP9Xdel individual had volumetrically larger cilia than the control (FIGURE 2C). 3D rendering of the lumenal cilia found in both the control (FIGURE 2E) and USP9Xdel lines, demonstrated that at day 31, the lumenal cilia in the USP9Xdel line are more disperse and loosely packed. While the counts and surface area of the lumenal cilia are comparable, the volumetric difference at this time point could be due to abnormalities in ciliary trafficking, when proteins cannot be trafficked out of the cilium, they bulge due to protein retention. This results in the abrogation of necessary signaling pathways and abnormal development. No significant difference was observed at day 43 in the volume, area, or count of cilia.

Additionally, at day 31, extra lumenal cilia (FIGURE 3A-B) differed significantly in number and area, with USP9Xdel rosettes have larger and more extra-luminal cilia. Interestingly, the USP9X patient cells maintain an extra lumenal ciliary distribution of early rosettes [36] longer than the control (FIGURE 2B; Figure 3B, C). This suggests that at earlier time points USP9Xdel progenitor cells may be delayed in differentiating. On day 35, the cells are transitioned to neural maintenance medium (NMM) lacking the necessary growth factors, specifically EGF and FGF, to maintain them in a primitive state. This supports the cells to differentiate into more mature, MAP2 expressing cells. At day 43, ciliary volume was found to be comparable between patient and control suggesting that at later timepoints USP9Xdel cells may differentiate more rapidly and thereby reduce the difference between the control and USP9Xdel individual (FIGURE 2D).

DISCUSSION

Here we report on an automated method for the segmentation and quantification of intracellular tubular-shaped structures, which we employed to begin to gain insight into changes that occur in organelle structure and localization in response to genetic perturbation. We used this method to quantify the effects of a LOF mutation affecting USP9X on cilia in neural rosettes. Our results demonstrate that 3D segmentation analysis is a powerful tool to assist in the elucidation of ciliary localization patterns, count and size during neural induction and maturation in health and disease. Utilizing unbiased analysis will allow for the investigation of ciliary associated structural and spatial dynamics that contribute to neuronal function, neural differentiation, neural progenitor proliferation, and neuroepithelial cell cycling.

Mutations in USP9X manifest as a severe heterogeneous congenital ciliopathy-like disorder that affects multiorgan systems, and in particular the brain [9,10]. Previous work demonstrates this protein localizes to the cilium [9] and centrioles [2] where it plays a role in the regulation of ciliogenesis and centriole duplication [1,2]. While no gross abnormalities in

ciliogenesis or ciliary architecture were observed in USP9X patient derived fibroblasts [9], we aimed to develop tools to ascertain ciliary abnormalities in the brain. To gain insight into the role of USP9X during neurodevelopment we quantitatively assessed the primary cilia in neuroepithelial rosettes.

During embryogenesis, USP9X is essential for cell fate decisions in the central nervous system [37], neuronal outgrowth and cortical architecture [6,38]. USP9X has a vast array of substrates and interacting partners (reviewed in [8]) that have been described to be involved in signal transduction pathways including Hedgehog signaling [39], mTOR [40,41] and WNT [42], all of which play a role in early neural development. In mammals, neurogenesis begins with the formation of neuroectoderm. Neuroectoderm gives rise to neuroepithelial progenitors that propagate neurogenesis in the neural tube. Neuroepithelial progenitors give rise to glial and basal progenitor cells. *In vivo* and *in vitro* neural rosettes form via apical constriction which involves the narrowing of the apical domain of apicobasal polarized cells (reviewed in [43]). The apically located primary cilia of the neuroepithelium extend into lumen of the neuroepithelia rosette, mimicking the *in vivo* development of the neural tube. It has previously been described that *in vitro*, early stage rosettes do not have cilia that localize to the lumen and instead have them dispersed throughout the neuroepithelial structure [36]. Accordingly, a hallmark sign of rosette maturation is the appearance of primary cilia in the lumenal space. This previous work [36] suggests that, in light of the increased levels of extra-lumenal cilia in the USP9Xdel rosettes observed at and prior to day 31, USP9Xdel cells may initially exhibit impaired differentiation as compared to control cells but with time are able to catch up in their maturation trajectory as defined by the localization of the primary cilium.

Previous work has demonstrated the Usp9x deletion in the mouse brain causes premature differentiation of cortical progenitors [42] and that NSC self-renewal and neurogenesis is impaired [44]. During murine neural development, the absence of USP9X has been correlated with a disruption in cell cycle and premature pattern of neural progenitor cells [6]. This potential divergence in results could be explained by species-specific differences, e.g. in mice, *Usp9x* does not escape x-inactivation [45] while in human it has been described to [46]. Premature differentiation of NPCs is often associated with microcephaly due to dysregulation of the NPC pool [47], however females with LOF mutations in USP9X did not exhibit symptoms of microcephaly. Instead, two of 17 cases described display macrocephaly [9], and macrocephaly has been previously associated with impaired differentiation [48]. Alternatively, Usp9x plays an important role in polarization, and disruption of polarization genes also results in premature differentiational of NPCs [49]. It is therefore possible that the extra lumenal cilia we observe at day 31 do not result from delayed maturation, but instead from disorganized polarization of

USP9Xdel neuroepithelium. Further experiments are necessary to determine the biological underpinnings of USP9Xdel on neuroepithelial differentiation.

MATERIALS & METHODS

Microscopy

Confocal Z-series stacks (acquired at 0.18 um intervals) of ciliary structures were collected on the Zeiss LSM880 confocal laser scanning microscope (405nm and 561nm diode lasers, argon (458, 488, 514nm) and a 633nm laser) equipped with the Airyscan detector, using the 63x Plan-Apochromat 1.4NA DIC oil immersion objective (Zeiss) and the 561 nm laser line. Zen 2.3 (black edition) software was used for Airyscan processing.

Image analysis

Image analysis was implemented using MATLAB 2018b. The raw tubular organelle analysis channel was median filtered using a 3x3x3 neighborhood. Next, a Gaussian filter of size 5 and standard deviation 2 was applied. After background subtraction, a global mask was defined by thresholding. In addition to the global mask, a local mask was defined via a difference of Gaussians, and subsequent thresholding. For computing the difference of Gaussians, the local background image was defined by convolution of the median filtered mitochondrial channel with a Gaussian filter of size 11 and standard deviation 1.25. This local background image was subtracted from a foreground image defined by convolution of the median filtered mitochondrial channel with a Gaussian kernel of size 11 and standard deviation 1. The local mitochondrial mask was defined by thresholding of the difference of Gaussians (>4). The final mitochondrial mask was defined by Boolean AND operation on the local and global mitochondrial masks and subsequent removal of objects with less than 7 pixels. For single cell analysis, this automated segmentation was combined with a manual segmentation of single cells using the MATLAB function roipoly. In contrast to this segmentation strategy, the extracted features were already previously described [15].

iPS cell generation and culture

The iPSCs and iNeurons were generated as previously described [50]. Control and UPS9X patient derived fibroblasts were reprogrammed to iPSCs through retroviral transduction of the Yamanaka factors Oct4, c-Myc, Sox2, and Klf4 [51]. USP9X patient and control iPSCs were maintained on Matrigel (VWR 356239), in E8 flex medium (Thermo Fisher Scientific A2858501)

supplemented with primocin (0.1 µg/ml, Invivogen ant-pm-1), and incubated at 37°C/5%CO2, with medium changes every 2-3 days, and passages 1-2 times per week using ReLeSR (Stem Cell Technologies). For a more detailed description, see [50].

Neuronal differentiation

Neuroepithelial rosettes were generated as previously described [19] using the dual SMAD inhibition protocol. in brief cells were dissociated using accutase and plated as single cells in E8 Flex medium supplemented with RevitaCell (ThermoFisher Scientific A2644501) in a 12 well plate coated with Matrigel. Once cells reached 95% confluence, they were switched to neural induction medium containing a 1:1 mixture of N2 and B27 medium (called neural maintenance medium NMM supplemented with 1 µM dorsomorphin (SelleckChem #S7306) and 10 µM SB431542 (called neural induction medium NIM). N2 medium is made up of DMEM/F12, N2 (GIBCO #17502-048), 5 µg/ml Insulin (GIBCO #13105002), 2mM GlutaMAX (GIBCO #35050038), 100 µM non-essential amino acids (Sigma-Aldrich #M7145), 100 µM 2-mercaptoethanol (GIBCO #21985023), primocin (Invivogen #ant-pm-2); B27 medium: Neurobasal (Invitrogen), B27 (GIBCO #0080085-SA), 2mM GlutaMAX, and primocin. Medium was changed every day for the first 10 – 12 days while being monitored for neuroepithelial induction based on change in morphology, cells were then split using ReLeSR to detach them in bulk from the Matrigel coated plate and then transferred onto PLO/laminin coated plates. Upon splitting, cells were kept for 24 hours in NIM and then switched to NMM supplemented with 10 ng/ mL EGF (PreproTech #AF-100-18B) and 10 ng/mL FGF (PreproTech #AF-100-18B). After P0 split onto laminin, NMM was changed every other day.

Immunofluorescence

To visualize the cilia, neuroepithelial cells were split onto nitric-acid treated coverslips coated with 50µg/mL poly-L-ornithine hydrobromide (PLO; Sigma-Aldrich #P3655-10MG) and 5 µg/mL human recombinant laminin 521 (BioLamina #LN521-02). At DIV 6, 10, 24, 31, and 42 cells were fixed using 4% PFA/Sucrose. Cells were imaged using a Zeiss LSM880 with Airyscan module, laser scanning microscope, equipped with 405nm and 561nm diode lasers, argon (458, 488, 514nm) and a 633nm laser, at 63X magnification (with oil).

Primary antibodies	Use	Host	Dilution	Manufacturer	cat #
ARL13B	Ciliary membrane marker	Mouse	1:300	NeuroMab	#75-287
CTIP2	Neuronal	Rat	1:200	Abcam	Ab18465
MAP2	Neuronal marker	Mouse	1:1000	Sigma	#ab16667
Sox2	NPC marker	Rabbit	1:300	Abcam	#ab97959
Nestin	NPC marker	Mouse	1:200	Thermo Scientific	#MA1-110
Pax6	NPC marker	Rabbit	1:300	Covance	#PRB-278P

Secondary antibodies	Dilution	Manufacturer	Prod. NO.
Goat anti-Rabbit Alexa Fluor 488	1:300	Invitrogen	#A11034
Goat anti-Mouse Alexa Fluor 586	1:300	Invitrogen	#A11031
Goat anti-Mouse Alexa Fluor 647	1:300	Invitrogen	#A21245
goat anti-guin.pig alexa Fluor 647	1:300	Invitrogen	#A21450

STATISTICAL ANALYSIS

Data are expressed as mean ± standard error of the mean (SEM). Analysis was done using one-way analysis of variance with Bonferroni post hoc correction, or two-tailed student's t-test, using GraphPad Prism 6 (GraphPad Software). P-values of $P<0.05$ and smaller, were deemed significant. Sample sizes were based on our previous experiences in the calculation of experimental variability, and are described, per experiment, in the corresponding figure legends.

REFERENCES

1. Das, A., Qian, J. & Tsang, W. Y. USP9X counteracts differential ubiquitination of NPHP5 by MARCH7 and BBS11 to regulate ciliogenesis. *PLoS Genet.* **13**, e1006791–24 (2017).
2. Kodani, A. *et al.* SFI1 promotes centriole duplication by recruiting USP9X to stabilize the microcephaly protein STIL. *J. Cell Biol.* **218**, 2185–2197 (2019).
3. Macrae, T. A. & Ramalho-Santos, M. The deubiquitinase Usp9x regulates PRC2-mediated chromatin reprogramming during mouse development. *Nat. Commun.* **12**, 1865 (2021).
4. Clancy, A. *et al.* The deubiquitylase USP9X controls ribosomal stalling. *J. Cell Biol.* **220**, e202004211 (2021).
5. Grou, C. P., Pinto, M. P., Mendes, A. V, Domingues, P. & Azevedo, J. E. The de novo synthesis of ubiquitin: identification of deubiquitinases acting on ubiquitin precursors. *Sci. Rep.* **5**, 12836 (2015).
6. Stegeman, S. *et al.* Loss of Usp9x Disrupts Cortical Architecture, Hippocampal Development and TGFβ-Mediated Axonogenesis. *PLoS One* **8**, e68287 (2013).
7. Yoon, S. *et al.* Usp9X Controls Ankyrin-Repeat Domain Protein Homeostasis during Dendritic Spine Development. *Neuron* **105**, 506-521.e7 (2020).
8. Murtaza, M., Jolly, L. A., Gecz, J. & Wood, S. A. La FAM fatale: USP9X in development and disease. (2015).
9. Reijnders, M. R. F. M. R. F. *et al.* De Novo Loss-of-Function Mutations in USP9X Cause a Female-Specific Recognizable Syndrome with Developmental Delay and Congenital Malformations. **98**, 373–381 (2016).
10. Au, P. Y. B. *et al.* Two females with mutations in USP9X highlight the variable expressivity of the intellectual disability syndrome. *Eur. J. Med. Genet.* **60**, 359–364 (2017).
11. Poretti, A., Huisman, T. A. G. M., Scheer, I. & Boltshauser, E. Joubert syndrome and related disorders: spectrum of neuroimaging findings in 75 patients. *AJNR. Am. J. Neuroradiol.* **32**, 1459–1463 (2011).
12. Walsh, D. M. *et al.* Acrocallosal syndrome: identification of a novel KIF7 mutation and evidence for oligogenic inheritance. *Eur. J. Med. Genet.* **56**, 39–42 (2013).
13. Andreu-cervera, A., Catala, M. & Schneider-maunoury, S. Neurobiology of Disease Cilia, ciliopathies and hedgehog-related forebrain developmental disorders. *Neurobiol. Dis.* **150**, 105236 (2021).
14. Foerster, P. *et al.* mTORC1 signaling and primary cilia are required for brain ventricle morphogenesis. *Development* **144**, 201–210 (2017).
15. Baumuratov, A. S. *et al.* Enteric neurons from Parkinson's disease patients display ex vivo aberrations in mitochondrial structure. *Sci. Rep.* **6**, 1–12 (2016).
16. Chambers, S. M. *et al.* Highly efficient neural conversion of human ES and iPS cells by dual inhibition of SMAD signaling. **27**, 275–280 (2009).
17. Tomishima, M. Neural induction Dual SMAD inhibition. (2008).
18. Shi, Y., Kirwan, P., Smith, J., Robinson, H. P. C. & Livesey, F. J. Human cerebral cortex development from pluripotent stem cells to functional excitatory synapses. *Nat. Neurosci.* **15**, 477–486 (2012).
19. Shi, Y., Kirwan, P. & Livesey, F. J. Directed differentiation of human pluripotent stem cells to cerebral cortex neurons and neural networks. **7**, 1836–1846 (2012).
20. Lee, J. H. Roles of Primary Cilia in the Developing Brain. *fncel-13-00218.tex* 1–10 (2019).
21. Huangfu, D. & Anderson, K. V. Cilia and Hedgehog responsiveness in the mouse. *Proc. Natl. Acad. Sci. U. S. A.* **102**, 11325–11330 (2005).

22. Ross, A. J. *et al.* Disruption of Bardet-Biedl syndrome ciliary proteins perturbs planar cell polarity in vertebrates. *Nat. Genet.* **37**, 1135–1140 (2005).

23. Wijgerde, M., McMahon, J. A., Rule, M. & McMahon, A. P. A direct requirement for Hedgehog signaling for normal specification of all ventral progenitor domains in the presumptive mammalian spinal cord. *Genes Dev.* **16**, 2849–2864 (2002).

24. Bay, S. N. & Caspary, T. What are those cilia doing in the neural tube? *Cilia* **1**, 1 (2012).

25. Briscoe, J. & Ericson, J. Specification of neuronal fates in the ventral neural tube. *Curr. Opin. Neurobiol.* **11**, 43–49 (2001).

26. Briscoe, J., Pierani, A., Jessell, T. M. & Ericson, J. A homeodomain protein code specifies progenitor cell identity and neuronal fate in the ventral neural tube. *Cell* **101**, 435–445 (2000).

27. Rambold, A. S., Kostelecky, B., Elia, N. & Lippincott-Schwartz, J. Tubular network formation protects mitochondria from autophagosomal degradation during nutrient starvation. *Proc. Natl. Acad. Sci. U. S. A.* **108**, 10190–10195 (2011).

28. Tang, Z. *et al.* Autophagy promotes primary ciliogenesis by removing OFD1 from centriolar satellites. *Nature* **502**, 254–257 (2014).

29. Shi, X. *et al.* Super-resolution microscopy reveals that disruption of ciliary transition-zone architecture causes Joubert syndrome. *Nat. Cell Biol.* **19**, 1178–1188 (2017).

30. Kolossov, V. L. *et al.* Airyscan super-resolution microscopy of mitochondrial morphology and dynamics in living tumor cells. *Microsc. Res. Tech.* **81**, 115–128 (2018).

31. Inavalli, V. V. G. K. *et al.* A super-resolution platform for correlative live single-molecule imaging and STED microscopy. *Nat. Methods* 1–11 (2019).

32. Iannetti, E. F. *et al.* Toward high-content screening of mitochondrial morphology and membrane potential in living cells. *Int. J. Biochem. Cell Biol.* **63**, 66–70 (2015).

33. Iannetti, E. F., Smeitink, J. A. M., Beyrath, J., Willems, P. H. G. M. & Koopman, W. J. H. Multiplexed high-content analysis of mitochondrial morphofunction using live-cell microscopy. *Nat. Protoc.* **11**, 1693–1710 (2016).

34. Wiemerslage, L. & Lee, D. Quantification of mitochondrial morphology in neurites of dopaminergic neurons using multiple parameters. *J. Neurosci. Methods* **262**, 56–65 (2016).

35. Goetz, S. C. & Anderson, K. V. The primary cilium: a signalling centre during vertebrate development. *Nat. Rev. Genet.* 1–14 (2010).

36. Banda, E. *et al.* Cell polarity and neurogenesis in embryonic stem cell-derived neural rosettes. *Stem Cells Dev.* **24**, 1022–1033 (2015).

37. Wood, S. A. *et al.* Cloning and expression analysis of a novel mouse gene with sequence similarity to the Drosophila fat facets gene. *Mech. Dev.* **63**, 29–38 (1997).

38. Homan, C. C. *et al.* Mutations in USP9X are associated with X-linked intellectual disability and disrupt neuronal cell migration and growth. *Am. J. Hum. Genet.* **94**, 470–478 (2014).

39. Breslow, D. K. *et al.* A CRISPR-based screen for Hedgehog signaling provides insights into ciliary function and ciliopathies. *Nat. Genet.* **50**, 460–471 (2018).

40. Bridges, C. R. *et al.* USP9X deubiquitylating enzyme maintains RAPTOR protein levels, mTORC1 signalling and proliferation in neural progenitors. *Sci. Rep.* **7**, 391 (2017).

41. Al-Hakim, A. K. *et al.* Control of AMPK-related kinases by USP9X and atypical Lys 29/Lys33-linked polyubiquitin chains. *Biochem. J.* **411**, 249–260 (2008).

42. Premarathne, S., Murtaza, M., Matigian, N., Jolly, L. A. & Wood, S. A. Loss of Usp9x disrupts cell adhesion, and components of the Wnt and Notch signaling pathways in neural progenitors. *Sci. Rep.* **7**, 8109 (2017).

43. Harding, M. J., McGraw, H. F. & Nechiporuk, A. The roles and regulation of multicellular rosette structures during morphogenesis. *Development* **141**, 2549–2558 (2014).

44. Oishi, S., Zalucki, O., Premarathne, S., Wood, S. A. & Piper, M. USP9X deletion elevates the density of oligodendrocytes within the postnatal dentate gyrus. *Neurogenesis* **3**, 1–9 (2016).

45. Berletch, J. B. *et al.* Escape from X inactivation varies in mouse tissues. *PLoS Genet.* **11**, e1005079–e1005079 (2015).

46. Carrel, L. & Willard, H. F. X-inactivation profile reveals extensive variability in X-linked gene expression in females. *Nature* **434**, 400–404 (2005).

47. Gabriel, E., Ramani, A., Altinisik, N. & Gopalakrishnan, J. Human Brain Organoids to Decode Mechanisms of Microcephaly. *Front. Cell. Neurosci.* **14**, 1–13 (2020).

48. Zhang, W. *et al.* Cerebral organoid and mouse models reveal a RAB39b-PI3K-mTOR pathway-dependent dysregulation of cortical development leading to macrocephaly/autism phenotypes. *Genes Dev.* **34**, 580–597 (2020).

49. Imura, T., Wang, X., Noda, T., Sofroniew, M. V. & Fushiki, S. Adenomatous polyposis coli is essential for both neuronal differentiation and maintenance of adult neural stem cells in subventricular zone and hippocampus. *Stem Cells* **28**, 2053–2064 (2010).

50. Klein Gunnewiek, T. M. *et al.* m.3243A>G-Induced Mitochondrial dysfunction impairs human neuronal development and reduces neuronal network activity and synchronicity. *Cell Rep.* **31**, 720227 (2020).

51. Takahashi, K. & Yamanaka, S. Induction of Pluripotent Stem Cells from Mouse Embryonic and Adult Fibroblast Cultures by Defined Factors. *Cell* **126**, 663–676 (2006).

SUPPLEMENTAL FIGURES

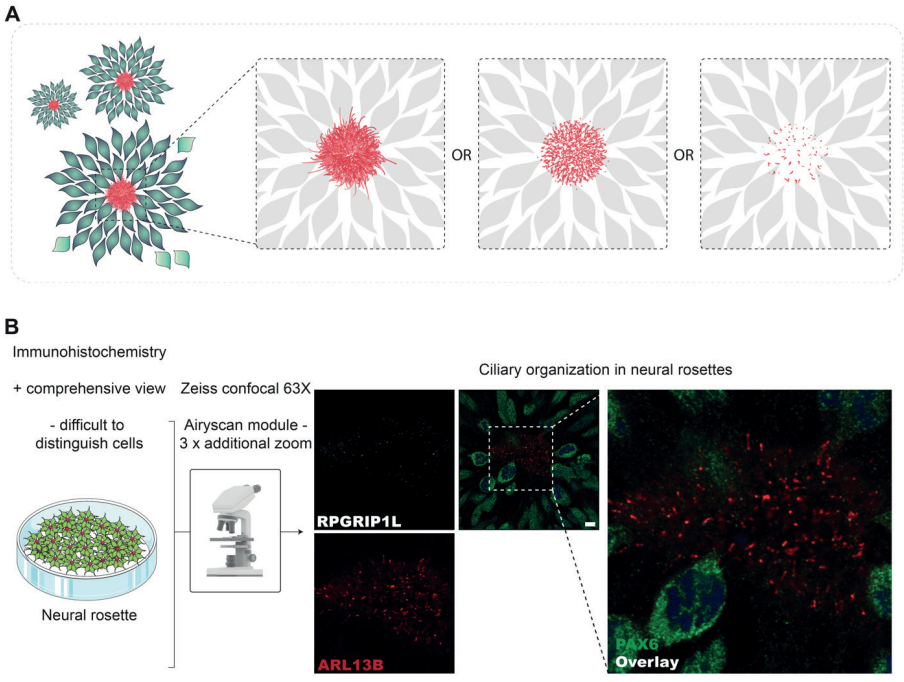

Supplemental FIGURE 1. Schematic representation of the biochemical processing pipeline, and visual representation of the staining strategy. (A) in vitro schematic of the variation observed in ciliated lumens of neuroepithelial rosettes. Samples are imaged at a high magnification and resolution (in this case, confocal microscopy using an Airyscan module for increased resolution at high magnification). (B) In vitro samples are immunohistochemically stained and assessed using the Zeiss confocal equipped with airyscan processing.

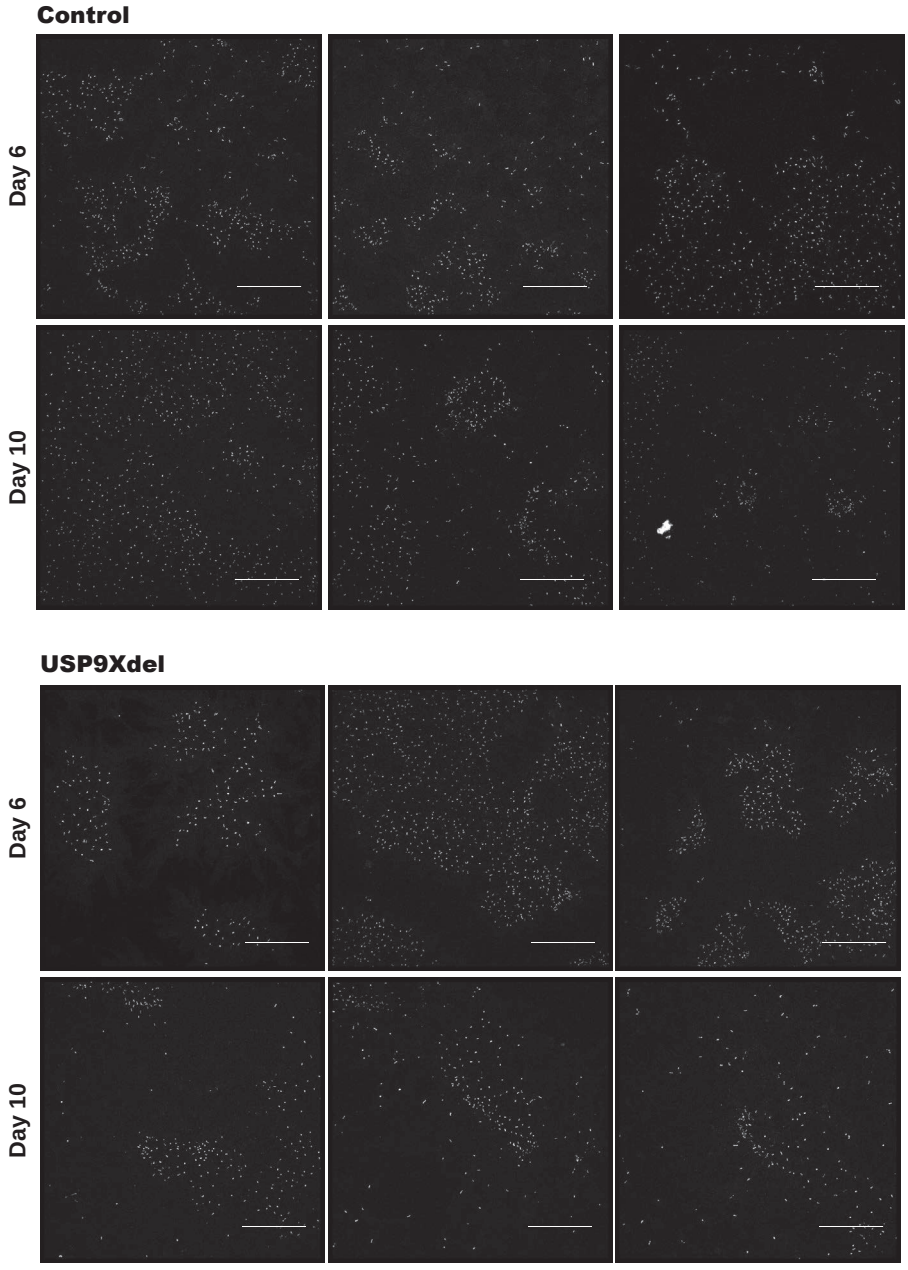

Supplemental figure 2: **Cilia localization across differentiating cultures as indicated by ARL13B staining on days 6 and 10 post dual SMAD inhibition treatment.** Images are compressed Z-stacks. Scale bars are 50 microns.

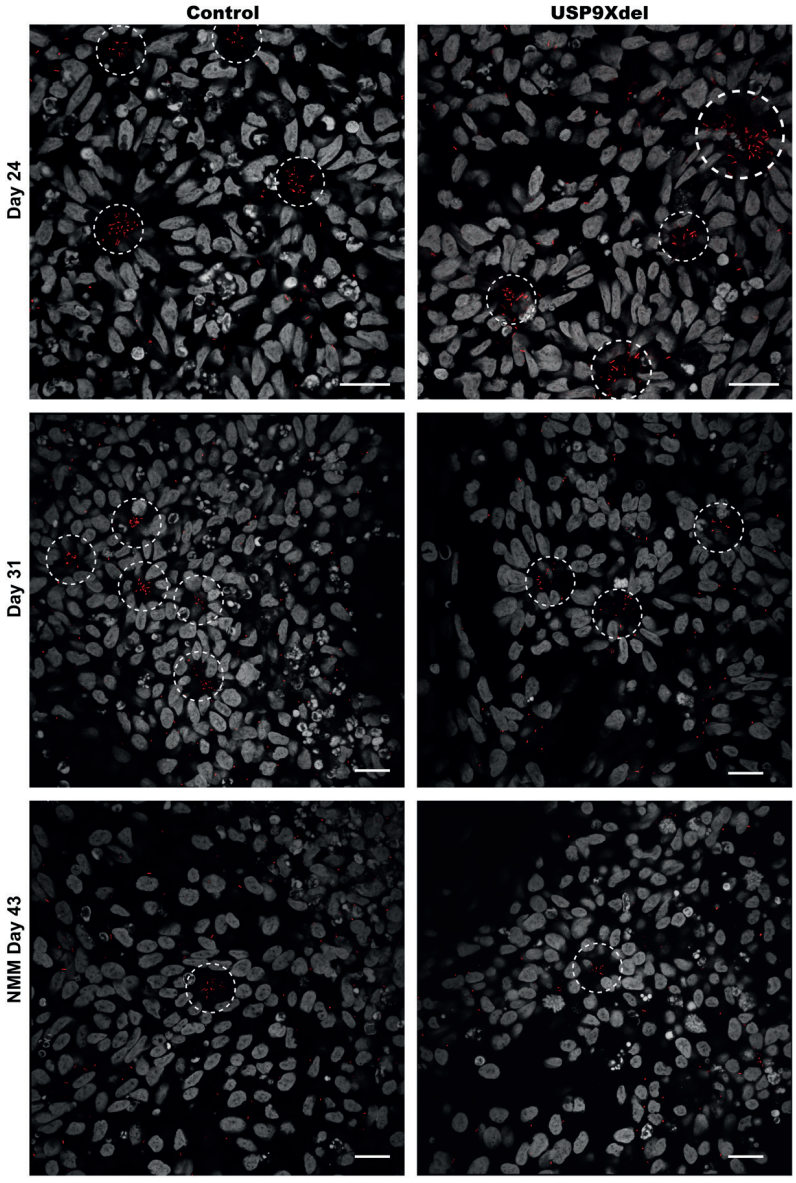

Supplemental figure 3: time course differentiation of neuroepithelium. Ciliary localization with DAPI (gray) across differentiating cultures as indicated by ARL13B (red) staining on days 24, 31 and 43 post dual SMAD inhibition induction. Ciliated lumens are indicated with a dashed white circle. Images are a single Z plane. Scale bars are 20 microns.

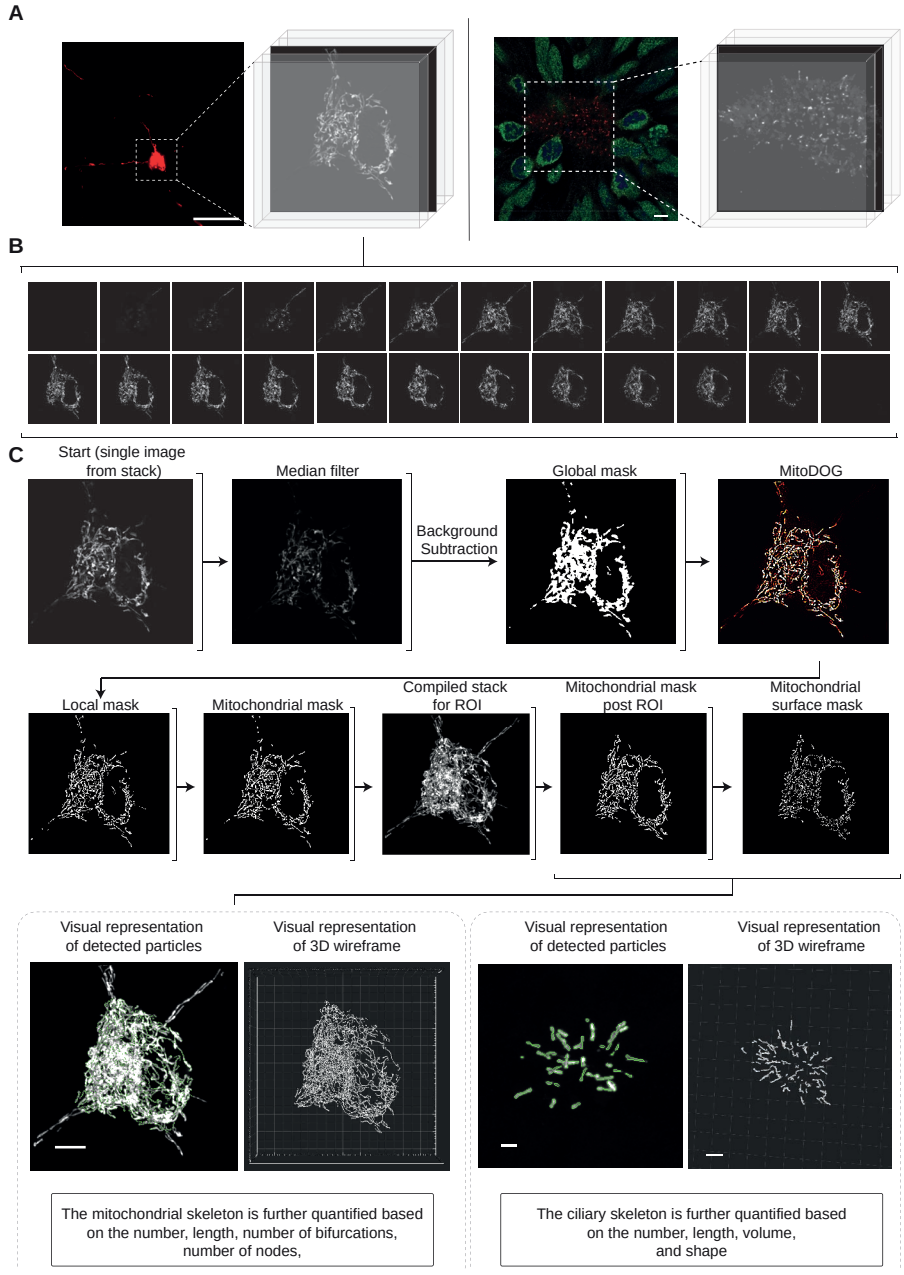
A
B
C
Start (single image from stack)
Median filter
Background Subtraction
Global mask
MitoDOG
Local mask
Mitochondrial mask
Compiled stack for ROI
Mitochondrial mask post ROI
Mitochondrial surface mask
Visual representation of detected particles
Visual representation of 3D wireframe
The mitochondrial skeleton is further quantified based on the number, length, number of bifurcations, number of nodes,
Visual representation of detected particles
Visual representation of 3D wireframe
The ciliary skeleton is further quantified based on the number, length, volume, and shape

◀**Supplemental FIGURE 4. Schematic representation of the separate processing steps included in the custom MATLAB protocol.** (A) By using Zeiss Airyscan module, we image the densely packed neuronal soma at higher resolution than possible with standard confocal microscopy. (B) To retain the 3D structure, we acquire several images in a z-axis orientation, starting and finishing "outside" of the neuron. (C) The images contained in the stack are subjected to several processing steps. A median filter is applied, followed by background subtraction to determine which signal represents mitochondrial signal. After background subtraction, a global mask was defined by thresholding. In addition to the global mask, a local mask was defined via a difference of Gaussians, and subsequent thresholding. For computing the difference of Gaussians, the local background image was defined by convolution of the median filtered mitochondrial channel with a Gaussian filter of size 11 and standard deviation 1.25. This local background image was subtracted from a foreground image defined by convolution of the median filtered mitochondrial channel with a Gaussian kernel of size 11 and standard deviation 1. The local mitochondrial mask was defined by thresholding of the difference of Gaussians (>4). The final mitochondrial mask was defined by Boolean AND operation on the local and global mitochondrial masks and subsequent removal of objects with less than 7 pixels.

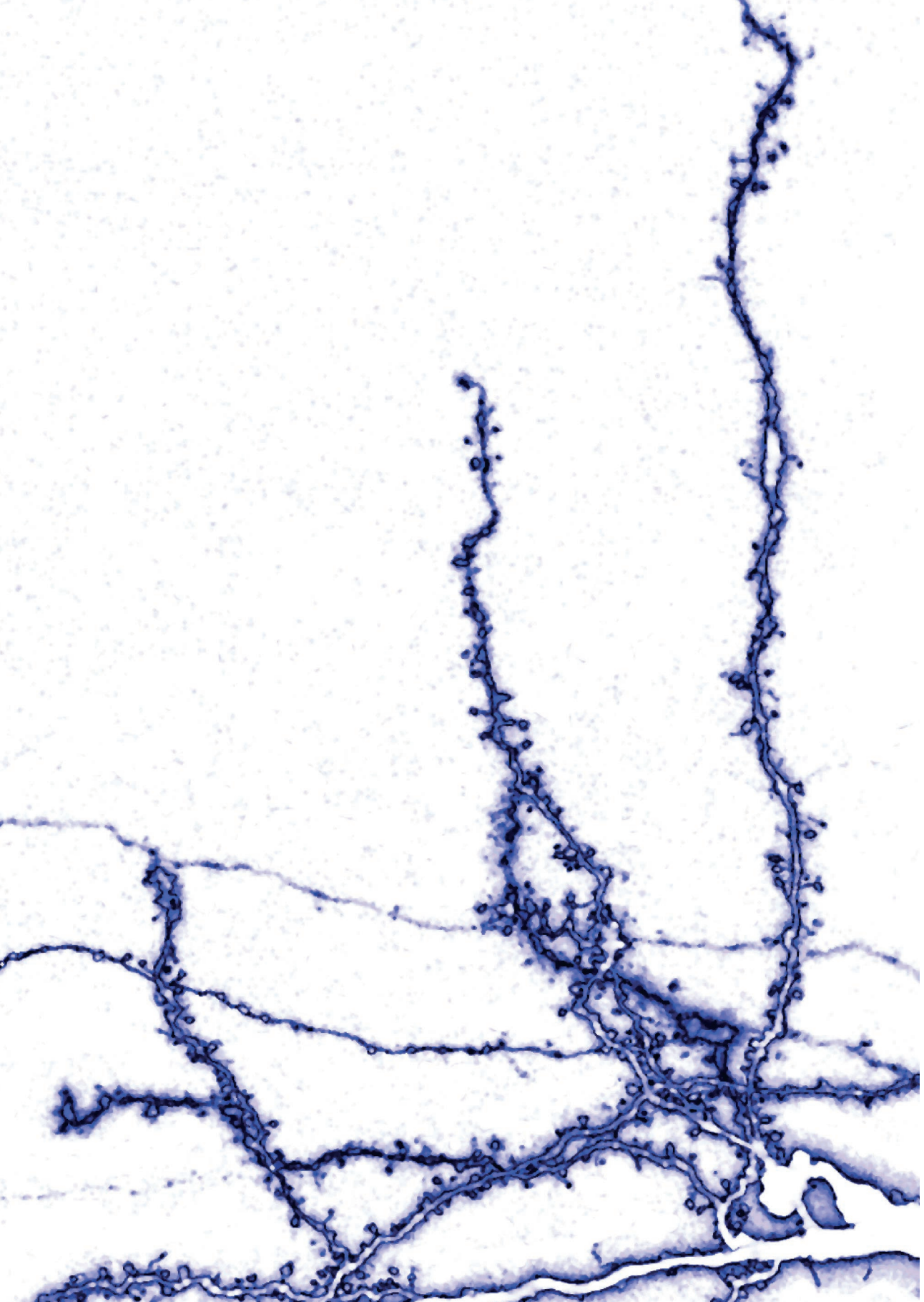

CHAPTER 6

General Discussion

GENERAL DISCUSSION

Ciliopathies are a heterogenous group of genetic disorders that manifest as a result of defects in the function or biogenesis of primary cilia. Advances in genetic diagnosis coupled with functional studies on proteomics datasets has furthered our understanding of the role of specific proteins in various structural domains of the cilium and how disruptions in these domains lead to disease in various tissue types. Despite this forward momentum, an understanding of how these neuronal disorders affect neural processes, such as brain development and function, remains poorly understood.

In this work I aimed to investigate biological mechanisms associated with genetic disorders that arise from primary cilium dysfunction. The research described in this thesis has led to the characterization of novel centrosomal/axonemal-, ubiquitin-proteasome system-, and microtubule-associated- ciliary proteins that when disrupted, result in disease. Herein, a variety of approaches were used to identify and characterize disease genes. In Chapter 2, *ARMC9* was discovered as a potential Joubert Syndrome (JBTS) candidate gene via whole-exome sequencing of the University of Washington (UW) Joubert Syndrome Research Program cohort. Assessment of protein localization in RPE1 cells and analysis of *ARMC9* patient-derived fibroblasts demonstrated that ARMC9 localized to the basal body of the primary cilia and transcripts of ARMC9 were upregulated during ciliogenesis. In Chapter 3, proteins interacting with ARMC9 were identified using tandem affinity purification and yeast two-hybrid screening. This proteomics-based approach enabled the identification of a new ciliopathy associated gene, TOGARAM1, and aided in elucidating affected signaling pathways. TOGARAM1, a TOG array protein, plays an essential role in modulating microtubule dynamics in the ciliary compartment, and JBTS-associated variants in both ARMC9 and TOGARAM1 resulted in decreased levels of the post translational modifications, specifically acetylation and glutamylation, of the ciliary axoneme. In addition to its association with ARMC9, TOGARAM1 was found to interact with CCDC66 and the JBTS-associated proteins CEP104 and CSPP1. Clinical assessment, functional analysis, and zebrafish modeling revealed that mutations in both *ARMC9* (Chapter 2) and *TOGARAM1* (Chapter 3) give rise to JBTS.

In Chapter 4, I describe loss-of-function (LOF) mutations in *USP9X* that lead to a female specific, multi-systems disorder. Affected females present with intellectual disability and stereotyped brain malformations reminiscent of ciliopathy-associated anatomical brain defects, such as malformation of axonal tracts including agenesis of the corpus callosum, asymmetrical ventricle formation and Dandy-Walker malformation. USP9X localizes to the ciliary axoneme however, in the functional characterization of fibroblasts derived from *USP9X* affected females, it became apparent that a relevant neuron-specific model was likely necessary to

unveil a tissue-specific phenotype. In Chapter 5, using iPSCs derived from fibroblasts obtained from the *USP9X* affected individuals described in Chapter 4, I set out to establish a model system for assessing USP9X specific mutations on cilia during neuronal development. While in its early stages, the work in Chapter 5 suggests segmentation analysis of the cilia present on neural progenitor cell (NPC) and other early neural cell types may indicate differences in ciliary phenotypes during neurogenesis.

CILIARY POST TRANSLATIONAL MODIFICATIONS

The genes we identified in our investigations all encode proteins that are required for cilium function. Interestingly, they are all, at least in part, required for proper coordination of post translational modification (PTM) of ciliary proteins, either via the regulation of polyglutamylation and acetylation of tubulin (ARMC9 and TOGARAM1 in Chapters 2 and 3) or ubiquitination (USP9X in Chapters 4 and 5). PTM of proteins involves a range of regulatory biological mechanisms that fine tune the functional capacity of the proteome by altering the interactome, localization, function, and/or stability of the modified proteins. Almost all eukaryotic proteins are post translationally modified and in humans, PTMs form interconnected networks of >50,000 residues in about 6,000 proteins [1].

2.1 Post translational modifications regulate microtubule dynamics

Microtubules (MTs) are tubular, cytoskeletal components consisting of αβ tubulin heterodimers organized in a head-to-toe, or plus- to minus-end fashion, to form protofilaments. These protofilaments associate laterally to form a hollow tubular structure allowing for dynamic changes in length and structure. MTs play an essential role in intracellular trafficking and cell division. MT assembly or polymerization occurs at the plus-end. MTs are dynamic structures that can respond to cellular factors by alternating between phases of growth, pause, and shrinkage. MT catastrophe or depolymerization occurs at increasing frequency with age but can also be induced by cellular factors such as fluctuations in the size and density of the protective GTP MT cap. Additionally blocking the MT protofilament at the growing end of the MT can induce catastrophe.

PTM function to generate a “tubulin code” to diversify the function, stability, and binding of a myriad of proteins that localize to MT. The eukaryotic cytoskeleton undergoes a variety of PTM that aid in cell cycle progression [2], cell type differentiation [3], and intracellular trafficking along microtubule networks [4–6]. PTM of tubulin are indispensable for proper MT function, including tubulin stabilization [7,8] and disassembly [9], and serve to influence local trafficking,

motility, and interactions [10,11]. Disruptions in the pattern, level, and distribution of MT PTMs disturb homeostasis within the ciliary compartment.

2.1.1 Defective tubulin glutamylation and acetylation in Joubert syndrome

Glutamylation occurs when the amino group of a free glutamate amino acid is conjugated to the carboxyl group of a glutamate side chain within a target protein and it occurs on tubulin via the action of a family of tubulin tyrosine ligase like (TTLL) proteins. Polyglutamylation decorates the axoneme and plays an important role in microtubule severing [9], IFT activity, and protein binding [6,12]. Several JBTS-associated proteins including ARMC9 and TOGARAM1 (Chapters 2 and 3) have been shown to affect the PTM of microtubules [13]. For example, polyglutamylation of the ciliary axoneme is in part regulated by the JBTS associated proteins ARL13B and CEP41 [14,15]. This is important for proper ciliary function as polyglutamylation levels act as a rheostat [9] that is fine tuned to maintain ciliary equilibrium. Changes in glutamylation that result from disruptions in ciliary glutamylases lead to hyperglutamylation, which reduce tubulin stability and result in premature ciliary disassembly due to an increase in the level of the severing enzyme, spastin [9]. Decreased levels of polyglutamylation result in decreased kinesin-2 mediated anterograde transport and thereby result in defective trafficking and hedgehog signaling [6]. Specifically, decreased levels of axonemal glutamylation inhibit hedgehog signaling via aberrant localization of SMO and GLI3, which is potentially a result of defective anterograde transport [6], as this mislocalization of SMO and GLI3 appears to be independent of defective KIF7 targeting [16].

Additionally, acetylation of the cilium is important for motor protein binding and movement, stability, and ciliary disassembly [11] and aberrancies in acetylation can result in microtubule instability as observed with dysregulation of the JBTS associated proteins KIF7 [17,18] and INPP5E5 [19]. Importantly, mutations in KIF7 [17,20,21] and INPP5E [22,23] result in abnormal hedgehog signaling.

Recently, a genome-wide screen of hedgehog signaling components in mouse fibroblasts found that more than 25 JBTS-associated genes modulate Hh signaling and additionally identified ARMC9 as a positive regulator of this signaling cascade [24]. That study also demonstrated that ectopically expressed ARMC9 translocates from the proximal end of the cilium to the ciliary tip upon the induction of Hedgehog signaling, thereby suggesting ARMC9 may possibly play a role in the trafficking and retention of Gli proteins [24]. Moreover, in the absence of ARMC9, they found that cilia were shorter, and decreased levels of acetylation and glutamylation were observed, consistent with our findings (Chapter 3). All ARMC9-TOGARAM1

complex members have both ciliary base and ciliary tip locations [25–29] indicating dynamic localization and potentially dynamic protein partnerships at each location. This suggests that a proper temporal spatial distribution is required for proper ciliary structure maintenance and function.

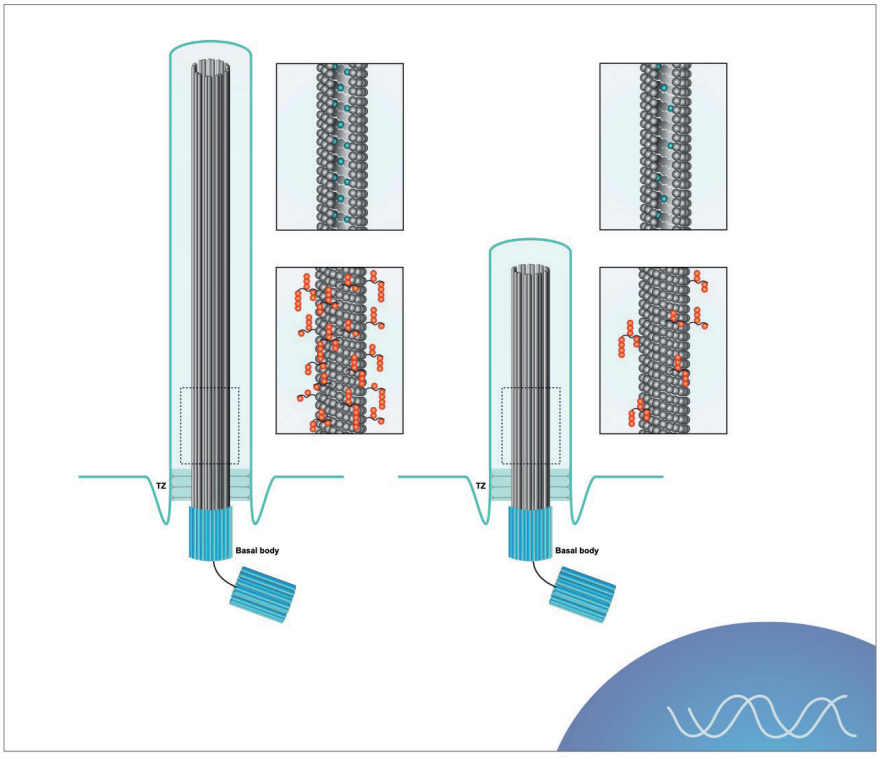

Figure 1: Post translational modifications of the ciliary axoneme. The ciliary axoneme under goes a variety of post translational modifications including acetylation within the microtubule lumen (shown in blue) and glutamylation (shown in red). Disruptions in these post translational modifications result in aberrancies in ciliary architecture and signal transduction.

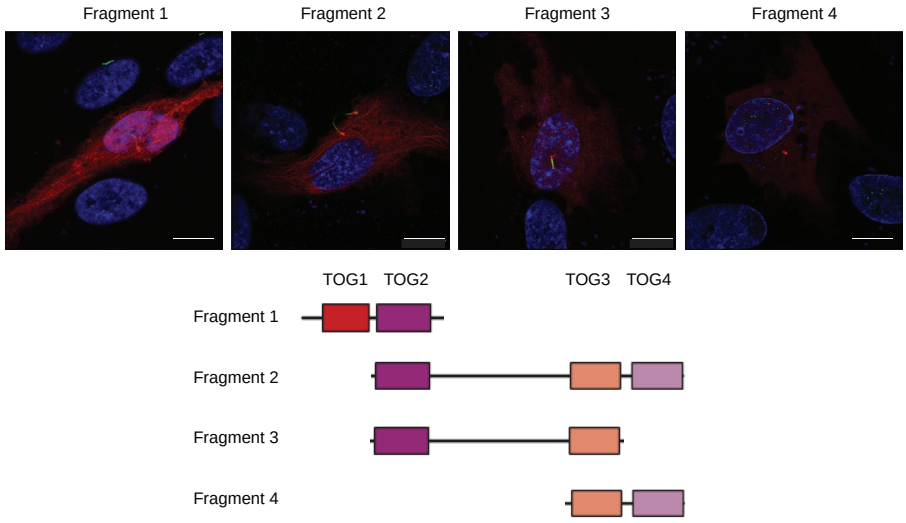

Figure 2: Fragements of TOGARAM1 have different binding affinities to the microtubule lattice. TOGARAM1 (red), ARL13B (green), scale bar 10 microns.

2.1.2 TOG-array domains regulate microtubule dynamics and stability

TOGARAM1, also known as Crescerin1 for the latin *crescere* meaning to grow, is a TOG array containing protein that regulates microtubule structure within the cilium [28]. TOG domains were first pinpointed in cytoskeleton-associated protein 5 (CKAP5), a MT polymerase then known as ch-Tog (clonic and hepatic tumor overexpressed gene) [30] or XMAP215 [31], which accumulates at MT plus ends [32]. TOGARAM1 has four TOG domains which function in concert to regulate microtubule dynamics. Domains TOG2 and TOG4 act to potentiate tubulin polymerization while TOG3 and TOG4 are essential for microtubule association and lattice binding activity [28]. Our studies assessing TOGARAM1 fragments and their capacity to localize to the cilium suggest that an intact TOG3 and TOG4 domain are required for ciliary formation, microtubule binding, and enrichment of TOGARAM1 at the tip, base, and along the ciliary axoneme.

We found that transfection in hTERT-RPE1 cells with a fragment containing TOG1 and TOG2 alone (fragment 1; figure 2) did not disrupt ciliary formation but the mRFP-tagged fragment could not enter the cilium, instead it appeared to collect at the ciliary base and did not show overt indicators of microtubule lattice binding (such as co-localization with a-tubulin). An intact TOG2 domain appears to be dispensable for ciliary formation and microtubule binding, but important for ciliary homeostasis. Work from Das et al. has demonstrated that the TOGARAM1 fragment containing amino acids 577-1776 (consisting of the linker region

and TOG domains 3 and 4) shows lattice binding activity at a frequency of approximately 56% and the degree of lattice binding is unchanged with full length TOGARAM1 containing an Y364E mutation, located within TOG2 [28]. We found similar results and the capacity for cilium formation with TOGARAM1 JBTS-variants R368W and L375P (Chapter 3) suggesting we might see comparable affects with a fragment lacking TOG1 and TOG2, however further work is needed to confirm this. Fragment 2 (figure 2) containing TOG2, the linker region, and TOG3 and 4 shows seemingly normal ciliary formation, microtubule binding, and localization to the tip and base of the cilium.

A fragment containing TOG2, the linker region and TOG3 (fragment 3; figure 2) allows for cilium formation but shows an enrichment of the fragment at the base and only low levels of localization along the axoneme, and limited microtubule binding was observed with this fragment. A fragment containing only TOG3 and TOG4 without the linker region showed abrogated cilium formation, focal enrichment, and no microtubule binding capacity. In chapter 3, we see that patient variants in the TOG2 domain result in an absence of ARMC9 binding but no apparent disruption in ciliary structure, while the patient variant in the TOG3 domain result in severely stunted cilia. Nonetheless we found the WT and all 3 patient variants were still able to bind microtubules (figure 2). Interestingly while KIF7 did not appear in any of our proteomics data, preliminary work suggested a decrease in KIF7 localization at the ciliary tip in unstimulated hTERT-RPE1 *TOGARAM1* mutant cells lines (figure 3).

We show that ARMC9 directly interacts with the TOG2 domain of TOGARAM1, and JTBS-associated variants in both genes lead to an attenuation of ciliary microtubule post translational modifications and a differential effect on microtubule stability (Chapter 3). Work done in various model organisms and mammalian cells has shown that a wide variety of microtubule binding proteins function in concert to coordinate, maintain, and polymerize microtubules [11,29,35,36]. Proteins containing tandem TOG domain repeats function to positively regulate microtubule growth and stability. Microtubule binding protein dysfunction can give rise to ciliary tip instability, resulting in aberrant microtubule dynamics and abnormal ciliary structure [37]. This affects cilium homeostasis, causing abrogated signal transduction and disease.

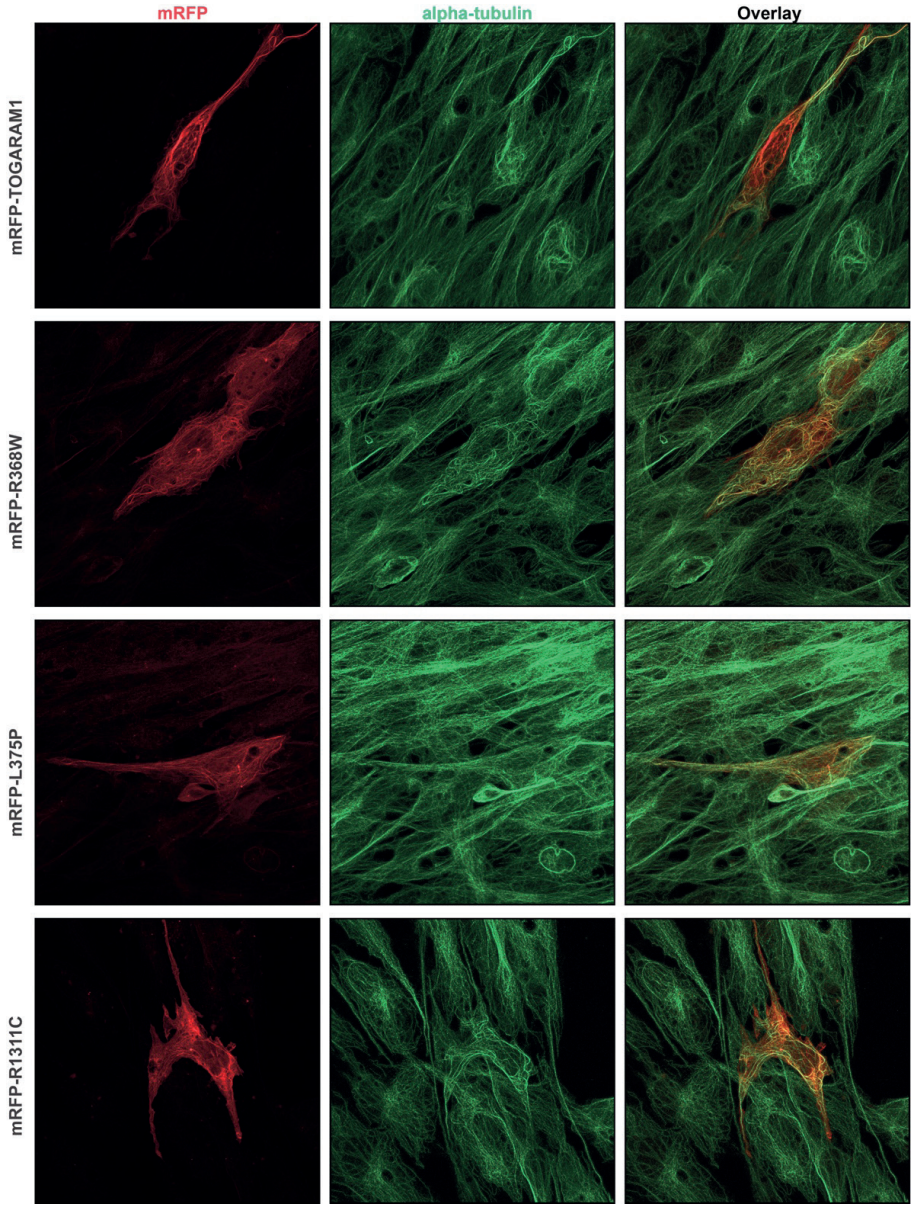

Figure 3: WT and mutant TOGARAM1 binds microtubules. TOGARAM1 (red), alpha-tubulin (green)
The ciliary tip compartment is essential for Hh signalling as important factors and mediators are sequestered there during different stages of pathway activation. KIF7 acts to organize the ciliary tip [33]. We found that disruptions of TOGARAM1 resulted in decreased SMO translocation to the ciliary tip, while SMO has been proposed to enter the cilium via lateral membrane diffusion and to a limited extent IFT-associated trafficking [34], the attenuated translocation likely results in abnormal Hh signaling.

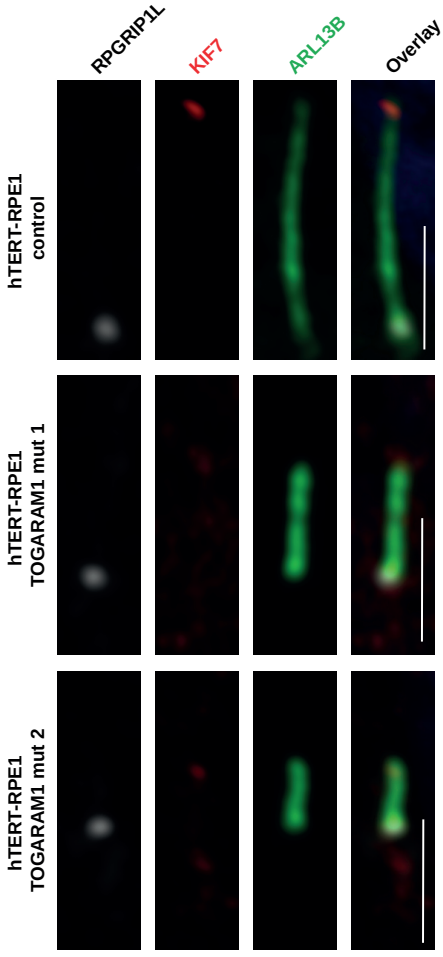

Figure 4: Decreased KIF7 localization in the ciliary tip in TOGARAM1 mut lines. RPGRIP1L (white), KIF7 (red), ARL13B (green), scale bar 2 microns

TOGARAM1 (CHE-12) and ARMC9 have been shown to, respectively, positively and negatively regulate the extension of B tubules in the ciliary tip of *Tetrahymena thermophila*, however loss of either TOGARAM1 or ARMC9 resulted in significantly shortened cilia. We showed that the interaction between ARMC9 and TOGARAM1 is contingent upon TOGARAM1 possessing an intact TOG2 domain (Chapter 3). The structure of TOG domains is highly conserved for microtubule binding, where the intra-HEAT loop within the discontinuous TOG domain binds tubulin. Previously, it was described that TOG domains function to positively regulate microtubule growth and dynamics [28]. Interestingly, we found that overexpression of wild type TOGARAM1 results in increased ciliary length. It has previously been shown that

different TOG domains in TOGARAM1 have differential microtubule binding capacity and likely function in concert to coordinate microtubule polymerization with the C-term TOG domains TOG3 and TOG4 working to promote microtubule lattice binding [28]. In hTERT-RPE1 cells, overexpression of the variants Arg368Trp and Leu375Pro, occurring in TOG2, results in a dissociation of TOGARAM1 from ARMC9, however protein localization and ciliary architecture remain intact when compared to wild type cells. Variant Arg1311Cys, which occurs in TOG3, maintains its interaction with ARMC9 but produces severely stunted cilia, suggesting that mutant TOGARAM1 is no longer able to support ciliary extension effectively. Concurrently, if ARMC9 functions as a negative regulator of microtubule growth in mammalian primary cilia as previously observed in Tetrahymena 19, this could in part, explain the resulting ciliary architecture observed with overexpression of the Arg1311Cys variant and its difference with the fragments with a disrupted TOG2 domain.

Relatively little is known about the biological function of ARMC9, however, Breslow et al. provided evidence to suggest it plays a role in modulation of Hh signaling. ARMC9 translocates to the ciliary tip shortly after Hh ligand binding, and in the absence of ARMC9, Hh stimulation results in decreased translocation of both GLI2 and GLI3 to the ciliary tip. As no effect was observed on translocation of SMO, the authors conclude that ARMC9 participates in trafficking and/or retention of Gli proteins at the ciliary tip. As ARMC9 localization at the tip is transient, and relatively shortly after stimulation (present at 4 hours post stimulation and absent after 30 hours) [24], it would be interesting to investigate if ARMC9 plays a role in tip structural organization, for example through its LisH Domain, as oppose to (or in addition to) complexing with Hh related proteins. The fact that we did not find Hh signaling components in our TAP dataset would be in line with this hypothesis, although many methodological explanations such as expression levels in HEK293T cells, or lack of Hh signaling responsiveness, could also explain this absence. Yamazoe et al., 2020 [38] recently demonstrated that the TOG domain in CEP104 is essential for the entry of SMO and the exit of GRP161 upon Hh activation, indicating that CEP104 plays an important role in cilium elongation and Hh signaling.

The importance of proper ciliary structure for intact ciliary function has been studied in detail [24,37,39–44]. Our work (Chapter 3) and that of others suggest that axonemal stability is foundational for proper ciliary function and dysregulation of post translational modifications of microtubules can compromise microtubule stability. Abrogated or abnormally enriched post translational modifications result in disruptions in protein binding [6,12] and dysregulation of the ciliary proteome. Changes in the capacity to interact with motor proteins can result in mislocalization of ciliary proteins which subsequently interferes with normal signal transduction. Therefore, manipulation of post translation modifications of microtubules and

analyzing subsequent changes in protein trafficking and signal transduction, could provide important insight into the mechanism of JTBS and our fundamental understanding of the proteome of the cilium in general but also of its subdomains.

2.2 UBIQUITINATION

Ubiquitin, a post translational modifying protein, most well characterized for its role in protein degradation, is emerging as an essential component of ciliary biology [45]. The post translational modification ubiquitination is a highly complex regulatory code that orchestrates a variety of cellular processes [45]. Ubiquitin acts in dynamic protein tagging to control an essential array of biological processes including protein turnover, transcription, DNA damage repair, endocytosis, autophagy, and immune homeostasis [45-46]. The fate of ubiquitinated substrates is determined by chain topology and specific enzymatic interaction partners. In addition to its role in protein turnover, the 76 amino acid, 8,5 kDa protein is attached to target substrate lysines to orchestrate essential cellular processes such transcription, endosomal sorting, autophagy, cell cycle, chromatin structure, and embryonic development. Ubiquitination is the process by which an exposed C-terminal end of ubiquitin is covalently linked to lysine residues in target substrates via a multi-enzymatic process with the aid of ATP in three essential steps: activation, conjugation, and ligation. These steps are orchestrated by an E1 activating enzyme, an E2 conjugating enzyme, and an E3 ligase. The diverse functional capacity of ubiquitination is due in part to the vast array of differential chain topologies that can be generated. Ubiquitin conjugates can exist as a single moiety, known as monoubiquitin, or polyubiquitin chain as the seven internal lysines and N-termini methionine can form different isopeptide linkages types with differing three-dimensional structures (K6, K11, K27, K29, K33, K48, K63, and Met1). The specific E2 and E3 enzymes recruited to the target substrate dictate the design of these chains (reviewed in [47]). Ubiquitin chain topology is likely a key factor in differential targeting of proteins to one of the three major degradation pathways in mammalian cells: the proteasome, the lysosome, or the autophagosome. Ubiquitin marks receptors to be endocytosed to the lysosome and organelles for disposal via autophagocytosis (reviewed in [48]). Transient interactions are formed between specialized ubiquitin binding domains and ubiquitin moieties and these interactions regulate the aforementioned processes. Defects in the ubiquitin systems lead to a variety of pathologies such as autoimmune diseases, neurodegenerative conditions and cancer (reviewed in [46]).

2.3 UBIQUITINATION OF CILIARY PROTEINS

Over the past decade the components of the ubiquitin proteasome system (UPS) have been recognized to play an indispensable role in the fate and function of target protein and forms an active regulatory component of ciliary signal transduction processes. Ubiquitin plays an essential role in flagellar disassembly. The ubiquitin proteasome system (UPS) coordinates flagellar absorption prior to cell cycle re-entry. Using flagella isolated from the green algae *Chlamydomonas reinhardtii*, Huang et al., demonstrated that these organelles contain a fully functional ubiquitin system, including both free ubiquitin and the enzymes necessary for activation, conjugation, and ligation [49].

2.3.1 Defective ubiquitination in ciliopathies

Aside from the essential role of proteasomal degradation in ciliary maintenance and disassembly, mutations in a number of E3 ligases, the enzymes that catalyzes the attachment of ubiquitin to target lysines, result in ciliopathies. Examples of these mutated E3 ligases include TOPORS in retinal degeneration [50], pVHL in VHL syndrome a disorder characterized by cysts in the kidneys, pancreas, and genital tract [51], and KLHL7, which is found in complex with Cullin E3 ligases, in retinitis pigmentosa [52–54]. Polycystin-2, the protein encoded by *PKD2* that is mutated in the renal ciliopathy Autosomal Dominant Polycystic Kidney Disease, (ADPKD) requires a proper balance between the serine/threonine kinase (NIMA-Related Kinase 1) NEK1 and the E3 ubiquitin ligase TAZ the proper protein maintenance required for normal ciliogenesis [55]. Ubiquitin in the ciliary compartment has further been characterize as essential for trafficking activated GPCR, including SSTR3 and GPR161, out of the cilium. Desai et al. and Shinde et al show that SMO translocation in to the ciliary compartment is actively trafficked out by the BBSome complex upon K63 ubiquitination [56,57]. SMO accumulates in the cilium in the absence of ligand in the absence of ubiqutination as it cannot be trafficked out by the BBSome complex.

Eguether and colleagues describe a role for CYLD in ciliogenesis [58]. CYLD is a DUB known to specifically catalyzes the removal of K63 and linear chains [59], which is especially interesting in light of the recent findings that the cilium is enriched with K63 ubiquitin chains [57]. Described mutations in the catalytic domain of CYLD result in appendage tumors known as cylindromas [60]. CYLD localizes to the centrosome and basal body in non-cycling cells via its interaction with the centrosomal protein CAP350. Researchers saw that multi-ciliated cells did not readily form cilia in the presence of catalytically inactive CYLD however they found that in the complete absence of CYLD, cells were able to undergo ciliogenesis [58]. A potential mechanisms for this is that in the absence of CYLD, another DUB is able to coordinate the activity necessary for

normal ciliogenesis however in the presence of the catalytically inactive form of CYLD, the mutated DUB acts as a dominant negative, thereby resulting in binding which blocks the removal of K63 and/or linear ubiquitin chains from ciliary proteins.

CYLD ubiqutination Cep70 and inactivates the enzyme Histone deacetylase 6 (HDAC6) to aid in primary cilium formation. HDAC6, aside from acting as a histone deacetylase to alter chromatin structure also, plays a role in the aggresome-autophagy pathway, which mediates destruction of damaged organelles and protein aggregates to prevent proteotoxic congestion of cellular compartments [75], and as previously mentioned, acts in ciliary disassembly [50]. CYLD knockout mice manifest with symptoms of polydactyly, impaired sperm production, and decreased number and length of cilia as well as disorganization of the ciliary axoneme in the skin, tracheal epithelium, and kidney tissue when compared to wild type mice. The ciliary shortening defect was partially rescued with administration of HDAC6 inhibitors [76]. siRNA depletion of CYLD in RPE1 cells resulted in decreased levels of centrosomal Cep70 which could account in part for the impairment in cilium formation [76]. However it is interesting that Eugether et al. found no ciliary defect in the absence of CYLD while Yang et al. found a phenotype reminiscent of ciliopathies in both the mouse model and in vitro culturing system. During axoneme extension, the KCTD17, a substrate adaptor, acting in concert with the Cul3 E3 ligases degrades the negative regulator, trichoplein, leading to inactivation of Aurora A kinase, and cilium elongation [21]. Trichoplein is located at the subdistal/medial zone of the mother centriole, and upon serum starvation, trichoplein is degraded via the proteasome. Utilizing a two-step E3 ligase screening technique Kasahara and colleagues identified KCTD17 as the substrate adaptor for the Cul3-RING E3 enzymes that poly-ubiquitination trichoplein leading to its proteasome mediated destruction. Aberrant activity of the trichoplein-Aurora A kinase axis results in the absence of KCTD17, thereby inhibiting cilium formation. Ciliogenesis perturbation results in response to proteasome inhibitor MG132. Indeed, Kasahara and colleagues show that cilium formation is almost completely abrogated in response to MG132 treatment, and they are able to attribute this dysfunction of the stabilization of trichoplein [21].

Ciliogenesis is intricately linked with the cell cycle and the cell cycle with its regulatory ubiquitin machinery. Ciliary assembly begins during the G1/G phase of the cell cycle and disassembly is initiated as the cell enters S phase (reviewed in [61]). The anaphase promoting complex (APC), which regulates the onset of anaphase and allows for sister chromatid separation, acts to destabilize microtubules in the cilium, thereby aiding in its deconstruction. APC achieves this by targeting the ciliary kinase Nek1 for degradation [62]. Wang et al have shown in their recent work on the role of APC in quiescent cilated cells, that the APC coactivator cdc20, shown to localize to the basal body, plays an important role in ciliary disassembly. Inhibition

of the APC-cdc20 complex results in elongated cilia while overexpression of cdc20 decreases ciliary formation [52,53]. Several mitotic regulators have been implicated in ciliogenesis including Aurora A kinase [63] and the NIMA-related kinases such as Nek1 [64–66]. Wang et al suggest that the E2 conjugating enzyme Ube2s is require in conjunction with APC-cdc20 for ciliary shortening [67]. These data suggest important co-factors involved in cell cycle regulation also play an important role in ciliary construction and deconstruction.

Immunofluorescence studies have been used to visualize the subcellular localization of proteasomal components and demonstrate an enrichment of proteasomal machinery near the mammalian centrosome [68–71]. Work from Gerhardt and colleagues implicated Rpgrip1l as an interactor of the 19S proteasomal subunit Psmd2, and demonstrated that it regulates proteasomal activity at the basal body via this interaction. Rpgrip1l deficient mice demonstrate severely disturbed ciliary signal transduction which was linked to a decrease in proteasomal activity due to the absence of the interaction between Rpgrip1l and Psmd2 [72]. Lui et al., showed that loss of ciliopathy associated proteins BBS4 or oral-facial-digital syndrome 1 (OFD1), intracellularly located at the centrosomal satellites, leads to accumulation of signaling mediators that are normally targeted to the proteasome for degradation. In normal conditions BBS4 and OFD1 associate with subunits of the proteasome and in conditions where BBS4 and OFD1 are functionally impaired, multiple proteasomal subunits that normally localized to the centrosome are absent [61,73–75].

2.3.2 USP9X, a deubiquitinating protein at the nexus of ciliary and neuronal processes

The removal of ubiquitin is mediated by isopeptidases known as deubiquitinating enzymes (DUBs). These enzymes act to hydrolyze the isopeptide linkages that conjugates ubiquitin to its substrate lysine or N-termini and in that way counteract the activity of E3 ligases. There are predicted to be approximately 95 DUBs encoded for by the human genome [76], and theses enzymes display a high degrees of specificity due to multiple layers of regulation that modulate their activity. Ubiquitin homeostasis is maintained through the action of DUBs as they coordinate the extent of substrate ubiquitination and the availability of free ubiquitin. Specific DUBs are responsible for post-translational processing of the ubiquitin precursor proteins UBA52 and RPS27A [77]. DUBs are capable of not only removing chains from target substrate but also editing chain topology, thereby rescuing a substrate from proteasome degradation, altering protein - protein interaction, or allowing a substrate to be modified by an additional post translational modifier such as a phosphate group.

USP9X encodes an X-linked DUB that plays a pleiotropic role in a variety of cellular processes and appears to be essential for fine tuning protein localization and signal transduction. Since the first male patients with *USP9X* mutations were characterized in 2014 by Homan et al. [78] and female patients (Chapter 4) in 2016 [79], extensive research has been done to unravel the role of USP9X in centrosomal and ciliary biology and understand its effect on neural development in humans. USP9X localizes to the centrosome and cilium and has been linked to numerous ciliopathy associated proteins in proteomic studies [80]. The subcellular localization of USP9X is dynamic and dependent upon cell type and cell cycle phase. USP9X **and USP7 are essential for proper chromosomal alignment at spindle poles and accurate division during anaphase, and play an important role in the spindle assembly check point.** USP9X associates strongly with the centrosomes during S and G2 phases, but declines in G_1. It is largely absent from the centrosomes during metaphase [81]. During S phase, SF11 acts to localize USP9X to the centrosome where it acts to deubiquitinate and stabilize STIL and promote centriole duplication [82]. During G0, G1, and S phase, NPHP5 recruits a portion of the cytoplasmic pool of USP9X to the centrosome where the DUB acts to protect NPHP5 from thereby supporting ciliary assembly. Beginning in the G_2 and extending into the M phase of the cell cycle, USP9X is translocated away from the centrosome, thereby allowing BBS11/TRIM32 to ubiquitinate NPHP5 via K63 chains resulting in its removal from the centrosome and ciliary disassembly [83].

USP9X plays an essential role in cell cycle progression and centrosome duplication [81]. During the G and S phase transition the single G_1 centrosome begins its duplication process which is completed during S phase such that two centrosomes are present in G_2 thereby acting to facilitate bipolar spindle formation during metaphase. During cytokinesis, the two centrosomes are segregated with one being designated into each daughter cell. An essential feature of centrosome replication is centriole duplication which occurs as the pre-existing mother centriole, that nucleated the cilium during G0 and G1, duplicates itself and forms a daughter centriole. This process is regulated in part by the kinase PLK4 and two SCF ubiquitin E3 ligases which act to ensure that only a single replication event occurs per cycle. The loss of USP9X impairs centrosome duplication and gain-of-function or overexpression results in centrosome amplification and chromosome instability. [81]

Work over the past decade has confirmed the essential role of USP9X in brain development and function. USP9X is highly expressed in neural progenitor cells (NPCs) during mouse [84] and zebrafish [85] embryogenesis. While overall expression levels are reduced in adulthood, they are maintained in the adult neural progenitor niches [86]. USP9X is essential for NPC polarization and organization during nervous system development and subsequent cortical architecture.

Loss of *USP9X* results in the disorganization of the ventricular, subventricular and cortical plate architecture during early brain development. Additionally specific deletion of *USP9X* from the dorsal telencephalon resulted in a reduction or complete loss of the corpus callosum and a decrease in hippocampal size [87].

USP9X regulates primitive identity in progenitor cell types [86] as well as the development and function of post-mitotic mature neurons. USP9X interacts with Ankyrin-G, a scaffolding protein that links the plasma membrane to the actin / beta-spectrin cytoskeleton, to regulate dendritic spine development and in the absence of USP9X synaptic abnormalities result, including decreased cortical spine density and size. The impairment results from a transient depletion of Ankyrin-G that leads to a persistent neuronal structural defects as well a behavioral issues [88]. Deletion of USP9X results in reduced hippocampal neuron outgrowth due to deregulation of TGFβ signaling. USP9X both positively and negatively regulates TGFβ signaling. It functions to promote TGFβ signaling via the deubiqutination and stabilization of Smad4. Deubiqutination allows Smad4 to form a complex with phosphorylated receptor Smads, translocate to the nucleus, and modulate transcriptional responses to TGFβ family ligands [89]. Mouse neurons lacking USP9X are unresponsive to TGFβ signaling activation [87]. Conversely USP9X suppresses TGFβ signaling by the stabilization of the E3 ligase SMURF1, which promotes the degradation of TGFβ receptors [90,91]. Interestingly TGFβ signaling directly regulates the function of USP9X in dendritic development via the serine/threonine kinase phosphorylation activity of the TGF-beta receptor I and II [92] by enhancing its the interaction between USP9X and Ankyrin-G [93], this activity is independent of the ability of USP9X to modulate TGFβ signaling [89].

The *drosophila fat facets* (*faf*), the USP9X homologue, was first identified in a mutagenesis screen as an essential protein in the development of the syncytial stage of embryogenesis and in photoreceptor fate determination [84]. Overexpression of *faf* disrupts synaptic outgrowth by increasing the number of synaptic boutons, synaptic branching, and attenuated synaptic transmission at the neuromuscular junctions. Interestingly, dysregulated endocytosis may be a causative feature in the altered synaptic growth [94]. Conversely, in a separate study the overexpression of faf lead to a loss of synaptic boutons due to a resultant Par1 overexpression, faf acts to deubiquitinate phosphorylated Par1 enhancing its activity, Faf overexpression rescued the defect [95].

2.4 CROSS TALK BETWEEN UBIQUITINATION AND PHOSPHORYLATION IN MTOR SIGNALING

We found that female patients with loss of function mutations in USP9X present with brain abnormalities including intellectual disability, agenesis of the corpus callosum, Dandy-Walker malformation, and asymmetric enlargement of the lateral ventricles (ventriculomegaly) (Chapter 4) [79]. Male patients also present with CNS disturbances including white matter abnormalities, thinning of the corpus callosum, widened ventricles and global delay [96]. Ventricular morphogenesis is a complex process that relies on proper microtubule regulation, ciliary formation, and properly tuned mTORC1 signaling [97].

The mammalian/mechanistic target of rapamycin (mTOR) is a serine-threonine kinase that is a key modulator of metabolism in eukaryotic organisms. It functions to modulates a variety of cellular processes including protein translation and degradation, metabolism and cytoskeleton dynamics. In mammals mTOR functions via two distinct complexes mTOR complex 1 (mTORC1) and mTOR complex 2 (mTORC2). Cilia play a role in restricting mTORC1 signaling which is essential for cellular quiescence.

It is possible that LOF mutations in USP9X result in disruptions in mTORC1 signaling via the primary cilium and thereby cause ventriculomegaly. Ventricular morphogenesis is disrupted in mutant RG cells that lack a primary cilium due to the absence of *IFT88* or *KIF3A.* Cilia regulate the size of the ventricular apical domain of radial glia cells via mTORC1 modulation. In the absence of the primary cilium, the orientation of the mitotic spindle is disrupted and there is an increase in basal progenitor number and a decreased number of cortical neurons at later stages. Enlarged apical domains of radial glia cells results in dilation of the ventricles. [98] USP9X likely plays a complex role in the modulation of mTOR signaling which may be cell type and developmental phase dependent. However, we found assessing mTOR in skin fibroblasts to be a precarious undertaking. The variability in results and the changes over time lead us to venture towards a more relevant cell types and disease model for neuronal ciliopathies and while the abnormalities we observe in individuals with LOF mutations in USP9X could indeed be linked to abnormalities in mTOR signaling via the primary cilium and further work is need to understand the observed defects in axonal tract formation.

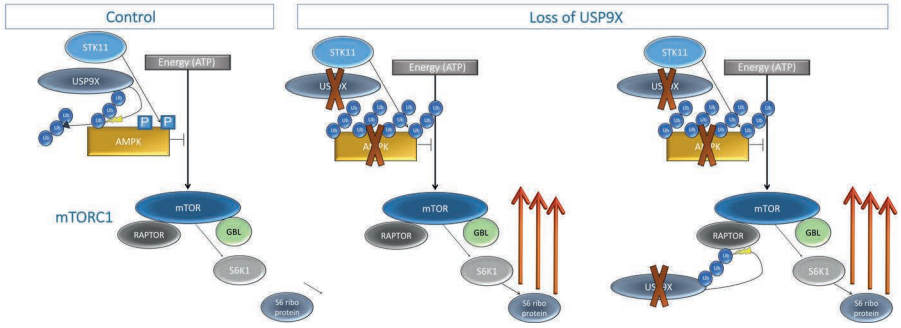

Figure 5: mTORC1 signaling in the presence and absence of USP9X.
mTOR associated proteins that localize to the ciliary compartment include liver kinase B1 (LKB1), AMP-activated protein kinase (AMPK), and polycystin-1 (PKD1) and 2 (PKD2). Several tumor suppressors and oncoproteins mediate mTORC1 signaling, a key regulatory complex consists of TSC1 and TSC2 which act to inhibit mTORC1 by activating at the GAP complex for the GTPase Rheb. In the absence of growth factors, LBK1 activity leads to the activation of AMPK which in term phosphorylates TSC2 leading to the inhibition of Rheb thereby decreasing signaling via mTORC1.

Much like its relationship with USP9X, mTOR signaling and the primary cilium have a complex and seemingly contradictory relationship. It has been shown that both TSC1 and TSC2 deficient cells possess longer cilia [99,100] however other studies have found shorter cilia in TSC2 deficient cells [100]. Additionally mTORC1 activation via Rheb overexpression leads to longer cilia [101]. And the induction of autophagy has been shown to both increase [102] and decrease ciliary length [103]. It is of course possible that mTORC1 activation must be titrated to either increase or decrease ciliary length, the increase in mTORC1 may provide the protein building blocks for elongations of the primary cilium thereby indirectly promoting ciliary lengthening whereas autophagy may act directly to support ciliary formation and elongation and the inhibition of this decreases ciliogenesis. These effects may be tissue, cell type, and stage of development dependent.

USP9X has been shown to be a regulator of mTOR via multiple axes, USP9X acts as a key regulator of AMPK-related kinase activation via the removal of ubiquitin chains to allow for LBK1 phosphorylation of NUAK1 and MARK4 (polarity proteins) leading to their subsequent activation (Figure 4). Furthermore, USP9X plays a complex and dynamic role in mTOR signaling, it has been shown to directly interact with mTOR, RAPTOR, and RICTOR, suggesting a role in the modulation of both mTORC1 and mTORC2 signaling. USP9X can exert influence over multiple points of mTOR signal transduction. Theoretically its role as a AMPK-like kinase interactor, specifically with MARK4 and NUAK1 [104], results in mTOR repression. Via its role as an interactor of both RAPTOR (mTORC1) [105] and RICTOR (mTORC2) [106] USP9X would

theoretically serve to activate mTOR signaling. In its association with RAPTOR, USP9X rescues RAPTOR from proteasomal degradation [105]. Via its interaction with RICTOR, USP9X enables the interaction between RICTOR and mTOR, thereby playing an essential role in the formation of the mTORC2 complex [106]. Not surprisingly seemingly conflicting data of the role of USP9X has emerged overtime, however due to the complex interplay between USP9X where it acts as both a positive and negative regulator, coupled with differential needs of mTOR signaling in varying cell types gives rise to the possibility that USP9X has differing roles in modulating mTOR signaling in different cell types, during different stages of development. While both mTOR and USP9X have been shown to be indispensable for proper neuronal development and plasticity, it would be interesting to assess the divergence between their mechanism of action. Specifically, mTOR has also been shown to play an important role in cytoskeletal plasticity via its regulation of actin dynamics. Andrews et al., demonstrated that mTOR signaling regulates the architecture of the neocortex by curating the organization, morphology, and mitotic behavior of oRG cells and the radial scaffold. mTOR acts to change the actin cytoskeleton via the activity of the Rho-GTPase CDC42.

REFERENCES

1. Minguez, P. *et al.* Deciphering a global network of functionally associated post-translational modifications. *Mol. Syst. Biol.* **8**, 599 (2012).
2. Verhey, K. J. & Gaertig, J. The Tubulin Code. *Cell Cycle* **6**, 2152–2160 (2014).
3. Magiera, M. M., Singh, P., Gadadhar, S. & Janke, C. Tubulin Posttranslational Modifications and Emerging Links to Human Disease. *Cell* **173**, 1323–1327 (2018).
4. Garcia-Gonzalo, F. R. *et al.* Phosphoinositides Regulate Ciliary Protein Trafficking to Modulate Hedgehog Signaling. *Dev. Cell* **34**, 400–409 (2015).
5. Nozaki, S. *et al.* Regulation of ciliary retrograde protein trafficking by the Joubert syndrome proteins ARL13B and INPP5E. *J. Cell Sci.* **130**, 563–576 (2017).
6. Hong, S.-R. *et al.* Spatiotemporal manipulation of ciliary glutamylation reveals its roles in intraciliary trafficking and Hedgehog signaling. *Nat. Commun.* **9**, 1713–1732 (2018).
7. Eshun-Wilson, L. *et al.* Effects of α-tubulin acetylation on microtubule structure and stability. *Proc. Natl. Acad. Sci. U. S. A.* **116**, 10366–10371 (2019).
8. Xu, Z. *et al.* Microtubules acquire resistance from mechanical breakage through intralumenal acetylation. *Science (80-.).* **356**, 328–332 (2017).
9. Valenstein, M. L. & Roll-Mecak, A. Graded Control of Microtubule Severing by Tubulin Glutamylation. *Cell* **164**, 911–921 (2016).
10. Dorota Wloga, Ewa Joachimiak & Hanna Fabczak. Tubulin Post-Translational Modifications and Microtubule Dynamics. *Int. J. Mol. Sci.* **18**, 2207–2218 (2017).
11. Wloga, D., Joachimiak, E., Louka, P. & Gaertig, J. Posttranslational Modifications of Tubulin and Cilia. *Cold Spring Harb. Perspect. Biol.* **9**, (2017).
12. He, K. *et al.* Axoneme polyglutamylation regulated by Joubert syndrome protein ARL13B controls ciliary targeting of signaling molecules. *Nat. Commun.* **9**, 3310–3314 (2018).
13. Verhey, K. J. & Gaertig, J. The tubulin code. *Cell Cycle* **6**, 2152–2160 (2007).
14. Lee, J. E. *et al.* CEP41 is mutated in Joubert syndrome and is required for tubulin glutamylation at the cilium. *Nat. Genet.* **44**, 193–199 (2012).
15. Revenkova, E., Liu, Q., Gusella, G. L. & Iomini, C. The Joubert syndrome protein ARL13B binds tubulin to maintain uniform distribution of proteins along the ciliary membrane. *J. Cell Sci.* **131**, jcs212324 (2018).
16. He, M. *et al.* The kinesin-4 protein Kif7 regulates mammalian Hedgehog signalling by organizing the cilium tip compartment. *Nat. Cell Biol.* **16**, 663–672 (2014).
17. Dafinger, C. *et al.* Mutations in KIF7 link Joubert syndrome with Sonic Hedgehog signaling and microtubule dynamics. *J. Clin. Invest.* **121**, 2662–2667 (2011).
18. Pedersen, L. B. & Akhmanova, A. Kif7 keeps cilia tips in shape. *Nat. Cell Biol.* **16**, 623–625 (2014).
19. Satir, P., Pedersen, L. B. & Christensen, S. T. The primary cilium at a glance. *J. Cell Sci.* **123**, 499–503 (2010).
20. Putoux, A. *et al.* KIF7 mutations cause fetal hydrolethalus and acrocallosal syndromes. *Nat. Genet.* **43**, 601–606 (2011).
21. Maurya, A. K. *et al.* Positive and Negative Regulation of Gli Activity by Kif7 in the Zebrafish Embryo. *PLoS Genet.* **9**, e1003955–15 (2013).

22. Bielas, S. L. *et al.* Mutations in INPP5E, encoding inositol polyphosphate-5-phosphatase E, link phosphatidyl inositol signaling to the ciliopathies. *Nat. Genet.* **41**, 1032–1036 (2009).

23. Hardee, I. *et al.* Defective ciliogenesis in INPP5E-related Joubert syndrome. *Am. J. Med. Genet. Part A* **173**, 3231–3237 (2017).

24. Breslow, D. K. *et al.* A CRISPR-based screen for Hedgehog signaling provides insights into ciliary function and ciliopathies. *Nat. Genet.* **50**, 460–471 (2018).

25. Satish Tammana, T. V, Tammana, D., Diener, D. R. & Rosenbaum, J. Centrosomal protein CEP104 (Chlamydomonas FAP256) moves to the ciliary tip during ciliary assembly. *J. Cell Sci.* **126**, 5018–5029 (2013).

26. Frikstad, K.-A. M. *et al.* A CEP104-CSPP1 Complex Is Required for Formation of Primary Cilia Competent in Hedgehog Signaling. *Cell Rep.* **28**, 1907–1922.e6 (2019).

27. Conkar, D., Bayraktar, H. & Firat-Karalar, E. N. Centrosomal and ciliary targeting of CCDC66 requires cooperative action of centriolar satellites, microtubules and molecular motors. *Sci. Rep.* **9**, 14217–14250 (2019).

28. Das, A., Dickinson, D. J., Wood, C. C., Goldstein, B. & Slep, K. C. Crescerin uses a TOG domain array to regulate microtubules in the primary cilium. *Mol. Biol. Cell* **26**, 4248–4264 (2015).

29. Louka, P. *et al.* Proteins that control the geometry of microtubules at the ends of cilia. *J. Cell Biol.* **217**, 4298–4313 (2018).

30. Charrasse, S. *et al.* Characterization of the cDNA and pattern of expression of a new gene over-expressed in human hepatomas and colonic tumors. *Eur. J. Biochem.* **234**, 406–413 (1995).

31. Fox, J. C., Howard, A. E., Currie, J. D., Rogers, S. L. & Slep, K. C. The XMAP215 family drives microtubule polymerization using a structurally diverse TOG array. *Mol. Biol. Cell* **25**, 2375–2392 (2014).

32. van der Vaart, B. *et al.* SLAIN2 links microtubule plus end-tracking proteins and controls microtubule growth in interphase. *J. Cell Biol.* **193**, 1083–1099 (2011).

33. Du Toit, A. KIF7 organizes cilia. *Nat. Rev. Mol. Cell Biol.* 1 (2014).

34. Milenkovic, L., Scott, M. P. & Rohatgi, R. Lateral transport of Smoothened from the plasma membrane to the membrane of the cilium. *J. Cell Biol.* **187**, 365–374 (2009).

35. Aher, A. *et al.* CLASP Suppresses Microtubule Catastrophes through a Single TOG Domain. *Dev. Cell* **46**, 40–58.e8 (2018).

36. Rezabkova, L., Kraatz, S. H. W., Akhmanova, A., Steinmetz, M. O. & Kammerer, R. A. Biophysical and Structural Characterization of the Centriolar Protein Cep104 Interaction Network. *J. Biol. Chem.* **291**, 18496–18504 (2016).

37. Seixas, C., Cruto, T., Tavares, A., Gaertig, J. & Soares, H. CCTα and CCTδ Chaperonin Subunits Are Essential and Required for Cilia Assembly and Maintenance in Tetrahymena. *PLoS One* **5**, e10704–13 (2010).

38. Yamazoe, T., Nagai, T., Umeda, S., Sugaya, Y. & Mizuno, K. Roles of TOG and jelly-roll domains of centrosomal protein CEP104 in its functions in cilium elongation and Hedgehog signaling. *J. Biol. Chem.* **295**, 14723–14736 (2020).

39. Alkanderi, S. *et al.* ARL3 Mutations Cause Joubert Syndrome by Disrupting Ciliary Protein Composition. *Am. J. Hum. Genet.* **103**, 612–620 (2018).

40. Shi, X. *et al.* Super-resolution microscopy reveals that disruption of ciliary transition-zone architecture causes Joubert syndrome. *Nat. Cell Biol.* **19**, 1178–1188 (2017).

41. Huang, P. *et al.* Structural Basis of Smoothened Activation in Hedgehog Signaling. **174**, 312–324.e16 (2018).

42. Huangfu, D. & Anderson, K. V. Cilia and Hedgehog responsiveness in the mouse. *Proc. Natl. Acad. Sci. U. S. A.* **102**, 11325–11330 (2005).

43. Huangfu, D., Liu, A., Rakeman, A. S. & Murcia, N. S. Hedgehog signalling in the mouse requires intraflagellar transport proteins why less severe than Shh mutants but similar to disruption of L / R nodal assymetry ! *Lett. to Nat.* **426**, 83–87 (2003).

44. Singla, V. & Reiter, J. F. The primary cilium as the cell's antenna: signaling at a sensory organelle. *Science* **313**, 629–633 (2006).

45. Wiegering, A., Rüther, U. & Gerhardt, C. The Role of Primary Cilia in the Crosstalk between the Ubiquitin¯Proteasome System and Autophagy. *Cells* **8**, (2019).

46. Rao, G., Croft, B., Teng, C. & Awasthi, V. Ubiquitin-Proteasome System in Neurodegenerative Disorders. *J. Drug Metab. Toxicol.* **6**, (2015).

47. Stewart, M. D., Ritterhoff, T., Klevit, R. E. & Brzovic, P. S. E2 enzymes: more than just middle men. *Cell Res.* **26**, 423–440 (2016).

48. Chen, R.-H., Chen, Y.-H. & Huang, T.-Y. Ubiquitin-mediated regulation of autophagy. *J. Biomed. Sci.* **26**, 80 (2019).

49. Huang, K., Diener, D. R. & Rosenbaum, J. L. The ubiquitin conjugation system is involved in the disassembly of cilia and flagella. *J. Cell Biol.* **186**, 601–613 (2009).

50. Chakarova, C. F. *et al.* TOPORS, implicated in retinal degeneration, is a cilia-centrosomal protein. *Hum. Mol. Genet.* **20**, 975–987 (2011).

51. Frew, I. J. *et al.* pVHL and PTEN tumour suppressor proteins cooperatively suppress kidney cyst formation. *EMBO J.* **27**, 1747–1757 (2008).

52. Friedman, J. S. *et al.* Mutations in a BTB-Kelch Protein, KLHL7, Cause Autosomal-Dominant Retinitis Pigmentosa. *Am. J. Hum. Genet.* **84**, 792–800 (2009).

53. Kigoshi, Y., Tsuruta, F. & Chiba, T. Ubiquitin Ligase Activity of Cul3-KLHL7 Protein Is Attenuated by Autosomal Dominant Retinitis Pigmentosa Causative Mutation. *J. Biol. Chem.* **286**, 33613–33621 (2011).

54. Oh, J. K. *et al.* Novel mutations in the 3-box motif of the BACK domain of KLHL7 associated with nonsyndromic autosomal dominant retinitis pigmentosa. *Orphanet J. Rare Dis.* **14**, 295 (2019).

55. Wolberger, C. Mechanisms for regulating deubiquitinating enzymes. *Protein Sci.* **23**, 344–353 (2014).

56. Desai, P. B., Stuck, M. W., Lv, B. & Pazour, G. J. Ubiquitin Links Smoothened to Intraflagellar Transport to Regulate Hedgehog Signaling. *bioRxiv* **219**, (2019).

57. Shinde, S. R., Nager, A. R. & Nachury, M. V. Lysine63-linked ubiquitin chains earmark GPCRs for BBSome-mediated removal from cilia. *bioRxiv* **219**, (2020).

58. Eguether, T. *et al.* The deubiquitinating enzyme CYLD controls apical docking of basal bodies in ciliated epithelial cells. *Nat. Commun.* **5**, 4585 (2014).

59. Sato, Y. *et al.* Structures of CYLD USP with Met1- or Lys63-linked diubiquitin reveal mechanisms for dual specificity. *Nat. Struct. Mol. Biol.* **22**, 222–229 (2015).

60. Poblete Gutiérrez, P. *et al.* Phenotype diversity in familial cylindromatosis: a frameshift mutation in the tumor suppressor gene CYLD underlies different tumors of skin appendages. *J. Invest. Dermatol.* **119**, 527–531 (2014).

61. Ramachandran, H. *et al.* Interaction with the Bardet-Biedl Gene Product TRIM32/BBS11 Modifies the Half-life and Localization of Glis2/NPHP7. *J. Biol. Chem.* **289**, 8390–8401 (2014).

62. Nordstrom-O'Brien, M. *et al.* Genetic analysis of von Hippel-Lindau disease. *Hum. Mutat.* n/a–n/a (2010).

63. Yim, H., Sung, C. K., You, J., Tian, Y. & Benjamin, T. Nek1 and TAZ interact to maintain normal levels of polycystin 2. *J. Am. Soc. Nephrol.* **22**, 832–837 (2011).

64. Borgal, L. *et al.* Casein kinase 1 α phosphorylates the Wnt regulator Jade-1 and modulates its activity. *J. Biol. Chem.* **289**, 26344–26356 (2014).

65. Borgal, L. *et al.* The ciliary protein nephrocystin-4 translocates the canonical Wnt regulator Jade-1 to the nucleus to negatively regulate β-catenin signaling. *J. Biol. Chem.* **287**, 25370–25380 (2012).

66. Su, X. *et al.* Bardet-Biedl syndrome proteins 1 and 3 regulate the ciliary trafficking of polycystic kidney disease 1 protein. *Hum. Mol. Genet.* (2014).

67. Wang, W., Wu, T. & Kirschner, M. W. The master cell cycle regulator APC-Cdc20 regulates ciliary length and disassembly of the primary cilium. *Elife* **3**, e03083 (2014).

68. Novarino, G., Akizu, N. & Gleeson, J. G. Modeling Human Disease in Humans: The Ciliopathies. *Cell* **147**, 70–79 (2011).

69. Davis, E. E. & Katsanis, N. The ciliopathies: a transitional model into systems biology of human genetic disease. *Curr. Opin. Genet. Dev.* **22**, 290–303 (2012).

70. Hildebrandt, F., Benzing, T. & Katsanis, N. Ciliopathies. *N. Engl. J. Med.* **364**, 1533–1543 (2011).

71. van Reeuwijk, J., Arts, H. H. & Roepman, R. Scrutinizing ciliopathies by unraveling ciliary interaction networks. *Hum. Mol. Genet.* **20**, R149–57 (2011).

72. Gerhardt, C. *et al.* The transition zone protein Rpgrip 1l regulates proteasomal activity at the primary cilium. *J. Cell Biol.* **210**, 115–133 (2015).

73. Chiang, A. P. *et al.* Homozygosity mapping with SNP arrays identifies TRIM32, an E3 ubiquitin ligase, as a Bardet-Biedl syndrome gene (BBS11). *Proc. Natl. Acad. Sci. U. S. A.* **103**, 6287–6292 (2006).

74. Sattar, S. & Gleeson, J. G. The ciliopathies in neuronal development: a clinical approach to investigation of Joubert syndrome and Joubert syndrome-related disorders. *Dev. Med. Child Neurol.* **53**, 793–798 (2011).

75. Nachury, M. V *et al.* A Core Complex of BBS Proteins Cooperates with the GTPase Rab8 to Promote Ciliary Membrane Biogenesis. *Cell* **129**, 1201–1213 (2007).

76. Remans, K., Bürger, M., Vetter, I. R. & Wittinghofer, A. C2 Domains as Protein-Protein Interaction Modules in the Ciliary Transition Zone. *CellReports* 1–9 (2014).

77. Choksi, S. P., Lauter, G., Swoboda, P. & Roy, S. Switching on cilia: transcriptional networks regulating ciliogenesis. *Development* **141**, 1427–1441 (2014).

78. Homan, C. C. *et al.* Mutations in USP9X are associated with X-linked intellectual disability and disrupt neuronal cell migration and growth. *Am. J. Hum. Genet.* **94**, 470–478 (2014).

79. Reijnders, M. R. F. M. R. F. *et al.* De Novo Loss-of-Function Mutations in USP9X Cause a Female-Specific Recognizable Syndrome with Developmental Delay and Congenital Malformations. **98**, 373–381 (2016).

80. Boldt, K. *et al.* An organelle-specific protein landscape identifies novel diseases and molecular mechanisms. *Nat. Commun.* **7**, 1–13 (2016).

81. Li, X. *et al.* USP9X regulates centrosome duplication and promotes breast carcinogenesis. *Nat. Commun.* **8**, 14866 (2017).

82. Kodani, A. *et al.* SFI1 promotes centriole duplication by recruiting USP9X to stabilize the microcephaly protein STIL. *J. Cell Biol.* **218**, 2185–2197 (2019).

83. Das, A., Qian, J. & Tsang, W. Y. USP9X counteracts differential ubiquitination of NPHP5 by MARCH7 and BBS11 to regulate ciliogenesis. *PLoS Genet.* **13**, e1006791–24 (2017).

84. Wood, S. A. *et al.* Cloning and expression analysis of a novel mouse gene with sequence similarity to the Drosophila fat facets gene. *Mech. Dev.* **63**, 29–38 (1997).

85. Evolutionary and Expression Analysis of the Zebrafish Deubiquitylating Enzyme, Usp9. 1–9 (2007).

86. Jolly, L. A., Taylor, V. & Wood, S. A. USP9X enhances the polarity and self-renewal of embryonic stem cell-derived neural progenitors. *Mol. Biol. Cell* **20**, 2015–2029 (2009).

87. Stegeman, S. *et al.* Loss of Usp9x Disrupts Cortical Architecture, Hippocampal Development and TGFβ-Mediated Axonogenesis. *PLoS One* **8**, e68287 (2013).

88. Yoon, S. *et al.* Usp9X Controls Ankyrin-Repeat Domain Protein Homeostasis during Dendritic Spine Development. *Neuron* **105**, 506-521.e7 (2020).

89. Dupont, S. *et al.* FAM/USP9x, a Deubiquitinating Enzyme Essential for TGFβ Signaling, Controls Smad4 Monoubiquitination. *Cell* **136**, 123–135 (2009).

90. Ebisawa, T. *et al.* Smurf1 Interacts with Transforming Growth Factor-β Type I Receptor through Smad7 and Induces Receptor Degradation. *J. Biol. Chem.* **276**, 12477–12480 (2001).

91. Xie, Y. *et al.* Deubiquitinase FAM/USP9X interacts with the E3 ubiquitin ligase SMURF1 protein and protects it from ligase activity-dependent self-degradation. *J. Biol. Chem.* **288**, 2976–2985 (2013).

92. Wrana, J. L., Attisano, L., Wieser, R., Ventura, F. & Massagué, J. Mechanism of activation of the TGF-beta receptor. *Nature* **370**, 341–347 (1994).

93. Yoon, S., Parnell, E. & Penzes, P. TGF-β-Induced Phosphorylation of Usp9X Stabilizes Ankyrin-G and Regulates Dendritic Spine Development and Maintenance. *Cell Rep.* **31**, 107685 (2020).

94. Bao, H., Reist, N. E. & Zhang, B. The Drosophila epsin 1 is required for ubiquitin-dependent synaptic growth and function but not for synaptic vesicle recycling. *Traffic* **9**, 2190–2205 (2008).

95. Lee, S., Wang, J.-W., Yu, W. & Lu, B. Phospho-dependent ubiquitination and degradation of PAR-1 regulates synaptic morphology and tau-mediated Aβ toxicity in Drosophila. *Nat. Commun.* **3**, 1312 (2012).

96. Johnson, B. V *et al.* Partial Loss of USP9X Function Leads to a Male Neurodevelopmental and Behavioral Disorder Converging on Transforming Growth Factor β Signaling. *Biol. Psychiatry* **87**, 100–112 (2020).

97. Park, S. M. *et al.* Brain Somatic Mutations in MTOR Disrupt Neuronal Ciliogenesis, Leading to Focal Cortical Dyslamination. *Neuron* **99**, 83–97.e7 (2018).

98. Foerster, P. *et al.* mTORC1 signaling and primary cilia are required for brain ventricle morphogenesis. *Development* **144**, 201–210 (2017).

99. Armour, E. A., Carson, R. P. & Ess, K. C. Cystogenesis and elongated primary cilia in Tsc1-deficient distal convoluted tubules. *Am. J. Physiol. Renal Physiol.* **303**, F584-92 (2012).

100. Rosengren, T., Larsen, L. J., Pedersen, L. B., Christensen, S. T. & Møller, L. B. TSC1 and TSC2 regulate cilia length and canonical Hedgehog signaling via different mechanisms. *Cell. Mol. Life Sci.* **75**, 2663–2680 (2018).

101. Takahashi, K., Nagai, T., Chiba, S., Nakayama, K. & Mizuno, K. Glucose deprivation induces primary cilium formation through mTORC1 inactivation. *J. Cell Sci.* **131**, (2018).

102. Sherpa, R. T., Atkinson, K. F., Ferreira, V. P. & Nauli, S. M. RAPAMYCIN INCREASES LENGTH AND MECHANOSENSORY FUNCTION OF PRIMARY CILIA IN RENAL EPITHELIAL AND VASCULAR ENDOTHELIAL CELLS. *Int. Educ. Res. J.* **2**, 91–97 (2016).

103. Pampliega, O. *et al.* Functional interaction between autophagy and ciliogenesis. *Nature* **502**, 194–200 (2014).

104. Al-Hakim, A. K. *et al.* Control of AMPK-related kinases by USP9X and atypical Lys 29/Lys33-linked polyubiquitin chains. *Biochem. J.* **411**, 249–260 (2008).

105. Bridges, C. R. *et al.* USP9X deubiquitylating enzyme maintains RAPTOR protein levels, mTORC1 signalling and proliferation in neural progenitors. *Sci. Rep.* **7**, 391 (2017).

106. Wrobel, L. *et al.* mTORC2 Assembly Is Regulated by USP9X-Mediated Deubiquitination of RICTOR. *Cell Rep.* **33**, (2020).

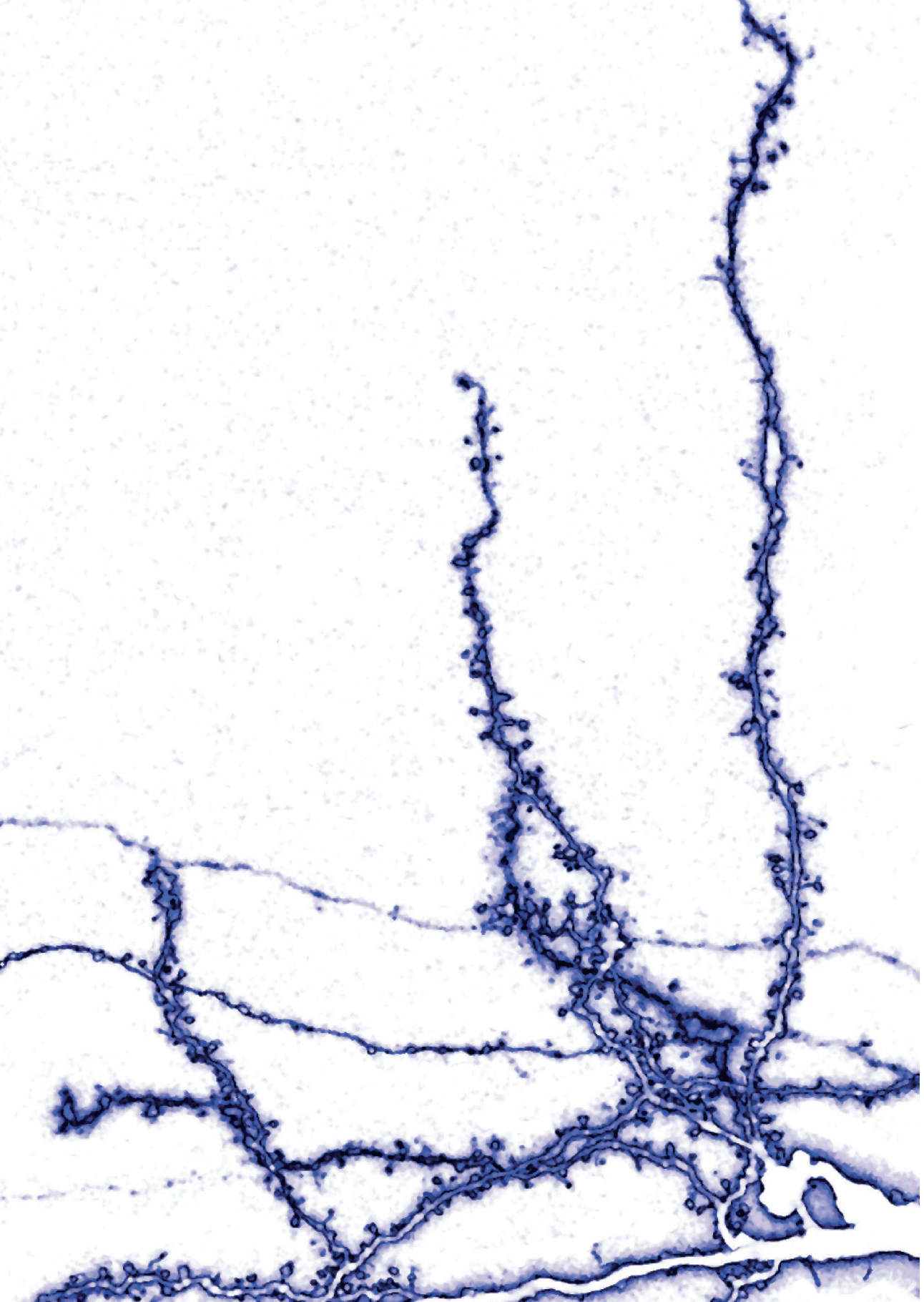

CHAPTER 7

Appendix
Data management
Curriculum vitae
Scientific publications
Acknowledgements

STATEMENT ON FAIR RESEARCH DATA MANAGEMENT

The data generated in the studies performed during my PhD were in accordance with the principles of the Declaration of Helsinki. The data is archived according to the Finable, Accessible, Interoperable, and Reusable (FAIR) principles. Experimental data obtained during my PhD at the Radboud university medical center (Radboudumc) were documented in validated, securely archived lab-journals or, in case of digital data, stored on secure data storage drives of the Radboudumc, Department of Human Genetics. All data is accessible by the associated authorized scientific staff members. Data, including exome sequencing data, in the published articles are available from the associated corresponding authors upon request. All zebrafish experiments were performed in accordance with local laws on animal protection of the associated collaboration institutes. All patient information and materials used for the studies in chapter 2, 3, 4, and 5 provided informed consent to their respective clinicians.

CURRICULUM VITAE

Originally from Los Angeles, California, Brooke Latour performed her undergraduate studies at Oberlin College in Ohio and obtained a bachelor's degree in biology. After graduation, she went on to work as a staff research scientist in the lab of Dr Bruce Walker at the Ragon Institute of MGH, MIT, and Harvard in Boston. There she was involved in research aimed at understanding the immune systems response to the human immunodeficiency virus (HIV) in an effort to facilitate HIV vaccine design. From there she moved back to Los Angeles to do research at the University of California, Los Angeles (UCLA), and it was here that she first realized her passion for developmental biology. At UCLA, under the supervision of Dr Denis Evseenko and Dr Gay Crooks, she studied mechanisms of blood development (hematopoiesis) and the hematopoietic stem cell niche. Specifically, this research focused on establishing a sustainable system for growing and supporting bone marrow ex vivo, which could be used for life-saving transplantation in patients with in-born blood diseases or cancer.

In 2012, she moved to the Netherlands, where she attended a biomedical sciences Master's (MSc) program in immunology and virology at the University of Utrecht. During her MSc studies she took a particular interest in genetic diseases and understanding how they affect organ formation. Following her MSc degree, she pursued a PhD in the group of Dr Ronald Roepman, studying the role of cilia in brain development. Cilia are highly specialized antenna-like structure that protrudes from the surface of most cell types in the human body and genetic disruptions in ciliary genes result in perturbed organogenesis. It was during her PhD that she first began working with Dr Nael Nadif Kasri to understand how particular genetic variants result in changes in early brain development. She began her postdoctoral work in 2019 with Dr Nadif Kasri, where she set up a protocol to generate cerebral organoids (brains-in-a-dish) in an effort to learn more about key aspects of brain development and elucidate the neurodevelopmental mechanisms that gives rise to Koolen de Vries Syndrome (KdVS). Currently she is a post-doctoral researcher and KdVS fellow in the Department of Human Genetics at the Radboud University Medical Center (Radboudumc), Netherlands where she studies mechanisms of brain development.

LIST OF SCIENTIFIC PUBLICATIONS

Brooke L Latour, Julie C Van De Weghe, Tamara Ds Rusterholz, Stef Jf Letteboer, Arianna Gomez, Ranad Shaheen, Matthias Gesemann, Arezou Karamzade, Mostafa Asadollahi, Miguel Barroso-Gil, Manali Chitre, Megan E Grout, Jeroen van Reeuwijk, Sylvia Ec van Beersum, Caitlin V Miller, Jennifer C Dempsey, Heba Morsy, Michael J Bamshad, Deborah A Nickerson, Stephan Cf Neuhauss, Karsten Boldt, Marius Ueffing, Mohammad Keramatipour, John A Sayer, Fowzan S Alkuraya, Ruxandra Bachmann-Gagescu, Ronald Roepman, Dan Doherty. "Dysfunction of the ciliary ARMC9/TOGARAM1 protein module causes Joubert syndrome." ***Journal of Clinical Investigation*** 130, 4423–4439 (2020).

Oud MM, **Latour BL**, Bakey Z, Letteboer SJ, Lugtenberg D, Wu KM, Cornelissen EAM, Yntema HG, Schmidts M, Roepman R, Bongers EMHF. "Cellular ciliary phenotyping indicates pathogenicity of novel variants in *IFT140* and confirms a Mainzer-Saldino syndrome diagnosis." ***Cilia***, 2018 Feb 23;7:1.

Latour B*, Van De Weghe JC*, Rusterholz TDS*, Grout ME, Aldinger KA, Shaheen R, Dempsey JC, Maddirevula S, Cheng YH, Phelps IG, Gesemann M, Goel H, Birk OS, Alanzi T, Rawashdeh R, Khan AO; University of Washington Center for Mendelian Genomics, Bamshad MJ, Nickerson DA, Neuhauss SCF, Dobyns WB, Alkuraya FS, Roepman R, Bachmann-Gagescu R, Doherty D**.** ***"****Mutations in ARMC9, which Encodes a Basal Body Protein, Cause Joubert Syndrome in Humans and Ciliopathy Phenotypes in Zebrafish."* ***The American Journal of Human Genetics*****,** 2017 Jul 6;101(1):23-36
*These authors contributed equally

Boldt K, van Reeuwijk J, Lu Q, Koutroumpas K, Nguyen TM, Texier Y, van Beersum SE, Horn N, Willer JR, Mans DA, Dougherty G, Lamers IJ, Coene KL, Arts HH, Betts MJ, Beyer T, Bolat E, Gloeckner CJ, Haidari K, Hetterschijt L, Iaconis D, Jenkins D, Klose F, Knapp B, **Latour B**, Letteboer SJ, Marcelis CL, Mitic D, Morleo M, Oud MM, Riemersma M, Rix S, Terhal PA, Toedt G, van Dam TJ, de Vrieze E, Wissinger Y, Wu KM, Apic G, Beales PL, Blacque OE, Gibson TJ, Huynen MA, Katsanis N, Kremer H, Omran H, van Wijk E, Wolfrum U, Kepes F, Davis EE, Franco B, Giles RH, Ueffing M, Russell RB, Roepman R; UK10K Rare Diseases Group. "An organelle-specific protein landscape identifies novel diseases and molecular mechanisms." ***Nature Communications*****, 2016** May 13;7:11491.

Latour B*, Reijnders MR*, Jolly L*, Mancini GM, Pfundt R, Wu KM, van Ravenswaaij-Arts CM, Veenstra-Knol HE, Anderlid BM, Wood SA, Cheung SW, Barnicoat A, Probst F, Magoulas

P, Brooks AS, Malmgren H, Harila-Saari A, Marcelis CM, Vreeburg M, Hobson E, Sutton VR, Stark Z, Vogt J, Cooper N, Lim JY, Price S, Lai AH, Domingo D, Reversade B; DDD Study, Gecz J, Gilissen C, Brunner HG, Kini U, Roepman R, Nordgren A, Kleefstra T. "*De Novo Loss-of-Function Mutations in USP9X Cause a Female Specific Recognizable Syndrome with Developmental Delay and Congenital Malformations.*" ***The American Journal of Human Genetics*,** 2016 Feb 4;98(2):373-81.
*These authors contributed equally

Wu L, Bluguermann C, Kyupelyan L, **Latour B**, Gonzalez S, Shah S, Galic Z, Ge S, Zhu Y, Petrigliano FA, Nsair A, Miriuka SG, Li X, Lyons KM, Crooks GM, McAllister DR, Van Handel B, Adams JS, Evseenko D. "*Human developmental chondrogenesis as a basis for engineering chondrocytes from pluripotent stem cells*." ***Stem Cell Reports*,** 2013 December 12: 1(6):575-89.

Brooke Latour *, Denis Evseenko,*, Wade Richardson, Mirko Corselli, Arineh Sahaghian, Yuhua Zhu, Rebecca Chan, Bruce Dunn, Gay Crooks. "*Lysophosphatidic Acid Mediates Myeloid Differentiation within the Human Bone Marrow Microenvironment.*" ***PLOS one*,** 2013 May 16;8(5).

*These authors contributed equally

Denis Evseenko, Yuhua Zhu, Katja Schenke-Layland, Jeffrey Kuo, **Brooke Latour**, Shundi Ge, Jessica Scholes, Gautam Dravid, Xinmin Li, W. Robb MacLellan, and Gay M. Crooks. "*Mapping the first stages of mesoderm commitment during differentiation of human embryonic stem cells*." ***Proc Natl Acad Sci U S A***, 2010 Aug 3;107(31):13742-7.

Ferreira MA, Mangion M, Brumme CJ, Zhao ZZ, Medland SE, Wright MJ, Nyholt DR, Gordon S, Campbell M, McEvoy BP, Henders A, Evans DM, Lanchbury JS, Pereyra F, **International HIV Controller Study* (LaTour B),** Walker BD, Haas DW, Soranzo N, Spector TD, de Bakker PI, Frazer IH, Montgomery GW, Martin NG. *Quantitative trait loci for CD4:CD8 lymphocyte ratio are associated with risk of type 1 diabetes and HIV-1 immune control*. ***The American Journal of Human Genetics***, 2010 Jan;86(1):88-92.
*authors listed in supplemental information

ACKNOWLEDGEMENTS

This thesis would not have been possible without the support and guidance of my supervisory team: Ronald and Nael.

Ronald, from the first time I met you at the interview, I was certain that your lab was exactly where I wanted to be. Thank you for opportunity to do my doctoral thesis with you and thank you for your mentorship. You are a source of encouragement and inspiration and I greatly appreciate your guidance, support, and ability to always find positivity in things. I am grateful that you allowed me the freedom to pursue every facet of my scientific creativity and to learn and grow as a scientist. Outside of the lab I also very much enjoyed the group BBQs, the port and wine tastings, the open air museum with your family, and the steak dinner with Dan. I am very glad our scientific paths have again intersected and I am excited to further explore and understand the role of cilia in brain development and disease with you.

Nael, I feel very fortunate that our paths crossed and landed me with the opportunity to continue my research in your lab. You provided me with structure and focus as well as the inspiration to continuously work to improve myself as a scientist, presenter, and teacher/supervisor. I appreciate how hard you work to create a sense of community in our group and I have very much enjoyed the lab retreats, dinners together, and party events. You have supported me and endeavored to help me learn to be a more practical and pragmatic researcher. I see the opportunities you have given me and I am grateful. Thank you.

I would also like to thank the doctoral thesis committee **prof. dr. Alessandra Cambi, prof. dr. Anna Ahkmanova**, and **prof. dr. Colin Johnson** for taking the time to read and evaluate my thesis.

I am grateful to all our collaborators whose invaluable contributions lead to the publication of our work together. **Han and Margot**, I consider the *USP9X* project to be my first project as a PhD student, there were certainly ups and downs as there often are with research projects (especially when they involve western blotting), but in the end I learned a lot from you both and it was a great pleasure to have the opportunity to work together. **Dan, Ruxandra, Julie, and Tamara** thank you for all of your efforts and insights, I am very proud of the work we did together on ARMC9 and TOGARAM1 and I think we make a great team. Additionally, **Dan** I very much appreciate all the time and effort you invested in the final push to get the TOGARAM1 manuscript out.

Dear paranymphs thank you for all the support, encouragement, and assistance you have given me during my PhD and in the time that followed. I am grateful to have you by my side at my defense.

Ka Man, I have thoroughly enjoyed the time we have spent together throughout my PhD and beyond. Our trips to Aesculaaf in the early days, beer tastings with Ollie and Jelle, hanging out with Luna and Freja, dinners out, GTs and sushi with Christian, and coffee were always great fun (and much needed). You are an absolute force of nature in the lab and you always go above and beyond, you never hesitated to help me with experiments or troubleshooting and your capacity for problem solving are well represented in this thesis. I remember while we were working on the *USP9X* paper you came in several times at 6 am to optimize the PCR so we could sequence the RNA from the exon skipping patient. Thank you for all that you do. One of the most memorable moments of my PhD experience was surviving the harrowing journey home from Cilia 2018 in Copenhagen with you, I feel like we make a good survivalist team. You have been a great friend and collaborator and I am so happy we have the opportunity to continue working together. Maybe Copenhagen 2025, the reunion tour?

Machteld, when I arrived at the Radboud, we immediately became good friends, I love our bbqs, fancy dinners, and NYEs with Coen and Martijn, as well as our bouldering and boxing dates. I enjoyed learning to culture urine derived renal epithelial cells from you and working on the IFT140 paper together, I am continuously impressed by your multi-tasking skills and seemingly effortlessly ability bring things together (though I do appreciate it is a lot of hard work). I have so many great memories of our time together in Ronald's lab, thank you for the support, reason, helpful intellectual discussions and afternoon coffees. I look forward to many more adventures together.

Teun, you made my PhD experience so much more survivable. I have greatly enjoyed all the excellent times we have had together: discussing science, brainstorming a convergence of our project (thank goodness mitochondria look so much like cilia), bouldering, matlab -ing, drinking and pipetting (not necessarily at the same time). I could not have asked for a better friend, support system, and like-minded person to exchange dark humor and cynical memes with. Thanks for that. I am forever grateful. While I miss you and Anouk greatly, I am happy you have found a new place to explore your ever expanding scientific curiosities and I am certain there will be many more brainstorming sessions, bouldering events, and beer drinking experiences in our future.

To the Genetic secretaries, **Ineke, Doménique, Miranda, and Baukje**, I am deeply thankful for all your help and seemingly endless knowledge of the interworking of the Radboudumc, we are so lucky to have you in the department. Additionally, **Ineke**, I wanted to say, thank you for your kind and helpful support, throughout the last 8 years I have asked you numerous (most likely rather irritating) questions and I so very appreciate your expertise and gracious assistance.

Saskia and Marlie, thank you for your hard work, assistance and your ability to maintain such a fastidious, clean and organized working environment.

In no specific order, a very special thanks to all of my Human Genetics colleagues, **Edgar, Ilse, Mireia, Theo, Lisette, Human, Tom, Galuh, Silvia, Rosanne, Celia, Ana, Margot, Christian, Laurens, Alex H, Richarda, Alex G, Ralph, Margo, Benny, Stefanie, Matthijs, Lonneke, Zeinab, Jason, Daniel, Bonnie, Jakob, Marc, Irene, and all of my protein and MNP lab mates,** who have offered their time, advice, career insight, brainstorming sessions, troubleshooting ideas, supplies, and/or a coffee break. These are some of the fundamentals of surviving a PhD and I am grateful for your help.

Marieke and Ben, thank you for your assistance with the airy scan. At a certain point during my PhD, I am pretty sure I spent more time with the LSM880 than I did at home. I very much appreciate your knowledgeable insight, problem solving capacity, and willingness to help me, even those few times when I sent panicked emails at 10 pm. Additionally **Ben**, thank you for "the whisky list," it will continue to be a source of joy for years to come.

Protein lab mates, past and present, **Machteld, Ka Man, Ideke, Mariam, Sylvia, Stef, Minh, Cenna, Siebren, Tess, Julio, Simone, Nikoleta, Satish, Jeroen, Dorus, Zeineb, Dinu, Kate** and of course honorary member **Margo**, I am grateful to you for the scientific discussions, great environment, extensive help, and emotional support.

Ideke, you are a treasure, from Y2H to LaLa Productions, some of the potentially most productive efforts of my PhD were spent with you. If you ever want to leave science to try and make it in Hollywood, let me know.

Stef, throughout my PhD you helped me a lot, specifically I really (really, really) appreciate the assistance and great work you did on the TOGARAM1 paper and I'm pretty sure you saved me from losing my mind, thank you for all your efforts and hard work.

Sylvia, you are an important contributor to this thesis and my overall PhD experience. Thank you for all the TAP, sequencing, WB, cloning, PCR, cell culture (the list goes on) assistance

as well as the restorative coffee breaks, thoughtful and supportive conversations, and good advice (both personally and professionally).

Minh, I have many lovely memories of our time together, it was my great pleasure to sit next to you during our overlap in Ronald's lab, we spent many late nights working, eating ramen, and discussing scientific possibilities and life in general. Arguably the time I came closest to being forcibly detained during my PhD was with you when, following Cilia 2018 in Copenhagen, we entered Birmingham, UK "under false pretenses" and the customs agent took our passports. As you said, if we can survive this, we can survive anything.

From the ubiquitome to Desem, **Mariam**, I have enjoyed our lunch and dinner dates, talks about life, cats, career, F1s, health, ubiquitin, cats, cilia, and everything else, cats. You are a pillar of the lab, from managing students to coordinating new projects, you throw yourself deeply into everything you do. Despite hating the idea of flex working, I am quite happy it has allowed us to be officemates so we can continue (if necessary) plotting to take over the world and other personality fitting career choices, thank you for all your help, guidance, advice, and realness.

To my MNP lab mates, from the moment I slowly crept my way into the group until now, **Teun, Britt, Monica, Anouk, Moritz, Astrid, Chantal, Eline, Naoki, Shan, Xiuming, Jon-Ruben, Ummi, Elly, Katrin, Emma, Rachel, Ilse, Imke, Ka Man, Marina, Yi, Marie, Dirk and Nael,** thank you for the collaboration, brainstorming sessions, technical support, and good times. I have really enjoyed working with all of you.

Katrin, thank you for taking me under your wing when I first started working with the MNP group during my PhD, you fastidiously taught me how to culture iPSCs and together with Vanessa we managed to set up the dual SMAD inhibition protocol to make NPCs. I remember the feeling of elation the first time we saw the formation of neuroepithelial rosettes under the microscope. You are a great scientist and I am happy we have had the opportunity to continue our work together.

Anouk, you are one of those very impressive people who just figures stuff out and gets it done. I appreciate your scientific expertise, your willingness to spend your time and efforts helping others (me), and how you graciously answered all of my RNAseq questions, even when I may have had to ask them more than once. You are a great scientist and friend. Thank you for all the great times bouldering, dining, BBQs, wine tastings, coffee chats and most recently visiting you and Teun in Leuven. I know we will have many more in the future.

Eline, from our recent trip to Leuven together with Sean and Ollie, all the way back to when you were an MSc student with Teun, thank you for all the lovely times together. I have enjoyed and appreciated the coffee and/or wine breaks, PhD movie making, scientific advice, dinners together and just hanging out. Also, you should probably put me in touch with your paranymphs so we can start plotting your movie.

Naoki, I remember when you first started in our group, you sent around an email introducing yourself and I tried to coerce you to come bouldering, while that failed I am very happy we have grown into such good friends. The squid BBQ, sushi parties, exquisite sake and prosecco, holiday dinners, and simply just hanging out, I have greatly appreciated the process of getting to know you better. You have also been a huge support with all things ephys related, thank you for your patience, assistance, ideas and time.

Chantal, thank you for all your hard work, you began assisting me with the *USP9X* iPSCs back in 2018, when you taught me how to plate MEAs and how to maintain iNeurons. Fast forward a few year and now we are on to making cerebral organoids, which I must say always look the most beautiful when you assist. Thank you.

Britt, thank you for all the MEA assistance, great times in and out of the lab, and most notably the delightful evenings of wine. I am so happy you have found a place in work and life that makes you happy and I very much look forward to visiting Belgium later in the year with you and Maarten.

Jon-Ruben, thank you for all the ephys insight and assistance, you have an impressive way of making something challenging and outside my comfort zone into something quite digestible, thank you for all the restaurant suggestions (you have not lead me astray yet) and your willingness to always discuss all things culinary. You are missed but I wish you a lot of joy in your new position in Utrecht.

Ilse, you have a lovely calming presence and an amazing capacity to get things done. Thank you for all the delightful and supportive talks, your willingness to help me both in and out of the lab, and the afternoon tea breaks at the trigon.

Moritz, I always feel a sense of restoration after our conversations, you are consistently full of ideas and inspiration and I immensely enjoy our brainstorming discussions together about anything and everything neuron related. While I miss you in the lab, I am hopeful our scientific paths will cross again in the future.

Silvia, Galuh, and Rosanne, I enjoyed our Monday movie nights, wine and sushi dinners at work, GTs and 4daagse festivals together. Thank you for the thoughtful conversations, late night company in the department, and rejuvenating coffee breaks. I enjoy your company immensely and am very happy we can continue these rituals in the years to come. Additionally, **Silvia**, thank you for always taking the extra effort to make me amazing Italian food without garlic and onions, playdates with David, iPSC advice and support, and the lovely dinners with Marc. **Galuh**, sharing an office with you during our PhDs was a lot of fun, I always enjoyed our spinning sessions, dance work outs (aka you just making fun of me), and working late with you.

Christian, the first time I met with you about the *USP9X* project, I thought you were terrifying, but several years later I have learned that is just one facet of your complex social charm. From Genetics borrels, GT and sushi evenings with Ka Man, and beer and pool at Piet Huismans to your career advice, kind reassurance and scientific contributions, thank you for the friendship and great times.

Dear **Ilse and Mireia**, my fellow late night workers, during my PhD the second half of my day was almost always spent with you, I really enjoyed our time together and appreciate the support, scientific expertise, opportunity to vent, poke bowls, and comradery. Additionally, **Ilse,** I miss you a lot but am very happy you have found a great place to further your scientific career, you are an exceptional scientist and they are very lucky to have you.

Edgar, from the first time I meet you I was impressed by your extensive scientific curiosity. One week you would have a hypothesis, the next week you would have set up the protocol entirely from scratch, and the third week you would have a data set and advice on the dos and don’ts of the experimental procedure. Much to my joy you also turned out to be a great and lovely person and I am happy we have remained good friends throughout the years and continue to go on (mostly culinary) adventures together with Eline and Ollie. Also **Eline**, I adore you and your love of cats. I look forward to many more dinners, home lab tours, and house visits.

Piotr and Anna, at some point very early on I realized I wanted to know you both for the rest of my life. I have immensely enjoyed all the time we have spent together, the good food and drinks, bouldering and BBQs, afternoon talks, Christmas dinners, Nixie, making perogies (even though all the ones Ollie and I made disintegrated), drinking wine, and just hanging out.

Alex and Laurens, my fellow lovers of Epicurean delights, thank you for your thoughtful insights, wonderful hospitality and dark humor. It is always greatly enjoyed.

Laurens, from the first time we met over beers to all of the wonderful beers times that followed, we have become great friends and you are someone I know I can always count on. I also appreciate that you were always direct with me (I enjoyed being told “I don’t think that thing you are asking for is actually what you want”). I miss you greatly but I know that we have many more memories ahead of us. Much love to you and **Pallavi**.

A special thanks to all my bouldering people: **Teun, Anouk, Anna, Piotr, Kate, Theo, Martijn, Marjolein, Sarah, Matze, and Imre**. The time I have spent climbing at GRIP provided me with excellent friends, a great work out, and the capacity to maintain my sanity, more or less.

Thank you to the members of the **Gay Crooks lab** at UCLA. **Denis, Judy, Lisa, Chintan, and Gay**, thank you for your mentorship. You helped me find the courage to explore new avenues and I am grateful for the support and guidance.

To my Utrecht friends, **Stephin, Koen, Remko, and Veerle**, though none of us are in Utrecht anymore, the time we spent together there laid the groundwork for my love of the Netherlands. Whether it was spinning and bar hopping, thesis writing and library coffee, or pilates and Keek, thank you for helping me acclimate to my life here. I adore you guys.

Hendrik, I knew we would be good friends from the first moment we met. From Halloween parties and Olivier’s to borrels at the Hubrecht and Japanese whisky bars, it has been a great joy to explore the (culinary) world with you. I still think we should go on the 8 hour food tour of Bologna with Charissa and Ollie. Much love to you and **Charissa**.

Alejo, it has been a joy getting to know you over the course of the last few years. After knowing you for only a few days from the course in Bertinoro, you offered to show Ollie and me around Milan. Shortly there after, you came to visit us in NL and the rest is history. From our scientific discussions, your extremely helpful advice, to beer festivals and 6 hour zoom dates, I absolutely adore you and am grateful for all you have brought to my life. Also I promise Ollie and I will come visit you in SF sometime soon. I miss you.

Aisha, Ish, you have always been an amazing friend, support, and partner in crime. Thank you for helping me survive the Ragon Institute as well as Boston. I miss you and love you dearly. Hopefully we can do a Euro tour sometimes but until then all the best and much love to you, Tiala, and all your family.

Dr Kane, every time something meaningful happens in my life, I think of you. Thank you for all you have done.

Dear **Janny, Merijn and Kevin, G and Isabelle**, thank you for all the support, kindness and lovely family get togethers. Our time together is always gezellig and continues to become even more so with the addition of Valerie, Colin, Sophie, and Zoey.

Thank you to my family, who has always supported me. **Grandpa,** I always felt as a fellow scientist we had a special connection. **Grandma** though you are not here anymore, the memories of you are always with me, it took a bit of growing up for me to realize how incredible it was of you to host me, a "spirited" and unruly child, for months on end every summer at the ranch, that time was magical as we built gardens together, painted, and hiked through the forest, in some ways you were like the older sister I always wanted, thank you for all the memories. **Aunt Sandy,** I definitely think your amazing, imaginative stories were a corner stone of my rich internal world. **Aunt Tam**, I have always enjoyed visiting you and Mike and Alex in your homes across North America. Your beautiful art, gardens and way of being are a great source of joy and connectedness.

Juliana, there is no one in this world I would rather have wine and donuts with. We do not get to see each other very often, but when we do I feel like no time has passed at all. Thank you for your support and friendship and willingness to travel across the world to visit me. Much love to you and your dad.

Sophie, I have always felt like we were sisters. From middle school to post graduate work we have seen a lot together, pool parties and sleep overs at your mom's house, movie screenings at your dad's, thanksgivings in Chicago, trips to the Natural History Museum, and behind the scenes at the Academy Museum, you are an amazing artist, mother and friend. I have enjoyed all our moments together and am looking forward to many more (and of course to meeting Fidel as soon as possible). Thank you for all your love and support. Much love to you and Victor.

Julia, my honorary paranymph. You have been an incredible friend for the last 30 years, you have supported me in ways I cannot put into words. I am forever grateful to you, I can say without a doubt your friendship has made both me and my life better. Thank you, I love you dearly. Also of course, love to Tashi and Simone.

To **my three parents**, no one deserves more gratitude than you. Thank you for your unwavering support and encouragement. I would not be who I am today without you and I love you. **Mom**, thank you for all your understanding, insights, and wisdom. **Dad and Kim**, thank you for believing in me and supporting my choice to go on this journey so far from home. I am grateful to all of you for helping me get to where I am today.

Ollie, my shared first and last co-author, team mate, co-parent of Sushi and Soba, and love of my life. Thank you for all the support, advice, and adventures. Thank you for helping me manage anything and everything that has come my way. From traveling the world to watching Netflix in pajamas, I have enjoyed every moment with you and look forward to all the adventures and evenings on the couch to come. I love you.